

---

# Measurement of the atmospheric neutrino energy spectrum

---



# Measurement of the atmospheric neutrino energy spectrum

ACADEMISCH PROEFSCHRIFT

TER VERKRIJGING VAN DE GRAAD VAN DOCTOR  
AAN DE UNIVERSITEIT VAN AMSTERDAM  
OP GEZAG VAN DE RECTOR MAGNIFICUS  
PROF. DR. D. C. VAN DEN BOOM  
TEN OVERSTAAN VAN EEN DOOR HET COLLEGE VOOR PROMOTIES  
INGESTELDE COMMISSIE,  
IN HET OPENBAAR TE VERDEDIGEN IN DE AGNIETENKAPEL  
OP MAANDAG 2 JULI 2012, TE 14:00 UUR

door

**Dimitrios Palioselitis**

geboren te Katerini, Griekenland

Promotor : Prof. dr. Paul M. Kooijman  
Co-promotor : Dr. M. Patrick Decowski

Faculteit der Natuurwetenschappen, Wiskunde en Informatica

The work described in this thesis is part of the research program of “het Nationaal Instituut voor Subatomaire Fysica (Nikhef)” in Amsterdam, the Netherlands. The author was financially supported by “de Stichting voor Fundamenteel Onderzoek der Materie (FOM)”, which is funded by “de Nederlandse Organisatie voor Wetenschappelijk Onderzoek (NWO)”.

Στους γονείς μου,  
Απόστολο και Ζωή



# CONTENTS

<b>Introduction</b>	<b>1</b>
<b>1 Atmospheric neutrinos</b>	<b>5</b>
1.1 Cosmic rays . . . . .	5
1.2 Origin and acceleration of cosmic rays . . . . .	8
1.3 Atmospheric neutrinos . . . . .	10
1.3.1 Primary cosmic ray spectrum . . . . .	13
1.3.2 Geomagnetic effect . . . . .	14
1.3.3 Atmospheric model . . . . .	15
1.3.4 Primary nucleon flux evolution . . . . .	16
1.3.5 Approximate analytic solution . . . . .	18
1.4 Conventional atmospheric neutrino flux calculations . . . . .	20
1.5 Prompt atmospheric neutrino flux calculations . . . . .	22
1.5.1 Extreme prompt flux calculation combinations . . . . .	27
1.6 Neutrino oscillations . . . . .	31
<b>2 The ANTARES detector</b>	<b>35</b>
2.1 Neutrino interactions . . . . .	35
2.2 Muon propagation . . . . .	37
2.2.1 Čerenkov radiation . . . . .	38
2.2.2 Muon propagation . . . . .	40
2.3 The ANTARES project . . . . .	40
2.4 Detector layout . . . . .	41
2.5 The site . . . . .	44
2.5.1 Water optical properties . . . . .	44
2.5.2 Optical background . . . . .	45
2.5.3 Sedimentation and biofouling . . . . .	45
2.6 Data acquisition . . . . .	47
2.6.1 Signal digitization . . . . .	47
2.6.2 Data transmission . . . . .	49
2.6.3 Data filtering and storage . . . . .	49

2.7	Trigger . . . . .	50
2.8	Detector calibration . . . . .	51
2.8.1	Time calibration . . . . .	51
2.8.2	Charge calibration . . . . .	53
2.8.3	Position calibration . . . . .	55
2.9	Detector history and status . . . . .	57
2.10	Other neutrino telescopes . . . . .	57
<b>3</b>	<b>Energy Reconstruction</b>	<b>59</b>
3.1	Muon energy loss . . . . .	59
3.1.1	Energy loss processes . . . . .	63
3.1.2	Light propagation and detection . . . . .	64
3.2	Monte Carlo simulation tools . . . . .	69
3.3	Track reconstruction . . . . .	71
3.4	Maximum likelihood energy reconstruction . . . . .	75
3.4.1	Probability density functions . . . . .	75
3.4.2	Likelihood function . . . . .	77
3.5	Energy reconstruction performance . . . . .	81
3.5.1	Energy resolution . . . . .	81
3.5.2	Offset correction . . . . .	84
3.5.3	Dependence on track reconstruction quality . . . . .	85
3.5.4	Effect of scattering model . . . . .	89
<b>4</b>	<b>Unfolding the atmospheric neutrino spectrum</b>	<b>91</b>
4.1	Continuous and discrete ill-posed problems . . . . .	92
4.2	Singular Value Decomposition (SVD) . . . . .	94
4.3	SVD regularized unfolding . . . . .	96
4.4	Performance and stability of the method . . . . .	103
4.5	Neutrino effective area . . . . .	114
4.6	Atmospheric neutrino energy spectrum . . . . .	116
4.7	Systematic Uncertainties . . . . .	118
4.8	Conclusions and outlook . . . . .	120
<b>5</b>	<b>Event selection</b>	<b>121</b>
5.1	Data selection . . . . .	121
5.2	Atmospheric muon background rejection . . . . .	124
5.2.1	Atmospheric muon background . . . . .	124
5.2.2	Selection criteria . . . . .	126
5.3	Data - Monte Carlo comparisons . . . . .	128
5.4	Distribution of the energy observable . . . . .	132
5.5	Summary . . . . .	133

---

<b>6 Measurement of the atmospheric neutrino spectrum</b>	<b>135</b>
6.1 Atmospheric neutrino energy deconvolution . . . . .	135
6.2 Systematic uncertainties . . . . .	136
6.3 Results . . . . .	142
6.4 Summary and outlook . . . . .	146
<b>Bibliography</b>	<b>149</b>
<b>Summary</b>	<b>161</b>
<b>Samenvatting</b>	<b>165</b>
<b>Acknowledgements</b>	<b>167</b>



# INTRODUCTION

When our ancestors turned their gaze to the night sky thousands of years ago, they were performing the first astronomical observations. The human eye, sensitive to the visible part of the electromagnetic spectrum, was the biological instrument able to observe distant bright objects on the sky. Many ancient civilizations developed a keen interest in astronomical objects among them the Babylonians, the Egyptians, the Greeks and the Chinese. The first observations using a telescope, invented in the Netherlands at the beginning of the 17th century, were performed by Galileo who was able to observe objects magnified as much as thirty times. In the course of the 19th century, astronomy was not anymore restricted to the visible part of the spectrum. Techniques were developed that allowed scientists to see a world hitherto invisible to the naked eye. Radiation beyond the infrared and ultraviolet edges of the spectrum, from gamma-rays to radio waves, was detected allowing men to expand their knowledge of the cosmos. Modern man has been privileged to see images of immense beauty from the far away corners of the visible universe with the help of the Hubble telescope, orbiting around the Earth.

Our civilization has been using light for these observations for millennia. But our Earth is not merely swimming in a sea of light. It was Victor F. Hess who, in 1912, discovered that high energy radiation is reaching our Earth from outer space. A few years later it was verified that these *cosmic rays* were charged particles. A new branch of astronomy was born, that used the influx of these charged particles for observational purposes. *Cosmic rays*, consisting mainly of protons and other nuclei and spanning many orders of magnitude in energy, reach our Earth. One of the questions that remains unanswered until the present day is where do these high energy *cosmic rays* come from and how are they accelerated to such high energies. Possible accelerator candidates include supernova remnants, gamma ray bursts and active galactic nuclei. The IceCube collaboration, however, has recently placed strong constraints on the neutrino production in gamma ray bursts [Abba 12], eliminating GRB's as prime candidates of *cosmic rays*.

Whereas light is attenuated in interstellar matter and charged particles are deflected from their original direction due to the presence of magnetic fields, neutrinos may open a new window to the universe, providing us with valuable information on the origin and acceleration mechanisms of the high energy *cosmic rays*. Neutrino astronomy is a relatively young research field. Neutrinos originating from the Sun were detected for

the first time by Raymond Davis and John Bahcall with the Homestake mine Chlorine experiment [Clev 98], shedding light into the energy production mechanism taking place in our Sun. Significant progress has been made in the following decades with the discovery that neutrinos oscillate [Fuku 98], i.e. they change their flavor as they travel, explaining the lower neutrino rates that Davis measured compared to the expectations. The supernova explosion in the Large Magellanic cloud in 1987 lead to an increased neutrino flux measured by the Kamiokande-II, IMB and Baksan neutrino detectors [Hira 87; Hain 88; Alek 88], confirming the theoretical models describing core collapse supernovae. Neutrinos that can be produced in the sources of cosmic rays are referred to as *cosmic neutrinos*. Neutrinos, massive, but lighter than any other known particle, interact only weakly with their environment. This makes the task of detecting them very challenging. By the time the reader will go through the pages of this introduction, trillions of them will have passed through his body, the book he is holding, the Earth itself, and will be in the mean time millions of kilometers away. Ingenious means must therefore be devised in order to capture these elusive particles. However, the high fluxes involved with these particles make this task less daunting. The ANTARES neutrino telescope was built for this purpose. It is located at the bottom of the Mediterranean sea, south of France. It consists of 12 vertical strings, equipped with photomultiplier tubes that detect the Čerenkov light that is produced by muons as they traverse the detector. Some of these muons will be the product of neutrinos that interacted in the vicinity of the detector, producing them.

High energy atmospheric neutrinos are the topic of this thesis. They are produced in particle cascades initiated by the interaction of *cosmic rays* with nuclei in the Earth's atmosphere, differentiating them from *cosmic neutrinos*. The search for cosmic sources of high energy neutrinos is not a trivial task. At relatively low energies, of the order of a few TeV, the atmospheric neutrino flux is so much higher than the expected galactic or extragalactic flux making it virtually impossible to extract a cosmic signal over this background. At higher energies, a cosmic component is expected to be visible above the steeply falling atmospheric neutrino spectrum. It is obvious that a precise knowledge of the atmospheric neutrino spectrum is of prime importance for neutrino astronomy, since it constitutes the irreducible background for these searches. The goal of this work is the measurement of the atmospheric neutrino energy spectrum. This measurement may also provide information about high energy scattering processes outside the reach of present day accelerators. This can be achieved by examining the component of the atmospheric neutrino flux that has its origins in the decay of charmed hadrons in the atmosphere.

The question we are called to answer is: how many neutrinos are produced in the atmosphere through collisions of high energy *cosmic rays* with air molecules and what is their energy? In order to achieve this we develop a muon energy reconstruction method, based on a maximum likelihood method approach. The reconstructed muon spectrum differs from the physical neutrino spectrum due to limited resolution effects. A singular value decomposition approach [Höck 96] is used to unfold the atmospheric neutrino energy spectrum. The AMANDA and IceCube collaborations, operating a neutrino detector immersed in the glacial ice of the South Pole have recently measured

this spectrum [Abba 10; Abba 11]. The work presented here is the first measurement of the atmospheric neutrino energy spectrum with an underwater deep sea detector, covering a neutrino energy range between  $10^{2.5}$  and  $10^{5.3}$  GeV.

This thesis is organized as follows. Chapter 1 outlines the theoretical framework of the present work, serving as an introduction to cosmic ray physics and describing the progress that has been made on the calculation of the atmospheric neutrino flux. The ANTARES detector and its principles of operation are described in chapter 2. The method we employ to reconstruct the energy of muons passing through the apparatus and the reconstruction performance are explained in detail in chapter 3. The methodology on how the distribution of the reconstructed muon energies can provide us with the atmospheric neutrino energy spectrum is examined in chapter 4. Chapter 5 focuses on the criteria applied for the final data sample selection. The measured atmospheric neutrino energy spectrum and an estimation of the measurement uncertainties are presented in chapter 6.



# ATMOSPHERIC NEUTRINOS

In the present chapter the theory behind the high energy atmospheric neutrino flux is described. Section 1.1 describes the status of our present knowledge of cosmic rays, the first ingredient for atmospheric neutrino production. The following three sections emphasize the calculation of the atmospheric neutrino flux and the description of its two components, namely the conventional flux due to pion and kaon decays and the prompt flux due to charm hadron decays. We conclude with a brief discussion on neutrino oscillations and their relevance to this work.

## 1.1 Cosmic rays

The planet we inhabit is constantly bombarded by charged particles called cosmic rays. The majority of cosmic rays originate from outside the Solar System and their energies span a range of many orders of magnitude, from a few MeV up to  $10^{14}$  MeV. Cosmic rays (CR) produced in the acceleration sources in the cosmos are referred to as *primordial*, in contrast to the *primary* cosmic rays, which are particles of cosmic radiation that reach the top of the Earth's atmosphere. Cosmic rays consist predominantly of protons, a fraction of  $\sim 94\%$ , followed by  $\sim 5\%$  Helium nuclei, while heavier elements account for only  $\sim 1\%$  of the bulk of cosmic rays [Revi 11]. The chemical abundance of the cosmic rays is very similar to the abundances of interstellar matter observed in our Solar System through chemical analysis of meteorites or solar photosphere spectroscopy (fig. 1.1). There are differences in the abundances observed for Lithium (Li), Beryllium (Be) and Boron (B), as well as Scandium (Sc), Titanium (Ti), Vanadium (V), Chromium (Cr) and Manganese (Mn). These differences are attributed to the spallation of heavier elements such as Carbon (C), Oxygen (O) and Iron (Fe) on interstellar matter on their way from their sources to the Earth.

The flux of cosmic rays is described by a steeply falling energy-dependent spectrum (fig. 1.2). To appreciate the steepness of the spectrum one has to consider that while at energies of a few GeV the influx of cosmic ray particles is around  $10^3 \text{ s}^{-1} \text{ m}^{-2}$ , for particles of energies close to  $10^{11}$  GeV, this number is  $10^{-2} \text{ km}^{-2} \text{ yr}^{-1}$ . It is evident that the determination of such low rates pose a significant experimental challenge. Especially

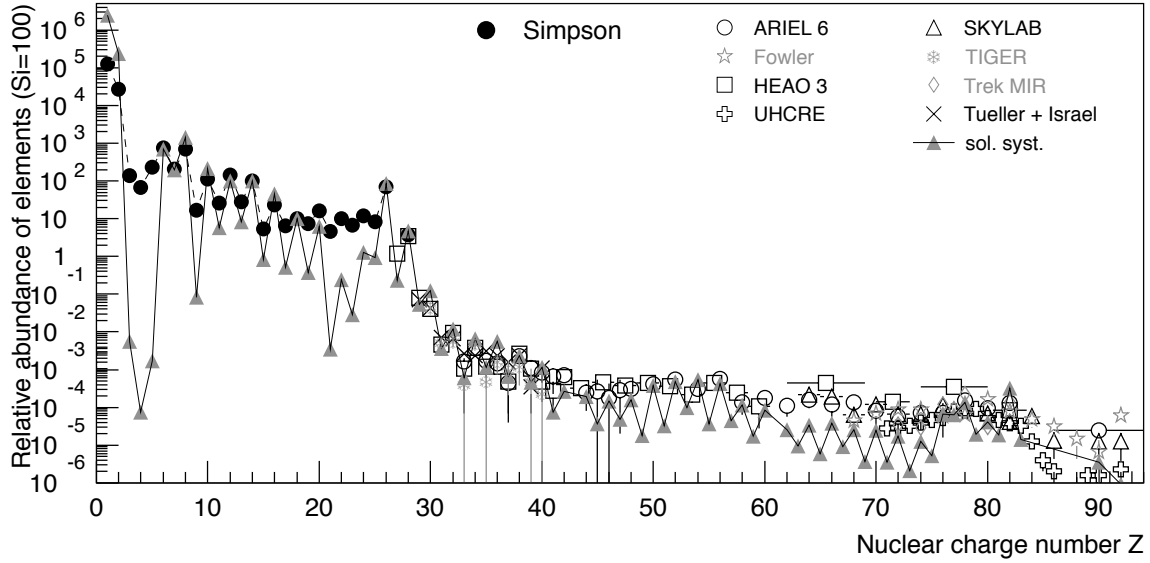


Figure 1.1: Elemental abundances in cosmic rays as a function of the atomic number, normalized to Silicon (Si). The elemental abundances in the Solar System are shown for comparison. Figure from [Blue 09].

for the highest energy cosmic rays, large detection areas are necessary in order to obtain sufficient statistics. The energy spectrum follows a power law of the form:

$$\frac{dN}{dE} \propto E^\gamma. \quad (1.1.1)$$

The steepness of the spectrum depends on the energy. The *spectral index*  $\gamma$  is approximately  $-2.7$  at energies up to several PeV, at which point the slope changes. This point in the spectrum is called the *knee*, and the *spectral index* changes to  $\gamma \simeq -3.1$  for higher energies. A flattening ( $\gamma \simeq -2.7$ ) at the *ankle* of the spectrum is observed at higher energies  $\sim 4 \times 10^{18}$  eV. Above  $4 \times 10^{19}$  eV the spectrum drops away steeply. Very little is known about the origin of these extremely high energy cosmic rays. Cosmic rays with energies of less than a few GeV are significantly affected by the solar wind, which consists mainly of charged particles such as protons and electrons. Magnetic irregularities carried by the solar wind can significantly alter the direction and reduce the rate of low energy particles that reach the Earth. Cosmic rays propagating in the galaxy are deflected by magnetic fields in the galaxy of the order of  $B \sim 3 \mu\text{G}$ , while extragalactic cosmic rays are deflected also by intergalactic magnetic fields of the order of nG.

The majority of cosmic rays up to energies of  $\sim 10^{18}$  eV is assumed to originate from within the Milky Way. Estimates of the maximum attainable energy in supernova remnant (SNR) acceleration give values in the range of  $10^{15} - 10^{18}$  eV [Bere 96; Luce 00]. Various models have been proposed to explain the origin of the *knee* [Hoer 04]. The steepening of the spectrum above the *knee* can be attributed to the fact that most cosmic ray accelerators within the galaxy have already reached their maximum energy.

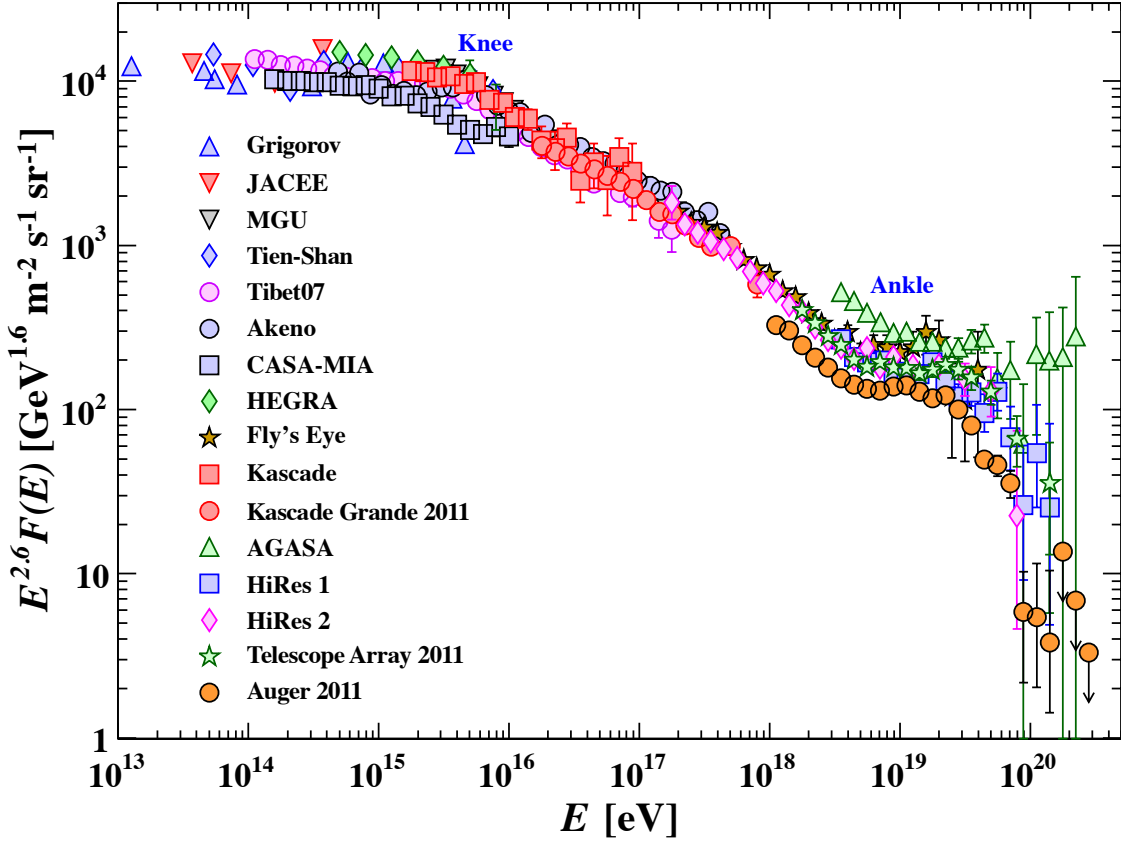


Figure 1.2: Measurements of the CR energy spectrum, figure from [Revi 11]. Low energy measurements can be performed directly by high-altitude balloon experiments. As the flux decreases dramatically for higher energies, very large ground based experiments are employed.

Another explanation is related to the leakage of particles from our galaxy, especially for the highest energies where the effect of intergalactic magnetic fields is weaker. For particles with higher  $Z$ , more energy is required to escape the galactic magnetic field. Therefore, the position of the knee depends on the atomic number. The maximum attainable energy in SNR's is also dependent on the atomic number of the particle accelerated. The iron knee would manifest itself at higher energies than the proton knee, consequently affecting the chemical composition of cosmic rays above  $\sim 10^{15}$  eV.

The flattening at the ankle is believed to be due to an extragalactic flux component, dominating over the softer, i.e. steeper, galactic component. In addition, the dip structure at the area of the *ankle* is interpreted as being due to energy losses of extragalactic protons through the:

$$p + \gamma_{CMB} \longrightarrow p + e^+ + e^- \quad (1.1.2)$$

interaction with the photons of the cosmic microwave background (CMB) [Bere 06]. For energies above  $\sim 6 \times 10^{19}$  eV, cosmic ray particles will interact inelastically with the

cosmic microwave radiation. Protons interacting with the 2.7 K CMB photons, produce pions via the  $\Delta$  resonance:

$$p + \gamma_{CMB} \longrightarrow \Delta^+ \longrightarrow p + \pi^0, \quad (1.1.3)$$

$$p + \gamma_{CMB} \longrightarrow \Delta^+ \longrightarrow n + \pi^+, \quad (1.1.4)$$

thus introducing a sharp cutoff in the spectrum for higher energies. In addition, photodissociation of heavy nuclei would have a similar effect on the spectrum. This was first realized by Greisen, Zatsepin and Kuz'min (GZK) [Grei 66; Zats 66]. The Akeno Giant Air Shower Array (AGASA) collaboration has reported events contradicting the GZK suppression [Take 98]. However, this was not observed by High Resolution Fly's Eye (HiRes) [Abba 08], the Pierre Auger Observatory [Abra 08; Abra 10] and Telescope Array [Tsun 11].

## 1.2 Origin and acceleration of cosmic rays

The origin of cosmic rays and their acceleration mechanisms are not identified or understood at present. It is assumed that cosmic rays produced in a certain source, are accelerated inside or near the source itself. In addition, cosmic rays can be accelerated in the intergalactic medium by interactions with gas clouds.

When a massive star of a certain mass range burns up all of its hydrogen fuel, the gravitational pressure due to the star's own mass dominates over the outward radiation pressure from the nuclear reactions that take place in its core. The star begins a gravitational collapse which increases the star's density and therefore temperature. At high enough temperatures, the process of helium burning begins in the star and equilibrium is once again restored. At a certain point, the helium is also exhausted and this process of equilibrium followed by gravitational collapse continues until the successive fusion processes lead to the production of elements of the iron group. At this stage, external energy is needed to create heavier elements. The fusion process stops and the star collapses under its own gravitational pull. During this implosion, stellar matter is ejected into interstellar space and a dense neutron star is created in the place of the once bright star. The ejected matter from this explosion, called type-II supernova (SN), creates a shock front at which particles can be accelerated. Another category of supernovae is the type-Ia supernova. They originate from the explosion of white dwarfs, stars that have completed their life cycle and are composed of carbon and oxygen. A white dwarf that surpasses the Chandrasekhar limit of around 1.38 solar masses due to accretion of mass from a companion object, cannot support gravitational pressure by electron degeneracy pressure alone. This pressure is attributed to the Pauli exclusion principle, forbidding electrons in a high density environment such as a white dwarf from occupying identical quantum states. Carbon fusion begins leading to the eventual supernova explosion of the star.

Particles gain energy by colliding and being reflected by the shock wave front, or by being trapped between two shock waves and accelerated as they reflect back and forth

between the two outward moving fronts. Particles accelerated in this way are provided with a relative energy gain:

$$\frac{\Delta E}{E} \propto \frac{u_s}{c}, \quad (1.2.1)$$

where  $u_s$  is the velocity of the shock. This type of acceleration mechanism is known as Fermi's first order acceleration and is linear in the shock velocity. The second order Fermi mechanism describes the acceleration of particles during their interaction with magnetic clouds. Particles scatter elastically in the magnetic cloud, eventually gaining energy:

$$\frac{\Delta E}{E} \propto \frac{u_s^2}{c^2}. \quad (1.2.2)$$

This mechanism is quadratic in the cloud velocity, hence its name. The timescales involved with particle acceleration of this type are very long due to the very low cloud velocities relative to the relativistic particle velocities.

During gravitational collapse, the radius of a star becomes significantly smaller. The dense matter leads to neutron production via electron capture:



The Fermi energy of electrons in the neutron star is higher than the maximum energy that electrons can acquire in neutron beta decay. Therefore, Pauli's principle forbids further neutron decay and the star turns into a spinning and dense neutron star. In order to conserve angular momentum during the collapse, the rotational frequency of the neutron star needs to increase. Additionally, the original magnetic field of the star is enhanced during the contraction. This can be understood by considering the conservation of magnetic flux  $\Phi \equiv \int \mathbf{B} d\mathbf{A}$ , leading to denser magnetic field lines as the surface area decreases. The extraordinarily high magnetic fields are usually not aligned with the rotational axis of the neutron star. The strong electric fields produced by the off-axis rotation of the magnetic dipole field, are in principle sufficient to accelerate charged particles up to the very high energies. Under crude energy considerations, the energy density of cosmic rays ( $\sim 1 \text{ eV/cm}^3$ ) can be supported by acceleration in shock waves as well as highly magnetized neutron stars (pulsars) [Grup 05].

Another possible acceleration source is a black hole or pulsar binary system. Matter is pulled by the star's companion, forming an accretion disk around the compact object. Extremely strong electromagnetic fields produced during the accretion process are capable of accelerating charged particles. Compact nuclei of active galaxies are also capable of accelerating charged particles up to extremely high energies. The jets of shock-accelerated electrons and protons in Active Galactic Nuclei (AGN) could initiate electromagnetic and hadronic cascades. The product of the electromagnetic cascades are high energy  $\gamma$  rays produced by inverse Compton scattering with electrons from the jet. In all cases where high energy protons are created and matter is available for interactions, pions and therefore high energy photons and neutrinos are produced. These are the sought after cosmic neutrinos.

### 1.3 Atmospheric neutrinos

In addition to galactic or extragalactic sources, neutrinos are produced in the Earth's atmosphere by collisions of primary cosmic rays with air nuclei. The fragments of the collisions between cosmic rays and atomic nuclei include pions, kaons and other unstable hadrons, that give rise to the atmospheric neutrino flux through their decay:

$$\pi^\pm \longrightarrow \mu^\pm + \nu_\mu(\bar{\nu}_\mu), \quad (1.3.1)$$

$$\mu^\pm \longrightarrow \bar{\nu}_\mu(\nu_\mu) + \nu_e(\bar{\nu}_e) + e^\pm \quad (1.3.2)$$

and similarly for kaons. Pions and kaons at high enough energies can interact before they decay, as discussed later in this section, with nuclei in the atmosphere producing secondary hadrons. The contribution to the neutrino flux from muon decay is sometimes neglected since most muons of sufficient energy will reach the Earth before decaying. Less than 15% of neutrinos with energies higher than 100 GeV come from muon decay. The flux due to muon decay decreases even further with increasing muon energy. The atmospheric muon neutrino flux is therefore predominantly associated with muon production rather than muon decay. This also means that muon neutrinos are in general produced at higher altitudes, since the muon lifetime is about two orders of magnitude larger than the pion lifetime. Muon decay is however responsible for the majority of electron neutrinos. The decay probabilities for pions, kaons and muons as a function of distance is illustrated in figure 1.3. Pions and kaons give rise to the so-called conventional atmospheric neutrino flux. The  $\nu_\mu/\bar{\nu}_\mu$  atmospheric flux ratio is close but higher

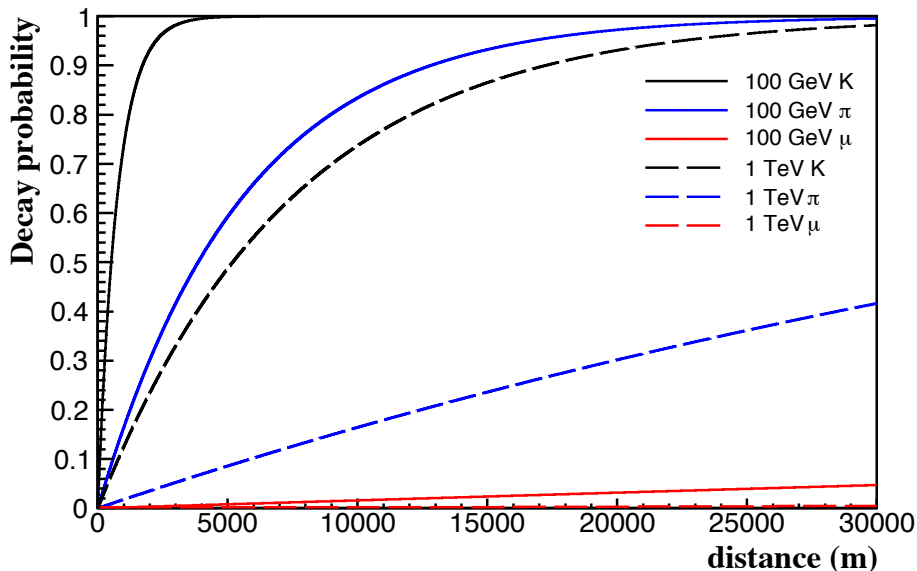


Figure 1.3: Decay probability as a function of the travelled distance for 100 GeV and 1 TeV  $\pi$ ,  $K$  and  $\mu$ . The contribution of neutrinos from muon decay is negligible compared to pion and kaon decay.

Particle	Content	$mc^2$ (MeV)	$c\tau$ (m)	lifetime $\tau$ (s)	$\epsilon_{\text{crit}}$ (GeV)
$D^+, D^-$	$c\bar{d}, \bar{c}d$	1870	$312 \times 10^{-6}$	$1040 \times 10^{-15}$	$3.8 \times 10^7$
$D^0, \bar{D}^0$	$c\bar{u}, \bar{c}u$	1865	$123 \times 10^{-6}$	$410 \times 10^{-15}$	$9.6 \times 10^7$
$D_s^+, D_s^-$	$c\bar{s}, \bar{c}s$	1969	$149 \times 10^{-6}$	$500 \times 10^{-15}$	$8.5 \times 10^7$
$\Lambda_c^+$	$udc$	2286	$60 \times 10^{-6}$	$200 \times 10^{-15}$	$2.4 \times 10^8$
$\mu^+, \mu^-$		106	659	$2.2 \times 10^{-6}$	1.0
$\pi^+, \pi^-$	$u\bar{d}, \bar{u}d$	140	7.8	$2.6 \times 10^{-8}$	115
$K^+, K^-$	$u\bar{s}, \bar{u}s$	494	3.7	$1.2 \times 10^{-8}$	855
$\Lambda^0$	$uds$	1116	$7.9 \times 10^{-2}$	$2.6 \times 10^{-10}$	$9 \times 10^4$

Table 1.1: Table with critical energies for various particles giving rise to the conventional and prompt atmospheric neutrino flux. The quark content, the mass, the decay length  $c\tau$  and the lifetime  $\tau$  of the particles are also listed.

than one for energies around 100 GeV and increases with energy to a value close to 2.5 for energies around 100 TeV [Lipa 93]. This can be attributed to the fact that cosmic rays consist mainly of protons that will produce larger numbers of  $\pi^+$  compared to  $\pi^-$ . This will in turn result in an increased  $\mu^+$  and  $\nu_\mu$  content over  $\mu^-$  and  $\bar{\nu}_\mu$ . For the highest energies, where kaons play the major role, the asymmetry is stronger, reflecting the fact that  $K^-[s\bar{u}]$  receives no contribution from the valence quark content of the incident nucleon.

Prompt leptons come from the charm-pair production in proton-nucleus collisions, their subsequent fragmentation into charm hadrons and finally, the hadrons' semi-leptonic decays. Short-lived charm mesons decay fast, before they have the chance to interact and lose energy, thus producing a harder spectrum than the conventional component of the flux.

The critical energy  $\epsilon_{\text{crit}}$  of the parent hadron is defined as the energy for which the decay and interaction lengths are equal. Above this critical energy, the hadron is more likely to interact and lose energy before eventually decaying into a neutrino, therefore producing a neutrino energy spectrum richer in low energies and depleted of higher energy neutrinos. Table 1.1 shows the critical energies for various hadrons produced in the particle cascades that take place in the atmosphere. Muon decays contribute to the atmospheric lepton fluxes only up to a few GeV's while charged pions and kaons have a significant contribution up to  $\sim 100$  TeV. At higher energies, the semi-leptonic decay of charmed hadrons, such as the short-lived D-mesons and  $\Lambda_c^+$ -hyperons, is the dominant source of high energy neutrinos in the atmosphere, despite their low production rate. The contributions to the atmospheric lepton fluxes from various mesons are shown in figure 1.4.

The prompt muon neutrino and electron neutrino fluxes are identical since charmed hadrons produce equal numbers of electron and muon neutrinos. The  $D_s$  is more important for  $\tau$  and  $\nu_\tau$ . The flux of prompt tau neutrinos arises mainly from  $D_s \rightarrow \tau\nu_\tau$  and B meson and  $\Lambda_b$  semileptonic decays, and is smaller than the prompt  $\nu_\mu$  flux by a factor of

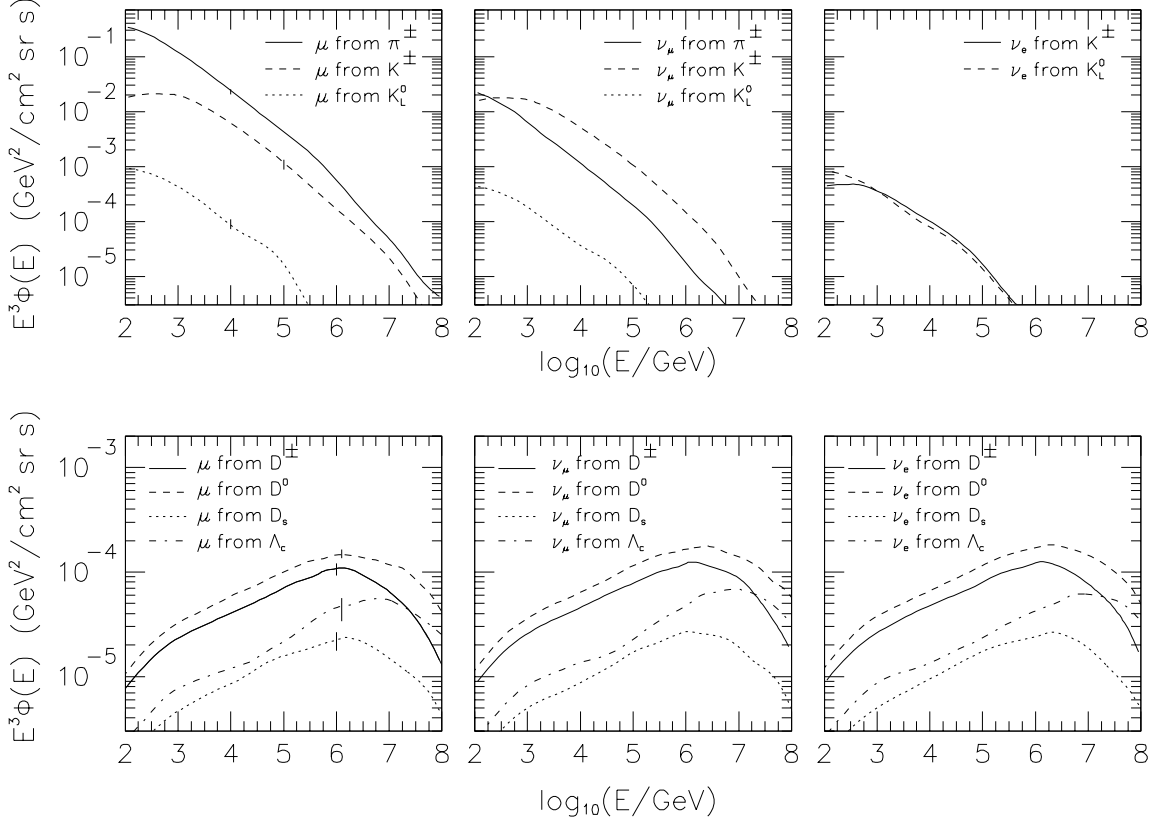


Figure 1.4: Atmospheric muon ( $\mu^- + \mu^+$ ) and neutrino ( $\nu + \bar{\nu}$ ) fluxes, weighted with  $E^3$  from decays of different parents. The top plots correspond to the conventional lepton flux, while the bottom plots to the prompt contribution. Figure from [Thun 96].

10 [Mart 03]. Since there is very little time for neutrino mixing in the atmosphere the contribution from tau neutrinos coming from conventional muon neutrinos is negligible. Above  $\sim 100$  GeV, kaons are the dominant source of conventional neutrinos, due to the larger critical energy compared to pions (see table 1.1).

In the most general sense, the flux of atmospheric neutrinos is a convolution of three factors:

$$\phi_{\nu_i} = \phi_p \otimes R_p \otimes Y_{p \rightarrow \nu_i} + \sum_A \{ \phi_A \otimes R_A \otimes Y_{A \rightarrow \nu_i} \}. \quad (1.3.3)$$

In this equation,  $\phi_p$  and  $\phi_A$  stand for the primary cosmic ray spectrum at the top of the atmosphere,  $R$  represents the effect of the Earth's geomagnetic field on the charged cosmic ray particles and  $Y$  is the yield of neutrinos per primary particle. Protons  $p$  and nuclei  $A$ , corresponding to the first and second term of equation (1.3.3) respectively, are treated differently due to different magnetic rigidity and energy per nucleon. The magnetic rigidity is defined as the total momentum divided by the total charge and affects the propagation through the geomagnetic field. Furthermore, a proton of rigidity

$\mathcal{R}$  has a total energy per nucleon  $E_p(\text{GeV}) = \sqrt{\mathcal{R}^2 + m_p^2}$ , while a nucleus with mass and atomic numbers  $A$  and  $Z$  respectively has  $E_A(\text{GeV}) = \sqrt{(Z/A)^2 \mathcal{R}^2 + m_p^2}$ . Magnetic rigidity is a measure of the effect of a magnetic field on a charged particle. For particles with low energy and high charge the magnetic rigidity is small and the particle is easily deflected by the magnetic field. On the other hand, the trajectories of low charge particles with large momenta and therefore high rigidity are not affected by the magnetic field.

### 1.3.1 Primary cosmic ray spectrum

The first ingredient in the calculation of the atmospheric neutrino flux is the primary cosmic ray spectrum. It is parametrized from existing measurements. The data is fitted to the primary spectrum in the conventional neutrino flux calculations by Gaiser *et al.* using the empirical relation [Gais 01]:

$$\phi(E_k) = K \times \left( E_k + b \exp \left[ -c\sqrt{E_k} \right] \right)^{-\alpha}, \quad (1.3.4)$$

where  $E_k$  is the kinetic energy per nucleon.

To calculate the prompt component, including energies below and above the knee, many authors [Cost 01] use a broken power law parametrization for the cosmic ray energy spectrum at the top of the atmosphere:

$$\phi_N(E_N, X = 0) = N_1 (E_N/1 \text{ GeV})^{-(\gamma_1+1)}, \quad E_N < E_{\text{knee}} \quad (1.3.5)$$

$$\phi_N(E_N, X = 0) = N_2 (E_N/1 \text{ GeV})^{-(\gamma_2+1)}, \quad E_N > E_{\text{knee}} \quad (1.3.6)$$

where the flux  $\Phi_N$  is given in units of  $\text{GeV}^{-1} \text{cm}^{-2} \text{s}^{-1} \text{sr}^{-1}$  and represents the differential flux of nucleons  $N$  with energy  $E_N$ , in GeV. The slant depth penetrated, defined as the integral of the atmospheric density along the path of the particle through the atmosphere, is given by  $X$  [ $\text{g}/\text{cm}^2$ ];  $X = 0$  corresponds to the top of the atmosphere. The normalization is given by  $N_i$  in units of  $\text{GeV}^{-1} \text{cm}^{-2} \text{s}^{-1} \text{sr}^{-1}$  and  $\gamma_i$  is the *spectral index*, representing the slope of the spectrum. Various normalizations, slope parameters as well as positions of the *knee* are used by different authors [Lipa 93; Naga 84; Buga 89; Volk 87; Thun 96], leading to different predictions of the atmospheric neutrino flux. The values for the various parameters used are shown in table 1.2.

Factors that can affect the flux of primaries at the top of the atmosphere include asymmetries due to the motion of the Earth and the effect of solar wind on the incoming flux. Anisotropies due to the motion of the Earth relative to the cosmic ray wind [Comp 35] are less than 1% and they do not affect the neutrino flux significantly. Before reaching the geomagnetic field of the Earth, the flux of primary cosmic rays is affected by the solar wind. Low energy particles are highly suppressed, while higher energy particles lose some energy before reaching the Earth. The effect of solar modulation, i.e. the variation in the intensity of the cosmic ray flux due to changes in solar activity as a function of time, is not important above 20 GeV.

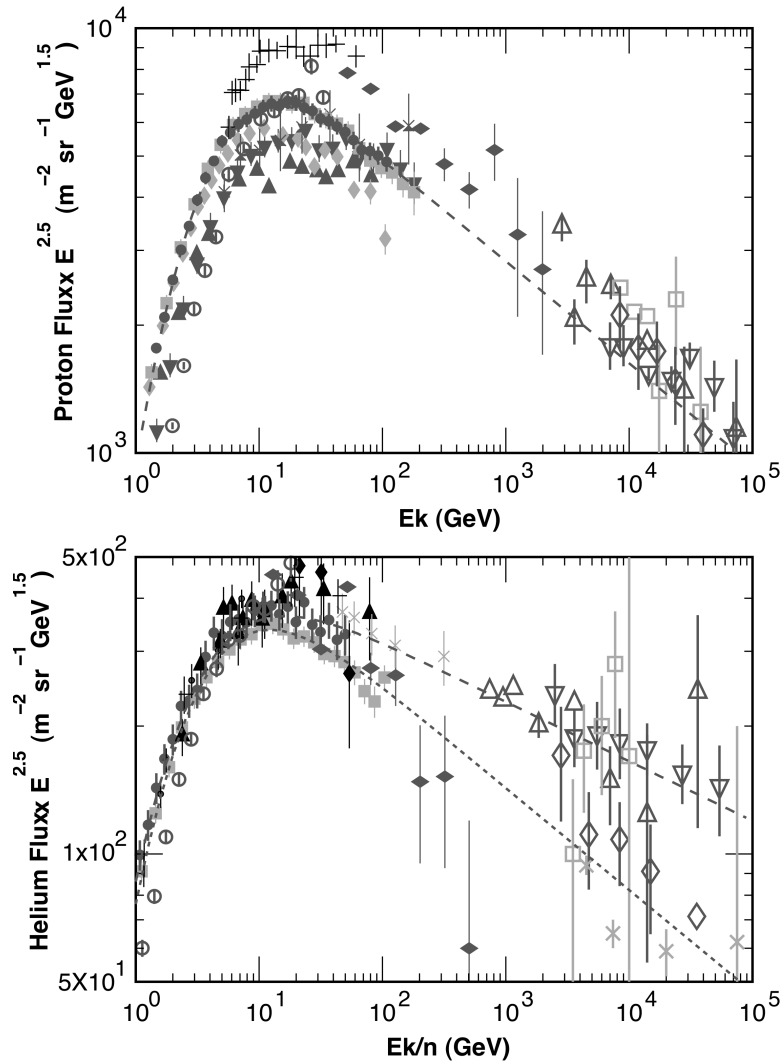


Figure 1.5: Measured flux of protons (top) and helium (bottom) as a function of kinetic energy. The dashed lines correspond to equation (1.3.4) after fitting the data points. Figure from [Gais 03].

### 1.3.2 Geomagnetic effect

The geomagnetic field of the Earth prohibits lower energy cosmic rays from entering the atmosphere. In addition, the trajectories of the secondary particles from the primaries that are energetic enough to enter the atmosphere are bent by the magnetic field. The position, direction and rigidity of a particle determines whether it can penetrate the magnetic field and reach the Earth. This effect for particles with a direction normal to the surface of the Earth is stronger for geomagnetic latitudes close to zero, i.e. near the equator, due to the vertical angle between the Earth's magnetic field and the direction of the particle ( $\mathbf{u} \times \mathbf{B}$ ). Low energy ( $\sim 1$  GeV) particles do not reach the atmosphere and do not produce secondaries. Intermediate energies ( $\sim 10$  GeV) exhibit

Author	$N_1$	$\gamma_1$	$N_2$	$\gamma_2$	$E_{\text{knee}}/\text{GeV}$
Lipari	1.7	1.7	-	-	-
Nagano <i>et al.</i>	1.35	1.62	630	2.02	$4.67 \times 10^6$
Bugaev <i>et al.</i> (F)	1.02	1.62	323	2.02	$1.9 \times 10^6$
Bugaev <i>et al.</i> (D)	1.02	1.62	193	2.02	$5.2 \times 10^5$
Thunman <i>et al.</i>	1.7	1.7	174	2	$5 \times 10^6$

Table 1.2: Table with values used in the parametrization of the primary cosmic ray flux.

a strong east-west asymmetry and high energy ( $\sim 100$  GeV) particles are not affected by the geomagnetic field [Gais 00]. The geomagnetic effect for the energies relevant for the present analysis, i.e. higher than  $\sim 100$  GeV is negligible. Charged cosmic ray particles' trajectories are affected by the Earth's magnetic field in a different way for a certain detector location, depending on their incoming direction. The effect of the magnetic field is an increased intensity of cosmic rays coming from the West, since the geomagnetic cutoff for particles arriving from the East is higher. This is known as the East-West effect illustrated in figure 1.6. The East-West asymmetry defined as:

$$A = \frac{N_E - N_W}{N_E + N_W}, \quad (1.3.7)$$

where  $N_E$  ( $N_W$ ) is the number of events traveling toward East (West), was measured by the Super-Kamiokande detector [Futa 99]. Its value for muon-like events is  $A = 0.08 \pm 0.04$ .

### 1.3.3 Atmospheric model

One of the steps in the calculation of the atmospheric lepton flux is the propagation of particles through the atmosphere, explained in detail in the following section, requiring detailed modeling of the traversed atmosphere. The slant depth, i.e. the distance of atmosphere traversed by the particle until a distance  $l_0$  from the ground along a direction at an angle  $\theta$ , is given by:

$$X(l_0, \theta) = \int_{l_0}^{\infty} \rho(h(l, \theta)) dl, \quad (1.3.8)$$

where  $\rho$  is the atmospheric density and  $h$  is the altitude:

$$h(l, \theta) = \sqrt{R_{\odot}^2 + 2lR_{\odot}\cos\theta + l^2} - R_{\odot}, \quad (1.3.9)$$

where  $R_{\odot}$  is the radius of the Earth,  $l$  is the distance from the ground and  $\theta$  is the angle between the zenith and the direction of the particle. An isothermal model is used for the density:

$$\rho(h) = \rho_0 e^{-h/h_0}, \quad (1.3.10)$$

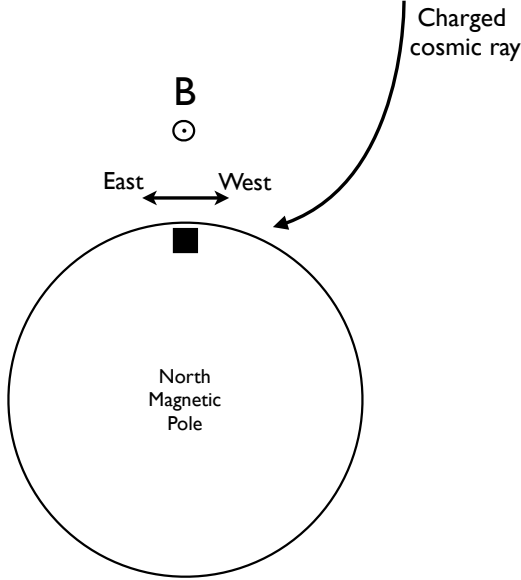


Figure 1.6: Illustration of the East-West effect. The view shown here is above the North magnetic pole. The rotation is counter clockwise in this view.

where  $h_0 = 6.4 \text{ km}$  and  $\rho_0 h_0 = 1300 \text{ g/cm}^2$ . This approximation describes sufficiently well the atmospheric density, or equivalently temperature, profile especially for altitudes in the range 10-40 km, where the majority of interactions take place [Thun 96]. A slightly different parametrization is used by Lipari [Lipa 93], distinguishing between lower and higher altitudes. A power law dependence of the form  $\rho(h) = \alpha(\beta - h)^\gamma$  is assumed up to 11 km and an exponential one above that. The two parametrizations of the atmospheric density are shown in figure 1.7.

### 1.3.4 Primary nucleon flux evolution

The nucleons constituting the primary cosmic ray flux are propagated in the atmosphere, being absorbed and regenerated in nucleon-air inelastic collisions. Both simulations and analytic approximations are used for the description of the flux evolution. Primary cosmic ray nucleons collide with nuclei in the atmosphere, producing secondary particles that either decay to give rise to the atmospheric lepton flux, or re-interact to produce more particles until all energy is dissipated in the form of electromagnetic and hadronic showers. The interaction length that governs the absorption is given by:

$$\lambda_N(E) = \frac{\rho(h)}{\sum_A \sigma_{NA}(E) n_A(h)}, \quad (1.3.11)$$

where  $\sigma_{NA}(E)$  is the inclusive inelastic cross section for collisions of nucleons with nuclei of atomic number  $A$  and  $n_A(h)$  is the number density of nuclei at altitude  $h$ . The average atomic number for atmospheric nuclei  $\langle A \rangle = 14.5$  is frequently used. It is based on the approximate atmospheric composition of 78.4% nitrogen, 21.1% oxygen and 0.5% argon, describing the composition up to 100 km [Alle 99].

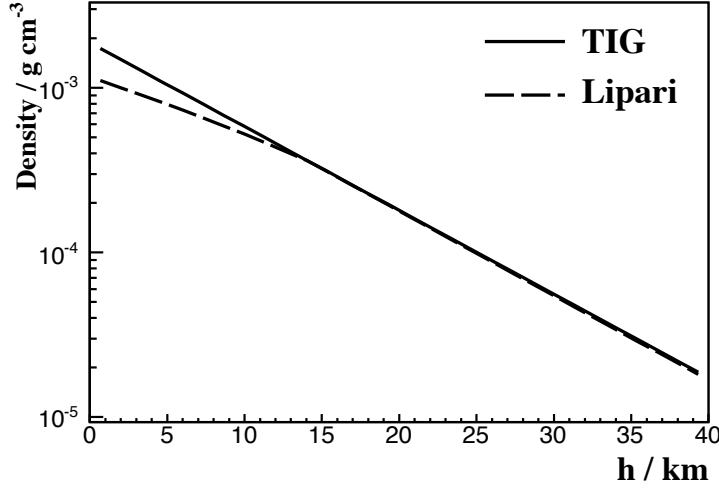


Figure 1.7: Atmospheric air density as a function of the altitude  $h$  for two different parametrizations, TIG [Thun 96] and Lipari [Lipa 93].

The incident cosmic ray flux is reduced by a term describing collisions that produce mesons or other unstable baryons. A second term is considered to account for nuclei fragments that are available for a second interaction. The development of the nucleon flux is given by the cascade equation:

$$\frac{d\phi_N}{dX} = -\frac{\phi_N}{\lambda_N} + S(NA \rightarrow NY). \quad (1.3.12)$$

The first term in this equation describes the absorption and the second the nucleon  $N$  regeneration through collisions with nuclei  $A$ :

$$S(NA \rightarrow NY) = \int_E^\infty dE' \frac{\phi_k(E')}{\lambda_k(E')} \frac{dn(NA \rightarrow NY; E', E)}{dE}. \quad (1.3.13)$$

The energy distribution of secondary hadrons,  $dn/dE$ , representing the number of hadrons with energy between  $E$  and  $E + dE$  is different for the case of production and decay. In hadron production, as is the case of equation (1.3.13), it is given by:

$$\frac{dn(k \rightarrow j; E_k, E_j)}{dE_j} = \frac{1}{\sigma_{kA}(E_k)} \frac{d\sigma(kA \rightarrow jY; E_k, E_j)}{dE_j}, \quad (1.3.14)$$

where  $\sigma_{kA}$  is the total inelastic cross section for  $kA$  collisions. In equation (1.3.14),  $k$  corresponds to the incoming hadron with energy  $E_k$  and  $j$  to the produced hadron with energy  $E_j$ . The flux of mesons and unstable baryons that was generated in nucleon-air interactions, is in turn decreased due to either decay or further collisions. A regeneration term due to hadron-air collisions is again considered. This meson and baryon flux is described in analogy to equation (1.3.12) by:

$$\frac{d\phi_M}{dX} = S(NA \rightarrow MY) - \frac{\phi_M}{\lambda_M} - \frac{\phi_M}{\lambda_M^{\text{dec}}} + S(MA \rightarrow MY). \quad (1.3.15)$$

The first term describes the hadron  $M$  production due to NA collisions. The second and third terms are responsible for the  $M$  absorption and decay respectively. Finally, the term  $S(MA \rightarrow MY)$  describes the  $M$  regeneration in analogy to (1.3.13). The decay length of particle  $j$  is given by:

$$\lambda_j^{\text{dec}}(E) = \gamma\beta c\tau_j\rho(X), \quad (1.3.16)$$

where  $\tau_j$  is the proper lifetime of particle  $j$  and  $\gamma$  the Lorentz boost factor. The atmospheric lepton flux originates from the mesons and baryons that decayed semileptonically in the previous step. This lepton flux is governed by the equation:

$$\frac{d\phi_l}{dX} = \sum_M S(M \rightarrow lY). \quad (1.3.17)$$

The summation is performed over all hadrons that decay into a lepton, i.e.  $M = \pi^\pm, K^\pm, K^0, D^\pm, D^0, D_s^\pm, \Lambda_c^\pm$ . The term  $S(M \rightarrow lY)$  that describes the lepton production from hadron decay is written as:

$$S(M \rightarrow lY) = \int_E^\infty dE_M \frac{\phi_M(E_M)}{\lambda_M^{\text{dec}}(E_M)} \frac{dn(M \rightarrow lY; E_M, E)}{dE}. \quad (1.3.18)$$

In analogy to (1.3.14), but for the case of decay, the energy distribution of the produced leptons  $j$  is given by:

$$\frac{dn(k \rightarrow j; E_k, E_j)}{dE_j} = \frac{1}{\Gamma_k} \frac{d\Gamma(k \rightarrow jY; E_j)}{dE_j}, \quad (1.3.19)$$

where  $\Gamma_k$  is the decay rate of particle  $k$ .

### 1.3.5 Approximate analytic solution

The final lepton flux  $\phi_l$  can be obtained by means of Monte Carlo simulations of the particle cascade initiated by the primary nucleon. However, approximate analytic solutions are frequently used. Detailed comparisons have shown that the two approaches give results that agree within 20% [Thun 96]. These analytic solutions are based on the approximate factorization of the primary particle fluxes into energy dependent and depth dependent parts, i.e.

$$\phi_i(E, X, \theta) = E^{-\beta_i} \phi_i(X, \theta). \quad (1.3.20)$$

The cascade equations described by (1.3.12) and (1.3.15) can be rewritten as:

$$\frac{d\phi_N}{dX} = -\frac{\phi_N}{\lambda_N} + Z_{NN} \frac{\phi_N}{\lambda_N}, \quad (1.3.21)$$

$$\frac{d\phi_M}{dX} = -\frac{\phi_M}{\lambda_M^{\text{dec}}} - \frac{\phi_M}{\lambda_M} + Z_{MM} \frac{\phi_M}{\lambda_M} + Z_{NM} \frac{\phi_N}{\lambda_N}. \quad (1.3.22)$$

The spectrum weighted moments  $Z_{kj}$  are defined as:

$$Z_{kj} \equiv \int_E^\infty dE' \frac{\phi_k(E', X, \theta)}{\phi_k(E, X, \theta)} \frac{\lambda_k(E)}{\lambda_k(E')} \frac{dn(kA \rightarrow jY; E', E)}{dE}. \quad (1.3.23)$$

Under the assumptions that the incoming spectrum falls as  $E^{-(\gamma+1)}$  and that the flux ratios are independent of the depth  $X$  since the fluxes develop rapidly in the atmosphere, the moments  $Z_{kj}$  can be expressed as:

$$Z_{kj} = \int_E^\infty dE' \left( \frac{E'}{E} \right)^{-\gamma-1} \frac{\lambda_k(E)}{\lambda_k(E')} \frac{dn(kA \rightarrow jY; E', E)}{dE}. \quad (1.3.24)$$

The nucleon flux  $\phi_N$ , solution of (1.3.21), can now be written in the form:

$$\phi_N(X, E) = \phi_N(0, E) e^{-\frac{X}{\Lambda_N}}, \quad (1.3.25)$$

where  $\phi_N(0, E)$  is the primary nucleon flux at the top of the atmosphere, and

$$\Lambda_N = \frac{\lambda_N(E)}{1 - Z_{NN}(E)} \quad (1.3.26)$$

is the nucleon attenuation length, with  $\lambda_N$  the interaction length of equation (1.3.11). The meson fluxes (equation (1.3.22)) are approximated in the low and high energy regime, i.e. for energies much lower or much higher than the critical energy, by neglecting the interaction and regeneration term for the former, and the decay term for the latter. The energy behavior for the two regimes is different, i.e.

$$\phi_M^{\text{low}} \propto E^{-\gamma}, \quad (1.3.27)$$

$$\phi_M^{\text{high}} \propto E^{-(\gamma+1)}. \quad (1.3.28)$$

The reason for the more flat energy spectrum at the low energy regime is the Lorentz  $\gamma = E/m$  factor in the decay length (1.3.16), appearing in the denominator of the flux (1.3.22). The lepton fluxes in the low and high energy regimes are finally written as:

$$\phi_l^{\text{low}} = Z_{M \rightarrow l, \gamma+1} \frac{Z_{NM}}{1 - Z_{NN}} \phi_N(E), \quad (1.3.29)$$

$$\phi_l^{\text{high}} = Z_{M \rightarrow l, \gamma+2} \frac{Z_{NM}}{1 - Z_{NN}} \frac{\ln(\Lambda_M/\Lambda_N)}{1 - \Lambda_N/\Lambda_M} \frac{\epsilon_M}{E \cos \theta} \phi_N(E), \quad (1.3.30)$$

where

$$Z_{M \rightarrow l, \beta+1} = \int_E^\infty dE_M \left( \frac{E_M}{E} \right)^{-\beta} \frac{\lambda_M^{\text{dec}}(E)}{\lambda_M^{\text{dec}}(E_M)} \frac{dn(M \rightarrow lY; E_M, E)}{dE}. \quad (1.3.31)$$

and

$$\epsilon_M = \frac{m_M c^2 h_0}{c \tau_M}. \quad (1.3.32)$$

This is the critical energy, discussed at the beginning of this section, describing the interplay between interaction and decay. The final lepton flux is obtained by interpolating between the two energy regimes as:

$$\phi_l = \sum_M \frac{\phi_l^{\text{low}} \phi_l^{\text{high}}}{\phi_l^{\text{low}} + \phi_l^{\text{high}}} \quad (1.3.33)$$

$$= \frac{\phi_N(E)}{1 - Z_{NN}} \sum_M \frac{Z_{NM} Z_{M \rightarrow l, \gamma+1}}{1 + A_M E \cos \theta / \epsilon_M}, \quad (1.3.34)$$

where

$$A_M = \frac{Z_{M \rightarrow l, \gamma+1}}{Z_{M \rightarrow l, \gamma+2}} \frac{1 - \Lambda_N / \Lambda_M}{\ln(\Lambda_M / \Lambda_N)}. \quad (1.3.35)$$

The main uncertainties that enter the calculation are the normalization and slope of the primary cosmic ray spectrum, the nucleonic attenuation and interaction lengths, particle production in pA collisions, and for the prompt contribution, the charmed hadron production details. The models of hadron production and decay, necessary ingredients for the atmospheric neutrino flux calculation, are based on accelerator data for scattering of protons on light nuclei. The differences arising from the different treatments are responsible for  $\sim 15\%$  of uncertainty in the final conventional neutrino fluxes.

## 1.4 Conventional atmospheric neutrino flux calculations

The two major conventional atmospheric neutrino calculations that we consider in the present work are the ones performed by Barr *et al.* [Barr 04] and Honda *et al.* [Hond 04; Hond 07], shown in figure 1.8. Barr *et al.* use the primary spectrum of Agrawal *et al.* [Agra 96] and the MC generator TARGET 2.1 [Enge 01] to simulate the hadronic interactions. Honda *et al.* use the modified DPMJET-III [Sanu 07; Roes 98; Enge 97] for the hadronic interactions modeling and the primary spectrum parametrization in equation (1.3.4), with the parameters taken from Gaisser *et al.* [Gais 02]. The small difference between the results of the two calculations is due to compensation of opposite effects originating from the different primary spectrum parametrization and hadron production treatment.

One approximation made in early one-dimensional (1D) calculations is that the neutrinos follow the direction of their parents. Three-dimensional (3D) calculations however, reveal important effects for energies in the sub-GeV region. At low energies, the transverse and longitudinal momenta of pions are comparable. In 1D calculations the transverse momentum of secondaries is neglected and the bending of charged secondaries in the geomagnetic field is not taken into account [Batt 00].

The 3D calculations are performed as follows. Cosmic ray showers are generated isotropically and uniformly over the Earth. The geomagnetic cutoff is calculated at each

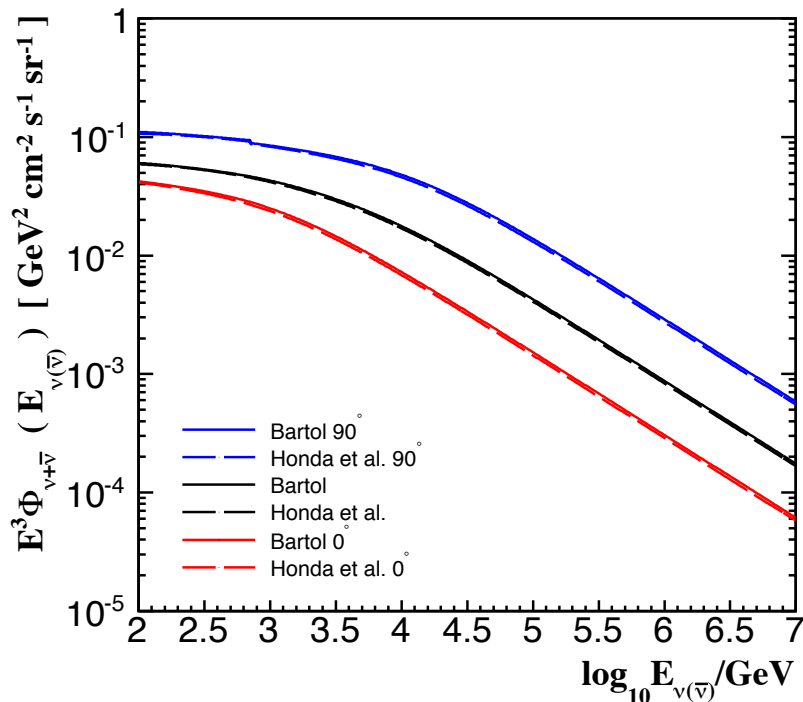


Figure 1.8: Conventional high energy atmospheric muon neutrino and antineutrino fluxes. The vertical, horizontal and zenith angle-averaged results are shown. The difference between the vertical ( $\theta = 0^\circ$ ) and horizontal ( $\theta = 90^\circ$ ) fluxes is driven by the cosine in equation (1.3.34), reflecting the amount of atmosphere traversed and therefore the available time for decay into neutrinos.

injection location for a given particle rigidity and the appropriate events are kept. A backtracking technique is applied to determine if the particles can overcome the rigidity cutoff. The history of the particle is examined by solving the equations of motion for the particle at the top of the atmosphere in the negative time direction. If the particle reaches a hypothetical sphere far away from the injection point it is kept. If the particle stays in the vicinity of the Earth or hits the Earth it is rejected. The information that this backtracking technique provides is whether a particle of a given rigidity can reach the top of the atmosphere. The parametrization of NASA [NASAa] and the IGRF2005 model [NASA b] are used for the Earth's magnetic field by Barr *et al.* and Honda *et al.* respectively.

Interactions of protons with almost tangential trajectories at the top of the atmosphere can produce secondary protons below the geomagnetic cutoff giving rise to the so-called second spectrum. This is taken into account in the calculation, but the effect is small due to the low intensity of the second spectrum itself. Honda *et al.* calculated the contribution of these albedo particles to be much smaller than 1%.

Very few events will eventually cross the detector area  $A$  ( $\sim A/R_\odot^2 \sim 10^{-10}$ ), while

the rest will be discarded. In 1D calculations only cosmic rays that point to the detector are sampled which makes the calculation extremely efficient. A brute force 3D calculation is very inefficient. Since most of the neutrinos in the 3D calculation do not cross the detector, the detector size has to be taken many times larger in order to increase the efficiency of the calculation, a frequently used approximation [Lipa 00; Hond 01]. The hypothetical detector is a circular disk centered at the real detector position. The neutrino flux is averaged over this surface, leading to less than 0.5% error [Barr 04]. The difficulty that arises by the change in the cross sectional area of the detector depending on the angle of incidence of the neutrino is addressed by assigning weights to the events. The angular distribution is binned to avoid divergences in the horizontal direction. Honda *et al.* have used different detector sizes and estimated the error to be less than 5%.

One of the most important results of the 3D calculations is an enhancement of low energy neutrino flux near the horizon compared to the 1D calculations and a decrease near the zenith. This effect is present in lower energies and decreases as the energies increase. The zenith distributions for 1D and 3D are identical for  $E_\nu > 5$  GeV while azimuthal differences are still present. The flavor ratio in the two calculations is the same. The azimuthal differences are attributed to the bending of primary particles as well as muons in the atmosphere. This effect is still present at neutrino energies around 10 GeV but decreases with increasing energy. The bending of protons affects all neutrino types in the same way, while for muons, since they bend in different directions according to their charge, particle/antiparticle differences are introduced. There are essentially no differences between the 1D and 3D calculations above 100 GeV.

The primary spectra below 100 GeV are parametrized with equation (1.3.4). This fit is based mainly on AMS [Alca 00a; Alca 00b] and BESS [Hain 04; Sanu 00] data. The errors above 100 GeV are attributed to uncertainties in the primary cosmic ray spectrum and the treatment of hadronic interactions. The uncertainties in the primary spectrum are at the level of 5% below 100 GeV, based on BESS [Sanu 00] and AMS [Alca 00a] measurements, and up to 10% for 10 TeV per nucleon [Gais 01]. The primary cosmic ray uncertainty is estimated by applying a power law extrapolation above 100 GeV. Using all measurements the uncertainty is estimated at 20% below 100 GeV and 30% above that. The different treatment of hadronic interactions gives a 20-25% uncertainty in the neutrino flux. Honda *et al.* estimated the uncertainty on the atmospheric neutrino flux below 10 GeV to be at the level of 7%, 14% at 100 GeV and 25% at 1 TeV, while above this energy it becomes difficult to reliably estimate the errors.

## 1.5 Prompt atmospheric neutrino flux calculations

In this section we briefly outline the most recent prompt neutrino flux calculations as well as some extreme case scenarios. The dominant partonic subprocess for charm production in perturbative QCD is  $gg \rightarrow c\bar{c}$  [Comb 79]. The leading order in the strong

coupling constant  $\alpha_S$  differential cross section for  $c\bar{c}$  production is given by:

$$\frac{d\sigma}{dx_F} = \int \frac{dM_{c\bar{c}}^2}{(x_1 + x_2)s} \sigma_{gg \rightarrow c\bar{c}}(s) g(x_1, \mu^2) g(x_2, \mu^2), \quad (1.5.1)$$

where  $\mu$  is the factorization scale,  $s$  is the center of mass energy,  $M_{c\bar{c}}$  is the  $c\bar{c}$  invariant mass and  $g(x, \mu^2)$  the gluon distribution function. The fraction of the proton momentum carried by the gluons is given by  $x$ , and  $x_F = x_1 - x_2$  is the Feynman variable. The fractional momenta carried by the gluons can be expressed as:

$$x_{1,2} = \frac{1}{2} \left( \sqrt{x_F^2 + \frac{4M_{c\bar{c}}^2}{s}} \pm x_F \right). \quad (1.5.2)$$

At high center of mass energies relevant for cosmic rays collisions in the atmosphere, the one gluon distribution function is at  $x_1 \sim x_F$  and the other at very small  $x_2 \ll 1$ . It is evident that in the high energy regime, the gluon density at very small- $x$  is needed for the calculation of the cross section.

For small  $x$ , leading order (LO) or next-to-leading order (NLO) QCD does not work well. The perturbative Dokshitzer-Gribov-Lipatov-Altarelli-Parisi (DGLAP) evolution equations describe rising parton distributions with increasing momentum transfer  $Q^2$  at small  $x$ . This treatment is only appropriate when  $\ln Q^2$  is much larger than  $\ln(1/x)$ . In the limit of large  $Q^2$  and small  $x$ , the leading  $\ln Q^2$  resummation within the DGLAP framework is supplemented by an approximation where only large leading  $\ln(1/x)$  terms are kept. This is called the double leading logarithm approximation (DLL). For the region of small  $x$  and  $Q^2$ , the Balitsky-Fadin-Kuraev-Lipatov (BFKL) equation resums the terms that are proportional to  $\alpha_S \ln(1/x)$  to all orders, using the full  $Q^2$  dependence without using only the leading  $\ln Q^2$  terms. The BFKL equation leads to a power growth of the gluon density in the small  $x$  regime.

The increase of the parton distributions at small  $x$ , predicted by both the DGLAP and BFKL equations, cannot continue indefinitely since this growth leads to unitarity violation. The parton number density becomes so large that partons cannot be considered free anymore. This is called saturation. Gluon recombination effects at this saturation level should limit the increase of the gluon distributions. As parton densities increase, these interactions and recombination effects among the constituents of the proton start to play an important role. The prompt flux is expected to decrease for very high energies due to saturation effects that take place in the charm production phase.

Martin *et al.* [Mart 03] uses three approaches to calculate the prompt contribution by employing different small  $x$  extrapolations for the gluon densities and including parton saturation effects. The first approach is an extrapolation of gluon density for  $x < 10^{-5}$  by DLL re-summation of  $\alpha_S \ln Q^2 \ln(1/x)$  terms within the DGLAP framework, leading to:

$$xg(x, Q^2) \simeq x_0 g(x_0, Q_0^2) e^{\sqrt{\frac{16N_C}{b} \ln \frac{\alpha_S(Q)}{\alpha_S(Q_0)} \ln \frac{x}{x_0}}} \quad (1.5.3)$$

small  $x$  behavior, denoted as MRST in figure 1.10 [Mart 02b]. Here,  $N_C = 3$  is the number of colors and  $b = 25/3$ . The scale  $Q_0^2 = 1 \text{ GeV}^2$  and  $x_0 = 0.25$  define the large  $Q^2$  and small  $x$  regions respectively.

The second approach is an extrapolation obtained by solving a unified DGLAP/BFKL equation denoted as KMS [Kwie 97] and using an  $xg(x, Q^2) \sim x^{-\lambda}$  extrapolation for  $x < 10^{-7}$ . The BFKL equation is modified to include DGLAP leading  $\ln Q^2$  contributions, so the method incorporates both resummed leading  $\ln(1/x)$  BFKL and  $\ln Q^2$  DGLAP contributions. This approach includes the main NLO effect at small  $x$ . The resulting gluon distribution can be applied to both small and large  $x$ . The third approach uses the phenomenological dipole model of Golec-Biernat and Wüsthoff (GBW) [Gole 98] to include saturation effects, that suppress the cross section at high energies.

In the deep inelastic scattering (DIS) case where a virtual photon probes the proton, the effect of saturation takes place when the photon wavelength  $1/Q$  is close to the size of the proton in the  $\gamma^*p$  process, and is related to the transition from the high  $Q^2$  to the low  $Q^2$  regime. The GBW saturation model considers the projectile virtual photon, in the rest frame of the proton target, splitting into a quark-antiquark pair. This  $q\bar{q}$  dipole then scatters on the proton. Under this phenomenological mechanism, the scattering process can be factorized into the photon wave function, describing  $\gamma^* \rightarrow q\bar{q}$ , convoluted with the quark-antiquark cross section describing the  $q\bar{q}$  scattering off the target. The second term is highly non perturbative and is modeled. In the DIS framework the cross section for the  $\gamma^*N$  scattering is factorized as:

$$\sigma(x, Q^2) = \int d^2\mathbf{r} \int_0^1 dz \sum_f |\Psi_f(z, \mathbf{r}, Q^2)|^2 \sigma_d(x, \mathbf{r}), \quad (1.5.4)$$

where  $z$  is the dipole momentum fraction carried by the quark, the summation is performed over quark flavors, and  $\mathbf{r}$  represents the transverse size of the  $q\bar{q}$  pair. The probability of finding a  $q\bar{q}$  pair with separation  $\mathbf{r}$  and fractional momentum  $z$  is described by the wavefunction  $\Psi$ . In heavy quark production in hadronic collisions the dipole is produced by a gluon, and the cross section is given in the same form as eq. (1.5.4), with  $\sigma_d$  replaced by  $\sigma_{dG} = \frac{9}{8}[\sigma_d(x, \mathbf{r}) + \sigma_d(x, (1-z)\mathbf{r})] - \frac{1}{8}\sigma_d(x, \mathbf{r})$  [Niko 96]. The dipole cross section for the scattering of the  $q\bar{q}$  color singlet pair on the proton, including saturation effects, is parameterized as [Gole 98]:

$$\sigma_d(x, \mathbf{r}) = \sigma_0 \left( 1 - e^{-\frac{r^2}{4R_s^2(x)}} \right), \quad (1.5.5)$$

where the saturation radius, i.e. the inverse of the saturation scale  $Q_s(x) = Q_0(x_0/x)^{\lambda/2}$  with  $Q_0 = 1 \text{ GeV}$ , is given by:

$$R_s(x) = \frac{1}{Q_0} \left( \frac{x}{x_0} \right)^{\lambda/2}. \quad (1.5.6)$$

The values of the parameters  $x_0$  and  $\lambda$ , characterizing the saturation radius, as well as the overall cross section normalization  $\sigma_0$  are determined from fits to DIS data.

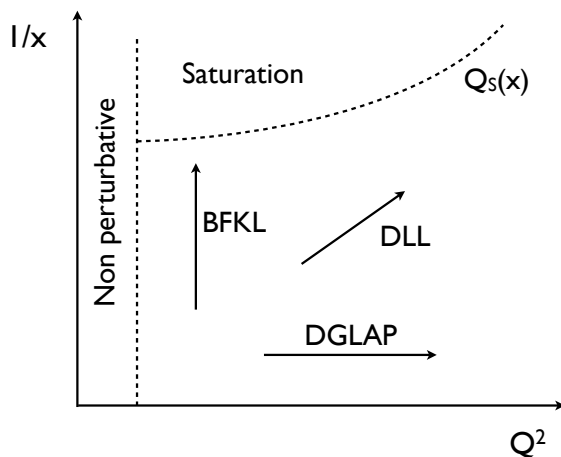


Figure 1.9: Various regions in the  $1/x$  vs  $Q^2$  plane. See text for discussion. The  $Q_s(x)$  line defines the saturation region.

The saturation scale defines the line on the  $(x, Q^2)$  plane where saturation sets in, illustrated in figure 1.9. It depends on  $x$  in such a way that one needs larger values of  $Q^2$ , or equivalently better resolving power, to probe the dense small  $x$  parton structure. The asymptotic behavior of  $\sigma_d$  describes well the saturation ( $r \rightarrow \infty$ ,  $\sigma_d \rightarrow \text{const}$ ) and color transparency ( $r \rightarrow 0$ ,  $\sigma_d \propto r^2$ ) effects.

In the GBW approach, only part of the absorptive effects are taken into account. Recombination of gluons that decrease the rate of  $c\bar{c}$  production due to increased gluon density, described by triple-Pomeron interactions, is not accounted for. At very high energies, this absorptive effect is expected to become stronger and decrease the  $c\bar{c}$  production. The dipole model was developed using a fixed impact parameter and a broadening of the nucleon's density distribution in position space with increasing collision energy is not included in the GBW saturation model. This will result in an increased cross section at higher energies. Martin *et al.* showed that these two effects combined essentially cancel.

The prompt fluxes calculated under these three approaches are shown in figure 1.10. The GBW cross section, and consequently the fluxes, becomes lower at high energies compared to MRST due to absorption effects, while they agree for lower energies. The  $x^{-\lambda}$  extrapolation to small  $x$  of the KMS approach leads to a higher growth than the double logarithmic DGLAP growth of MRST. For lower energies the KMS results fall below the MRST and GBW. While for small  $x$ ,  $\ln(1/x)$  effects enhance the cross section, as  $x$  increases LO DGLAP evolution dominates and the KMS result needs to be scaled by a factor  $K \sim 2$ , decreasing with increasing energy as the BFKL regime is being approached. This is illustrated in figure 1.11. Since the primary cosmic ray flux for energies above  $10^6$  GeV falls as  $E^{-(\gamma+1)}$ , with  $\gamma = 2.02$ , the moments of the Feynman  $x$  distribution:

$$\sigma Z_c \equiv \int \frac{d\sigma^c}{dx} x^{2.02} dx, \quad (1.5.7)$$

are plotted for the three different models.

Enberg *et al.* [Enbe 08] calculated the prompt flux component using an improved

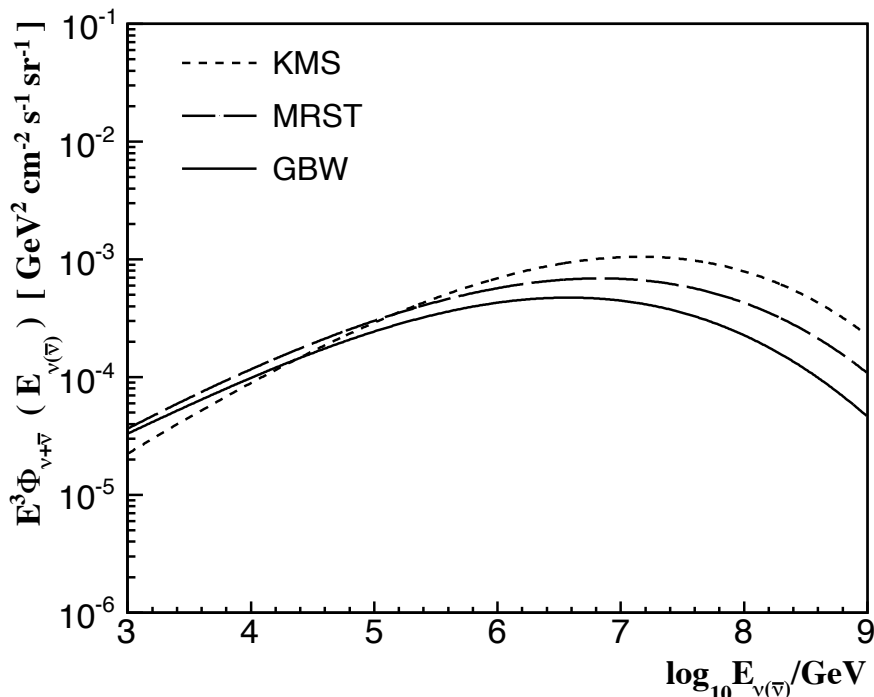


Figure 1.10: Prompt neutrino and antineutrino fluxes calculated by Martin *et al.* under different approaches for the charm production cross section (see text). The fluxes are plotted with the *NeutrinoFlux* [Mont] class in *SeaTray* [Kopp 09]. The difference between calculations with (GBW) and without taking saturation into account becomes apparent above  $10^6$  GeV.

dipole model parametrization (DM) [Ianc 04] with fit parameters from [Soye 07]. In this model, the parametrization for the dipole cross section is obtained by interpolating between two regions. The first region describes saturation and the second, where  $r \ll R_s(x) = 1/Q_s(x)$ , describes color transparency using the result obtained in pQCD with the BFKL equation.

In the work of Enberg *et al.* fragmentation functions are used to describe charm fragmentation into hadrons. The general form of the cross section for hadron production including fragmentation is:

$$\frac{d\sigma(pp \rightarrow hX)}{dE_h} = \int_{E_h}^{\infty} \frac{dE_c}{E_c} \frac{d\sigma(pp \rightarrow cX)}{dE_c} D_c^h(E_h/E_c). \quad (1.5.8)$$

The charmed hadron cross section is calculated in LO QCD using the Kniehl and Kramer (KK) parametrization for the fragmentation functions  $D_c^h(z = E_h/E_c)$  [Knie 06]. Fragmentation reduces the energy of the charmed hadron, resulting in a flux reduction of 60-70%. The results obtained using the KK fragmentation functions and the older Peterson *et al.* [Pete 83] fragmentation functions differ by  $\sim 10\%$ . Martin *et al.* takes fragmentation into account by assigning an average lower value to the hadron momen-

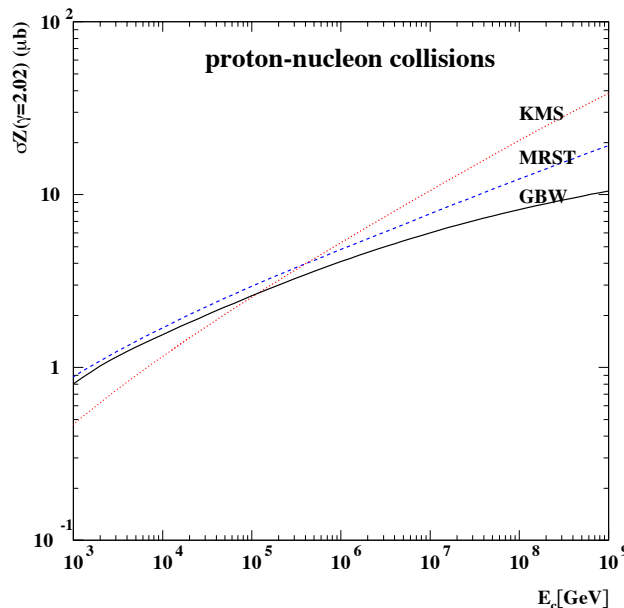


Figure 1.11: Charm production Z-moment as a function of energy for the KMS, MRST and GBW approaches. Figure from [Mart 03].

tum fraction.

The theoretical uncertainties estimated for DM indicate that the prompt flux using this model can vary by up to a factor of 2. The calculation of Martin *et al.* (GBW) is approximately a factor of 2-3 below DM due to the different parametrization of the dipole cross section  $\sigma_d$ . Theoretical uncertainties arise from choices of gluon distribution (small  $x$  behavior), charm quark mass and the choice of renormalization and factorization scales. Martin estimates an uncertainty of about a factor of 3 in the prompt muon neutrino fluxes.

### 1.5.1 Extreme prompt flux calculation combinations

Costa [Cost 01] performed the prompt neutrino flux calculation using various combinations of ingredients that affect the final result. The prompt neutrino flux results presented here correspond to calculations using three different charm production models (pQCD, RQPM, QGSM) as a basis and applying different combinations of other ingredients in the calculation to obtain the maximum variability in the spectrum in each case.

The first model used for describing charm production is the Quark Gluon String Model (QGSM) [Kaid 86]. It is a non-perturbative QCD calculation describing hadron collisions and multiparticle production at high energies, combining  $1/N$  QCD expansion with Regge theory and the partonic structure of hadrons. Regge theory describes high energy soft processes where perturbative QCD cannot be applied due to small momentum transfer. Proton interactions are described by the exchange of a colorless

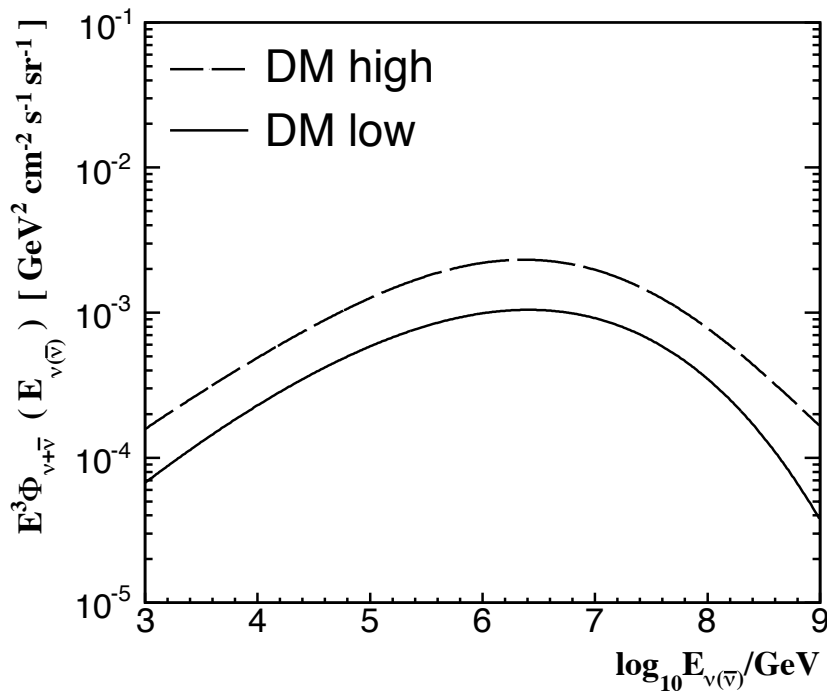


Figure 1.12: Prompt neutrino and antineutrino flux calculated by Enberg *et al.* with the improved dipole model (DM). The upper and lower limit of the predicted flux are shown. The PDF's used to estimate the high and low limits of the DM prompt spectrum are the MRST 2001 LO [Mart 02a] and CTEQ 6L [Pump 02a] gluon distributions.

and flavorless multiple gluon object, called the Pomeron. The scattering amplitudes are parametrized by analytical functions  $\alpha(t)$ , called Regge trajectories, and they exhibit a power law behavior  $\sim s^{\alpha(t)}$ . During the initial stage of the interaction producing charm, strings are formed between the valence and sea quarks of the colliding hadrons and the hadronization process is associated with the breaking of these quark strings. The distribution functions of the constituent quarks and their fragmentation functions into hadrons, necessary to calculate the amplitudes, are approximated using Regge theory.

Another phenomenological non-perturbative approach is the Recombination Quark Parton Model (RQPM) used by Bugaev *et al.* [Buga 89; Buga 98]. In the RQPM model the projectile contains an intrinsic charm component and the total inclusive cross-section depends strongly on the charm structure function of the incoming hadron. Hadronization is described by recombination between charm quarks and the fragments of the projectile that take place due to parton interactions in the final state. The cross section is a convolution of parton distribution functions and recombination functions.

Finally, a pQCD approach has been employed. The LO calculation of Thunman *et al.* [Thun 96] includes next-to-leading order (NLO) effects by a constant scaling, while Gelmini *et al.* [Gelm 00a; Gelm 00b] explicitly calculate the NLO contribution. Charm quark fragmentation is simulated using the Lund string model [Ande 83] in PYTHIA

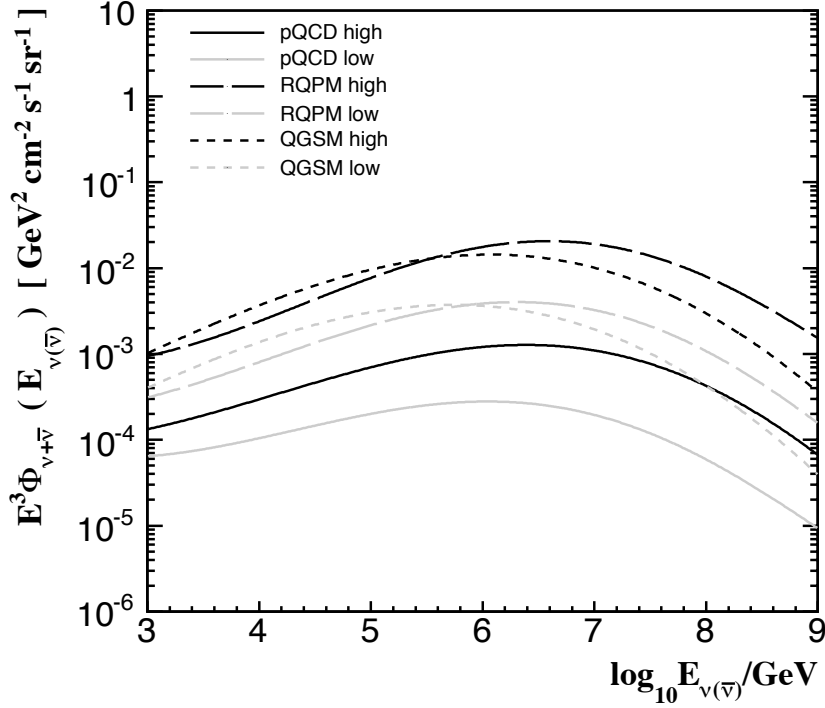


Figure 1.13: Extreme prompt neutrino and antineutrino fluxes calculated by Costa for three different approaches to the hadronization process (see text for various combinations).

and the small  $x$  parton density functions are power law extrapolated as  $x^{-\lambda}$ . The theoretical uncertainties in these perturbative calculations arise from different ranges of quark masses, factorization and renormalization scales, as well as different assumptions for the parton distribution functions at small  $x$ .

In order to obtain the highest prompt flux contribution the following ingredients were used. The Akeno group parametrization [Naga 84] is used for the primary flux, a power law dependence for  $\lambda_N(E)$  [Naga 84], scaling violation for  $Z_{NN}(\gamma)$  [Thun 96] and a constant  $\lambda_i(E)$  [Volk 85]. For the minimum configuration the Lipari [Lipa 93] primary flux parametrization below the knee and the Bugaev [Buga 89] above, a constant  $\lambda_N(E)$  [Lipa 93], a constant  $Z_{NN}(\gamma)$  with knee [Cost 95] and a  $\log(E)$  dependence for  $\lambda_i(E)$  [Buga 98] were used. The results for the three different charm production models using the ingredients that provide the minimum and maximum configurations are shown in figure 1.13. There is a variation of two orders of magnitude in the flux between the highest and lowest predictions, with RQPM and QGSM behaving similarly, and pQCD being significantly lower.

The nucleonic interaction length is governed by the  $\sigma_{NA}$  behavior (eq. 1.3.11). Different parametrizations of the cross section do not affect the resulting fluxes significantly. The same conclusion is true for the nucleonic Z-moments (see section 1.3.5). Therefore,

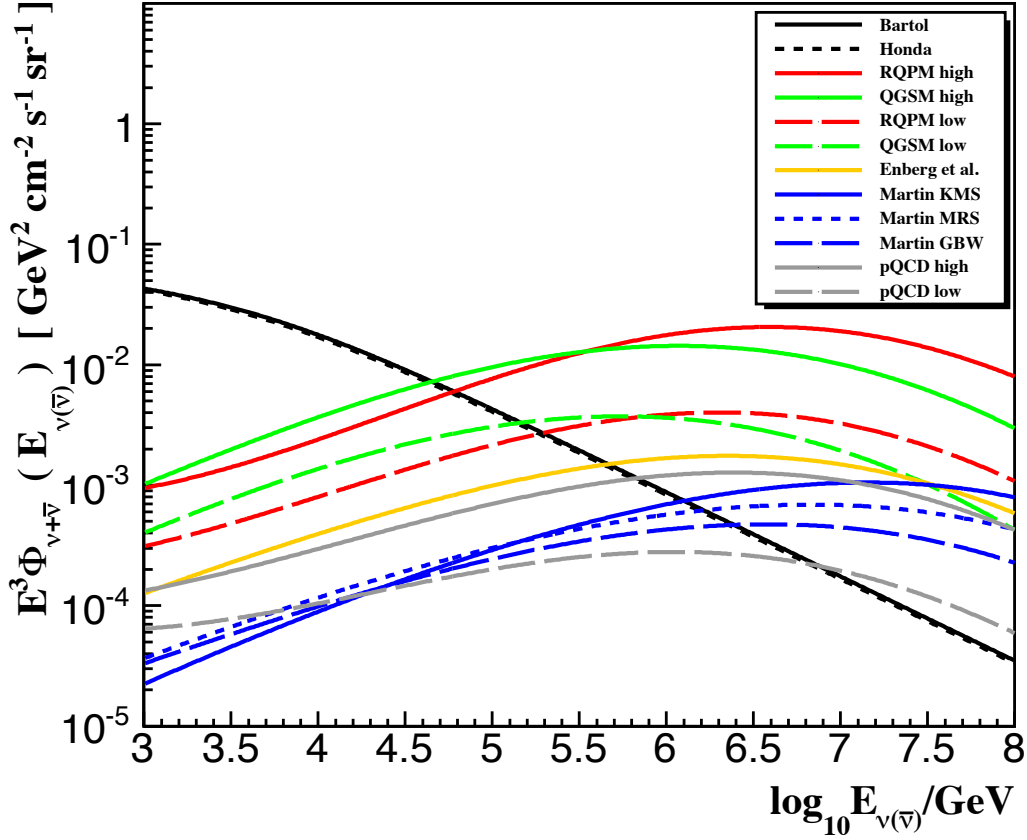


Figure 1.14: Conventional and prompt atmospheric neutrino fluxes. All predictions described in the previous sections are summarized in this plot.

the major role is played by the parametrization of the primary CR spectrum and the details of charm production. Below the critical energy, most high energy prompt neutrinos are produced early in the atmosphere. Above the critical energy though, when interaction and decay lengths of charmed hadrons are comparable, the zenith angle starts affecting the flux. For zenith angles that correspond to more horizontal directions, more atmosphere is encountered, and very high energy charm hadrons have more time to decay before reaching the Earth. This allows for a higher prompt neutrino flux at near horizontal directions for very high energies. The critical energy for charmed hadrons is too high, above  $10^7$  GeV, to have an effect on the present analysis.

In figure 1.14 we summarize the conventional and prompt fluxes described in this chapter. There is a large amount of uncertainty on the crossover energy, i.e. the energy above which the prompt contribution will dominate the conventional one, spanning around two orders of magnitude in the neutrino energy from  $\sim 10^{4.7}$  GeV to  $\sim 10^7$  GeV.

## 1.6 Neutrino oscillations

Recent experimental research has shown that neutrinos oscillate and therefore mix and possess a small but nonzero mass. The effect of neutrino oscillations was observed by the Super-Kamiokande collaboration in Japan in 1998, observing atmospheric muon neutrino disappearance [Fuku 98]. Oscillation of solar  $\nu_e$  into  $\nu_\mu$  and  $\nu_\tau$  was observed by the Sudbury Neutrino Observatory (SNO) [Ahma 02] in Canada. The Kamioka Liquid Scintillator Anti-Neutrino Detector (KamLAND) [Eguc 03; Arak 05] also observed disappearance of  $\bar{\nu}_e$  by using electron antineutrinos from nuclear power plants. These data can be explained by assuming three flavor neutrino mixing in vacuum.

The neutrino flavor states  $|\nu_l\rangle$  with  $l = e, \mu, \tau$  are expressed as a superposition of mass eigenstates:

$$|\nu_l\rangle = \sum_i U_{li}^* |\nu_i\rangle, \quad (1.6.1)$$

with  $i = 1, 2, 3$ . Flavor states are thus obtained from the mass eigenstates by a transformation using the  $3 \times 3$  Pontecorvo-Maki-Nakagawa-Sakata (PMNS) unitary matrix  $U$  [Maki 62]. The mixing matrix can be parametrized by three angles and by CP violating phases, one in the case where the massive neutrinos  $\nu_i$  are Dirac particles and three if they are Majorana particles. The PMNS matrix is therefore parametrized as:

$$U = \begin{pmatrix} c_{12}c_{13} & s_{12}c_{13} & s_{13}e^{i\delta} \\ -s_{12}c_{23} - c_{12}s_{23}s_{13}e^{i\delta} & c_{12}c_{23} - s_{12}s_{23}s_{13}e^{i\delta} & s_{23}c_{13} \\ s_{12}s_{23} - c_{12}c_{23}s_{13}e^{i\delta} & -c_{12}s_{23} - s_{12}c_{23}s_{13}e^{i\delta} & c_{23}c_{13} \end{pmatrix} \times \begin{pmatrix} e^{i\alpha_1/2} & 0 & 0 \\ 0 & e^{i\alpha_2/2} & 0 \\ 0 & 0 & 1 \end{pmatrix}, \quad (1.6.2)$$

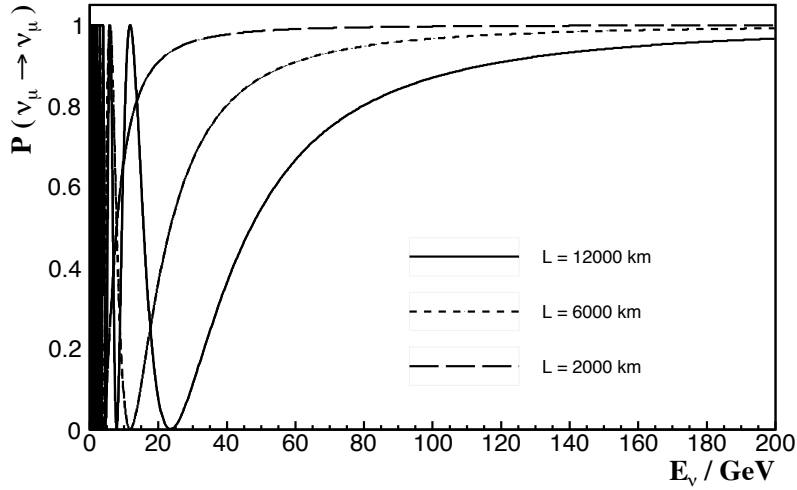
where  $c_{ij} = \cos \theta_{ij}$  and  $s_{ij} = \sin \theta_{ij}$  represent the three mixing angles  $\theta_{ij}$  and  $\delta$  and  $\alpha_k$  are the Dirac and Majorana CP violation phases, respectively.

Taking the time evolution of a flavor state one can calculate the probability that after a certain time  $t$ , or equivalently distance  $L$  from the neutrino production until its detection, the neutrino remains in the same state  $P(\nu_l \rightarrow \nu_l)$  or oscillates into a different flavor  $P(\nu_l \rightarrow \nu_x)$ . The neutrino oscillation probabilities depend on the neutrino energy  $E$ , the distance travelled  $L$ , the mixing angles  $\theta_{ij}$  and the squared mass differences  $\Delta m_{ij}^2 \equiv m_i^2 - m_j^2$ , with  $i \neq j$ . The flavor neutrino transition probability in vacuum is given by:

$$P(\nu_\alpha \rightarrow \nu_\beta) = \delta_{\alpha\beta} - 4 \sum_{i>j} \Re(U_{\alpha i}^* U_{\beta i} U_{\alpha j} U_{\beta j}^*) \sin^2 \left[ 1.27 \Delta m_{ij}^2 \frac{L/\text{m}}{E/\text{MeV}} \right] + 2 \sum_{i>j} \Im(U_{\alpha i}^* U_{\beta i} U_{\alpha j} U_{\beta j}^*) \sin \left[ 2.54 \Delta m_{ij}^2 \frac{L/\text{m}}{E/\text{MeV}} \right]. \quad (1.6.3)$$

$\Delta m_{\odot}^2 \equiv \Delta m_{21}^2$	$7.58_{-0.26}^{+0.22} \times 10^{-5} \text{ eV}^2$
$\sin^2 \theta_{12}$	$0.306_{-0.015}^{+0.018}$
$ \Delta m_{32}^2  \equiv  \Delta m_{atm}^2 $	$2.35_{-0.09}^{+0.12} \times 10^{-3} \text{ eV}^2$
$\sin^2 \theta_{23}$	$0.42_{-0.03}^{+0.08}$
$\sin^2 2\theta_{13}$	$0.092 \pm 0.021$

Table 1.3: Values of mixing angle and mass differences.

Figure 1.15: Muon neutrino survival probability as a function of the neutrino energy for three different values of  $L$ .

Global fits to data from solar, atmospheric, reactor and accelerator experiments give the values shown in table 1.3 [Fogl 11], including the recent measurement of  $\theta_{13}$  by the Daya Bay collaboration [An 12] with a  $5.2\sigma$  significance.

For the case of ANTARES the contribution of the mass splitting  $\Delta m_{21}^2$  can be neglected and equation (1.6.3) simplifies significantly. Therefore, in the two neutrino flavor mixing approximation, valid when one mass splitting is much larger than the other, the probability that a produced muon neutrino is detected as a muon neutrino after traveling distance  $L$  is:

$$P_{\nu_{\mu} \rightarrow \nu_{\mu}} = P_{\bar{\nu}_{\mu} \rightarrow \bar{\nu}_{\mu}} = 1 - \sin^2(2\theta_{23}) \sin^2 \left[ 1.27 \Delta m_{32}^3 \frac{L/\text{km}}{E/\text{GeV}} \right]. \quad (1.6.4)$$

This probability is shown in figure 1.15 as a function of the neutrino energy for three different values of  $L$ . For the purposes of the present analysis, the effect of neutrino

---

oscillations is negligible. The relevant energies are above a few hundred GeV, where a longer baseline  $L$  is necessary to observe a reduction in the flux of  $\nu_\mu$ . Work is ongoing within the ANTARES collaboration to study neutrino oscillation [Guil 11].



# THE ANTARES DETECTOR

The spectrum of atmospheric neutrinos falls very steeply as a function of energy as discussed in the previous chapter. In addition, the small neutrino interaction probability results in low rates at the surface of the Earth. Therefore, very large detectors need to be built in order to detect neutrinos, especially at the highest energies. The basic idea consists of building a three dimensional array of light detectors inside an appropriate transparent medium [Mark 61]. The detector must be simple and cost effective since the instrumented volume has to be large. The medium needs to be transparent in order to allow for the detection of the muon's Čerenkov radiation and to make the reconstruction of the muon direction possible. The detector also has to be shielded against the high flux of atmospheric muons. For this reason, neutrino detectors are often built deep underground or, as in the case of ANTARES, at the bottom of the sea. The ANTARES detector is optimized to detect upward going neutrinos that have traversed our planet, using the Earth as an absorber for other high energy particles, in particular muons.

In section 2.1 we briefly discuss neutrino interactions and different event topologies. Section 2.2 describes the propagation of the muon produced in the charged current neutrino interaction. In the following 3 sections the ANTARES detector is described in detail. Sections 2.6 and 2.7 address the data acquisition and triggering. The calibration methods used in ANTARES are described in section 2.8. Finally, the current status of the ANTARES detector and other neutrino telescopes are presented in the last 2 sections.

## 2.1 Neutrino interactions

Neutrinos, being electrically neutral, interact only through the weak force. At higher energies, relevant for the study of cosmic neutrinos, the neutrino interaction cross section is dominated by the deep inelastic scattering off the target nucleons. At 6.4 PeV the  $\bar{\nu}_e e \rightarrow W^-$  channel is open, leading to  $W^-$  production. This is known as the Glashow resonance [Glas 60]. However, the main channels are the charged-current (CC) and neutral-current (NC) deep inelastic scattering. In the former case, a neutrino of arbitrary flavor produces a hadronic cascade and a lepton of the same flavor through the

exchange of a  $W^\pm$  boson with a target-nucleon  $N$ ,

$$\nu_l + N \rightarrow l^- + X, \quad (2.1.1)$$

$$\bar{\nu}_l + N \rightarrow l^+ + X. \quad (2.1.2)$$

In the neutral-current case the neutrino exchanges a  $Z$  boson with the target-nucleon  $N$ , producing a cascade  $X$ ,

$$\nu + N \rightarrow \nu + X. \quad (2.1.3)$$

The diagrams of the charged and neutral current processes are shown in figures 2.1 and 2.2 respectively.

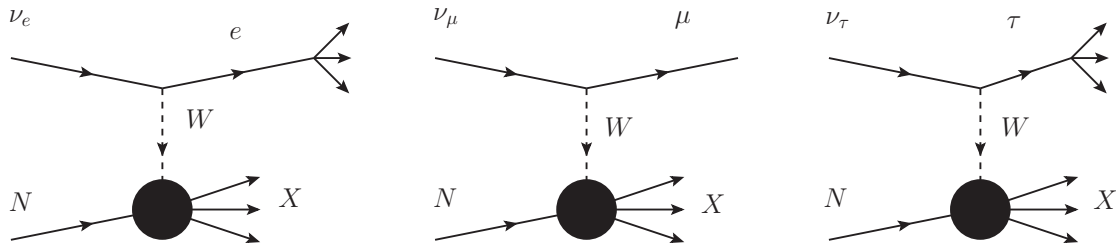


Figure 2.1: Charged current neutrino interactions. A neutrino of arbitrary flavor interacts with a nucleon producing a hadronic cascade and a lepton. In the case of anti-neutrinos a positively charged lepton of the same flavor is produced. Different flavors give rise to different event topologies.

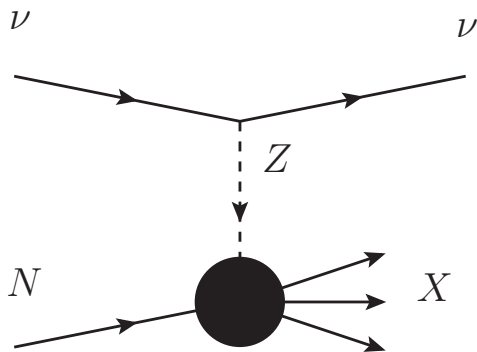


Figure 2.2: During a neutral current interaction a neutrino scatters elastically by the exchange of a  $Z$  boson with the nucleon, leading to a hadronic cascade.

Depending on the neutrino flavor, the lepton detection signature in the detector can differ significantly. Muon neutrinos ( $\nu_\mu$ ) produce muons that in turn manifest themselves as long tracks inside the instrumented volume. Electrons on the other hand, produced by electron neutrinos ( $\nu_e$ ), initiate electromagnetic showers that, unless they happen inside the detector, are unlikely to be detected. A high energy electron coming from

a charged current neutrino interaction has a high probability to radiate bremsstrahlung photons after a few centimeters of water. The larger the change in acceleration of the electron, the larger the energy of the bremsstrahlung photon. For electrons of a given energy, bremsstrahlung losses are higher for propagation materials with higher atomic number. An electromagnetic shower is rapidly initiated and as soon as the energy of the constituents of the shower falls below a certain threshold energy, the shower production stops. For a 10 TeV electron, the shower length, defined as the distance within which 95% of the total energy has been deposited in the medium, is only around 7.5 meters, very small compared to the average distance between the photomultiplier tubes used to detect Čerenkov light. Tau neutrinos ( $\nu_\tau$ ) can give rise to a variety of signatures. Taus from charged current neutrino interactions travel some distance before they decay and produce a shower. Their decay length is  $l_\tau = \gamma c t_\tau \sim 50(E_\tau/\text{PeV})$  m. Due to their short lifetime they can travel from a few meters to a few kilometers. Depending on whether the primary and decay showers are inside or outside the detector, the event topology will be different. The most striking is the “double bang” signature where both showers connected by a track are visible within the detector [Lear 95]. The NC channel gives the same signature for all neutrino flavors and part of the energy is unobserved with the outgoing neutrino.

The leading order differential cross section for the neutrino CC interactions is given by [Povh 02]:

$$\frac{d^2\sigma_{\nu N}}{dx dy} = \frac{2G_F^2 m_N E_\nu}{\pi} \frac{M_W^4}{(Q^2 + M_W^2)^2} [xq(x, Q^2) + x(1-y)^2 \bar{q}(x, Q^2)], \quad (2.1.4)$$

where  $G_F$  is the Fermi coupling constant,  $m_N$  and  $M_W$  are the masses of the nucleon and the W boson respectively,  $Q^2$  represents the square of the four momentum transfer between the neutrino and the nucleon,  $q(x, Q^2)$  and  $\bar{q}(x, Q^2)$  are the parton distribution functions for quarks and anti-quarks, and finally  $x = Q^2/2m_N(E_\nu - E_l)$  and  $y = (E_\nu - E_l)/E_\nu$  are the Feynman-Bjorken variables. The (anti-)neutrino-nucleon cross sections are shown in figure 2.3. The cross section rises linearly with the neutrino energy up to around  $10^4$  GeV. Above this energy, it is possible for the invariant mass  $Q^2$  to be larger than the W-boson rest mass resulting in a decrease in the slope of the cross section. The slope still remains substantial through the scaling violations of the quark distribution functions.

## 2.2 Muon propagation

If the muons that are produced by the CC interaction of the neutrino in the vicinity of the detector are energetic enough they can reach the instrumented volume. The signal they create allows for their directional reconstruction. The angle between the parent neutrino and the resulting muon can be small, especially at higher energies. This means that the muon retains the neutrino directional information to a good approximation. Consider the momentum transfer from a neutrino  $\nu$  with momentum  $p_\nu = (E_\nu, \vec{p}_\nu)$  to

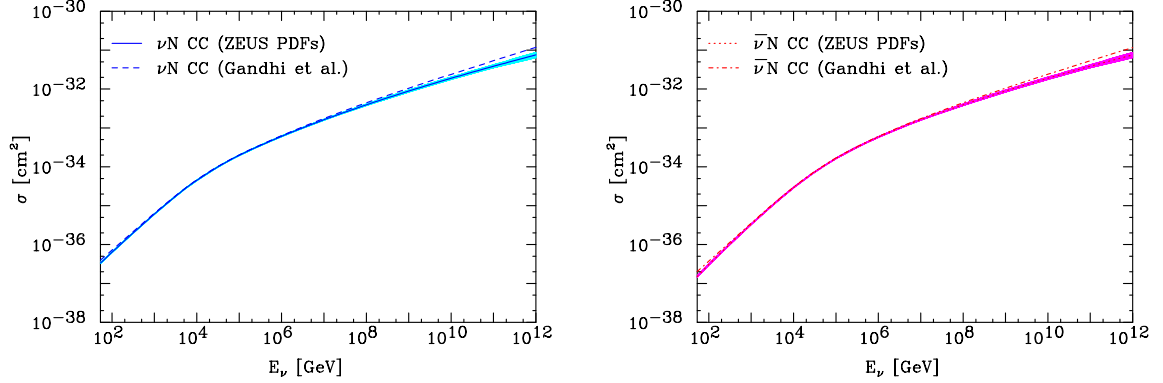


Figure 2.3: The total CC cross-section for neutrinos (left) and antineutrinos (right). The shaded band indicates the  $\pm 1\sigma$  uncertainties. [Coop 08], [Gand 98].

the nucleon  $N$ ,

$$Q^2 = -q^2 = (p_\nu - p_l)^2, \quad (2.2.1)$$

where  $p_l$  is the four momentum of the final state lepton. Neglecting the masses of the neutrino and the produced lepton we end up with,

$$Q^2 = 4E_\nu E_\mu \sin^2 \frac{\Delta\theta}{2}, \quad (2.2.2)$$

where  $\Delta\theta$  is the angle between the neutrino and the outgoing lepton. The kinematically allowed region is given by the Bjorken  $x$  as  $0 \leq x \leq 1$ . The momentum transfer can be expressed as  $Q^2 = sxy = 2E_\nu m_p xy$ . The produced lepton will only have a fraction of the parent neutrino energy, i.e.  $E_\mu = (1 - y)E_\nu$ , thus the following empirical relation, determined from Monte Carlo simulations, can describe the angular difference between the parent neutrino and the produced muon directions,

$$\Delta\theta \leq \frac{1.5^\circ}{\sqrt{E_\nu [\text{TeV}]}}. \quad (2.2.3)$$

Since neutrinos are not deflected by galactic or extra-galactic magnetic fields it is possible to trace the detected muon back to its source and thus use the detector as a pointing device, i.e. a telescope.

## 2.2.1 Čerenkov radiation

When a charged particle travels through a medium it polarizes the atoms around its trajectory. These electric dipoles are symmetrically oriented around the track when the particle is moving with a speed  $u$  smaller than the speed of light  $c/n$  in the medium, where  $n$  is the index of refraction of the medium under consideration. If  $u > c/n$  this symmetry is broken and dipole radiation is emitted, known as Čerenkov radiation [Cere 37]. Čerenkov light is emitted at a fixed angle, creating a cone of light around the particle's track, and this fact makes it useful for reconstruction purposes. The

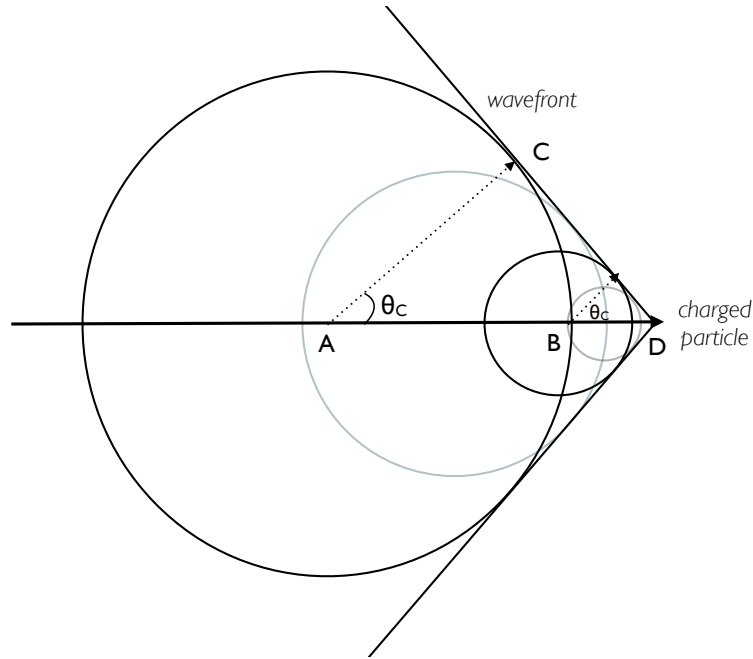


Figure 2.4: Schematic view of Čerenkov light emission. As the charged particle propagates faster than the speed of light in the medium, radiation is emitted under a fixed angle  $\theta_C$ .

Čerenkov angle can be calculated with the help of figure 2.4 as follows. Consider a charged particle traveling with velocity  $u_l = \beta \cdot c$  emitting spherical waves of light along its trajectory. A spherical wave emitted at point A will reach point C at the same time as the charged particle arrives at point D. The cosine of the angle  $\Theta_C$  is given by:

$$\cos\Theta_C = \frac{AC}{AD} = \frac{t \cdot c/n}{t \cdot \beta \cdot c} = \frac{1}{\beta \cdot n}, \quad (2.2.4)$$

where for relativistic particles ( $\beta \simeq 1$ ) and water as the propagation medium ( $n = 1.33$ ) the value of this angle is about  $41.2^\circ$ . The spherical waves emitted at every point on the trajectory collectively create a wavefront in the shape of a cone.

The number of Čerenkov photons emitted per unit track length  $x$  and wavelength  $\lambda$  is [Jack 99]:

$$\frac{d^2N}{dx d\lambda} = \frac{2\pi\alpha Z^2}{\lambda^2} \left(1 - \frac{1}{\beta^2 n^2}\right), \quad (2.2.5)$$

where  $Z$  is the charge of the particle and  $\alpha$  the electromagnetic coupling constant. In the optical part of the spectrum ( $350 \text{ nm} \leq \lambda \leq 600 \text{ nm}$ ) which is of interest to us, this amounts to almost 200 emitted photons per cm.

As the muon propagates through the medium, the Čerenkov light it produces is affected by absorption and scattering. The absorption is characterized by the absorption length  $\lambda_{abs}$ , which is the average distance at which a fraction of  $(1 - 1/e)$  of the photons is absorbed. Correspondingly, scattering is characterized by the scattering length  $\lambda_s$  in

the same way. Absorption and scattering are discussed in more detail in sections 2.5.1 and 3.1.2.

### 2.2.2 Muon propagation

The muon loses energy while passing through matter. The main processes involved are ionization, which is considered a continuous energy-loss process, and a series of stochastic processes that play an important role at higher energies. These processes are pair production, photo-nuclear interactions and Bremsstrahlung radiation emission. Additionally, the direction of the muon is affected by multiple Coulomb scattering off atomic nuclei. The energy-loss of the muon as well as the propagation of the Čerenkov photons will be examined in detail in chapter 3. The stochastic nature of these radiative energy-losses makes the reconstruction of the energy of the particle a challenging task.

## 2.3 The ANTARES project

The ANTARES<sup>1</sup> collaboration (fig. 2.5) was formed in 1996 with the objective to construct and operate a neutrino telescope in the Mediterranean sea [Amra 00]. The collaboration consists of physicists, engineers and sea scientists from 29 institutes and 7 European countries<sup>2</sup>. The first ANTARES line was deployed in spring of 2006 [ANTA 09], and the telescope was completed in May 2008 with the deployment of the last line.



Figure 2.5: The location of the institutes in the ANTARES collaboration.

The ANTARES detector is located approximately 42 km south of Toulon in France, at a depth of 2475 m on the bottom of the Mediterranean sea. It is currently the largest

<sup>1</sup>Astronomy with a Neutrino Telescope and Abyss environmental REsearch

<sup>2</sup>France, Germany, Italy, the Netherlands, Romania, Russia, Spain, Morocco

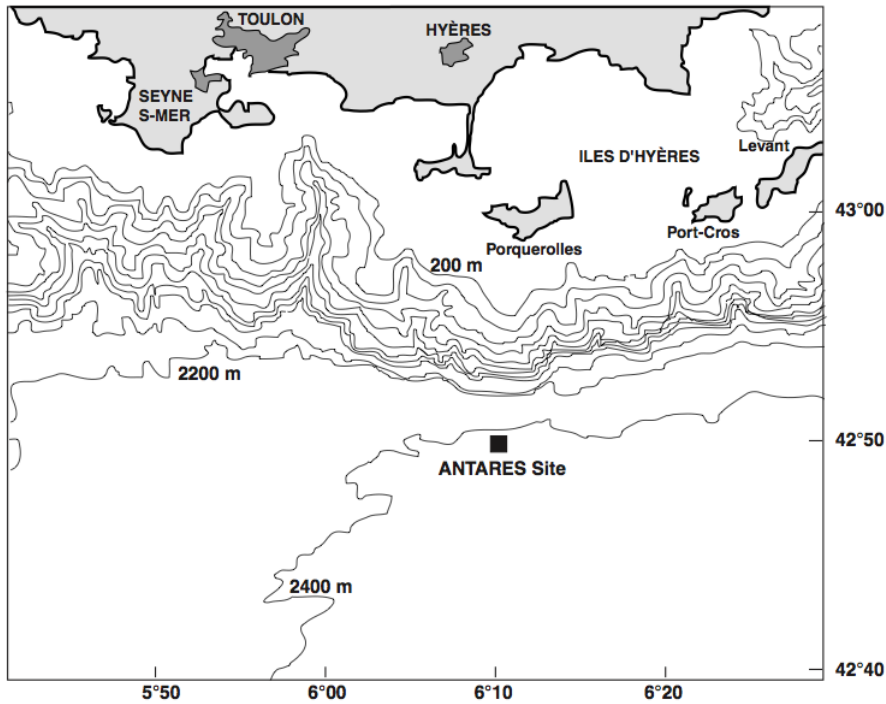


Figure 2.6: Depth contour plot near the ANTARES site. The ANTARES detector is located near Toulon, France. The coordinates are  $42^{\circ}50'$  N and  $6^{\circ}10'$  E.

neutrino telescope in the northern hemisphere and is sensitive to a large part of the southern sky, including most of the galactic center region.

## 2.4 Detector layout

The ANTARES detector consists of 12 vertical strings, each one holding photomultiplier (PM) tubes for Čerenkov light detection. ANTARES comprises 885 detector units, called optical modules (OM) [ANTA 02], shown in figure 2.7. The OM is a sphere containing the PM tube. A single storey consists of three such optical modules mounted on the optical module frames (OMF). Five storeys complete a single ANTARES sector. The optical modules point downwards at a  $45^{\circ}$  angle with respect to the vertical. The OMF is a mechanical structure which, in addition to the OM's, supports a titanium container holding the local control module (LCM) and housing offshore electronics and processors. Five storeys together constitute a sector which is an individual unit in terms of power and data transmission. A line is a chain of 25 OMF's, i.e. 5 sectors, linked by an electro mechanical cable (EMC). The distance from storey-to-storey is 14.5 m and the first storey of each line is located 100 m from the bottom of the sea. The reason for this is to leave enough space to allow for the development of the Čerenkov cone from upgoing particles. The inter-line spacing varies between 65-70 m. A schematic view of

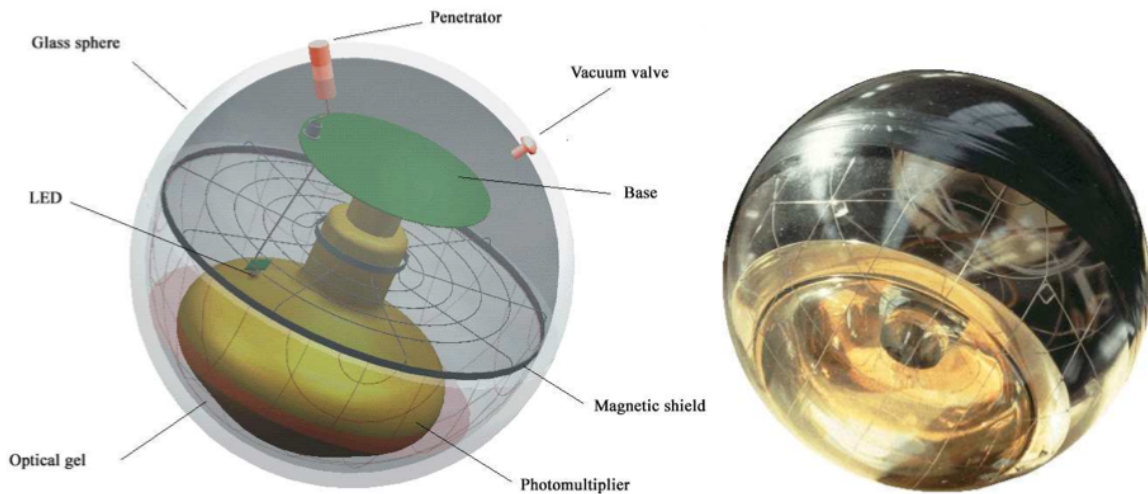


Figure 2.7: Schematic view and photo of the ANTARES optical module. The PM tube is glued on the inside of a pressure resistant glass sphere. A penetrator is used for the electrical connection of the PM tube with the rest of the detector. The tube is shielded against the Earth's magnetic field. Additional LED components are used for the calibration of the PM tubes' signals.

the detector is given in figure 2.8. Each line is anchored to the bottom of the sea with the bottom string socket (BSS) and a dead weight, and is held vertical by a buoy at the top. Every BSS contains a string control module (SCM), a string power module (SPM), calibration instruments and an acoustic release system. The acoustic release system allows for the recovery of the complete line. The SPM houses the power supplies for all sectors in a line while the SCM contains electronics for slow control. The full configuration is octagonal as seen in figure 2.9. In each sector, one LCM is the master LCM (MLCM) and its role is to handle data distribution between all LCM's in the sector. A Dense Wavelength Division Multiplexer (DWDM) multiplexes the data signal from the 5 sectors onto one pair of optical fibers. Data and power are transmitted between the lines and the shore via the 40 km long main electro-optical cable (MEOC) connected to the junction box (JB), and interconnecting link cables (ILC). Data arrives onshore in a PC farm located at the shore station (La Seyne sur Mer) where the ANTARES control room is located and data filtering is applied. Filtered data are copied and stored remotely at a computer center in Lyon once a day. The instrumentation line (IL07) contains oceanographic sensors for measurements of environmental parameters. Line 12 and IL07 contain hydrophones which are used to test the feasibility of acoustic neutrino detection. The IL07 and the top sector of Line 12 do not contain OMs.

Each OM consists of a pressure resistant glass sphere, 43 cm in diameter and 15 mm thickness. It contains a Hamamatsu R7081-20 hemispherical PM tube [Hama] with a diameter of 25 cm and an effective sensitive area of  $440 \text{ cm}^2$ . Each PM tube has 14 amplification stages and a nominal gain of  $5 \times 10^7$  at a high voltage of 1800 V.

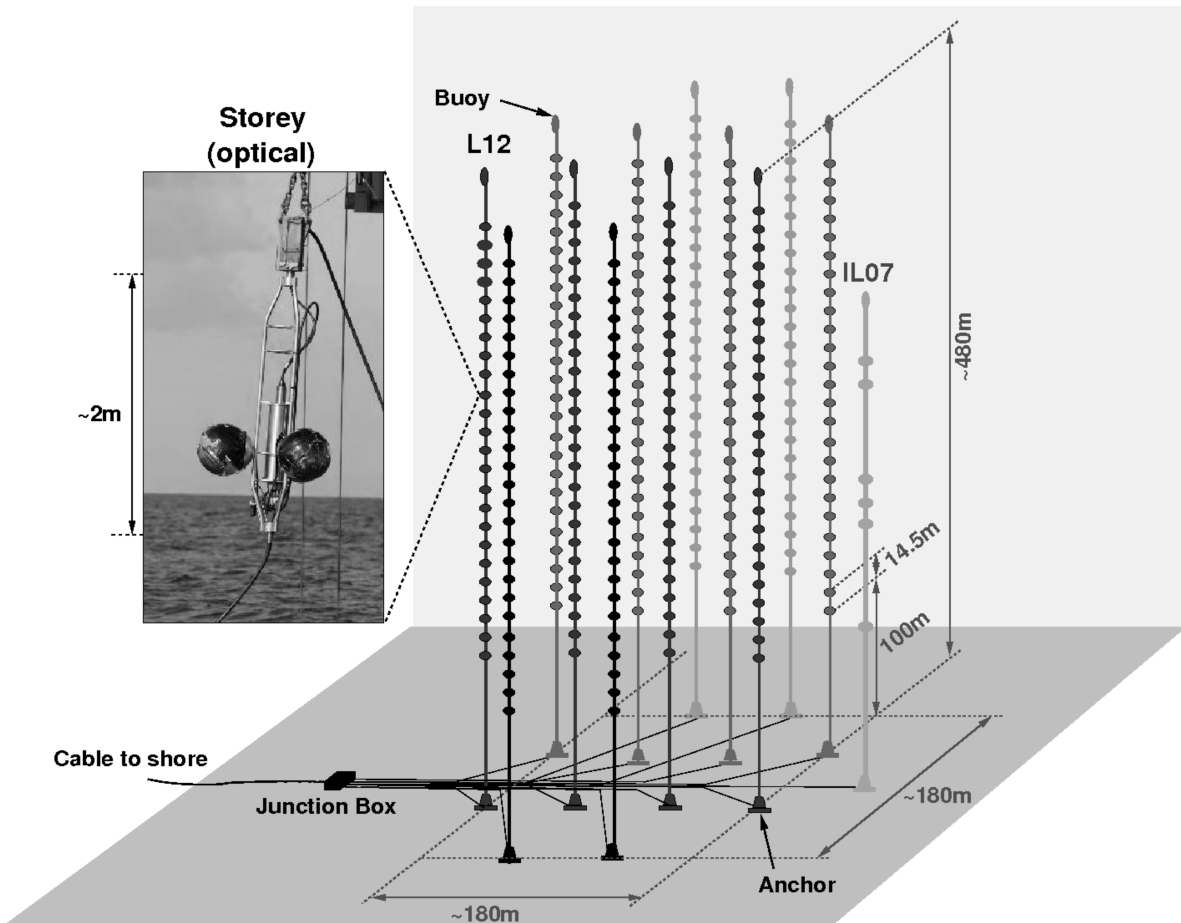


Figure 2.8: Schematic view of the ANTARES 12-line detector. The inter-line spacing varies between 65-70 m. The lines are connected to the Junction Box. The cable to shore transmits power and data to and from the detector.

The wavelength sensitivity range of the PM tubes is 300-600 nm. The peak quantum efficiency (QE) is 23% at light wavelength of 350-450 nm. The charge resolution and transit time spread (TTS) of the PM tubes are 40% and  $\sim 1.5$  ns respectively. The dark count rate at the 0.25 photoelectron level is about 2 kHz. Each PM tube is surrounded by a  $\mu$ -metal cage to minimize the influence of the magnetic field of the Earth on its response. The high voltage is provided by an electronics board mounted on each PM tube's socket. Each OM also contains an LED calibration system explained in more detail in section 2.8. The PM tube is glued to the outer glass sphere by means of a transparent silicon rubber gel. The glass hemisphere behind the PMT is painted black and contains a penetrator which provides the power and data transmission connection to the outside.

An integral part of the ANTARES detector is AMADEUS (**ANTARES Modules for the Acoustic DEtection Under the Sea**), a set-up of acoustic sensors, which is used for a feasibility study towards a future acoustic neutrino detector. It consists of six acoustic

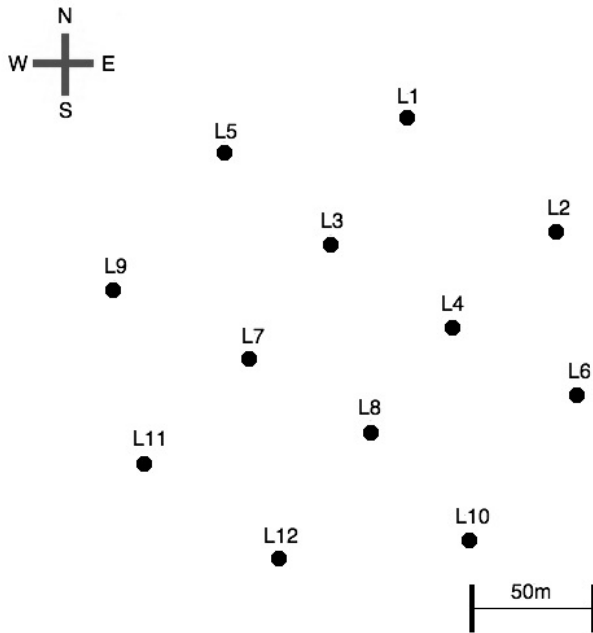


Figure 2.9: Positions of the anchors of the ANTARES lines on the seabed.

storeys (AS) and 34 sensors. A detailed description of the acoustic components can be found in [Graf 08].

## 2.5 The site

During the R&D phase of the experiment, extensive measurements were carried out in order to determine environmental parameters and optical water properties [ANTA 04].

### 2.5.1 Water optical properties

The performance of the detector depends on the optical properties of sea water, since light propagation in a medium is affected by absorption and scattering. Absorption reduces the amount of light that reaches the OMs while scattering affects the path of the photons and their arrival time on the OMs. Absorption and scattering reduce the intensity of light as,

$$I(x, \lambda) = I_0(\lambda)e^{-x/\lambda_{abs}(\lambda)}e^{-x/\lambda_s(\lambda)}, \quad (2.5.1)$$

where  $x$  is the optical path travelled by light and  $\lambda_{abs}$  and  $\lambda_s$  the absorption and scattering lengths, respectively. The absorption length as a function of the photon wavelength is shown in figure 2.10. Figure 2.11 illustrates the wavelength dependence of the scattering length.

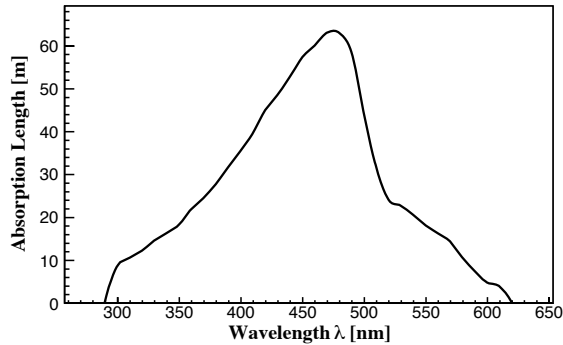


Figure 2.10: Absorption length in water as a function of the wavelength.

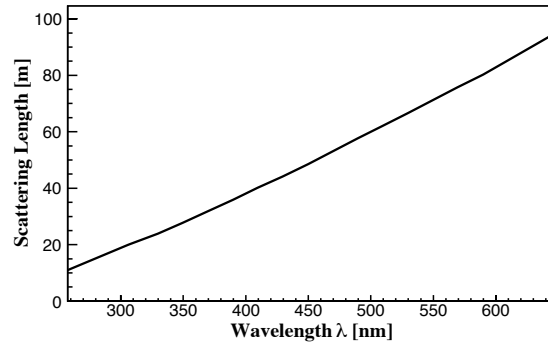
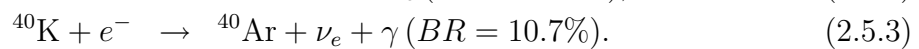
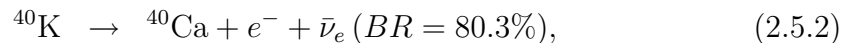


Figure 2.11: Scattering length in water as a function of the wavelength.

## 2.5.2 Optical background

There are two background contributions to photon detection in sea water. The first one is the decay of the radioactive potassium isotope  $^{40}\text{K}$ ,



The emitted electron energy in (2.5.2) can take values up to 1.33 MeV. A large fraction of these electrons is above the Čerenkov threshold for light production. The photons emitted in the electron capture process (2.5.3) have an energy of 1460 keV. These photons can lead to Compton scattering producing electrons above the Čerenkov threshold. The second optical background contribution comes from luminescence produced by various organisms (bioluminescence). Bioluminescence can give rise to optical background up to several orders of magnitude above the  $^{40}\text{K}$  contribution and these bursts can last for seconds. In figure 2.12 the typical counting rate on a PM tube, i.e. hit frequency, as a function of time is illustrated.

The fraction of time during which the instantaneous background rate exceeds the baseline rate by at least 20% is called burst fraction. After monitoring deep sea currents, it was found that the baseline component is correlated neither with the sea current nor with the burst frequency. However, long-term variations of the baseline were observed. A strong correlation between bioluminescence and sea current velocity has been observed, as shown in figure 2.13.

## 2.5.3 Sedimentation and biofouling

The optical modules are exposed to particle sedimentation and biofouling. This can adversely affect light transmission through the glass sphere of the optical module. Extensive *in situ* measurements have been performed in order to study this effect [ANTA 03]. The average loss of light transmission is small, estimated to be only around 2% at

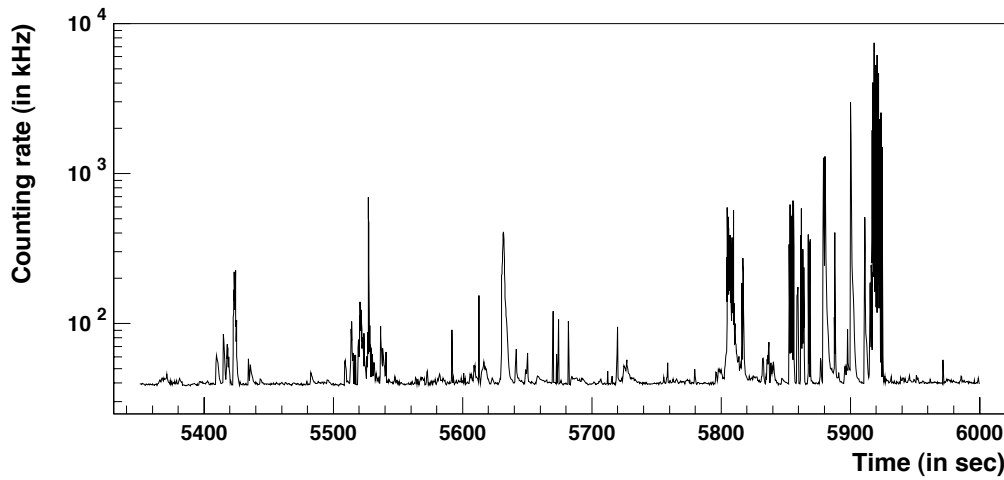


Figure 2.12: Typical photomultiplier tube counting rate as a function of time. The almost flat background indicates the presence of potassium decay light while the bursts correspond to bioluminescence. Figure taken from [Amra 00].

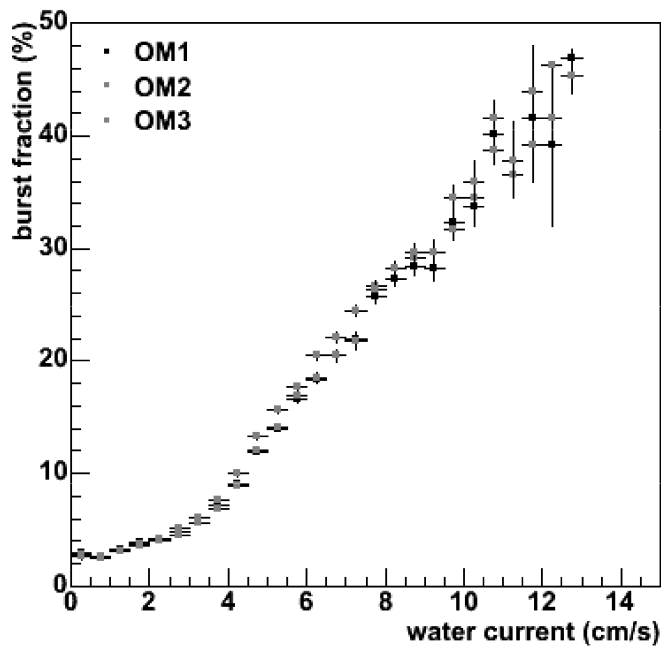


Figure 2.13: Correlation between the burst fraction and the sea current velocity, measured at the ANTARES site. An increased bioluminescence activity is observed for higher current velocities. Taken from [Chia 10].

the equator of the sphere housing the photomultiplier tube, decreasing with increasing zenith angle. Additionally it exhibits a tendency to saturate with time. Even though the sedimentation rate at the site can be quite high, these sediments are washed away by the sea currents. The light transmission as a function of time is shown in figure 2.14.

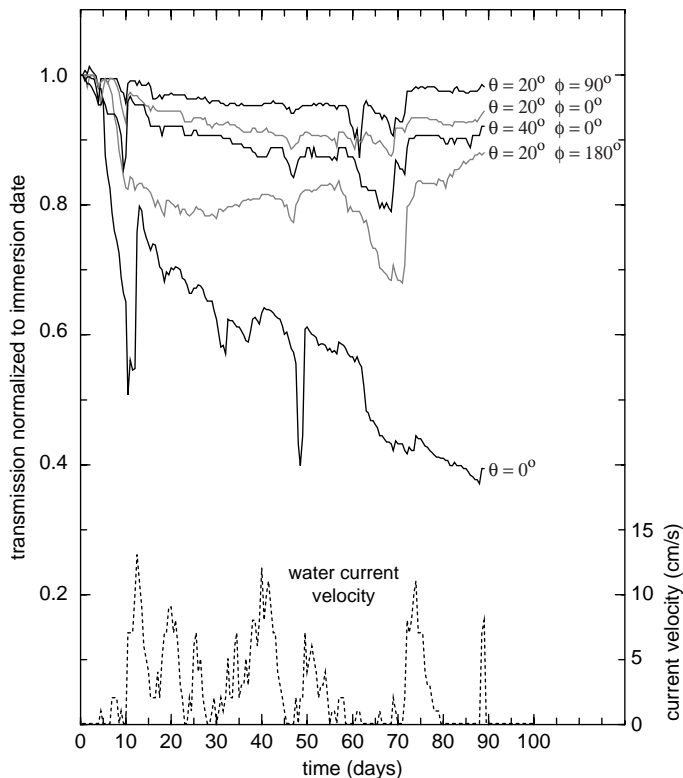


Figure 2.14: Light transmission as a function of time for vertically mounted spheres. The transmission is normalized to the transmission at the immersion date. The angles at the figure indicate the zenith  $\theta$  and azimuth  $\phi$  angles of the photodiode. The  $\theta = 0$  curve corresponds to the top of the sphere where the effect of sedimentation is largest. The increase in light transmission after a period of decreasing transmission is correlated with the sea current velocity indicating that sediments are washed away during high current velocity. Image taken from [ANTA 03].

## 2.6 Data acquisition

The role of the data acquisition (DAQ) system of ANTARES [Agui 07] is to convert the analogue signal recorded by the PM tubes into a digital format that can be used for physics analyses. This includes preparing the detector for data taking, converting the analog PM tube signal and transporting, filtering and storing the data. In addition, the run settings are archived. The DAQ system is a large network of processors, both on-shore and off-shore. The off-shore processors, integrated in custom made electronics, are connected to the on-shore processors (standard PC's) by the electro-optical cable on the sea-bed. A schematic view of the data acquisition system is shown in figure 2.15.

### 2.6.1 Signal digitization

A photon hitting the photo-cathode of a PM tube can produce an electrical signal on the anode. The probability of an electron emission induced by a photon is given by the quantum efficiency (QE) of the PM tube and is a function of the incident photon wavelength. The wavelength dependence of the quantum efficiency is shown in figure 2.16.

If the signal amplitude exceeds a certain voltage threshold, the signal is read-out and digitized by a custom application-specific integrated circuit, the Analogue Ring Sampler (ARS) [Fein 03]. The threshold is typically set to 0.3 photoelectrons to suppress the PM tube's dark current although this can vary among different PM tubes. The ARS can

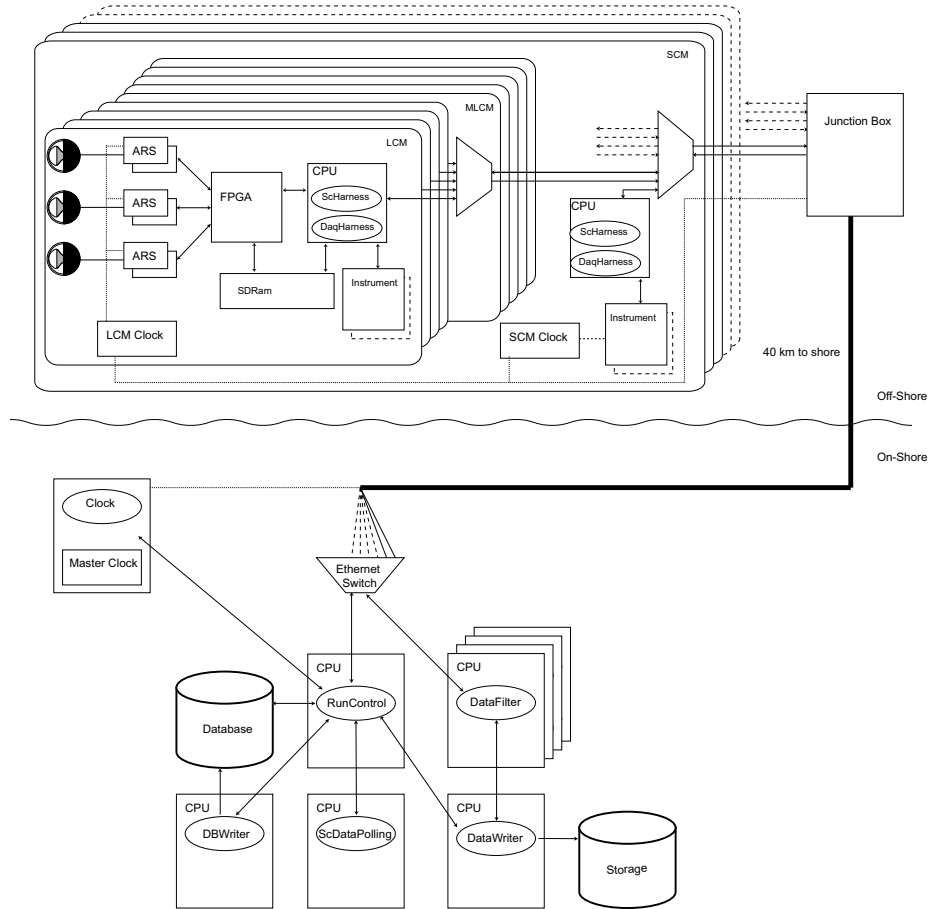


Figure 2.15: A schematic view of the ANTARES data acquisition system. The pulses recorded by the PMT's are digitized and sent to shore, via the Junction Box and the 40 km cable, where filtering and storage takes place.

distinguish between single photoelectron pulses (SPE) and more complex waveforms. The criteria used to discriminate the two classes are based on the amplitude of the signal, the time above threshold or the occurrence of multiple peaks within the time gate. Only charge and time information is recorded for SPE events. In cases of large or double pulses, the ARS can sample the PM tube's signal continuously with a tunable sampling frequency of 150 MHz up to 1 GHz holding the analog information on 128 switched capacitors. For physics data taking only SPE hits are used. A local clock is used by the ARS chips for the determination of the arrival time of the hit. The time resolution of the system is better than 0.4 ns. The charge of the analog signal is integrated and digitized by the ARS over a certain period of time using two 8-bit ADC's. The integration gate is typically set to 40 ns. After this period, the ARS's exhibit a dead time of around 200 ns. Each PM tube is read by 2 ARS's operating in a token-ring scheme to minimize the effect of the dead time. The combined charge

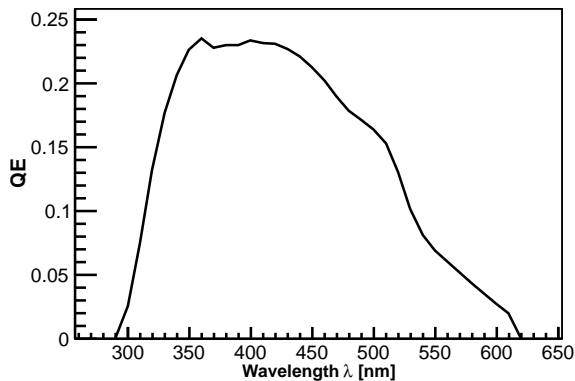


Figure 2.16: PM tube quantum efficiency as a function of the incident light wavelength without taking into account the glass and gel surrounding the tube. The efficiency of the PM tube peaks around 350 nm to 450 nm. The glass and gel of the optical module affect the light transmission in the lower end of the wavelength range, lowering the efficiency.

and time information is called a level 0 (L0) hit. All 6 ARS chips in an LCM are read out by a Field Programmable Gate Array (FPGA) that arranges the hits produced in a time window into a dataframe and stores it in a 64 MB Synchronous Dynamic Random Access Memory (SDRAM). The complete set of dataframes from all ARS's that correspond to the same time window is called a *TimeSlice*. A 20 MHz clock is used to provide a common time for all ARS's. It is synchronized to the GPS time with an accuracy of  $100 \mu\text{s}$ . Through the optical fiber network, all local clocks on the different storeys are synchronized with the master clock.

## 2.6.2 Data transmission

Each offshore CPU runs two programs controlling the data transmission. **DaqHarness** handles the transfer of dataframes from the SDRAM to the control room, while **SCHarness** handles the transfer of calibration and monitoring data (slow-control data). Transmission Control Protocol and Internet Protocol (TCP/IP) is used for communication between the CPU's and for data transport. The LCM's in a sector are connected to the MLCM in the same sector using an optical bidirectional 100 Mb/s link. These links are merged using the Ethernet switch of the MLCM into a single Gb/s Ethernet link. Each string is connected with an electro-optical cable to the junction box which in turn is connected to the shore station with the 40 km long electro-optical cable. The data are transported using dense wavelength division multiplexing technique (DWDM) [Seni 92]. Each sector and each string use a unique pair of wavelengths to transmit data along a single optical fibre to shore. The **ControlHost** package [Guri 95] is used for data transfer and communication among the processes in the DAQ system.

## 2.6.3 Data filtering and storage

All data, after the off-shore digitization, are transported to shore without any further selection. The total data output of the detector in periods of low bioluminescence (60-90 KHz per PMT) is 0.3-0.5 GB/s. Since most of it is optical background it has to be filtered appropriately. Trigger algorithms are applied to identify signals from

particles traversing the detector by searching for space-time correlations in the data. Such physics events selected by the `DataFilter` program, are subsequently written to disk with the program `DataWriter`. The `DataFilter` looks for a set of correlated hits in the full detector in a window of about  $4\ \mu\text{sec}$ . If an event is found, all hits during this time window are stored. If ANTARES receives external GRB alerts all detector activity is recorded for a few minutes. Data filtering or triggering is examined in more detail in the following section.

## 2.7 Trigger

Physics data taking runs in ANTARES last for about three hours. The average data rate of 625 MB/s for each detector string is reduced after filtering to  $\sim 0.15$  MB/s for the whole detector. The duration of the run along with the start and end times, as well as the trigger conditions are stored in the database. The majority of the data is optical background due to potassium decays or bioluminescence. This overwhelming background can be reduced by a factor of  $10^4$  on the first filtering (triggering) stage [Jong 05a]. Such a reduction is achieved by searching for hits within 20 ns in different PM tubes of the same storey or single hits with an amplitude higher than 3 photo-electrons. Hits satisfying these criteria are called L1 hits. All other hits are called L0. This kind of selection is based on the assumption that background hits should be uncorrelated and signal hits correlated. Two recorded hits on two different PM tubes are considered causally related if they satisfy,

$$|\Delta t| \leq \frac{n_g}{c} \cdot d, \quad (2.7.1)$$

where  $\Delta t$  is the time difference between hits,  $d$  is the distance between the PM tubes and  $n_g/c$  is the group velocity of light in water. In this time window an additional  $\pm 20$  ns is included to allow for uncertainties in the hit positions, time and light scattering. Hits satisfying this condition constitute a cluster. If this cluster is large enough (typically 5 L1 hits) it is stored as a physics event. Physics events contain L1 hits that fired the trigger as well as all L0 hits in  $\pm 2.2\ \mu\text{s}$  from the first and last L1 hit. The reason for this is that this is the time it takes for a relativistic muon to travel approximately 650 m i.e. traverse the detector. The hits contained in a physics event are illustrated in figure 2.17.

In addition to this first level selection, a second trigger level (e.g. 3N trigger) can be applied. This includes a scan over a certain number of directions searching for coincidences compatible with the Čerenkov light emission hypothesis. The expected time of a Čerenkov photon is:

$$t_i = t_0 + \frac{1}{c} \left( z_i - \frac{r_i}{\tan\theta_C} \right) + \frac{1}{u_g} \frac{r_i}{\sin\theta_C}, \quad (2.7.2)$$

where  $t_0$  is simply an initial reference time on the muon track. The first term in equation (2.7.2) describes the distance along the track up to the point where the Čerenkov photon

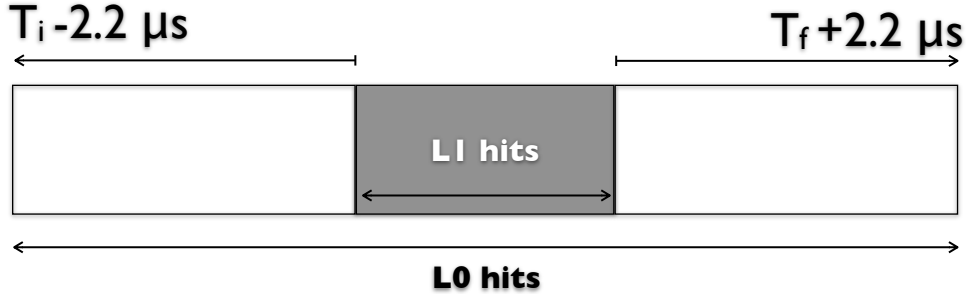


Figure 2.17: A physics event consists of the cluster of correlated L1 hits as well as all L0 hits within a certain time window. This window is defined as the time  $2.2 \mu\text{s}$  before the time of the first L1 hit ( $T_i$ ) up to  $2.2 \mu\text{s}$  after the last L1 hit ( $T_f$ ).

was emitted and the second term is the path from the point of photon emission to the PM tube. This is illustrated in figure 2.18 for two illuminated PM tubes, where  $t_i = (t_1, t_2)$ ,  $z_i = (z_1, z_2)$  and  $r_i = (r_1, r_2)$ . Two hits are considered compatible with the Čerenkov hypothesis if:

$$|t_2 - t_1| \leq \frac{z_2 - z_1}{c} + \frac{R}{c} \tan \theta_C + 20 \text{ ns}, \quad (2.7.3)$$

where we used the assumption that  $\cos \theta_C = 1/n_g$ . The 20 ns are added to account for uncertainties on the time calibration, light scattering, and position of the storey. Additional clusters can be formed by L1 hits. An example of this is the T3 trigger [Carr 07]. It accepts more background hits, increasing the sensitivity in the low energy region with the drawback of triggering on additional events that will be reconstructed badly i.e. it exhibits a higher efficiency at the expense of lower purity. A T3 cluster is defined as at least 2 L1 hits in 3 consecutive storeys within a time window of 100 ns for adjacent and 200 ns for next to adjacent storeys.

## 2.8 Detector calibration

The precision of track and energy reconstruction is strongly dependent on the precision of time, position and charge measurements. In this section, the calibration systems used in ANTARES are discussed.

### 2.8.1 Time calibration

The time calibration in ANTARES [Agui 11] is performed using pulses from LED and laser devices. A timing resolution on the recorded PM tube signals of 1 ns is required to

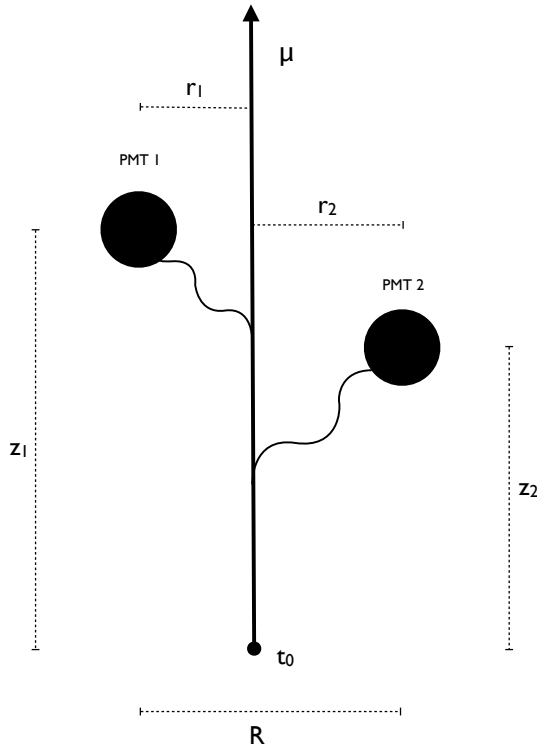


Figure 2.18: Schematic view of a muon illuminating two PM tubes. Photons, indicated by the wavy lines, are emitted under the Čerenkov angle  $\theta_C$  with respect to the track. The time difference between the two hits, assuming that light was emitted under the Čerenkov angle, is constrained by equation 2.7.3. See text for details.

ensure the reliability of track and energy reconstruction. The internal clock calibration system measures the time offsets of each storey. It consists of the master clock on-shore and a bi-directional optical communication system connected to all LCMs. The relative offset of each local clock can be measured by using a calibration signal sent by the master clock and echoed back. The clock system assigns an absolute event time with a GPS master clock synchronization accuracy of  $100 \mu\text{s}$ . The optical beacon system [ANTA 07] is used to calibrate the relative offsets between the PM tubes. Four blue (472 nm) LED beacons on storeys 2,9,15 and 21 of each detector line and two green (592 nm) laser beacons on the BSS of L7 and L8 are used for this purpose. The LED beacons are used for intra-line calibration purposes while the laser beacon, being much more powerful and able to illuminate all the lines, is used for inter-line calibration. An initial set of time offsets is determined in the laboratory prior to deployment. After deployment, these values may change due to different factors such as temperature changes or stresses in the cables. Using the optical beacon system they are monitored periodically and readjusted as necessary. A second calibration system consisting of a blue (470 nm) LED inside each OM is used to measure time offsets between the PM tube photo-cathode and the read-out electronics. Internal LED and optical beacon measurements reveal less than 0.5 ns contribution of the electronics to the photon arrival time resolution. Thus, time resolution is dominated by the transit time spread of the PM tubes which is about 1.5 ns, and light scattering and chromatic dispersion, which depends on the distance travelled by the photon. The calibration system just described provides a relative time calibration of better than 1 ns.

## 2.8.2 Charge calibration

The integrated charge of the PM tube signal has to be converted into the number of photoelectrons that created this pulse. The relation between the signal amplitude and the number of photoelectrons is given by the transfer function of the Amplitude-to-Voltage Converter (AVC). This function is important for the measurement of the amplitude in the PM tube pulse, as well as for the correction of the time slewing of the PM tube signal i.e. the influence of the pulse amplitude and the pulse rise time on the threshold-crossing time, illustrated in figure 2.19. The first step in charge calibration is

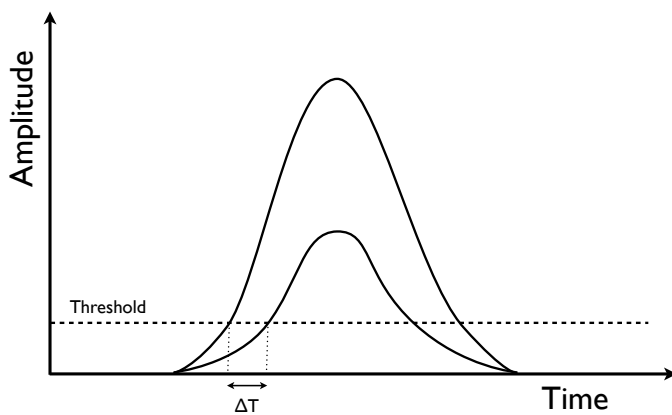


Figure 2.19: Illustration of the time slewing effect. Differences in pulse shape and/or amplitude affect the threshold crossing time.

performed on the test bench where the AVC transfer function is determined. In order to do this, a pulse generator sends a direct signal to a pair of ARS's operating in a token-ring scheme. The pulse has a triangular shape with 4 ns rise time and 14 ns fall time. The transfer function and the dynamic range of the ADC's exhibit a linear behavior and can be parametrized by the slope and intercept of the function. In addition to the test bench calibration, regular *in situ* calibration runs have to be performed. These runs are used to determine the pedestal value of the AVC channel, namely the offset  $AVC_{0pe}$  value corresponding to zero photoelectrons, and the single photoelectron peak which is studied by looking at minimum bias events, since light from potassium decays and bioluminescence produce in their majority single photons on the photocathode level. The charge spectrum, ignoring contributions from the second and higher photoelectron peaks, can be described as [Jong 05b]:

$$f(x) = Ae^{-a(x-x_{th})} + Be^{-\frac{(x-x_1)^2}{2\sigma^2}}, \quad (2.8.1)$$

where the first term corresponds to the contribution of the dark current. The second term describes the single photoelectron peak as a gaussian with mean  $x_1$  and standard deviation  $\sigma$ . The effects of the dynamic nonlinearity (DNL) of the AVC can be minimized by considering the integral of the AVC spectrum:

$$\int_0^x f(x')dx' = \frac{A}{-a}e^{-a(x-x_{th})} + \frac{B}{\sqrt{\pi}}\Gamma\left(\frac{1}{2}, \frac{(x-x_1)^2}{2\sigma^2}\right), \quad (2.8.2)$$

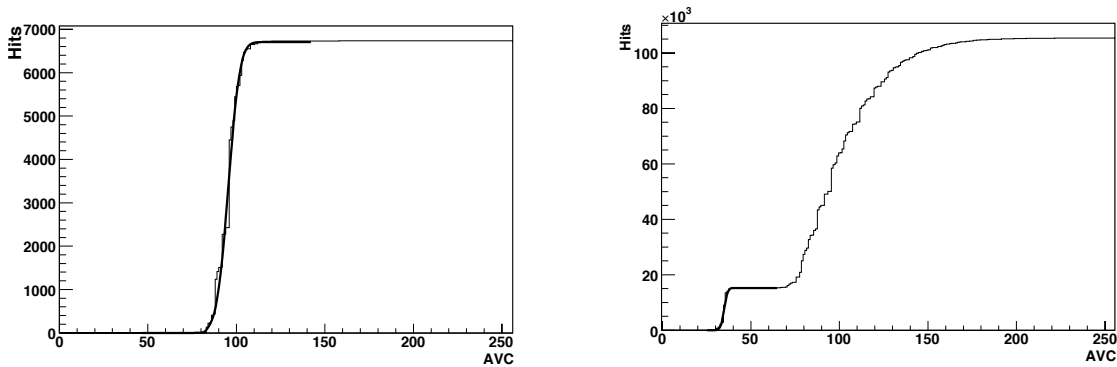


Figure 2.20: Examples of integrated single photoelectron spectrum (left) and integrated pedestal spectrum along with the corresponding fits. Images taken from [Fehr 10].

where  $\Gamma$  is the incomplete gamma function. A fit on the integrated spectrum leads to the determination of the single photoelectron peak. The same procedure is applied to identify the pedestal region as shown in figure 2.20. The parametrization used is:

$$\frac{C}{\sqrt{\pi}} \Gamma\left(\frac{1}{2}, \frac{(x - x_0)^2}{2\sigma_0^2}\right). \quad (2.8.3)$$

Measuring the pedestal and single photoelectron peak values, the transfer function can be determined.

Charge measurements in AVC channels appear to be affected by time measurements in the TVC channel. This is known as the “cross-talk effect” and can be attributed to a cross-talk of the capacitors inside the ARS pipeline. Plotting AVC against TVC values, as shown in figure 2.21, makes it possible to determine the correction to be applied. After applying this correction most of the hits in a minimum bias event have a charge of one photoelectron.

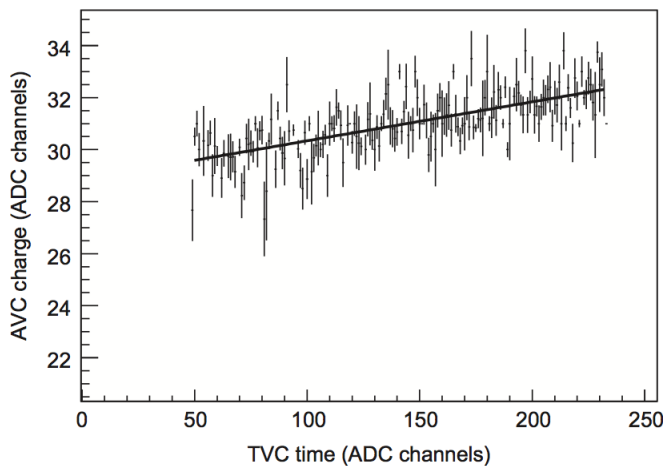


Figure 2.21: Example of the cross-talk effect affecting the charge measurement channel [Agui 10].

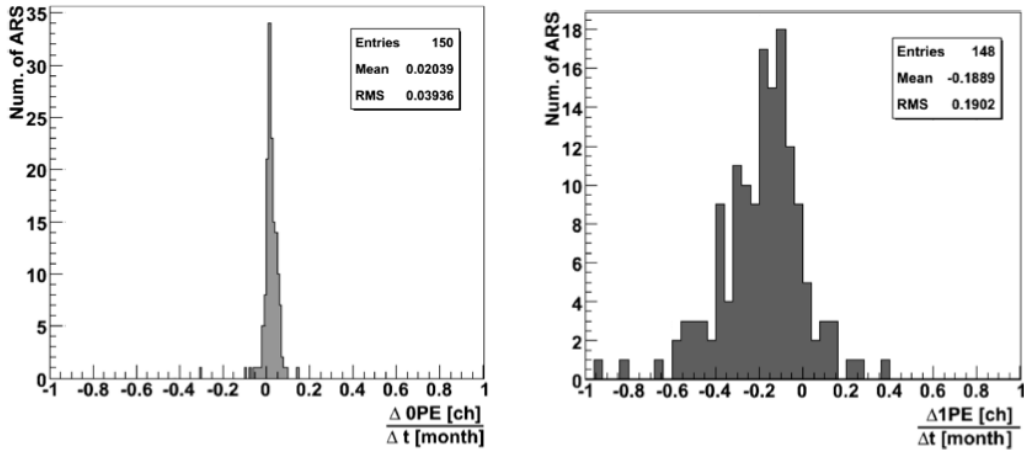


Figure 2.22: Change per month of the charge pedestal (left) and the single photoelectron peak (right) of Line 1 [Fehr 10].

Due to the spread of the PM tube gain, the photoelectron peak is described by a gaussian function with mean  $AVC_{1pe}$ . If the parameters of the gaussian distribution for one photoelectron are  $\mu_1$  and  $\sigma_1$ , then for the coincidence of  $N$  photoelectrons the parameters of the gaussian distribution are,

$$\mu_N = N \cdot \mu_1, \quad (2.8.4)$$

$$\sigma_N^2 = N \cdot \sigma_1^2. \quad (2.8.5)$$

The transfer function is expressed as ,

$$Q [p.e.] = f(AVC) = \frac{AVC - AVC_{0pe}}{AVC_{1pe} - AVC_{0pe}}, \quad (2.8.6)$$

where  $AVC$  is the corrected  $AVC$  value taking into account the “cross-talk effect”.

Light from potassium decay is also used to monitor how the detector response evolves with time. A gain drop of the PM tubes is observed and is attributed to the aging of the phototube. The charge pedestal value is almost constant in time, while the photoelectron peak drops by around 0.02 photoelectrons per month as can be seen in figure 2.22. The systematic error on charge calibration is estimated at around 30% [Fehr 10; Bare 09].

### 2.8.3 Position calibration

Due to the flexible nature of the lines, water currents can displace the position of the optical modules, especially on top storeys. As with timing and charge information, knowledge of the position of the optical modules is of high importance for a precise event reconstruction. For this purpose a High Frequency Long Baseline (HFLBL) acoustic

system is used to monitor the positions of five hydrophones along each line. The hydrophones are mounted on storeys 1, 8, 14, 20 and 25. A transmitter-receiver is installed at the anchor of each line and some additional autonomous transponders are used. The emitters send high frequency acoustic signals in the 40-60 kHz range and the distances are obtained by measurements of the travel times of the acoustic waves. The distances are used to triangulate the position of each receiver with respect to the emitters on the sea floor. Furthermore, a system of compasses and tiltmeters is used to measure the orientation and inclination of each storey. The shape of each line is reconstructed by performing a global  $\chi^2$ -fit based on a model of the mechanical behavior of the line under the influence of the sea currents. The relative positions of each OM are calculated from this fit using the known geometry of each storey. In order to determine these positions as accurately as possible, knowledge of the water current flow and the sound velocity in sea water is used. These are measured using acoustic doppler current profilers (ADCP) for the water current flow, conductivity-temperature-depth (CTD) sensors to monitor the temperature and salinity of the water and sound velocimeters to monitor the sound velocity in sea water. The relative positions of all the optical modules is monitored with an accuracy better than 20 cm [Ardi 09]. The horizontal movement of a line with respect to the BSS position is illustrated in figure 2.23. The absolute positioning of each anchored detector component is calculated with an accuracy of about 1 m by acoustic triangulation from a surface ship equipped with differential GPS.

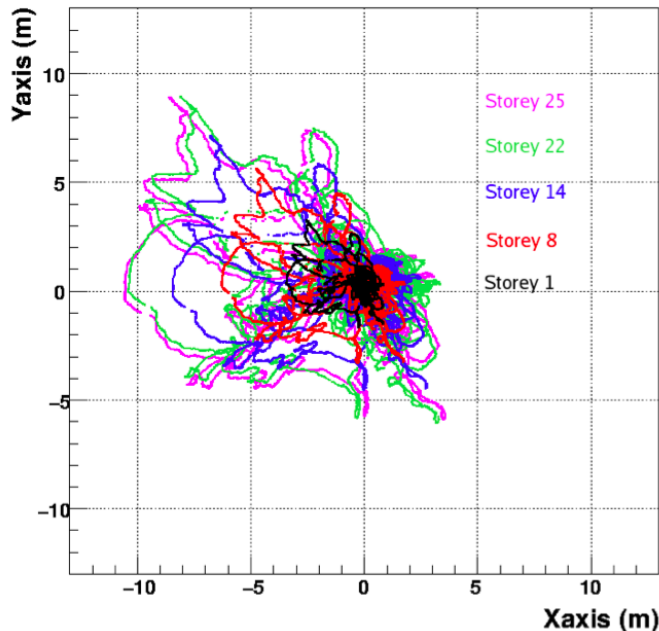


Figure 2.23: The horizontal displacement of the hydrophones on Line 11 with respect to the BSS (0,0) for a period of six months. The East-West tendency of the Line heading is due to the Ligurian current at the detector site. The top storeys of the line experience larger amounts of displacement due to the water current. Image taken from [Brow 09].

## 2.9 Detector history and status

During the period between 1996 and 1999 several site campaigns were performed, aiming to evaluate quantities such as the refraction index, scattering and absorption lengths as well as background rates. A 350 m line with seven photomultipliers was deployed at a depth of 1200 m from the end of 1999 until June 2000. Tests of acoustic positioning as well as the first atmospheric muon data measurements were performed. The MEOC was installed in October of 2001. In December 2002, the junction box and a prototype-sector-line (PSL) were deployed. It contained one LED beacon, a sound velocimeter, a pressure sensor, hydrophones and an acoustic transceiver. A mini instrumentation line (MIL), containing time calibration, positioning and monitoring devices was deployed in February 2003. During the next month, the prototype and the mini instrumentation line were connected to the junction box, where they stayed for the next couple of months. In March 2005, a mechanical test line (Line 0), containing all the mechanical elements of a full string but without the electronics, was built and deployed along with an improved mini instrumentation line (MILOM). The test line was recovered after two months. The first ANTARES complete line (Line 1) was deployed in February 2006 and in March of the same year it was connected and data taking started. In July 2006, Line 2 was deployed and it has been operational since September 2006. In January 2007, Lines 3,4 and 5 were connected, making ANTARES the most sensitive neutrino telescope in the Northern hemisphere. By the end of 2007, Lines 6 to 10 were connected, effectively doubling the size of ANTARES. The last two lines were connected in May 2008, thereby completing the construction of the ANTARES telescope. On June 24th 2008, the cable providing power to the junction box broke down, interrupting the detector's power supply. A sea operation took place on the 6th of September, the cable was repaired and data taking resumed normally. During the following years several lines have been non-operational and action had to be taken for their recovery and redeployment. Line 6 was disconnected from October 2009 until November 2010. Line 9 was not operational from July 2009 until November 2010. A problem with the cable connecting Line 10 did not allow data taking with this line from January 2009 until November 2009. Finally, Line 12 was disconnected from March 2009 until November 2009 and did not take data due to a cable problem during the period from September 2010 to November 2010.

## 2.10 Other neutrino telescopes

The ANTARES detector is not the only neutrino detector that has been constructed or is already operational. In this section, past, present and future efforts towards neutrino astronomy will be summarized.

The DUMAND project (**D**eep **U**nderwater **M**uon **A**nd **N**eutrino **D**etection) [Aoki 98] started around 1976 with the goal to construct a neutrino telescope at 4800 m in the Pacific Ocean off Keyhole Point on the Big Island of Hawaii. The attempt however was not successful. After the connection of the prototype strings, short circuits occurred and the connection to the shore was lost. In 1996 funding was ceased and the project

was cancelled.

The BAIKAL neutrino telescope was the first working setup which proved the feasibility of optical neutrino detection technique, detecting several of these elusive particles in 1996. It was deployed in the Siberian lake Baikal [Balk 01] and consisted of 18 strings with 192 PM tubes (NT-200 setup) at a depth of 1 km. The 68.5 m strings were distributed in a circular geometry with a 22 m radius. This setup was extended in 2005 by 3 additional strings of 200 m length with 36 PM tubes (NT-200+ setup) at a distance of 100 m from the detector center to increase shower effective area. Contrary to ANTARES, fresh lake water gives no background contributions from  $^{40}\text{K}$  decays but a contribution from bioluminescence is present. In addition to that, maintenance operations are easier, using the frozen lake surface as a basis for these operations. On the other hand, the reduced absorption length as well as the small depth of the lake lead to more background from atmospheric muons.

AMANDA (**A**ntarctic **M**uon **A**nd **N**eutrino **D**etection **A**rray) [Andr 99] is located near the Scott-Amundsen South Pole station in the Antarctic Ice. In 1997, 10 strings were immersed in glacial ice at a depth of 1500-2000 m. 302 PM tubes, 8-inch in diameter were used. In 2000, the apparatus was enhanced to AMANDA-II adding 9 more strings reaching a total of 677 PM tubes. AMANDA was switched off in 2009.

The IceCube neutrino observatory [Gold 02] is the  $\text{km}^3$ -sized successor of AMANDA and has recently been completed in the Antarctic Ice. It is configured as a collection of 80 strings of over 1000 m length, separated by 125 m, with 4800 PM tubes in total. A complementary surface air-shower array, IceTop, serves as a calibration device. IceCube is already operational.

A number of projects exist in the Mediterranean aiming towards the construction of a cubic kilometer neutrino telescope. NESTOR (**N**eutrino **E**xtended **S**ubmarine **T**elescope with **O**ceanographic **R**esearch) [Rapi 09] is a Greek collaboration and it initiated the first project for a neutrino telescope in the Mediterranean sea. NEMO (**N**eutrino **M**editerranean **O**bservatory) [Amor 07] is an Italian collaboration. The KM3NeT project [Katz 06b; Katz 06a] is a joint effort of the ANTARES, NEMO and NESTOR collaborations to design and construct the next generation telescope with a size of about  $5 \text{ km}^3$ .

## ENERGY RECONSTRUCTION

In this chapter, a method to reconstruct the energy of muons traversing the detector is presented. The method attempts to maximize the agreement of the expected amount of light in the optical modules with the amount of light that is actually observed. We construct a maximum likelihood function modeling the muon traversal through the detector and keeping the energy of the muon as the free parameter.

In section 3.1, the energy-loss processes that take place when a charged particle passes through matter as well as the propagation of light in the same medium are discussed. The Monte Carlo simulation tools used in this work are summarized in section 3.2. Section 3.3 contains a description of the track reconstruction method which is used in the present analysis. The maximum likelihood energy reconstruction is described in section 3.4 and the performance of the method is examined in section 3.5.

### 3.1 Muon energy loss

Charged particles lose energy while traversing matter. The mean rate of energy-loss is given by the Bethe-Bloch equation [Revi 06],

$$-\frac{dE}{dx} = Kz^2 \frac{Z}{A} \frac{1}{\beta^2} \left[ \frac{1}{2} \ln \frac{2m_e c^2 \beta^2 \gamma^2 T_{max}}{I^2} - \beta^2 - \frac{\delta(\beta\gamma)}{2} \right]. \quad (3.1.1)$$

Here,  $K = 4\pi N_A r_e^2 m_e c^2$  is a constant,  $z$  is the charge of the incident particle,  $Z$  and  $A$  are the atomic number and atomic mass of the absorber respectively,  $\beta$  is the velocity of the incident particle,  $\gamma$  is the Lorentz factor,  $I$  is the mean excitation potential of the atoms in the medium and  $T_{max}$  is the maximum kinetic energy which can be transferred to a free electron in a single collision. The potential  $I$  is essentially the average orbital frequency  $h\bar{\nu}$  of bound electron states in the atoms, where  $h$  is Planck's constant. The calculation of the mean excitation potential is a challenging task and its values for various absorption materials are deduced by energy-loss measurements. The value of  $I$  for water is 75 eV [Leo 94]. The term  $\delta$  corresponds to the density effect correction [Ferm 40]. It is included in order to take into account the effect on the

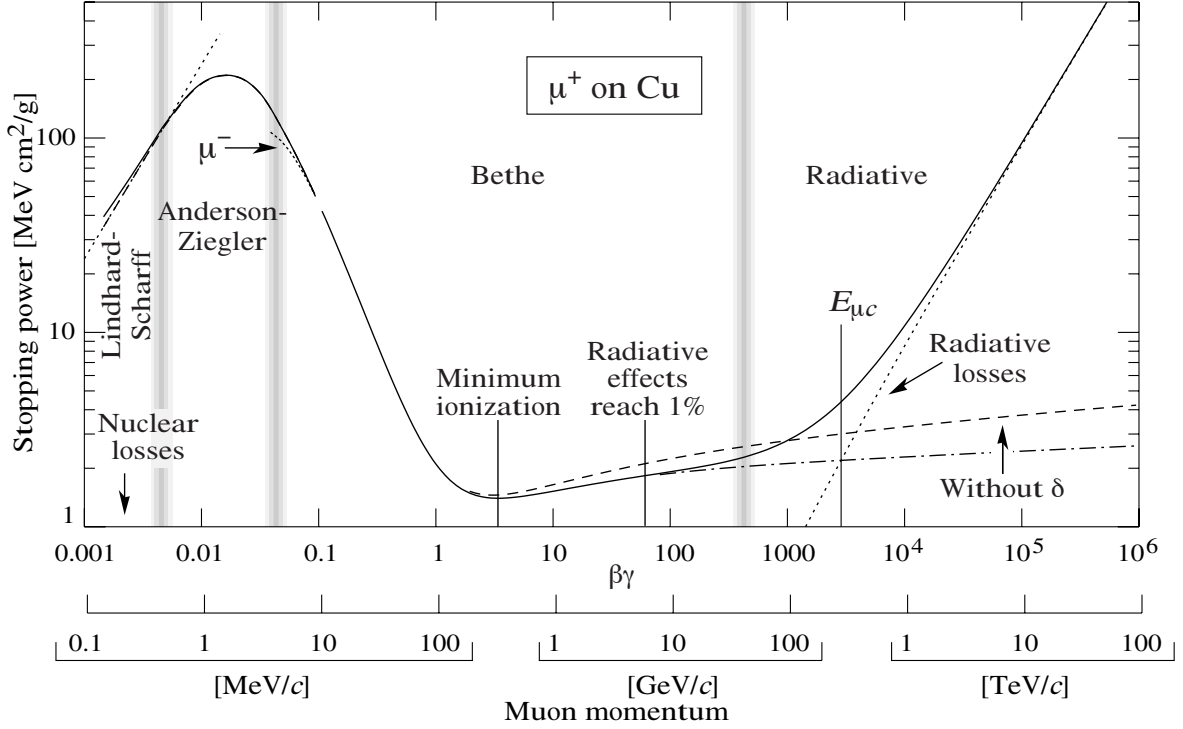


Figure 3.1: Stopping power for positively charged muons in copper. The Bethe-Bloch equation describes the central region of this figure, i.e. muon momenta from  $\sim 5$  MeV/ $c$  to  $\sim 50$  GeV/ $c$ , with an accuracy of a few percent. Figure taken from [Revi 06].

ionization energy-loss, of the polarization of the medium induced by the passage of the charged particle. This effect results in a reduced energy-loss due to ionization especially for electrons further away from the track. The mean energy-loss for positively charged muons in copper is shown in figure 3.1. For materials with decreasing  $Z$ , there is a slow increase in the rate of energy-loss, because the ratio  $Z/A$  tends to increase. Relativistic particles with mean energy-loss rates close to the minimum of the Bethe-Bloch curve are called minimum ionizing particles (MIP). The energy range of interest in the present work is between a few hundreds of GeV to a few hundreds of TeV.

A muon traveling through rock or water will lose energy due to ionization, pair production, photo-nuclear interactions and Bremsstrahlung radiation. The average energy-loss per unit path length can be expressed in the following way:

$$-\frac{dE}{dx} = \left(\frac{dE}{dx}\right)_I + \left(\frac{dE}{dx}\right)_P + \left(\frac{dE}{dx}\right)_N + \left(\frac{dE}{dx}\right)_B, \quad (3.1.2)$$

where the four indices I,P,N and B correspond to the above mentioned processes respectively. The energy-loss processes can be divided into continuous and stochastic. When the number of discrete collisions over a macroscopic path length is very large and additionally each collision contributes a small fraction of the total energy-loss, the process is considered continuous. On the other hand, stochastic processes occur rarely

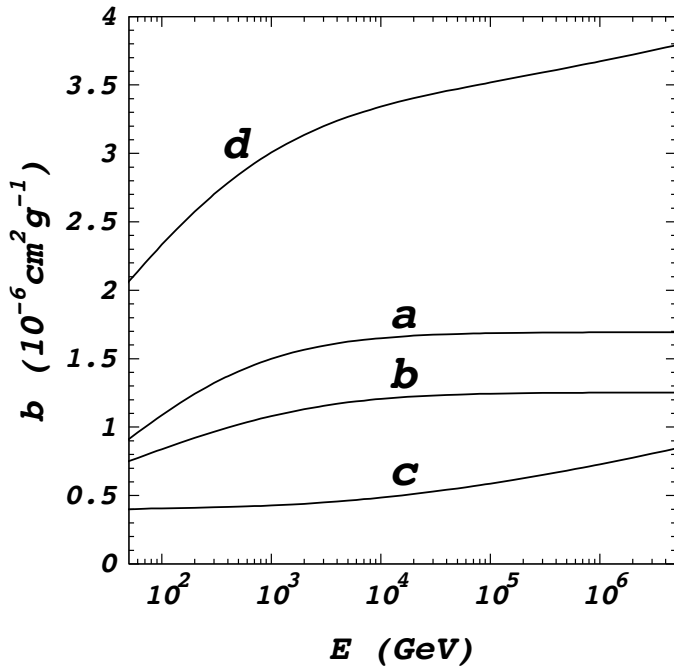


Figure 3.2: Evolution of  $b(E)$  as a function of the muon energy. Curves a, b and c correspond to pair production, Bremsstrahlung and photo-nuclear interactions respectively. Curve d is the total contribution. The propagation medium is water (Figure from [Klim 01]).

and a single instance can be responsible for a large fraction of the total energy-loss leading to large energy-loss fluctuations. Distinguishing between continuous and stochastic processes, equation (3.1.2) can be written as:

$$-\frac{dE}{dx} = a(E) + b(E)E. \quad (3.1.3)$$

The first term is due to the ionization, a quasi continuous process, while the second term includes the contributions from stochastic processes. These terms are energy-dependent as can be seen in figure 3.2.

The energy-loss per unit track length  $\frac{dE}{dx}$  in water as a function of the muon energy is shown in figure 3.3. The curve shown here corresponds to the right part of the Bethe-Bloch curve shown in figure 3.1. One sees that up to a few hundred GeV the energy-loss is almost constant while for higher energies it rises linearly with the energy. This is due to the fact that ionization losses increase logarithmically with energy and linearly with the atomic number  $Z$ , while radiative losses increase approximately linearly with energy and quadratically with  $Z$ , therefore causing the stochastic processes to dominate above approximately 1 TeV. This is called the critical energy, indicated as  $E_{\mu c}$  in figure 3.1, and it is defined as the energy at which the ionization energy-losses are equal to the radiative energy-losses i.e.  $a(E_{\mu c}) = b(E_{\mu c}) \cdot E_{\mu c}$ . The quadratic dependence of radiative losses on  $Z$  is responsible for the lower critical energy in the case of copper. Assuming that  $a(E)$  and  $b(E)$  are constant, a frequently used approximation, equation (3.1.3) can be written as:

$$-\frac{dE}{dx} \simeq a + b \cdot E, \quad (3.1.4)$$

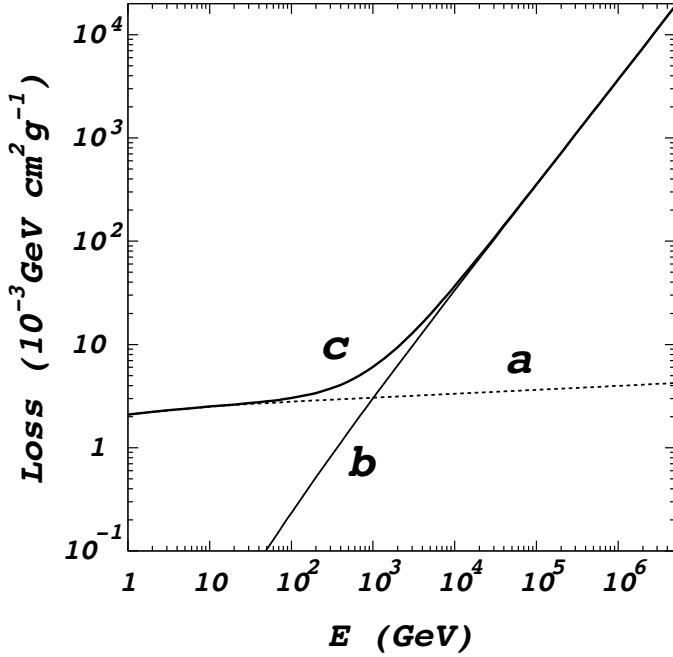


Figure 3.3: Energy loss as a function of the muon energy. Curve a corresponds to energy losses due to ionization ( $a(E)$  term) while curve b corresponds to the radiative processes ( $b(E)E$  term). Curve c describes the total energy losses. (Figure from [Klim 01])

where for water,  $a \simeq 2.67 \text{ MeV/cm}$  and  $b = b_P + b_B + b_N \simeq (1.7 + 1.2 + 0.5) \cdot 10^{-6} \text{ cm}^{-1}$ . Integrating (3.1.4) one can calculate the mean range of a muon with initial energy  $E_0$ ,

$$R = \frac{1}{b} \ln\left(1 + \frac{b}{a} E_0\right). \quad (3.1.5)$$

This is the average distance travelled by a muon with initial energy  $E_0$  before it loses all of its energy.

The challenge in reconstructing the muon energy lies in the fact that for lower energies the light yield of the muon is almost constant, making it difficult to distinguish between e.g., a 100 GeV and a 500 GeV muon. In addition, light from potassium decay and bioluminescence contribute a significant amount of background light for such low energy events. For higher energies, the difficulty in reconstructing the muon energy arises from the stochastic nature of the energy-loss processes. A muon may lose a significant fraction of its energy within a short track length by a very bright shower. The fraction of the muon energy that is carried away by Bremsstrahlung photons increases as the energy of the muon and the atomic number of the absorber increase. The photon energy spectrum is continuous and it is possible for a muon to lose all of its energy in a single shower. If a very large shower happens to be outside the detector, its light will not be detected leading to an underestimate of the muon energy at the point of its creation and therefore of the parent neutrino energy. The energy we attempt to estimate in the present work is the energy of the muon in the vicinity of the detector. This energy is not the same as the parent neutrino energy, a problem that we address in chapter 4.

### 3.1.1 Energy loss processes

The most relevant energy-loss process for energies less than  $\sim 1$  TeV is ionization. When a muon scatters with atoms from the surrounding medium it transfers energy to atomic electrons. This process is described well by the Bethe-Bloch formula and it corresponds to the almost flat part of the curve, before radiative effects dominate the energy-losses. The total energy-loss due to ionization caused by a minimum ionizing particle is about 2 MeV/cm. Energy is also carried away by the Čerenkov photons but it is negligible compared to the other processes. The energy-loss due to Čerenkov photons from a relativistic muon traveling in water can be expressed as [Leo 94]:

$$-\frac{dE}{dx} = \frac{\alpha\hbar}{c} \int \omega d\omega \sin^2\Theta_C, \quad (3.1.6)$$

where  $\alpha$  is the fine structure constant. Integrating from a minimal wavelength of 100 nm ( $n(100 \text{ nm}) \simeq 1$ ) we find a contribution of the order of  $\sim 0.05$  MeV/cm, much smaller than the ionization energy-loss.

Above  $\sim 1$  TeV, the stochastic processes explained below start to dominate over the ionization energy-losses. These stochastic processes are characterized by large energy fluctuations and the generation of electromagnetic and hadronic showers. The energy-loss  $dE/dx$  is not continuous, especially for higher muon energies. For that reason, the energy-loss rate (3.1.2) or (3.1.4) is interpreted as the average muon energy-loss along  $dx$ . The main energy-loss process at such energies is pair production. In the presence of an atom, the muon can produce an electron-positron pair transferring part of its energy to the nucleus. A diagram illustrating this process is shown in figure 3.4. In addition to pair production, energy is lost via photo-nuclear interactions. These are processes where a muon interacts inelastically with a nucleon inside the medium (figure 3.5). Finally, Bremsstrahlung radiation (figure 3.6), which takes place when a muon decelerates due to electromagnetic interactions with atoms from the medium,

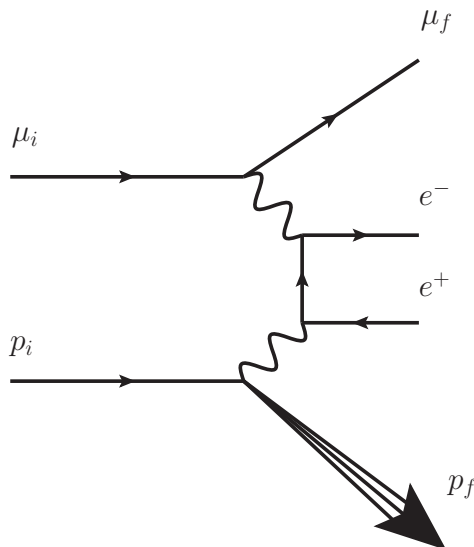


Figure 3.4: Pair-production Feynman diagram. The incoming (outgoing) muon is indicated as  $\mu_i$  ( $\mu_f$ ) while the target nucleus is  $p_i$ . A hadronic shower is included in the final state when the momentum transfer is large enough, i.e. above the pion production threshold.

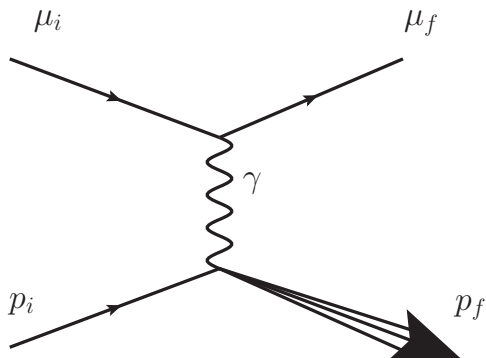


Figure 3.5: Nuclear interaction Feynman diagram. The incoming (outgoing) muon is indicated as  $\mu_i$  ( $\mu_f$ ) and the target nucleus as  $p_i$ .

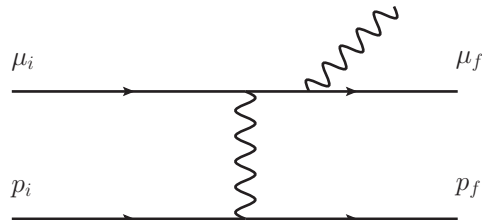


Figure 3.6: Bremsstrahlung Feynman diagram. The initial (final) states are indicated with a subscript  $i$  ( $f$ ).

contributes to the energy-loss. This deceleration may cause the emission of very high energy photons. The radiative cross section as a function of the fractional energy-loss ( $x = E_{\text{loss}}/E_\mu$ ) for pair production goes roughly as  $1/x^2$  to  $1/x^3$  while for bremsstrahlung the dependence is less steep, i.e.  $1/x$ . This is the reason why “hard” energy-losses are more probable in bremsstrahlung while pair production losses are closer to being treated as continuous [Keln 67; Mo 69; Ginn 86].

### 3.1.2 Light propagation and detection

#### Direct Čerenkov light

A charged particle traveling through a medium faster than the speed of light in that medium emits Čerenkov radiation (see section 2.2.1). The energy carried away by these photons is negligible compared to the energy lost due to stochastic processes or ionization losses as discussed in the previous section. Čerenkov light is emitted under a fixed angle  $\cos \Theta_C = \frac{1}{\beta \cdot n}$ , where  $n$  is the index of refraction for that medium, creating a cone of light around the particle’s track. The number of Čerenkov photons emitted per unit track length  $\frac{d^2N}{dx d\lambda}$  is given in equation (2.2.5). The number of detectable photons per unit wavelength and per unit area at a distance  $R$  from the muon track is given by the number of photons emitted by a track segment  $L$ , divided by the circular disk area created by the photons from that segment,

$$\Phi_0(R, \lambda) = \frac{d^2N}{dx d\lambda} \frac{1}{2\pi R \sin \Theta_C}, \quad (3.1.7)$$

illustrated in figure 3.7.  $L$  is defined as the track segment that is viewed by the optical module under the Čerenkov angle  $\Theta_C$ .

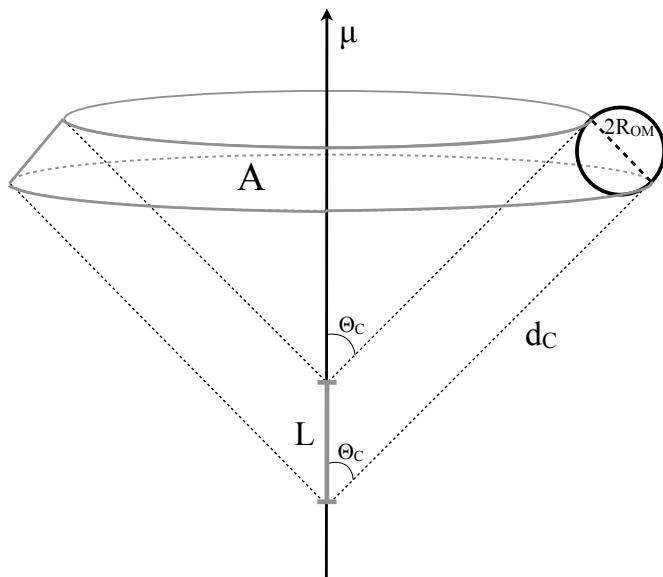


Figure 3.7: The number of detectable photons that reach an optical module is related to the area  $A$ , which is the area covered by the photons emitted under the Čerenkov angle  $\Theta_C$  by the track segment  $L$ .

### Light from electromagnetic showers

Along with Čerenkov radiation from the muon, there is also light originating from electromagnetic and hadronic cascades. Bremsstrahlung and pair production are the two processes responsible for the electromagnetic cascades. Hadronic showers occur when a nuclear interaction takes place, producing more hadrons that in turn re-interact and give rise to a hadronic cascade. Electromagnetic cascades consist exclusively of electrons, positrons and photons, and point mainly in the forward direction. Photons create electron-positron pairs that emit Bremsstrahlung radiation. These photons in turn produce more  $e^+ - e^-$  pairs. The process continues until all energy is dissipated. Hadronic cascades have a more variable composition and a larger transverse spread. They consist predominantly of pions, muons as well as an electromagnetic component due to the cascades initiated by the photons produced by  $\pi^0$  decays.

As discussed in section 3.1, the term  $b(E)E$  of equation (3.1.3) takes into account the stochastic processes. The number of detectable photons per unit wavelength and per unit shower energy is given by:

$$\frac{d^2 N}{dE d\lambda} = \frac{dx}{dE} \frac{d^2 N}{dx d\lambda}, \quad (3.1.8)$$

where  $\frac{dx}{dE}$  is the equivalent bare muon track length per unit of shower energy. Based on Geant [Agos 03; Amak 06], a toolkit to simulate the passage of particles through matter, its value is estimated and found to be about  $4 \text{ m GeV}^{-1}$  for water. Since light from showers is not emitted under a fixed angle, the Čerenkov cone is distorted and the angular distribution of shower light emission,

$$\frac{d^2 P_\star}{d \cos \theta d\phi} = c e^{b|\cos \theta - \cos \Theta_C|^\alpha}, \quad (3.1.9)$$

needs to be taken into account [Mira 02]. The values of the three parameters are  $\alpha = 0.35$ ,  $b = -5.4$  and  $c = \frac{1}{2\pi} \frac{1}{0.06667}$ . This leads us to the number of detectable

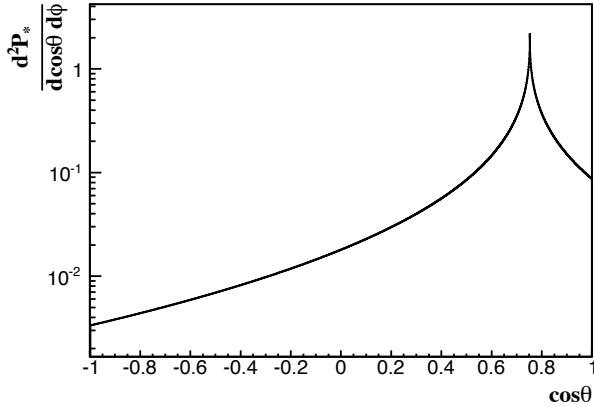


Figure 3.8: Angular distribution of light emitted by an electromagnetic shower. The probability density is strongly peaked around the Čerenkov angle.

photons originating from electromagnetic showers per unit wavelength, track length and solid angle,

$$\Phi_1(\cos\theta, E, \lambda) = \frac{d^2 N(E)}{dx d\lambda} \frac{d^2 P_*}{d\cos\theta d\phi}, \quad (3.1.10)$$

where the number of detectable photons per unit wavelength and per unit track length due to electromagnetic showers is:

$$\frac{d^2 N(E)}{dx d\lambda} = b(E) E \frac{d^2 N}{dE d\lambda}. \quad (3.1.11)$$

The probability distribution of the angle of emission is shown in figure 3.8.

There are two processes that affect light propagation in water, light absorption and light scattering. The way they are introduced into the calculation of the detected light in the optical modules is examined in the following two paragraphs.

### Light absorption

Light is attenuated as it traverses a certain medium. Individual photons are being absorbed by atoms in the medium via the photoelectric effect. The atomic electron that absorbs the photon is subsequently ejected from the atom carrying away energy equal to the energy of the photon minus the electron's binding energy. This results in a reduced intensity of the initial photon flux. Absorption can be accounted as follows. If the initial flux is  $\Phi$ , then after a distance  $d$  this flux will be  $\Phi'$ :

$$\Phi' = \Phi \cdot e^{-\frac{d}{\lambda_{abs}}}, \quad (3.1.12)$$

where  $\lambda_{abs}$  is the absorption length, i.e. the distance at which  $\sim 63\%$  of the photons will have been absorbed. The absorption length as a function of the photon wavelength is shown in figure 2.10.

### Light scattering

Light scattering off particles in the medium affects the number of detectable photons that reach the optical modules. Incident electromagnetic radiation deforms the charge

distribution of the scattering particle, forming an oscillating dipole that radiates light. The scattering angle, effectively the direction of light after the scattering, has to be taken into account. Particles with size much larger than the incident light wavelength contribute to small angle scattering, known as Mie scattering [Mie 08], due to destructive interference from light radiated from different parts of the scattering particle. Rayleigh scattering [Rayl 71] refers to scattering from particles with sizes much smaller than the wavelength that contribute to large scattering angles since the particle is subject to a uniform electric field. Rayleigh scattering is the limiting case of the Mie solution to Maxwell's equations for particles that satisfy:

$$\alpha \ll \frac{\lambda}{2\pi n}, \quad (3.1.13)$$

where  $\alpha$  is the radius of the scattering particle,  $\lambda$  is the incident light wavelength and  $n$  the refractive index. The flux of direct photons reaching the OM's will be reduced by the number of photons that are scattered along the way. A term that will effectively reduce the number of direct photons needs to be included when the contribution of the direct photon flux is calculated. Analogously to light absorption, the flux is reduced as:

$$\Phi' = \Phi \cdot e^{-\frac{d}{\lambda_s}}, \quad (3.1.14)$$

where  $\lambda_s$  is the wavelength-dependent scattering length, which is shown in figure 2.11.

Various models have been developed to describe the scattering angle probability density function  $\frac{dP_s}{d\Omega_s}(\theta_s)$ . The scattering probability depends only on the scattering angle  $\theta_s$ , defined as the angle between the photon direction before and after scattering. This is due to the rotational symmetry of light scattering. Two different scattering models' parametrizations are considered in the present work [Bail 00]. The  $f_4$ -model is based on the so-called "medsea" parametrization which is a combination of two Henyey-Greenstein functions. They are defined as:

$$f_{HG}(g; \cos \theta_s) = \frac{1}{4\pi} \frac{1 - g^2}{(1 + g^2 - 2g \cos \theta_s)^{\frac{3}{2}}}, \quad (3.1.15)$$

where  $g$  is the average cosine of the scattering angle. The parametrization for the probability density function of the scattering angle is defined as:

$$\frac{dP_s}{d\Omega_s} = p \cdot f_{HG}(g_1; \cos \theta_s) + (1 - p) \cdot f_{HG}(g_2; \cos \theta_s). \quad (3.1.16)$$

The Henyey-Greenstein functions are normalized to unity for the full solid angle. In the  $f_4$ -model, the following values are used:

$$\begin{aligned} p &= 1, \\ g_1 &= 0.77, \\ g_2 &= 0. \end{aligned}$$

For  $g = 0$  the probability density is uniform for all scattering angles while as  $g$  approaches unity the density peaks strongly in the forward direction, i.e.  $\theta_s = 0^\circ$ .

The second model under consideration is the  $p0.0075$ -model which is a combination of Rayleigh and Mie scattering. The parametrization used for this model is:

$$\frac{dP_s}{d\Omega_s} = p \cdot f_R(\beta; \cos \theta_s) + (1 - p) \cdot f_{HG}(g; \cos \theta_s), \quad (3.1.17)$$

where  $g = 0.924$  and  $p = 0.17$ , i.e. 17% contribution from Rayleigh scattering. The Rayleigh term  $f_R$  is given by:

$$f_R(\beta; \cos \theta_s) = \frac{1}{4\pi} \frac{1}{1 + \frac{\beta}{3}} (1 + \beta \cos^2 \theta_s). \quad (3.1.18)$$

The  $\beta$  term is a measure of the spherical symmetry of the particles on which scattering takes place and is equal to one for a perfect sphere. For water molecules  $\beta = 0.853$ . The distribution of the scattering angle due to large particles in the  $p0.0075$ -model is obtained from *in situ* measurements. The probability distributions of the scattering angle for the  $f_4$  and  $p0.0075$  models are shown in figure 3.9. The higher contribution to large angle scattering in the  $p0.0075$ -model is due to the Rayleigh term that is not present in the  $f_4$ -model as well as the fact that the term  $g = 0.77$  in the Henyey-Greenstein function favors forward scattering.

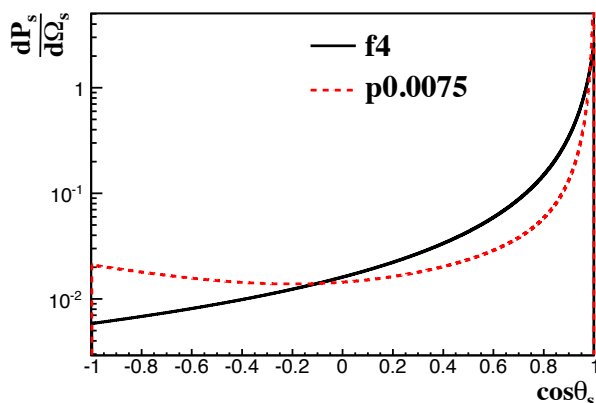


Figure 3.9: Parametrization of the scattering angular distribution of light for the  $f_4$  and  $p0.0075$  models.

### Light detection

After taking into account photon emission and propagation, the only term missing to have an estimate of the expected charge that will be measured by the optical modules is the response of the PM tube. Therefore, the charge that we expect to measure is a convolution of three factors. They describe how much light is emitted from the muon, how photons are propagated and attenuated in the medium before they finally reach the OM's and how the PM tubes translate this light into a measured charge pulse. The detection efficiency depends on the wavelength of light as well as the angle of incidence of the photon on the PM tube. The angular acceptance accounts for the angle of incidence, defined as the angle between the photomultiplier axis and the direction of the incident photon. The PM tube quantum efficiency (see fig. 2.16), together with the glass and gel opacity to light, is taken into account.

## 3.2 Monte Carlo simulation tools

In this section we give an overview of the simulation chain and the software packages used to generate the neutrino and muon events in the detector. The standard ANTARES simulation tools are used for the generation of muons and neutrinos, the propagation of muons and other secondary particles towards and through the detector along with photon emission and propagation, and finally the simulation of the optical modules' response. The simulation we use corresponds to the best available description of the true data taking conditions, using information about the rates, the condition of the optical modules and the run duration from the corresponding data runs. In this way, a realistic run-by-run simulation of the physics and data taking process is achieved [Rivi 12].

Assuming an initial flux of neutrinos at the surface of the Earth, the rate of detected neutrino events is expressed as:

$$R = \iiint \frac{d^2\Phi(E_\nu, \hat{d})}{dE d\Omega} P_\odot(E, \hat{d}) \rho(\vec{x}) N_A \sigma_{CC}(E) P_{\text{det}}(E, \hat{d}, \vec{x}) dE d\Omega d\vec{x}. \quad (3.2.1)$$

The differential neutrino flux at the surface of the Earth  $\frac{d^2\Phi(E_\nu, \hat{d})}{dE d\Omega}$  is given in units of  $\text{GeV}^{-1}\text{sr}^{-1}\text{m}^{-2}\text{s}^{-1}$ .  $P_\odot(E, \hat{d})$  is the probability of a neutrino traversing the Earth without undergoing an interaction,  $\rho(\vec{x}) N_A$  is the number of nucleons per unit volume in  $\text{m}^{-3}$  and  $\sigma_{CC}(E)$  is the total charged current neutrino-nucleon interaction cross section in  $\text{m}^2$ . The detection probability is given by  $P_{\text{det}}$  and depends on:

- the energy and direction of the muon at the neutrino interaction vertex,
- the muon energy, position and direction when it reaches the detector and the probability for this to happen,
- the muon light yield and the detector's response to this signal, and
- the reconstruction and event selection process.

The first step in the simulation chain is to generate a flux of neutrino events in the vicinity of the detector, that have a chance of producing a detectable muon signal. This is done with `Genhen v6r3` [Bail 02a]. Neutrino events are generated isotropically inside a large cylinder around the detector. The size of this cylinder is determined in such a way so that all neutrinos that are able to produce a detectable muon inside the detector will be simulated, and it is based on the maximum range that a muon can travel. A muon can be detected if it reaches the *can*, defined as the area surrounding the ANTARES instrumented volume extending typically up to 2-3 light attenuation lengths away. Muons outside the *can* are too far away to produce detectable light, therefore only the propagation of particles from their generation point to the *can* is simulated and not the photon emission and development of electromagnetic and hadronic showers. The propagation of the muon from the neutrino interaction vertex to the *can* is simulated with the `MUSIC` package [Anto 97]. The energy losses of the muon as well as the changes

on its direction due to multiple Coulomb scattering are included in the simulation. The charged current neutrino interactions are simulated in the **LEPTO** package [Inge 97] using the CTEQ6-DIS parton distribution functions [Pump 02b]. The uncertainty in the cross section is estimated at approximately 3% in the energy range between  $10 - 10^8$  GeV. The flux of neutrinos is attenuated as they propagate inside the Earth. This information is included in  $P_{\odot}(E, \hat{d})$  of equation (3.2.1) and is given by:

$$P_{\odot}(E, \hat{d}) = e^{-\rho(\hat{d})N_A\sigma(E)}, \quad (3.2.2)$$

where  $\rho(\hat{d})$  is the amount of matter traversed by the neutrino on its way to the detector and depends on the direction of the neutrino. Neutrinos with very high energies are more probable to undergo an interaction due to the increased cross section. Additionally, neutrinos that travel in the vertical direction traverse more matter, including the denser core of the Earth, which leads to a significant suppression of the very high energy vertical neutrino flux.

The atmospheric muon background is simulated with **MUPAGE v3r5** [Carm 09]. It is based on parametrizations describing the muon flux as a function of the muon energy and angular distribution on the surface of the *can*. The generated number of events correspond to one tenth of the livetime, therefore the atmospheric muon Monte Carlo distributions shown in later chapters are scaled up by a factor of ten.

The muon propagation inside the *can* and the light that reaches the optical modules is simulated with the **KM3 v3r7** package [Bail 02b]. Since the tracking of every single photon emitted is computationally very inefficient, a set of tables is constructed taking into account the absorption and scattering of light and storing the average photon fields produced by the muon for different distances, positions and orientations of the OMs with respect to the track. The number and times of hits on the optical modules are then sampled from these tables. For the tracking of particles other than muons, a Geant based simulation is used in the package **Geasim v4r10** [Brun]. In this, only the attenuation of light is considered, while photon scattering is not simulated. The effect of the OM angular acceptance and efficiency is included in this step.

Finally, the simulation of the electronics response such as the charge integration and the dead time is performed with the **TriggerEfficiency** program [Jong 09]. In this step optical background hits are added and the online triggers used in real data are simulated. Optical background hits are generated according to a Poisson distribution based on real measured rates in order to reproduce the specific run's data taking conditions. Signal as well as background hits are generated after simulating the electronics response such as the charge threshold, time integration and dead time. The trigger logics that were used during the corresponding data run are finally applied. The events used in the present analysis are triggered with either the 3N or T3 triggers and reconstructed with the methods described in the following sections.

### 3.3 Track reconstruction

Before proceeding to the details of the energy reconstruction, a brief description of the track reconstruction algorithm is given since it is an essential ingredient for the energy reconstruction algorithm. It is also important for the understanding and discussion of the results of the energy reconstruction. Track reconstruction is performed in four consecutive fitting procedures [Heij 04]. The first stages provide a starting point for the last fit that gives the best results. The reconstruction algorithm looks for parameters defining the geometry of the track, i.e. the direction  $\vec{d} \equiv (d_x, d_y, d_z)$  and the position  $\vec{p} \equiv (p_x, p_y, p_z)$  of the muon at some fixed time  $t_0$ , that maximize the probability of them being compatible with the observed hits. It is based on the time residuals of the hits in an event:

$$r_i = t_i - t_i^{th}, \quad (3.3.1)$$

where  $t_i$  is the time of the hit and  $t_i^{th}$  is the expected time of hit coming from a Čerenkov photon given the input track. At first a hit pre-selection based on the time and amplitude of the hits is performed to remove the majority of background hits.

The first stage of the track reconstruction procedure is a linear prefit. Hits with an amplitude of more than 3 photoelectrons or clusters of hits on a floor within 25 ns are used with the additional assumption that they occur on points along the muon track. An OM recording a hit with a high amplitude is more likely to be located closer to the track. Using the amplitude information and the orientation of the PMT, the distance of the muon track from the OM is estimated and therefore the hit position that is most likely to lie on the muon track. This leads to a linear relation of the form:

$$\mathbf{y} = \mathbf{H}\Theta, \quad (3.3.2)$$

where  $\mathbf{y} = [x_1, y_1, \dots, z_n]$  is the vector with the hit positions,  $\Theta = [p_x, d_x, p_y, d_y, p_z, d_z]^T$  is the vector containing the track parameters i.e. position and direction, and  $\mathbf{H}$  is a matrix containing the hit times:

$$\mathbf{H} = \begin{bmatrix} 1 & ct_1 & 0 & 0 & 0 & 0 \\ 0 & 0 & 1 & ct_1 & 0 & 0 \\ 0 & 0 & 0 & 0 & 1 & ct_1 \\ 1 & ct_2 & 0 & 0 & 0 & 0 \\ 0 & 0 & 1 & ct_2 & 0 & 0 \\ 0 & 0 & 0 & 0 & 1 & ct_2 \\ \vdots & \vdots & \vdots & \vdots & \vdots & \vdots \\ 0 & 0 & 0 & 0 & 1 & ct_n \end{bmatrix}. \quad (3.3.3)$$

The first estimate of the track parameters in vector  $\Theta$  is obtained through a  $\chi^2$ -minimization,

$$\chi^2 = [\mathbf{y} - \mathbf{H}\Theta]^T \mathbf{F} [\mathbf{y} - \mathbf{H}\Theta], \quad (3.3.4)$$

which at this point is not a very accurate result but serves as the starting point for the steps that follow. The matrix  $\mathbf{F}$  is the inverse of the hit position error-covariance matrix, which is assumed to be diagonal.

The second stage is based on an M-estimator fit. M-estimators work in a similar fashion to maximum likelihood or least squares estimators, by maximizing some function  $g$ . It is not as accurate as a maximum likelihood fit but it has the benefit of not being too sensitive to the start value. A  $\chi^2$  estimator of the form  $g(r) = -r^2$  on the other hand is not suitable since it does not take into account background hits. The function of time residuals  $r$  chosen in this case is:

$$g(r_i) = -2\sqrt{1 + r_i^2/2} + 2, \quad (3.3.5)$$

and the resulting estimator is called ‘‘L1-L2’’ [Zhan 97]. Function (3.3.5) was chosen in such a way to exhibit a linear and quadratic behavior for large and small values of  $r$  respectively. Studies have shown that the use of additional information on the amplitude of the hits  $A_i$ , as well as information on the angular acceptance of the PMT’s lead to an improved performance of the M-estimator. Finally the function to be maximized is:

$$g = \sum_i \kappa \left( -2\sqrt{1 + A_i r_i^2/2} \right) - (1 - \kappa) f_{ang}(a_i), \quad (3.3.6)$$

where the relative contribution of each term is expressed through the parameter  $\kappa = 0.05$ , optimized using simulated events. The angular response of the PM tube as a function of the photon angle of incidence, calculated under the Čerenkov hypothesis for the photon emission angle, is described by  $f_{ang}$ . The hit selection for this stage accepts hits with time residuals from -150 ns to 150 ns and distances smaller than 100 m from the first track fit result. The reason for this is to keep hits that have the highest probability of being due to photons emitted from the muon track. Discarding hits far away from the track or with very large time residuals, hits that are most likely due to optical background are eliminated. Hits with amplitudes of more than 2.3 photoelectrons are also kept, since they are unlikely to be due to potassium decay.

The third step is a maximum-likelihood fit where the hit selection is based on the track output of the M-estimator fit. The likelihood of the event is the product of the likelihoods of each hit:

$$P(\text{event}|\text{track}) = \prod_i P(t_i|t_i^{th}, a_i, b_i, A_i), \quad (3.3.7)$$

where ‘‘event’’ refers to the collection of hits and ‘‘track’’ to the parameters defining the position and direction of the muon that is being reconstructed. The cosine of the angle of incidence of the photon on the OM is denoted as  $a_i$ ,  $b_i$  is the photon path length and  $A_i$  the amplitude of the hit. Hits that are part of a coincidence, have an amplitude larger than 2.5 p.e. or have a residual within  $-0.5 \times R$  and  $R$ , where  $R$  is the root-mean-square of the residuals used in the previous step, are selected. This selection ensures that the majority of hits due to optical background are rejected. The size of the interval  $[-0.5 \times R, R]$  depends on how close the track from the previous step is to the true track. The PDF used in this step was developed in the work of Hubaut [Huba 99] and does not include the contribution of optical background hits. Additionally, this

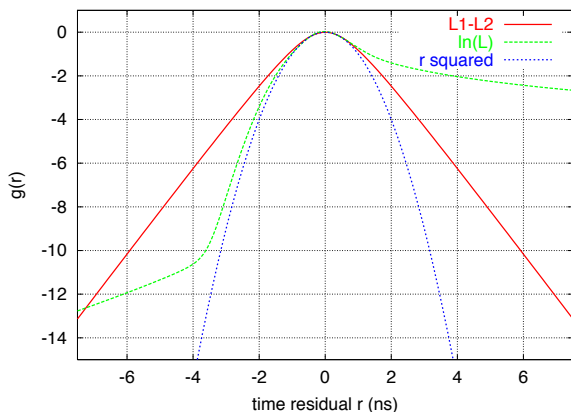


Figure 3.10: Functions of the time residuals used in the first steps of the track reconstruction. The M-estimator (red) and the logarithm of the likelihood (green) are plotted together with the least-squares function (blue) for comparison. The unphysical tail for large negative residuals was added to help the convergence of the minimization routine. Figure taken from [Heij 02].

probability density function depends only on the time residuals. The M-estimator and the log-likelihood as a function of the time residuals are shown in figure 3.10 together with the least-squares estimator  $g(r) = -r^2$ .

The last two steps are repeated using different starting points as input tracks. For this reason a series of rotations and translations are performed to the result of the prefit which are in turn used again as the starting point to the M-estimator stage. The track with the best likelihood per degree of freedom from the maximum likelihood fit is kept and used as a starting point for the last stage of the reconstruction. This is a maximum likelihood fit with an improved PDF which replaces the one in equation (3.3.7). The new PDF is the sum of the probability densities for signal hits and optical background hits:

$$P(t_i | t_i^{th}, a_i, b_i, A_i) = \frac{1}{N_{\text{total}}} [P_{\text{signal}} N_{\text{signal}} + R_{\text{background}}], \quad (3.3.8)$$

where  $N_{\text{total}}$  and  $N_{\text{signal}}$  are the total number of hits and the number of signal hits, i.e. not background, respectively and  $R_{\text{background}} = \frac{N_{\text{bg}}}{T} = N_{\text{bg}} P_{\text{bg}}$  is the optical background rate.  $T$  is the time window of the selection of hits in the event and  $N_{\text{bg}}$  the expected number of background hits. The parametrization of  $P_{\text{signal}}$  is obtained from the work of Heijboer [Heij 04]. A hit selection is also performed here, keeping hits in local coincidences or hits with a higher amplitude than 2.5 photoelectrons within a time residual window of -250 to 250 ns.

A dedicated variable  $\Lambda$  is defined to characterize the quality of the fit as:

$$\Lambda \equiv \frac{\log L}{N_{\text{DOF}}} + 0.1(N_{\text{comp}} - 1), \quad (3.3.9)$$

where the first term is the log-likelihood value per degree of freedom at the maximum and  $N_{\text{comp}}$  is the number of compatible solutions found by the reconstruction algorithm. This number is equal to the number of M-estimator starting points that result in a track direction within  $1^\circ$  from the result with the best likelihood per degree of freedom. In general,  $\Lambda$  has a higher value for well-reconstructed events. This is shown in figure 3.11 where the distribution of the reconstruction error  $\beta$ , defined as the difference between the generated and reconstructed muon direction, is plotted before and after a cut of  $\Lambda$  at

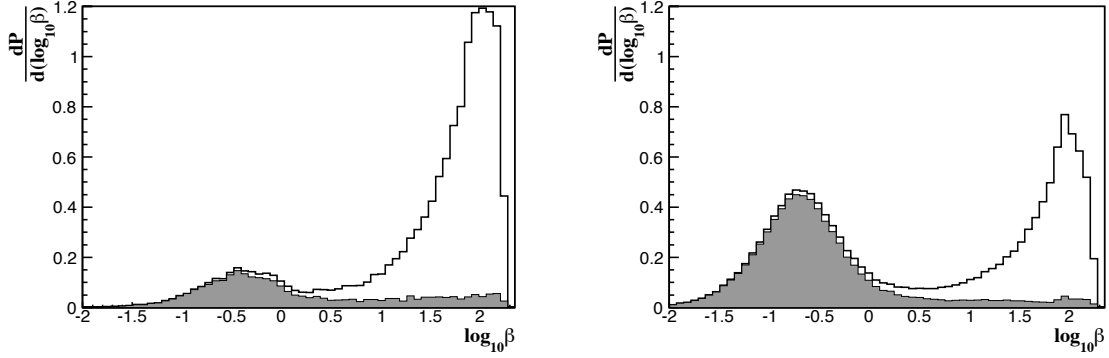


Figure 3.11: Distribution of the angular track reconstruction error  $\beta$  of all tracks (white). The shaded area is the distribution after performing a  $\Lambda$  cut, rejecting values lower than  $-5.3$ . The left plot corresponds to upward going tracks with a spectrum following the atmospheric neutrino spectrum. The right plot corresponds to an  $E^{-2}$  flux. See text for explanation.

$-5.3$ , a commonly used value in many ANTARES analyses. A large fraction of the badly reconstructed events is rejected in this way. The left plot corresponds to a spectrum weighted with the atmospheric neutrino flux, while the plot on the right corresponds to a flux weighted with  $E^{-2}$ . The differences on the two plots are attributed to the fact that the  $E^{-2}$  flux, being less steep than the atmospheric neutrino flux, consists of more high energy neutrino events and therefore has on average more signal hits in the event. After the  $\Lambda$  quality cut, the median of the angular error distribution for the atmospheric and  $E^{-2}$  fluxes is  $0.72^\circ$  and  $0.23^\circ$ , with an efficiency of 21% and 51% respectively. The angular resolution achieved as a function of the neutrino energy, after a quality cut of  $\Lambda > -5.3$ , is shown in figure 3.12.

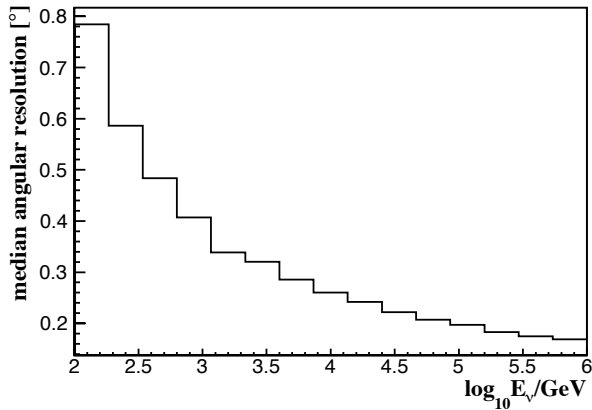


Figure 3.12: Median angular difference between the generated and reconstructed muon as a function of the parent neutrino energy for upward-going neutrinos reconstructed with  $\Lambda > -5.3$ .

## 3.4 Maximum likelihood energy reconstruction

Several energy reconstruction methods based on maximum likelihood have been developed in other experiments [Miov 01; Wins 08]. The energy reconstruction method developed here is outlined as follows. The expected number of photoelectrons in a certain optical module coming from a given track is calculated as a function of energy. A function which gives the likelihood that the measured amount of light in the optical modules is the result of a given muon track is defined. The probability density functions for the arrival times of the photons are introduced and calculated in [Jong 10] and will be discussed in the following section. The directional information obtained after track reconstruction is considered *a priori* correct. In what follows we will first use the directional information from the generated Monte Carlo muon. In later sections the effect of directional reconstruction on the energy estimation will be examined. A standard one-dimensional minimizer is used to find the energy for which the likelihood function has a maximum.

### 3.4.1 Probability density functions

The arrival times of the photons on the optical modules are important in the estimation of the energy. The expected arrival time of the photons  $t_0$ , assuming a Čerenkov cone hypothesis, corresponds to the shortest optical path from the point of emission to the position of the PM tube. This means that the distribution of the arrival time of light will peak at  $t = t_0$ . If there was no scattering or dispersion, the arrival time would be completely determined by the emission angle of the emitted photon with respect to the muon track. However, due to dispersion the dependence of the arrival time on the wavelength must also be considered. In addition, since light can be emitted in all directions during an electromagnetic shower the arrival time depends on the position of the shower on the track. Scattering affects the photon path from the emission point to the optical module which is now not uniquely defined anymore. This is an important point since the direction of the photon after scattering determines the angle of incidence on the optical module and consequently the angular acceptance value for this angle. The solid angle under which the photomultiplier is seen is evaluated from the scattering point and not from the point of emission.

#### Direct light

When considering direct light from the muon, the arrival time distribution is still affected by dispersion, and consequently the photon arrival times depend on the wavelength. The angle of photon emission is fixed and there is no scattering. The probability density function can be expressed as:

$$\frac{dP_{dm}}{dt} = \Phi_0(R, \lambda) A \left( \frac{\partial t}{\partial \lambda} \right)^{-1} \epsilon(\cos \theta_{\text{inc}}) QE(\lambda) e^{-\frac{d}{\lambda_{\text{abs}}}} e^{-\frac{d}{\lambda_s}}, \quad (3.4.1)$$

where  $\Phi_0$  is the detectable photon flux given in equation (3.1.7),  $A = 0.044 \text{ m}^2$  is the PMT photocathode area,  $\epsilon$  is the angular acceptance as a function of the incidence

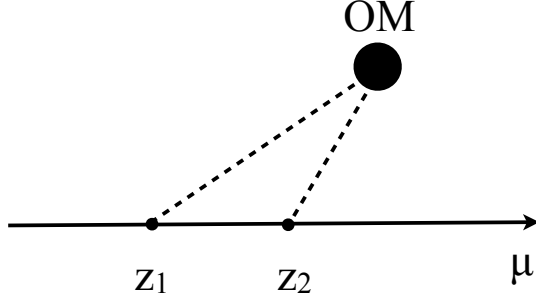


Figure 3.13: Schematic diagram of shower positions  $z_1$  and  $z_2$  along the muon track, with the same arrival time of light on the OM.

angle  $\theta_{\text{inc}}$ ,  $QE(\lambda)$  is the quantum efficiency as a function of the wavelength and  $R$  is the vertical distance of the PMT from the track. For a direct photon from the muon, the arrival time depends only on the wavelength of the light which is taken into account through the  $\frac{\partial t}{\partial \lambda}$  term.

For direct light from electromagnetic showers, since the photons are emitted in all directions, the arrival time depends on the point  $z$  on the muon track where the light was emitted. Moreover, there are two points on the track  $z_1$  and  $z_2$  that can have the same timing characteristics as illustrated in figure 3.13. The probability density function for the arrival times of light is:

$$\frac{dP_{dEM}}{dt} = \int d\lambda \sum_{z_1, z_2} \left( \frac{dt}{dz} \right)^{-1} \Phi_1(\cos \theta, E, \lambda) d\Omega \epsilon(\cos \theta_{\text{inc}}) QE(\lambda) e^{-\frac{d}{\lambda_{\text{abs}}}} e^{-\frac{d}{\lambda_s}}, \quad (3.4.2)$$

where  $\Phi_1$  is the flux given by equation (3.1.10) and  $d\Omega$  is the solid angle of the PMT, as viewed from the photon emission point.

### Scattered light

For scattered light from the muon one has to integrate over the azimuthal photon emission angles and positions. In addition, the optical path is not uniquely defined and depends on the photon scattering point along its path as shown in figure 3.14. For light that scattered once, the arrival time  $t$  of the photon on the OM is given by:

$$ct = z + n_g(|\vec{u}| + |\vec{v}|), \quad (3.4.3)$$

where  $|\vec{u}|$  and  $|\vec{v}|$  are the distances travelled by the photon before and after scattering,  $z$  is the photon emission point along the muon track and  $n_g$  is the index of refraction corresponding to the group velocity of light. The corresponding probability density function for scattered muon light is:

$$\frac{dP_{sm}}{dt} = \iiint d\lambda dz d\phi \frac{1}{2\pi} \frac{dN}{dx} \frac{1}{\lambda_s} \left( \frac{\partial t}{\partial u} \right)^{-1} \epsilon(\cos \theta_{\text{inc}}) QE(\lambda) e^{-\frac{d}{\lambda_{\text{abs}}}} \frac{dP_s}{d\Omega_s} d\Omega. \quad (3.4.4)$$

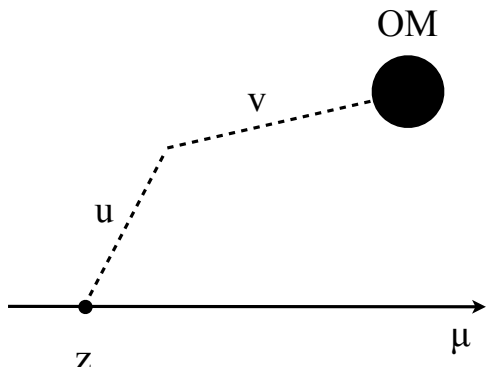


Figure 3.14: Two dimensional illustration of the optical path followed by a photon emitted at  $z$  and scattered after traveling a distance  $u$ .

For a photon that scattered only once, the arrival time depends only on the position of the scattering along its path which is taken into account through the  $\partial t/\partial u$  term.

In the case of scattered light from electromagnetic showers, the probability density function is

$$\begin{aligned} \frac{dP_{sEM}}{dt} &= \iiint d\lambda dz d\phi d\cos\theta \Phi_1(\cos\theta, E, \lambda) \frac{1}{\lambda_s} \times \\ &\times \left(\frac{\partial t}{\partial u}\right)^{-1} \epsilon(\cos\theta_{inc}) QE(\lambda) e^{-\frac{d}{\lambda_{abs}}} \frac{dP_s}{d\Omega_s} d\Omega, \end{aligned} \quad (3.4.5)$$

where  $\Phi_1$  is the flux in equation (3.1.10) and  $P_s$  is the probability density function for the light scattering angle (equations (3.1.16) and (3.1.17)) discussed in section 3.1.2.

In what follows, the time integrated values of the probability density functions are used in order to obtain the number of expected photoelectrons in a given time window. The optical background is considered constant and equal to 60 kHz per optical module. This is not the case for real data. When events in data are reconstructed, the average measured rate over all OM's is used instead. These hits are added in the calculation of the expected number of photoelectrons by multiplying that rate with the time window under consideration.

### 3.4.2 Likelihood function

We define the likelihood function as follows:

$$\mathcal{L}(E) = \frac{1}{N_{OM}} \prod_i^{N_{OM}} L_i(E). \quad (3.4.6)$$

The product is taken over all optical modules, whether there was a hit recorded or not. Optical modules that are further than 300 m away from the track are not taken into account, since it is not expected to have any significant amount of light so far away from the track. This corresponds to an ideal situation where all phototubes are active. When this method is applied to real data, dead phototubes are excluded.  $L_i(E)$  is the

probability of observing a pulse amplitude  $A_i$  given a certain expected amplitude on the  $i^{th}$  optical module. These individual likelihood functions  $L_i(E)$  are constructed as:

$$L_i(E) = \begin{cases} P(A; \langle n_{pe} \rangle) = \sum_{n_{pe}=1}^{n_{pe_{max}}} P(n_{pe}; \langle n_{pe} \rangle) \cdot P(A; n_{pe}) & \text{hit} \\ P(0; \langle n_{pe} \rangle) = e^{-\langle n_{pe} \rangle} + P_{\text{threshold}}(\langle n_{pe} \rangle) & \text{no hit} \end{cases} \quad (3.4.7)$$

The first equation of (3.4.7) consists of two terms, the Poisson probability of having  $n_{pe}$  photoelectrons given that the expectation is  $\langle n_{pe} \rangle$ ,

$$P(n_{pe}; \langle n_{pe} \rangle) = \frac{\langle n_{pe} \rangle^{n_{pe}} e^{-\langle n_{pe} \rangle}}{n_{pe}!}, \quad (3.4.8)$$

as well as a Gaussian term which expresses the probability that  $n_{pe}$  photoelectrons in the photocathode will yield an amplitude  $A$ ,

$$P(A; n_{pe}) = \frac{1}{\sqrt{2\pi\sigma^2}} e^{-\frac{1}{2} \left( \frac{A - N(n_{pe})}{\sigma} \right)^2}. \quad (3.4.9)$$

For this term,  $N$  and  $\sigma$  are derived from the known calibration values of the mean and width of the single photoelectron peak (see equations (2.8.4) and (2.8.5)):

$$N = n_{pe} \cdot \mu_{SPE}, \quad (3.4.10)$$

$$\sigma^2 = n_{pe} \cdot \sigma_{SPE}^2. \quad (3.4.11)$$

The values used in this work are  $\mu_{SPE} = 1$  and  $\sigma_{SPE}^2 = 0.3$ . The energy dependence of the likelihood function is expressed in calculating the expected number of photoelectrons  $\langle n_{pe} \rangle$  as will be discussed shortly. The summation in equation (3.4.7) is performed with  $n_{pe_{max}} = 80$ . A cut at 40 photoelectrons was imposed when either the charge of the hit or the expected number of photoelectrons was above this value to account for saturation effects. The probability of having a hit is renormalized in order to take into account the tail of the distribution  $P(n_{pe}; \langle n_{pe} \rangle) \cdot P(A; n_{pe})$  that falls below the threshold value (and even into negative values) of the observed charge, which is in particular relevant for low values of  $\langle n_{pe} \rangle$ .

The second equation of (3.4.7) is used when there is no hit recorded on the optical module under consideration. The first term is the Poisson probability of observing zero photoelectrons when the expected value is  $\langle n_{pe} \rangle$ . The second term takes into account the threshold effect, i.e. the probability that a photon conversion in the optical module will give an amplitude below the threshold level. This is especially relevant for low energy events that produce only a small amount of light. The *threshold* probability is given by:

$$P_{\text{threshold}}(\langle n_{pe} \rangle) = \sum_{n_{pe}=1}^{n_{pe_{max}}} P(n_{pe}; \langle n_{pe} \rangle) \int_0^{A_{th}} P(A; n_{pe}) dA, \quad (3.4.12)$$

where  $A_{th}$  is the threshold amplitude. In general, this is different for every optical module. In the simulation its value is set to 0.3 photoelectrons and this is the value that is used in the energy estimation as well, both in the Monte Carlo for performance studies as well as in real data.

The goal of the energy reconstruction is of course to find the most probable energy of the event, given the light signature of the passing muon in the detector. As mentioned earlier, the energy dependence is contained in the expected number of photoelectrons  $\langle n_{pe} \rangle$ . The expected number of photoelectrons in a given time interval  $(t_{min}, t_{max})$  is the time integral of the probability densities:

$$\langle n_{pe} \rangle = \int_{t_{min}}^{t_{max}} dt (\mathcal{P}_{dm} + \mathcal{P}_{sm} + \mathcal{P}_{dEM} + \mathcal{P}_{sEM}) + R_{bg}(t_{max} - t_{min}), \quad (3.4.13)$$

where the probability densities  $\mathcal{P}_x$  are:

$$\mathcal{P}_{dm}(R, \theta_{\odot}, \phi_{\odot}, t) = \frac{dP_{dm}}{dt}(R, \theta_{\odot}, \phi_{\odot}, t), \quad (3.4.14)$$

$$\mathcal{P}_{sm}(R, \theta_{\odot}, \phi_{\odot}, t) = \frac{dP_{sm}}{dt}(R, \theta_{\odot}, \phi_{\odot}, t), \quad (3.4.15)$$

$$\mathcal{P}_{dEM}(R, \theta_{\odot}, \phi_{\odot}, t) = \frac{dP_{dEM}}{dt}(R, \theta_{\odot}, \phi_{\odot}, t) \cdot E', \quad (3.4.16)$$

$$\mathcal{P}_{sEM}(R, \theta_{\odot}, \phi_{\odot}, t) = \frac{dP_{sEM}}{dt}(R, \theta_{\odot}, \phi_{\odot}, t) \cdot E'. \quad (3.4.17)$$

The subscripts used above stand for direct light from the muon ( $dm$ ), scattered light from the muon ( $sm$ ), direct light from electromagnetic showers ( $dEM$ ) and scattered light from electromagnetic showers ( $sEM$ ). Here,  $R$  is the distance of the track from the optical module, and  $\theta_{\odot}$  and  $\phi_{\odot}$  are the relative zenith and azimuth angles of the PMT with respect to the track. The probability densities for electromagnetic showers have been normalized to 1 GeV. This is the reason why the last two equations are scaled by the energy  $E'$  (see equation 3.1.11).

In order to take into account the average energy-loss of the muon, from the moment of entering the vicinity of the detector creating the first hit until the moment it reaches the optical module under consideration, energy  $E'$  is expressed as:

$$E' = \left( \frac{a}{b} + E \right) e^{-bL} - \frac{a}{b}, \quad (3.4.18)$$

where  $E$  is the free parameter of the likelihood function. Equation (3.4.18) is obtained after an integration of equation (3.1.4), answering the question on how much is the energy  $E'$  of a muon of initial energy  $E$  after traveling a path length  $L$ . Distance  $L$  is calculated under the assumption that the hits are created by photons emitted under the Čerenkov hypothesis. The constants  $a = 0.27$  GeV/m and  $b = 3.4 \cdot 10^{-4}$  m<sup>-1</sup> are the ones in the average energy-loss equation (3.1.4) and their exact values are taken from [Klim 01].

The algorithm searches for hits on the PM tubes within a time window of  $(t_0 - 10$  ns,  $t_0 + 390$  ns), where  $t_0$  is the expected arrival time of the photon under the Čerenkov

hypothesis, given a certain track geometry. When a hit is recorded on the PMT at time  $t_{hit}$ , the time integration window of equation (3.4.13) is taken to be  $(t_{hit}, t_{hit} + 40 \text{ ns})$ . This corresponds to the integration time of the ARS. When no hit is observed the probability densities are integrated for the entire period of  $(t_0 - 10 \text{ ns}, t_0 + 390 \text{ ns})$ . Finally, the term  $R_{bg}(t_{max} - t_{min})$  corresponds to the optical background contribution to the expected number of photoelectrons in the time window  $(t_{min}, t_{max})$ .

The next step is to find the energy for which  $-\log \mathcal{L}$ , i.e. the natural logarithm of equation (3.4.6), is minimum. The shape of the likelihood function as a function of the energy (i.e. the free parameter of the likelihood function) is shown in figure 3.15 for a few example events of different energies for illustration purposes. The most probable energy is given by the energy value which minimizes  $-\log \mathcal{L}(E)$ . The gradual underestimation observed for increasing energies will be discussed later in this chapter when the overall performance of the method is examined in more detail.

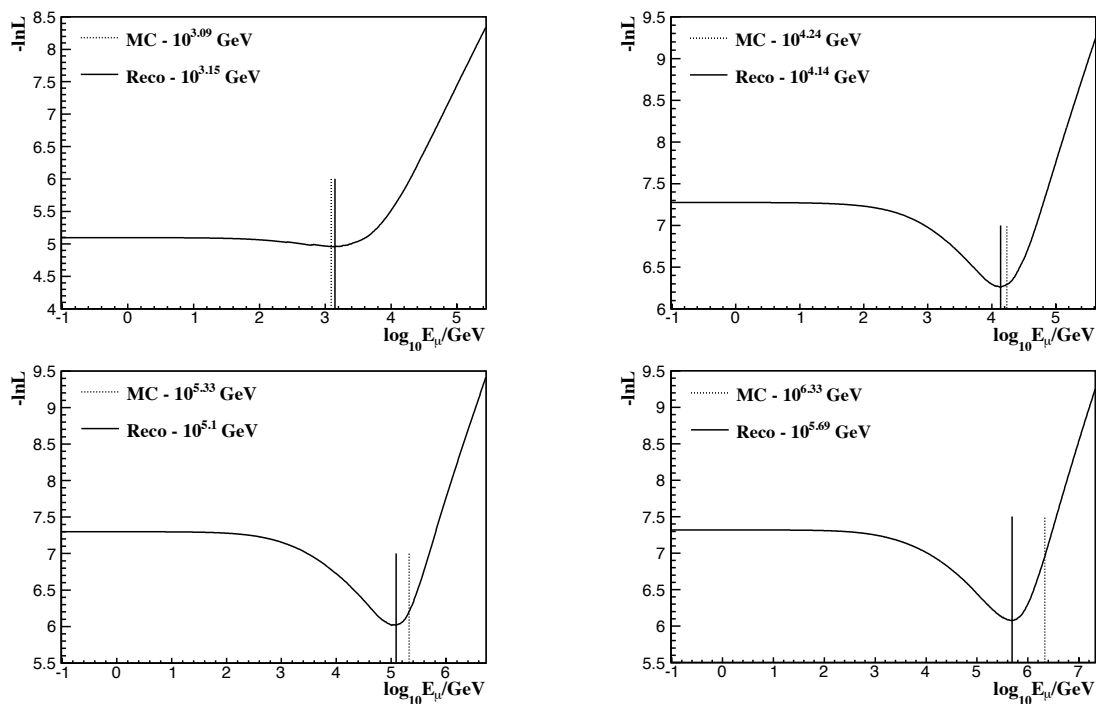


Figure 3.15: Natural logarithm of the likelihood function,  $-\log L$ , as a function of energy for random simulated muons of energy  $10^{3.09} \text{ GeV}$ ,  $10^{4.24} \text{ GeV}$ ,  $10^{5.33} \text{ GeV}$  and  $10^{6.33} \text{ GeV}$  (in reading order). The minima correspond to the energy estimate found by the energy reconstruction algorithm shown by the solid line. The dashed line corresponds to the generated Monte Carlo muon energy.

## 3.5 Energy reconstruction performance

The results of the energy reconstruction as well as the performance will be discussed in the following sections. The Monte Carlo sample that is used consists of upward-going neutrino events. Realistic optical background hits are generated according to a Poisson distribution, with the mean rate determined from the average rate over all PMT's taken from real data. A flat, i.e. constant, background of  $R_{bg} = 60$  kHz is used at the energy reconstruction level (equation 3.4.13). For the photomultiplier simulation, 2 ARS's per optical module were considered, each with an integration time of 40 ns and a dead time of 250 ns. The events were triggered with both the 3N and T3 triggers, described in section 2.7.

### 3.5.1 Energy resolution

The correlation between the true Monte Carlo muon energy and the reconstructed energy is shown in figure 3.16. The Monte Carlo sample consists of upward-going neutrinos and the true Monte Carlo direction has been used as the input to the energy reconstruction to decouple the performance of the energy reconstruction from that of the track reconstruction. Figure 3.16 shows that there is a good correlation between the true muon energy and the output of the energy reconstruction. However a progressive underestimation of the energy is visible for higher muon energies. The energy of a muon event with energy close to  $10^6$  GeV, for example, will be underestimated by almost one order of magnitude. From now on we define:

$$\delta \log E \equiv \log_{10} \frac{E_{Reco}}{E_{MC}}. \quad (3.5.1)$$

The underestimation is more visible in figure 3.17 where  $\delta \log E$  is plotted against the logarithm of the muon Monte Carlo energy. For a perfect energy reconstruction method this plot would be a straight line at  $\delta \log E = 0$ . The deviations from zero indicate the bias of the method while the spread is a measure of the resolution. The quality of the energy reconstruction depends on the muon energy. A typical measure of the energy resolution is the standard deviation from a Gaussian fit of the  $\delta \log E$ , assuming that a Gaussian fit describes this distribution well. A few distributions of  $\delta \log E$  for different ranges in energy are shown in figure 3.18. The distributions of  $\delta \log E$  are reasonably well described by Gaussian distributions. There are still tails present and the mean of the Gaussian fit is slightly shifted from the mean of the distributions. The deviations from a Gaussian shape can be expected since the distributions shown in figure 3.18 are essentially projections of slices in  $\log_{10} E_{MC}$  on the  $\delta \log E$  axis (see fig. 3.17). The fact that the slices in Monte Carlo energy have a finite width and are not mono-energetic, as well as the presence of some mis-reconstructed events, lying far away from the mean creating the tails of these distributions, are responsible for the observed deviations.

To evaluate the overestimation or underestimation of the energy we observe the behavior of the mean of the Gaussian fit. The mean and standard deviation are shown

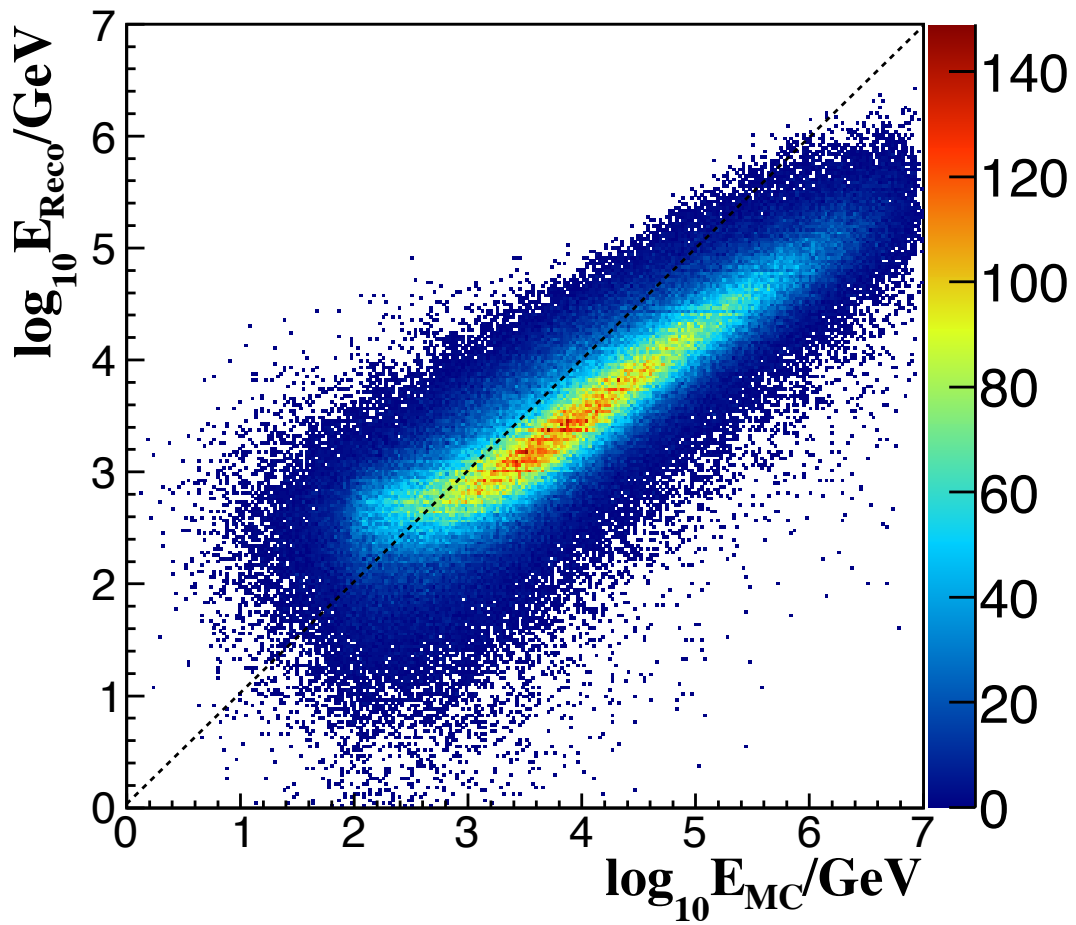


Figure 3.16:  $\log_{10} E_{Reco}$  against  $\log_{10} E_{MC}$  for an upward-going muon neutrino sample. The true Monte Carlo direction of the muon is used. The dashed line corresponds to  $E_{Reco} = E_{MC}$ .

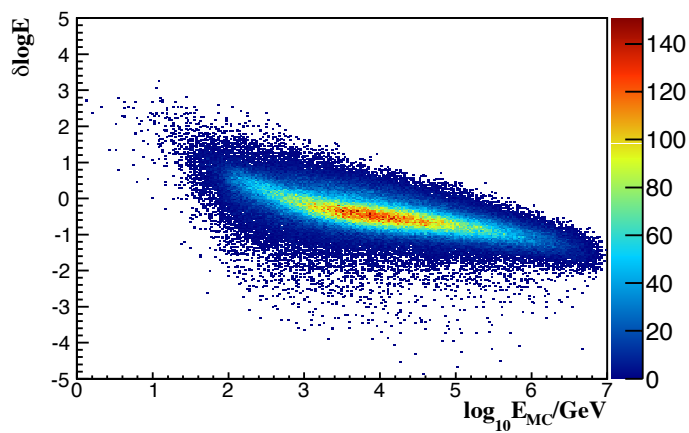


Figure 3.17:  $\delta \log E$  as a function of  $\log_{10} E_{MC}$  for an upward-going muon neutrino sample. An ideal energy reconstruction performance would result in a straight  $\delta \log E = 0$  line.

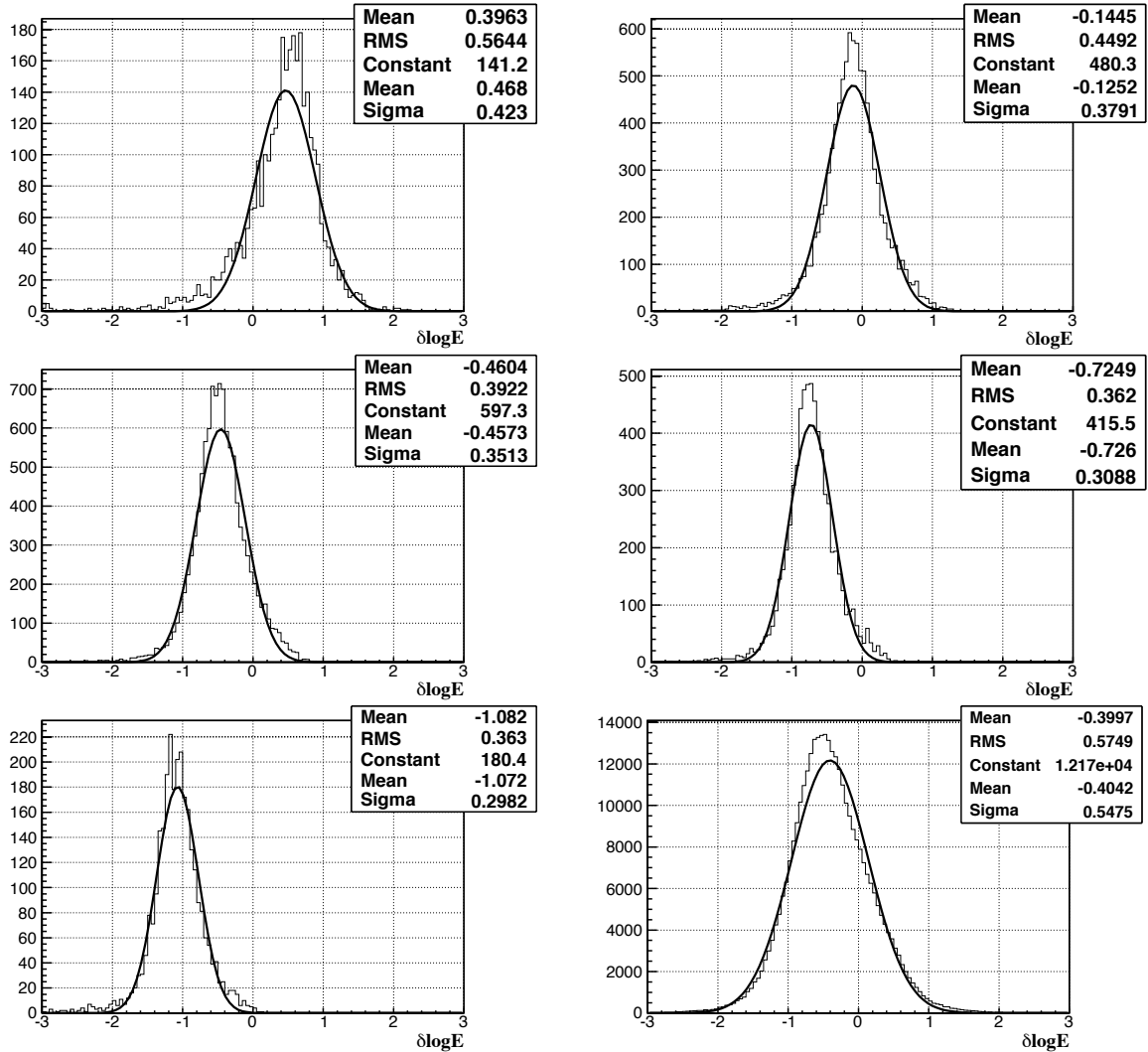


Figure 3.18: Distributions of  $\delta \log E$  for muon tracks with true Monte Carlo energy in six different energy ranges (in reading order  $10^{1.95} - 10^{2.05}$  GeV,  $10^{2.95} - 10^{3.05}$  GeV,  $10^{3.95} - 10^{4.05}$  GeV,  $10^{4.95} - 10^{5.05}$  GeV,  $10^{5.95} - 10^{6.05}$  GeV and  $0 - 10^7$  GeV). The solid line represents a Gaussian fit.

in figures 3.19 and 3.20. For higher muon energies the reconstructed energy is systematically below the true energy. This is partially due to the saturation of the optical module signal at 20 photoelectrons. For lower energies, especially below 1 TeV, the light that is emitted by the muon is weakly dependent on its energy, as discussed in section 3.1, resulting in an overestimation. The resolution remains fairly stable over the whole energy range and the value of the standard deviation of the Gaussian fits is well below 0.4. Since the Gaussian fits only approximately describe the distribution of  $\delta \log E$ , an additional check is performed to examine the percentage of the events that belong inside one, two and three standard deviations from the mean of the Gaussian fit. If the fit were to describe the distribution perfectly the fraction of events should

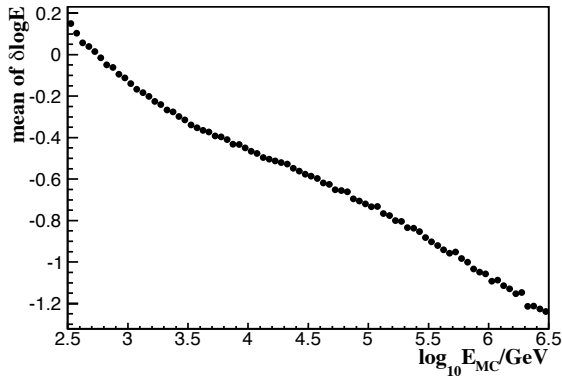


Figure 3.19: Mean of Gaussians fitted to the distributions of  $\delta \log E$  for different bins of  $\log_{10} E_{MC}$ .

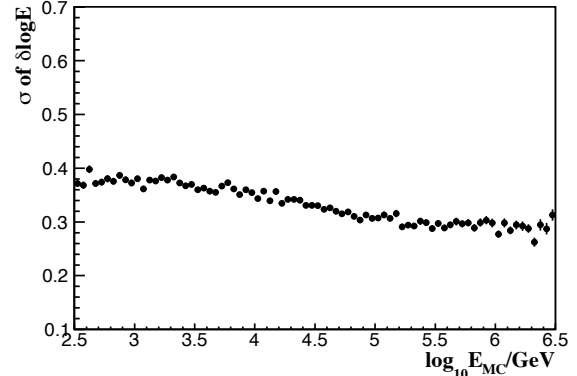


Figure 3.20: Sigma of Gaussians fitted to the distributions of  $\delta \log E$  for different bins of  $\log_{10} E_{MC}$ .

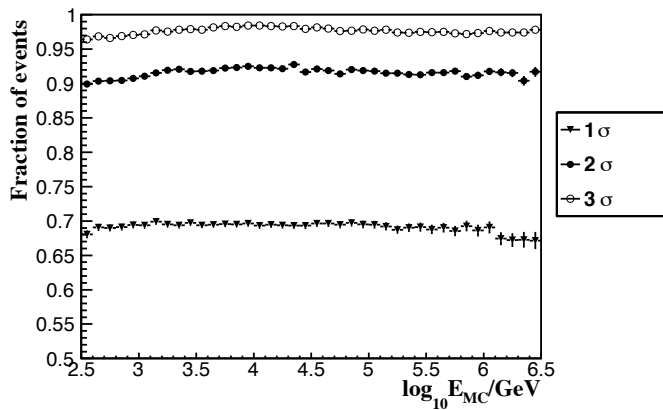


Figure 3.21: Fraction of events that belong inside one, two and three  $\sigma$  deviations from the mean of the Gaussian fit applied to the  $\delta \log E$  distribution in bins of the true Monte Carlo muon energy.

be 68%, 95% and 99.7% respectively. The fraction of events for one, two and three standard deviations is shown in figure 3.21 as a function of the energy. The agreement is fairly reasonable with the tails of the distributions created by outlier events causing a minor discrepancy in the area between two and three standard deviations.

The energy reconstruction quality shows no dependence on the muon direction as shown in figure 3.22, where the value of  $\delta \log E$  is plotted against both the zenith and the azimuth angle of the track's true Monte Carlo direction for upward going events.

### 3.5.2 Offset correction

The bias that is present, gradually underestimating the true energy as we move to higher values, can be corrected by applying a simple linear correction. This is relevant if one wants to examine the energy of a single event. For a collective study, i.e. examining the energy spectrum, such a correction is not necessary since it will be accounted for in the unfolding procedure. We address the issue of applying this event-by-event correction here. The mean true energy is plotted against slices of reconstructed energy and a linear fit is applied as shown in figure 3.23. This line gives the most probable true muon

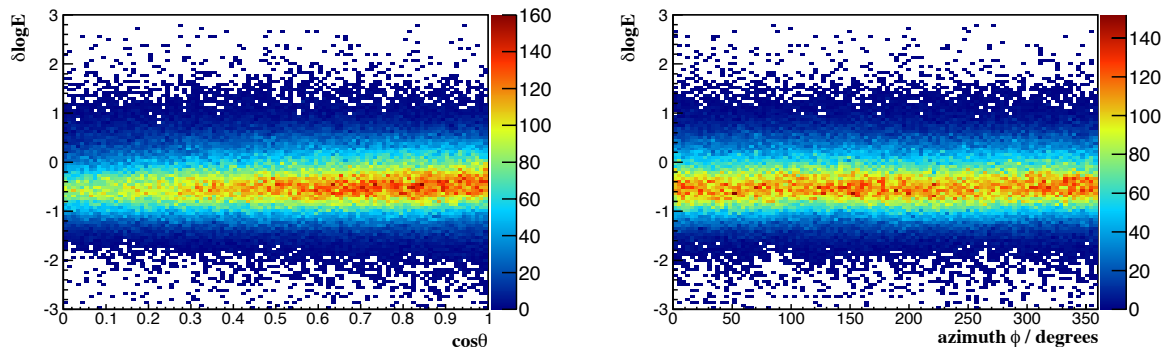


Figure 3.22: Dependence of energy reconstruction on the zenith and azimuth angle of the muon direction.

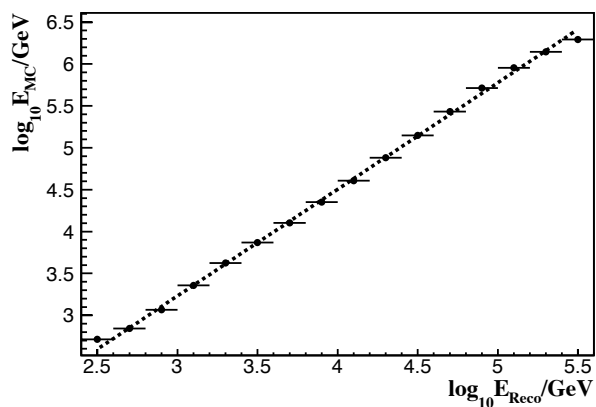


Figure 3.23: Correlation between the true Monte Carlo energy ( $E_{MC}$ ) and the output of the energy reconstruction ( $E_{Reco}$ ). A linear fit is applied to determine the relation between these two quantities,  $\log_{10} E_{MC} = a + b \cdot \log_{10} E_{Reco}$ , where  $a = -0.58$  and  $b = 1.27$ .

energy for a given reconstructed energy value. The fit is applied in the energy range of  $10^{2.5}$  GeV to  $10^{5.5}$  GeV of the reconstructed energy where the correlation exhibits a linear behavior. For lower energies the limited contribution of energy-losses compared to background light leads to an overestimation of the true energy, while for higher energies the electronics saturation leads to an underestimation. This is visible in figures 3.16 and 3.17 where one sees the flattening of the distribution for energies below  $\sim 10^{2.5}$  GeV and above  $\sim 10^{5.5}$  GeV. The mean and  $\sigma$  of the Gaussian fits per slice of reconstructed energy are shown in figures 3.24 and 3.25. The mean appears to be close to zero over the whole energy range and the resolution achieved is at the level of 0.4 in the logarithm of the energy for energies above around 2-4 TeV. As mentioned earlier, such a correction is useful when we need the energy estimate of a single event. This correction will not be used in the work presented here, unless explicitly stated otherwise.

### 3.5.3 Dependence on track reconstruction quality

In this section we will examine the dependence of the energy resolution on the quality of the track reconstruction. The performance of the energy estimation is expected to be strongly dependent on the quality of the track reconstruction. An error in the

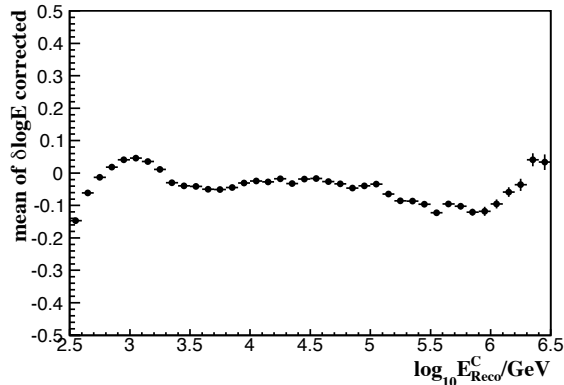


Figure 3.24: Mean from the Gaussian fits after applying a linear correction.

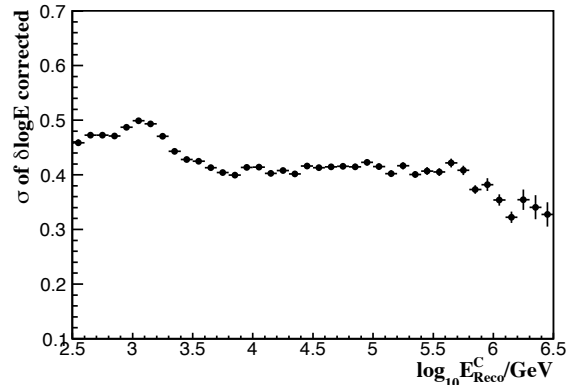


Figure 3.25:  $\sigma$  from the Gaussian fits after applying a linear correction.

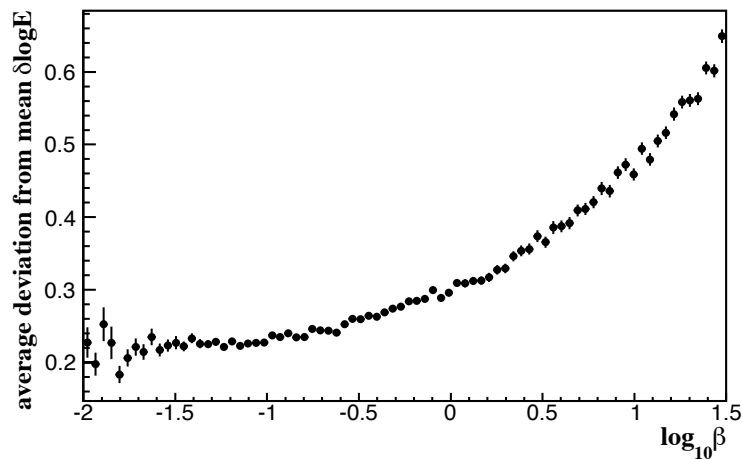


Figure 3.26: Average deviation from the mean  $\delta \log E$  as a function of the track reconstruction error  $\beta$ .

directional information of the track can result in different expected photon fluxes on the optical modules which in turn will lead to a reduced energy reconstruction performance. In this case, the direction that was the result from the track reconstruction has been used instead of the generated muon direction. The output of the track reconstruction is used to calculate parameters such as the distance of the track from the optical modules or the orientation of the modules with respect to the track that in turn are fed into the likelihood function of the energy reconstruction. Large deviations from the correct values, attributed to mis-reconstructed events, are propagated to large deviations from the true muon energy.

The average deviation from the mean  $\delta \log E$  for a known Monte Carlo energy as a function of the angular error from the track reconstruction  $\beta$ , defined as the angle between the true Monte Carlo and reconstructed muon tracks, is shown in figure 3.26. This quantity is a measure of the energy resolution. It is clear from the figure that the quality of the energy reconstruction worsens as the error from the track reconstruction becomes larger. The same conclusion can be drawn by looking at the dependence of the

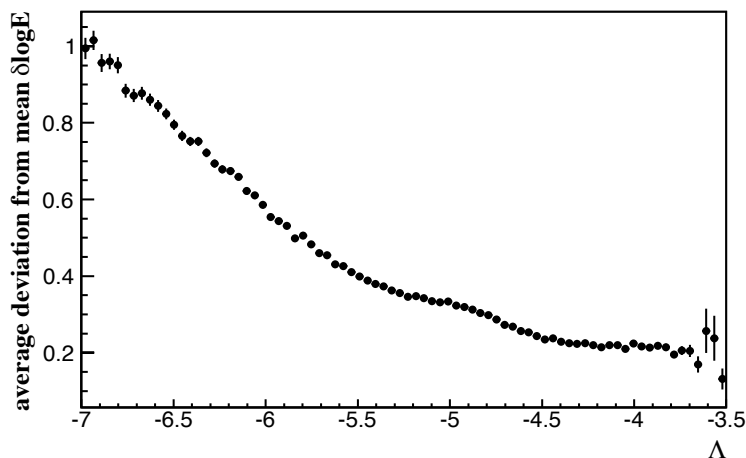


Figure 3.27: Average deviation from the mean  $\delta \log E$  as a function of the track reconstruction quality parameter  $\Lambda$ .

average deviation from the mean  $\delta \log E$  on the track reconstruction quality parameter  $\Lambda$ , shown in figure 3.27. Lower values of  $\Lambda$  that correspond to poorly reconstructed tracks also characterize events with poorly reconstructed energies. This is shown in figure 3.28 where a cut at  $\Lambda < -5.3$  improves the resolution, indicated by a reduction of the spread of the  $\delta \log E$  distribution. The  $\sigma$  of the Gaussian fits is decreased by more than 0.05, reaching the same level of performance as using the true Monte Carlo direction and position. The effect of poorly track-reconstructed events is manifested as long tails in the  $\delta \log E$  distributions, especially for higher energy events. These tails disappear when a quality cut is applied, providing a more reliable Gaussian shape.

In order to evaluate how efficient the energy reconstruction is, one needs to see what fraction of the number of the events, where the track fit was successful, ended up having their energy reconstructed. In few cases, the shape of the log-likelihood function is monotonically decreasing and the maximum is at the lower end of the maximization range of energies. We consider that the energy reconstruction of these events failed. As we will soon see, this fraction is negligible. We define the efficiency of the energy

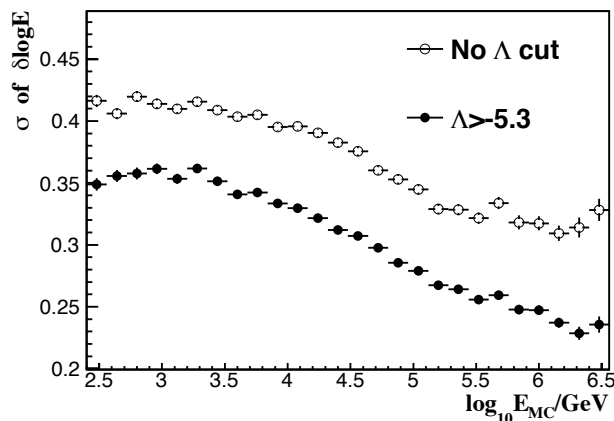


Figure 3.28: Energy resolution for all reconstructed events as well as events after a  $\Lambda$  quality cut of  $\Lambda > -5.3$ .

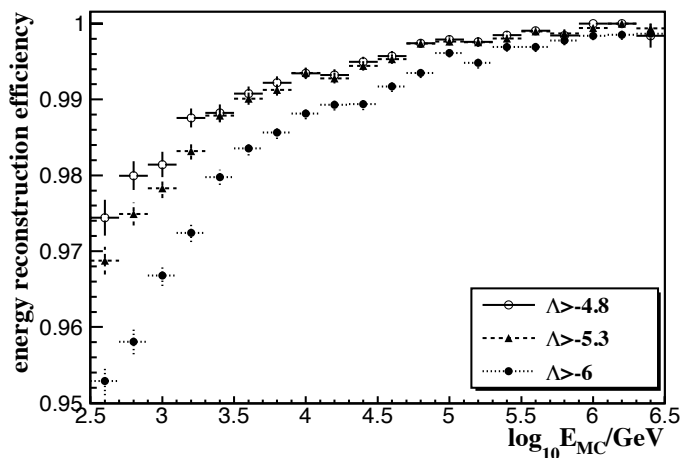


Figure 3.29: Energy reconstruction efficiency for different values of  $\Lambda$  cut, indicated on the figure.

reconstruction as:

$$\text{Efficiency} = \frac{\# \text{ of tracks with reconstructed energy}}{\# \text{ of tracks with reconstructed direction}}. \quad (3.5.2)$$

The reconstruction efficiency for different  $\Lambda$  values as a function of the true Monte Carlo energy is shown in figure 3.29. The more events with poor track reconstruction we use in the sample the more the efficiency drops. The efficiency of the energy reconstruction algorithm is fairly high, reconstructing successfully more than 90% of the events in all cases. There is of course a dependence on the  $\Lambda$  quality parameter as shown in the figure. For very well track-reconstructed events ( $\Lambda > -5.3$ ) the efficiency is above 96%, increasing to 100% for higher energies. The efficiency drops when more poorly reconstructed tracks are included in the sample. Imposing no quality cut on the  $\Lambda$  variable one sees that the efficiency is decreased, especially for events with low or high energy, indicating that the energy reconstruction fails to estimate the energy of poorly reconstructed tracks. Similarly to equation (3.5.2), we define the efficiency related to the choice of the track reconstruction quality cut  $\Lambda$  as:

$$\text{Efficiency} = \frac{\# \text{ of tracks selected after } \Lambda \text{ cut}}{\# \text{ of tracks with reconstructed direction}}. \quad (3.5.3)$$

The efficiencies for different values of  $\Lambda$  cut are shown in figure 3.30.

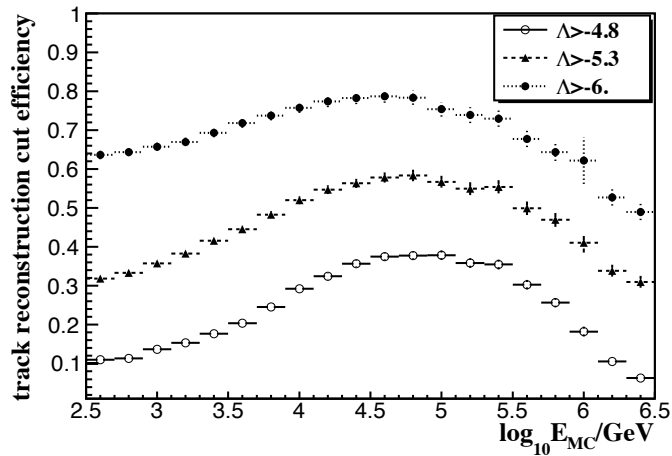


Figure 3.30: Track reconstruction efficiency for different values of  $\Lambda$  cut, indicated on the figure.

### 3.5.4 Effect of scattering model

In this section we examine the effect of the scattering model that is assumed in the probability density functions in order to calculate the expected number of photoelectrons in the optical modules. The energy reconstruction method described in this chapter is applied using the  $f4$  and  $p0.0075$  models described in section 3.1.2. In the Monte Carlo simulations, the  $p0.0075$ -model was used to describe light scattering. The ratio between the output of the energy reconstruction  $E_{Reco}(f4)$  using the  $f4$ -model and the energy  $E_{Reco}(p0.0075)$  using the  $p0.0075$ -model is shown in figure 3.32. Using the  $f4$ -model systematically leads to lower energy values than the ones obtained with the  $p0.0075$ -model. The effect is more prominent at lower energies (below a few TeV), but always remains less than 4%. This can be attributed to the fact that the majority of light emitted from the muon and the showers along the track is towards the forward direction, peaking at the Čerenkov angle. The  $f4$ -model favors forward scattering on a broader range of angles than the  $p0.0075$ -model (see figure 3.9). If the assumption of the  $f4$ -model used to reconstruct the energy produces more hits for a certain muon

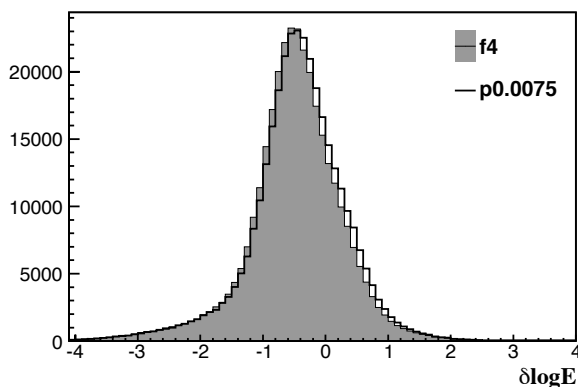


Figure 3.31: Distribution of  $\delta \log E$  for different scattering models used in the calculation of the PDFs. The reconstructed track has been used instead of the true muon direction and no additional cuts are applied.

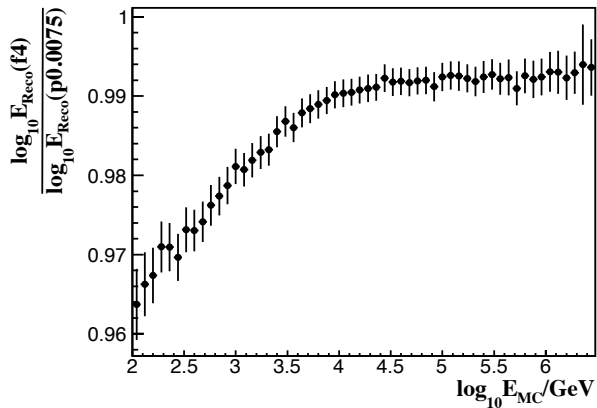


Figure 3.32: Ratio between the energy reconstruction output using the  $f_4$  and  $p0.0075$  models for the calculation of  $\langle n_{pe} \rangle$ . Using the  $f_4$ -model results in lower energies (in  $\log_{10} E_{Reco}$ ) by 1% up to  $\sim 4\%$  below 1 TeV.

energy than the  $p0.0075$ -model used in the simulation, the reconstructed energy will end up lower than the true muon energy, which is what is illustrated in the figures. Finally, the uncertainty of the light absorption length in sea water is expected to have a more significant impact to the energy reconstruction result than the one due to the use of different scattering models. This effect will be examined in more detail in the following chapter.

# UNFOLDING THE ATMOSPHERIC NEUTRINO SPECTRUM

In order to obtain the energy spectrum of atmospheric neutrinos, solely assigning the output of the energy reconstruction to each event is not enough. The stochastic nature of energy losses, the limited resolution of the reconstruction method and the detection inefficiencies distort the energy spectrum we aim to measure. In addition, the fact that we only detect part of the muon energy traversing the detector, which is not the same as the parent neutrino energy, make the need of a different approach all the more apparent. For these reasons, the use of unfolding or deconvolution techniques in order to reconstruct the true underlying distribution is of prime importance.

The first section of this chapter contains the definition and general information on the nature of continuous and discrete ill-posed problems, such as the one we are facing here. The second section examines how the method of singular value decomposition can be of use in the unfolding procedure, when addressing these problems. A comprehensive and more detailed treatment of such problems is found in the literature [Hans 98]. The method we apply for the unfolding of the neutrino energy spectrum is described in detail in section 4.3. This method was developed by Höcker and Kartvelishvili [Höck 96], and the tools used to perform the unfolding were developed by Adye [Adye] as part of the ROOT framework [ROOT]. The feasibility of this unfolding method was investigated and applied to Monte Carlo simulations in the past within the ANTARES collaboration [Zorn 05]. In the following section, the performance of the unfolding method is tested on Monte Carlo simulations, and the stability of the algorithm under different assumptions of the true underlying neutrino spectrum is examined. The neutrino effective area is introduced in section 4.5 as the next step towards the reconstruction of the atmospheric neutrino energy spectrum. This is presented in section 4.6 for a realistic detector simulation and physical neutrino energy distributions. In the last two sections, a study of the systematic uncertainties and a summary of the results are given.

## 4.1 Continuous and discrete ill-posed problems

As was mentioned at the beginning of this chapter, the reconstructed muon energy spectrum is the result of the distortive effect that the detector and the reconstruction process have on the true neutrino spectrum. The problem we are called to solve is a set of linear equations of the form  $Ax = b$ . Vector  $x$  represents the true underlying distribution, vector  $b$  is the measured distribution and matrix  $A$ , called the response matrix or the kernel, is the transformation matrix between these two distributions, and it describes the effect of the detector on the true spectrum. When matrix  $A$  is singular, or nearly singular as we shall see is our case, the problem is called a discrete ill-posed problem.

Let us first examine the continuous case. The linear inverse problems we are considering are of the form:

$$\int_{\Omega} \text{input} \times \text{operation} d\Omega = \text{output}, \quad (4.1.1)$$

of which the Fredholm integral of the first kind:

$$\int_0^1 K(t, s)f(t)dt = g(s), \quad 0 \leq s \leq 1 \quad (4.1.2)$$

is a characteristic example. The integration of function  $f$  with a square integrable kernel  $K$ , i.e. :

$$\int_0^1 \int_0^1 K(t, s)^2 dt ds < \infty, \quad (4.1.3)$$

has a smoothing effect on the function, which means that high frequency components are damped. This is related to the Riemann-Lebesgue lemma which states that for  $f(t) = \sin(2\pi pt)$  with parameter  $p$ , the function  $g$  of the Fredholm integral goes to zero as  $p$  goes to infinity. The problem arises from the inverse process, which will tend to amplify the high frequency components of function  $g$ . Kernel  $K$  can be written as an infinite series:

$$K(s, t) = \sum_{i=1}^{\infty} \mu_i u_i(s)v_i(t), \quad (4.1.4)$$

called the singular value expansion of the kernel, where  $u_i$  and  $v_i$  are the orthonormal singular functions of  $K$  and the non-negative  $\mu_i$  are called the singular values of  $K$ . The sum of the square of the singular values of  $K$  is equal to the square of the norm of  $K$ . A very important relation between the kernel and the singular values is:

$$\int_0^1 K(s, t)v_i(t)dt = \mu_i u_i(s), \quad i = 1, 2, \dots \quad (4.1.5)$$

What this equation tells us is that any singular function  $v_i$  is mapped onto  $u_i$ . The amplification or suppression of this mapping depends on the value of  $\mu_i$ . Using (4.1.4) and (4.1.5), the solution of (4.1.2) can be written as

$$f(t) = \sum_{i=1}^{\infty} \frac{(u_i, g)}{\mu_i} v_i(t). \quad (4.1.6)$$

Here,  $(u, g) \equiv \int_0^1 u(s')g(s')ds'$  is the usual inner product. The behavior of the singular values  $\mu_i$  and the singular functions  $v_i$  and  $u_i$  depend on the properties of the kernel. The smoother the kernel, the faster the singular values will decay to zero [Smit 37]. The degree of smoothness of the kernel is measured by the number of continuous partial derivatives (order of differentiation). Additionally, the smaller the singular value the more oscillatory the corresponding orthonormal function will be. The oscillatory nature of these orthonormal functions is related to the Riemann-Lebesgue lemma but the above statement is almost impossible to prove in general. In order to have a square integrable solution  $f$  to the problem  $\int Kf = g$ , i.e. ensure the convergence of the series in equation (4.1.6), the following condition must be satisfied:

$$\sum_{i=1}^{\infty} \left( \frac{(u_i, g)}{\mu_i} \right)^2 < \infty. \quad (4.1.7)$$

This is called the Picard condition and it means that in the solution  $f$ , the coefficients  $(u_i, g)$  must decay faster than the corresponding singular values.

Discrete ill-posed problems arise from the discretization of ill-posed problems such as the Fredholm integral equation of the first kind. In such problems all the singular values of the Kernel matrix  $A$  gradually decay to zero. This is in contrast to rank-deficient problems where there is a well-defined gap in the spectrum of singular values and the rank of the matrix can be considered lower. This is relevant in problems where the response matrix is very large and calls for a dimensional reduction. In the case of discrete ill-posed problems we cannot use the notion of numerical rank since there is no clear cutoff in the distribution of the singular values and thus no straightforward way of reducing the size of the kernel.

Due to small singular values, ill-posed problems are practically underdetermined. A system of linear equations is underdetermined when there are fewer equations than unknowns. Equivalently the response matrix is degenerate, i.e. it does not have an inverse, its determinant is zero and the system has either no solution or an infinite number of solutions. This brings up the need to include further information about the expected solution in order to get useful and stable results, a process called regularization. Various regularization schemes exist. The one we will use is referred to as Tikhonov regularization. Other schemes include the truncated singular value decomposition approach (TSVD), applied by determining at which term the solution expansion will be truncated. Iterative methods are also used, particularly in 2D or 3D applications where the size of the response matrix is large and the computation time becomes an important factor. The idea of Tikhonov regularization is to minimize  $\{\rho(f)^2 + \lambda^2\omega(f)^2\}$ , where  $\rho(f) = \|\int_0^1 K(s, t)f(t)dt - g(s)\|_2$  is the residual 2-norm, defined as:

$$\|\mathbf{x}\|_p \equiv \left( \sum_i^n |x_i|^p \right)^{1/p}, \quad p = 2, \quad (4.1.8)$$

for a vector  $\mathbf{x} = [x_1, x_2, \dots, x_n]$ . The term  $\omega(f)$ , called the smoothing norm, is the constraint we impose on the solution  $f$ . The *regularization parameter*  $\lambda$  indicates the

magnitude of this constraint. The discretized regularized problem can be expressed as:

$$\min\{\|Ax - b\|_2^2 + \tau^2\Omega(x)^2\} \quad (4.1.9)$$

where the smoothing term often has the form  $\Omega(x) = \|Cx\|_2$ . Matrix  $C$  can be the identity matrix or as we will see later in our case a derivative operator. Regularization decreases the size of the covariance matrix of the solution and subsequently the variance in each energy bin as well as the bin-to-bin fluctuations, as we will see in section 4.4. This however introduces a bias to the solution and the goal is to find the optimal trade-off between the two. The kind of bias introduced, depends on the nature of the smoothing term. In the present work we impose a constraint on how much the solution is allowed to fluctuate, requiring a smooth energy distribution.

## 4.2 Singular Value Decomposition (SVD)

The singular value decomposition (SVD) is the factorization of a matrix into a product of two orthogonal matrices and a diagonal matrix with non-negative entries. It is a technique that is widely used in the solution of linear systems of equations and the filtering of noisy signals. As will be illustrated below, the SVD is a valuable tool in discriminating between significant components in the solution and terms that contribute to statistical noise.

Let  $A \in \mathfrak{R}^{n \times n}$  be a square matrix. The discussion that follows can be applied for a general rectangular matrix  $A \in \mathfrak{R}^{m \times n}$ . However, since in this analysis the response matrix we use is a square matrix, we consider  $m = n$  from now on. The singular value decomposition of matrix  $A$  is:

$$A = USV^T = \sum_{i=1}^n u_i s_i v_i^T, \quad (4.2.1)$$

where

$$U = (u_1, u_2, \dots, u_n) \in \mathfrak{R}^{n \times n} \quad \text{and} \quad (4.2.2)$$

$$V = (v_1, v_2, \dots, v_n) \in \mathfrak{R}^{n \times n} \quad (4.2.3)$$

are orthogonal matrices ( $U^T U = V^T V = I_n$ ). Matrix  $S = \text{diag}(s_1, s_2, \dots, s_n)$  is a diagonal matrix with singular values  $s_1 \geq s_2 \geq \dots \geq s_n \geq 0$ , ordered in decreasing value by construction. The vectors (or orthonormal columns of  $U$  and  $V$ )  $u_i, v_i$  are called the left and right singular vectors, respectively. The SVD is related to the eigenvalue decomposition of the symmetric semi-definite matrices  $AA^T$  and  $A^T A$ , since  $AA^T = US^2U^T$  and  $A^T A = VS^2V^T$ . As with the continuous case (see equation (4.1.4)), the singular values  $s_i$  decay gradually to zero and at the same time, the singular vectors  $u_i$  and  $v_i$  become more oscillatory, i.e. they tend to have more sign changes in their elements as index  $i$  increases. If  $A$  is orthogonal all singular values are equal to 1. For a degenerate matrix at least one singular value is zero and the rank of the matrix is equal to the number of non-zero singular values.

From (4.2.1), the following relations can be obtained,

$$Av_i = s_i u_i, \quad \|Av_i\|_2 = s_i \quad (4.2.4)$$

and

$$A^T u_i = s_i v_i, \quad \|A^T u_i\|_2 = s_i. \quad (4.2.5)$$

If a singular value  $s_i$  is small, then there exists a certain linear combination of the columns or rows of matrix  $A$  such that  $\|Av_i\|_2$  or  $\|A^T u_i\|_2$  is small. This means that matrix  $A$  is nearly rank-deficient and that the singular vectors corresponding to small singular values are the numerical null vectors of matrix  $A$  and its transpose. In other words, the null space of  $A$  is spanned by oscillating vectors, i.e. vectors with many sign changes.

In order to see how small singular values can be a major problem, consider an arbitrary vector  $x$ , in the basis of the singular vectors  $v_i$

$$x = \sum_{i=1}^n (v_i^T x) v_i \quad (4.2.6)$$

and the mapping

$$Ax = \sum_{i=1}^n s_i (v_i^T x) u_i. \quad (4.2.7)$$

Since small singular values  $s_i$  correspond to highly oscillating vectors, this mapping damps the high frequency components of  $x$  more than the low frequency ones. The inverse problem of  $Ax = b$  suffers from exactly the opposite effect i.e. amplification of high frequency oscillations in our data vector  $b$  propagating in a dangerous fashion to the solution  $x$ . If the inverse of matrix  $A$  exists, then

$$A^{-1} = \sum_{i=1}^n v_i s_i^{-1} u_i^T \quad (4.2.8)$$

and

$$x = \sum_{i=1}^n s_i^{-1} (u_i^T b) v_i. \quad (4.2.9)$$

It is easy to see how division by small singular values  $s_i$  amplifies the high frequency components in  $b$ . In case of rank-deficient matrices, i.e. when the rank of the matrix is smaller than its order, the Moore-Penrose pseudoinverse  $A^\dagger \equiv \sum_{i=1}^{\text{rank}(A)} v_i s_i^{-1} u_i^T$  is used instead of  $A^{-1}$  and the summation is only up to  $\text{rank}(A)$  instead of  $n$ . A pseudoinverse matrix  $A^\dagger$  satisfies  $AA^\dagger A = A$ ,  $A^\dagger AA^\dagger = A^\dagger$  and furthermore  $AA^\dagger$  and  $A^\dagger A$  are Hermitian matrices.

The ill-posedness of the problem at hand is measured by the 2-norm condition number of matrix  $A$ , defined as

$$\text{cond}(A) \equiv \frac{s_1}{s_{\text{rank}(A)}}. \quad (4.2.10)$$

The condition of a matrix tells us how sensitive our system is to perturbations in the data vector  $b$ . If the condition is close to one, small fluctuations in  $b$  remain small in  $x$ , while for  $\text{cond}(A) \gg 1$  they can propagate into large unphysical fluctuations in the solution.

If the regularization term  $C$  is the unit matrix  $I$ , then the problem is in standard form, while otherwise it is said to be in general form. For Tikhonov regularization with  $C \neq I$ , bringing the problem in standard form means

$$\min\{\|Ax - b\|_2^2 + \lambda^2\|Cx\|_2^2\} \rightarrow \min\{\|\bar{A}\bar{x} - \bar{b}\|_2^2 + \lambda^2\|\bar{x}\|_2^2\}. \quad (4.2.11)$$

In the case where  $C$  is square and invertible, which is our case as will be seen in the following section,  $\bar{A} = AC^{-1}$ ,  $\bar{b} = b$  and  $\bar{x} = Cx$ .

For Tikhonov regularization, the solution of (4.2.11) can be written in standard form as

$$x_{reg} = \bar{x} = \sum_{i=1}^n f_i \frac{u_i^T b}{s_i} v_i, \quad (4.2.12)$$

where the filter factors  $f_i$  are given by

$$f_i = \frac{s_i^2}{s_i^2 + \lambda^2}. \quad (4.2.13)$$

The filtering sets in for components for which  $s_i < \lambda$  damping the highly oscillating components of the solution. In the next section we will examine more closely how to solve the problem of the atmospheric neutrino spectrum deconvolution using a singular value decomposition approach to data unfolding as suggested in [Höck 96].

### 4.3 SVD regularized unfolding

As discussed earlier, the energy spectrum of atmospheric neutrinos cannot be obtained by piling up the energy of individual events. This can be seen in figure 4.1, where the true energy spectrum of atmospheric neutrinos after triggering, reconstruction and selection cuts, is shown together with the true muon energy spectrum at the detector level, as well as the spectrum obtained after reconstructing the energy with the method described in chapter 3. The selection criteria applied in what follows, are the same that we will use for real data and will be described in detail in chapter 5. The true muon spectrum is higher than the neutrino spectrum at lower energies and lower for energies above  $\sim 1$  TeV. The muon loses energy after its production until it reaches the *can*, defined as a hypothetical cylinder extending several attenuation lengths away from the instrumented volume. The energy plotted here is the energy of the muon entering this *can*. Furthermore, when the muon is created, it carries away with it merely a fraction of the parent neutrino energy. This is the reason why the muon distribution is more populated at lower energies and less so at the higher end of the spectrum. Additionally, the output of the energy reconstruction, provides us with a spectrum that is distorted

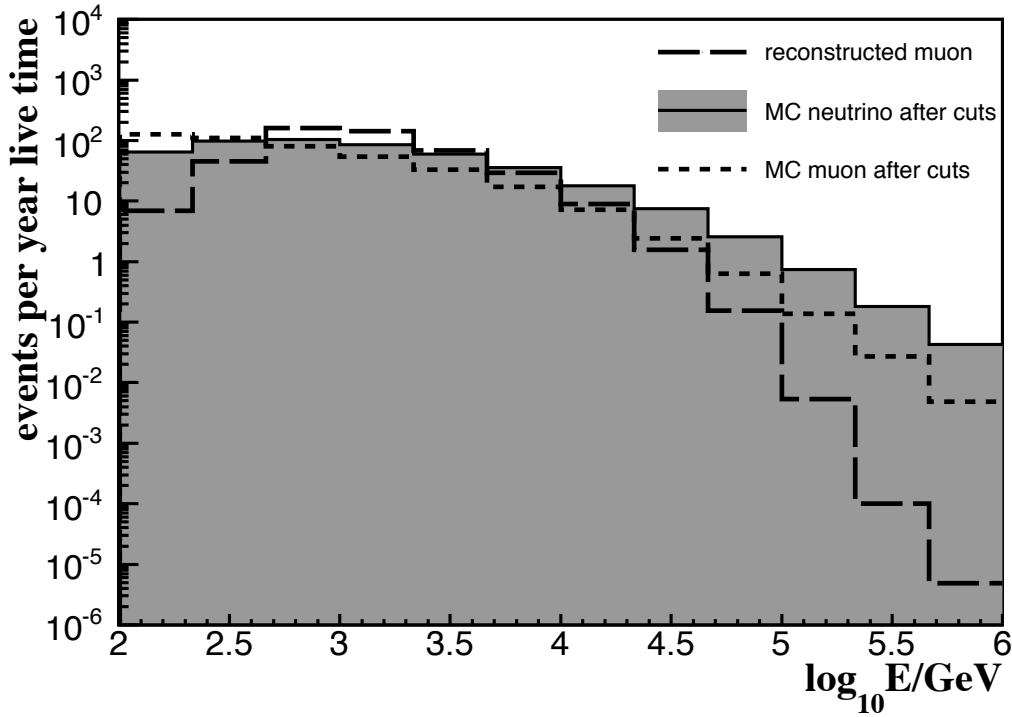


Figure 4.1: Number of events per year live time as a function of energy after the application of quality cuts. The selection criteria applied for all the distributions shown here are  $\Lambda > -4.8$ , an angular error estimate from the track fit  $\hat{\beta} < 1^\circ$ , tracks triggered with 3N or T3 trigger and reconstructed as upward going with the method described in section 3.3. The unfolding helps us recover the true neutrino spectrum from the distorted muon energy distribution.

even further. It is evident from this, that there is a need for an additional step towards the neutrino energy spectrum reconstruction.

Consider vector  $b$ , the distribution of the measured observable,  $\log_{10} E_{\text{Reco}}$  in our case, and  $x$  the underlying true distribution of  $\log_{10} E_\nu$ . The distortions are described by the operation of matrix  $\mathcal{A}$  on  $x$ ,

$$\mathcal{A}x = b. \quad (4.3.1)$$

Matrix  $\mathcal{A}$  is a probability matrix where each element  $\mathcal{A}_{ij}$  gives the probability for an event that was generated in the  $j$ -th bin of  $x$  to be found in bin  $i$  of  $b$  after the measurement. Matrix  $\mathcal{A}$  is calculated by means of Monte Carlo simulation of a realistic detector and is shown in figure 4.2 for the case of the ANTARES detector. The vertical axis represents the true neutrino energies and the horizontal axis the reconstructed muon energies. The different ranges on the axes reflect the bias we encountered on chapter 3 leading to a smaller range of values for the reconstructed energies.

Any attempt to tackle the problem directly by simply inverting  $\mathcal{A}$  and obtain a solution in the form of  $x = \mathcal{A}^{-1}b$ , leads to a rapidly oscillating solution and huge errors

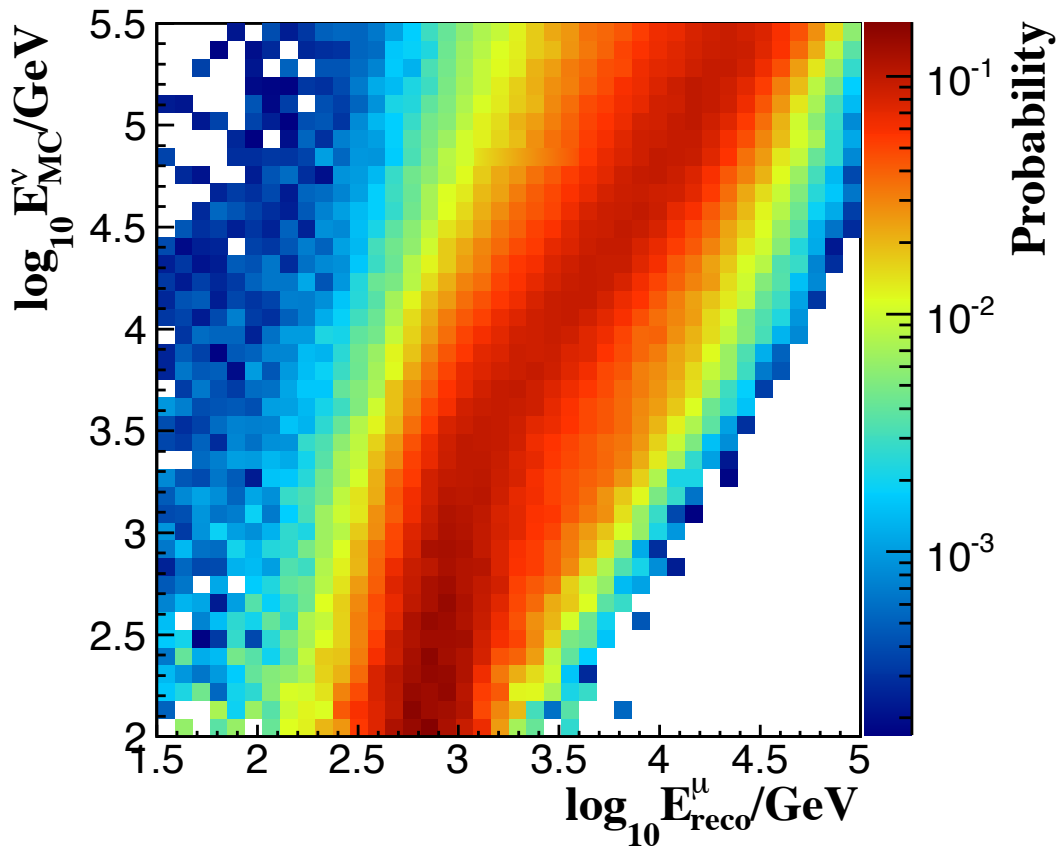


Figure 4.2: Probability matrix obtained from Monte Carlo simulations the ANTARES detector, applying the maximum likelihood energy reconstruction strategy to obtain the  $\log_{10} E_{\text{Reco}}$  values. The events used for the construction of this matrix are the ones selected after the quality cuts.

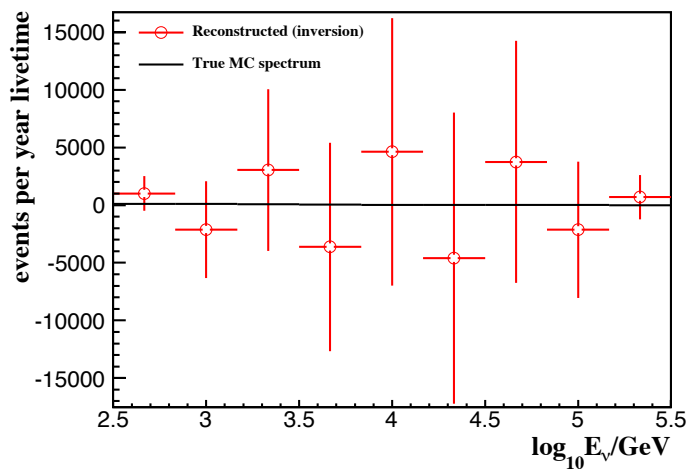


Figure 4.3: Reconstructed spectrum from the direct solution of the linear system, applying a response matrix inversion. The solution is meaningless due to the large fluctuations and errors (see text for explanation).

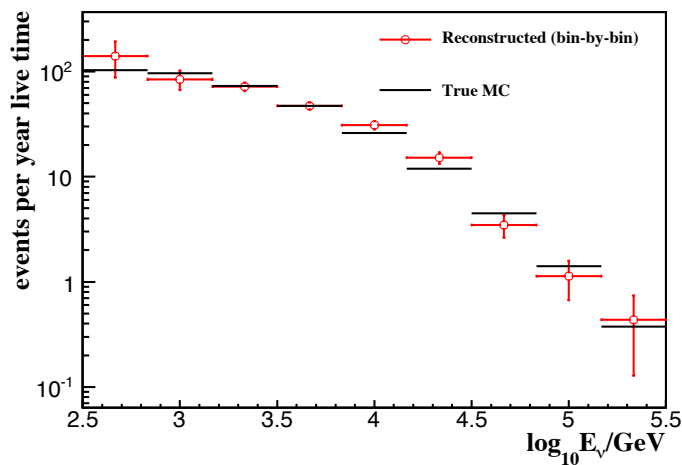


Figure 4.4: Reconstructed spectrum with the use of bin-by-bin correction factors. The result is close to the true distribution since the true spectrum was used for the determination of the correction factors (see eq. (4.3.2)).

as is illustrated in figure 4.3. This is a result of the fact that matrix  $\mathcal{A}$  is ill-conditioned as discussed in the previous section and any minor fluctuation in the data vector  $b$  has the risk of propagating catastrophically into the result. The errors on the reconstructed spectrum are as large as the values themselves, and the rapidly oscillating solution makes the result meaningless. In conclusion the smoothing effect of the kernel does not allow for such a treatment of the problem.

Another way to address the problem of recovering the true structure of the spectrum is to apply a bin-by-bin correction to the reconstructed spectrum,

$$\text{corrected content}_i = \frac{\text{MC true content}_i}{\text{MC measured content}_i} \times \text{observed content}_i, \quad (4.3.2)$$

according to an expected measured distribution obtained from Monte Carlo simulations. The result of such a strategy is shown in figure 4.4. The result seems satisfactory at first sight, however it will be affected by statistical fluctuations at the bin level and by incorrect or inaccurate assumptions on the underlying spectrum. The latter problem is usually addressed by iterating the procedure.

A better approach is to unfold the neutrino energy spectrum using a singular value decomposition based deconvolution method, described in what follows. The system of linear equations (4.3.1) can be treated as a least squares problem which has to be minimized as in equation (4.1.9), i.e. ,

$$\min\{(\mathcal{A}x - b)^T B^{-1}(\mathcal{A}x - b)\}, \quad (4.3.3)$$

where  $B$  is the covariance matrix of the measured vector  $b$ . Consider now a vector  $w = x/x^{ini}$  representing the deviation of the unknown vector  $x$  from the initial Monte Carlo vector  $x^{ini}$  used to train the probability matrix. The vector  $x^{ini}$  is a reasonable assumption of the unknown spectrum. Multiplying each column of the probability matrix  $\mathcal{A}$  with the number of events generated in the corresponding bin of vector  $x^{ini}$ , one gets

$$\sum_{j=1}^n A_{ij} w_j = b_i, \quad (4.3.4)$$

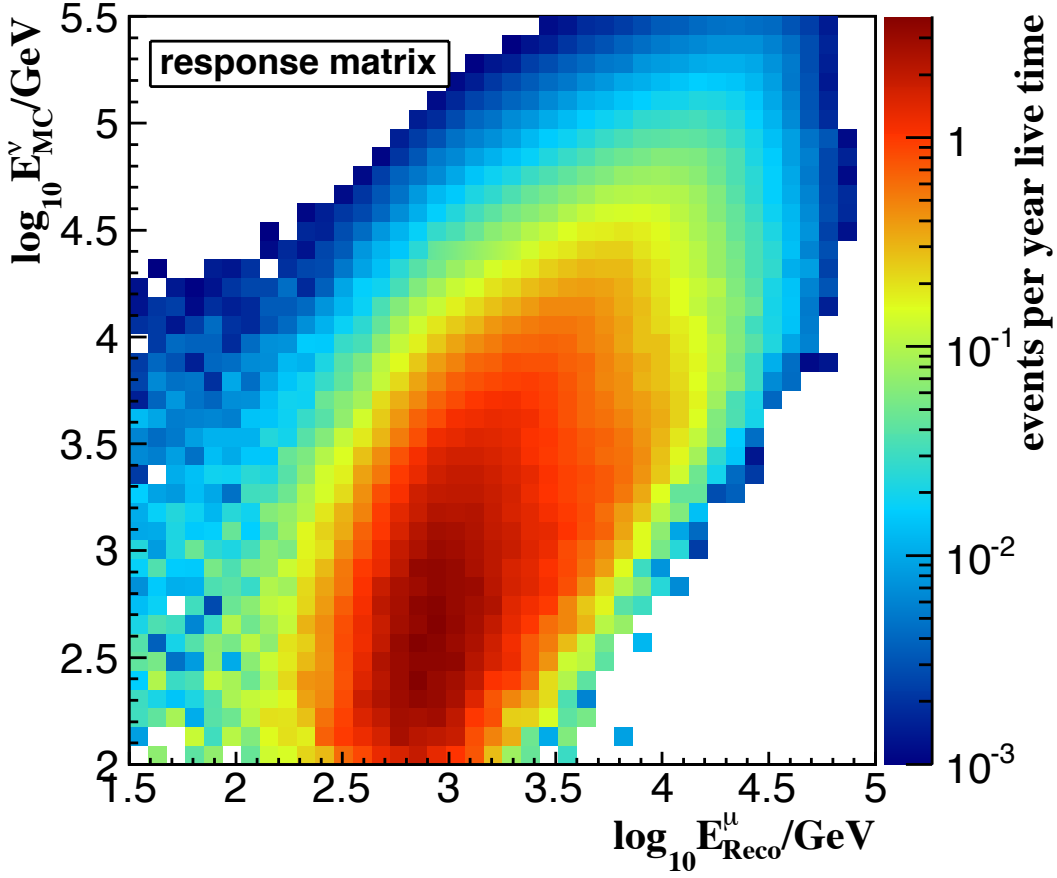


Figure 4.5: Response matrix obtained from Monte Carlo simulations of the ANTARES detector. The elements  $A_{ij}$  are the number of events that migrated from bin  $j$  to bin  $i$  due to the measurement process. It has been constructed by assuming the conventional and prompt atmospheric neutrino fluxes from [Hond 07] and [Mart 03] respectively.

where  $A$  is now the *number of events matrix* instead of the probability matrix  $\mathcal{A}$ . The entries  $A_{ij}$  of this matrix, which we from now on call the response matrix, represent the number of events generated in bin  $j$  but end up in bin  $i$ . The response matrix  $A$  is shown in figure 4.5. It essentially maps the distribution of reconstructed energy values to the true neutrino energies.

At the end of the unfolding procedure we have to multiply the solution vector  $w$  by  $x^{ini}$  to obtain the correctly normalized solution  $x$ . The reasons behind rescaling the unknown vector  $x$  are twofold. First, if the initial Monte Carlo distribution  $x^{ini}$  is reasonably close to the one being unfolded, the unknown vector  $w$  will be smooth and require less terms in the decomposition. Secondly, some of the columns or rows of the response matrix  $A$  may contain very few events and some elements of the matrix may have only one entry. In the probability matrix  $\mathcal{A}$  this corresponds to probability one, giving unreasonably high weight in the particular equation. The number of events

response matrix on the other hand gives a larger weight to better determined equations in the system. In terms of the exact analytical solution to the problem, the original and the rescaled systems are equivalent. In other words, such a rescaling attempts to account for intrinsic errors on the response matrix due to finite statistics.

The next step is to perform the SVD of  $B$  which yields  $B = QRQ^T$ , with  $R_{ii} = r_i^2 \neq 0$ ,  $R_{ij} = 0$  for  $i \neq j$  and  $B^{-1} = QR^{-1}Q^T$ . Substituting  $B$  in (4.3.3) gives:

$$(\tilde{A}w - \tilde{b})^T(\tilde{A}w - \tilde{b}) = \min, \quad (4.3.5)$$

where

$$\tilde{A}_{ij} = \frac{1}{r_i} \sum_m Q_{im} A_{mj}, \quad \tilde{b}_i = \frac{1}{r_i} \sum_m Q_{im} b_m, \quad (4.3.6)$$

leading to the system  $\sum_j \tilde{A}_{ij} w_j = \tilde{b}_i$ . The new covariance matrix is now the identity matrix and each equation has the same significance.

Instead of minimizing (4.3.5), we add a regularization term to control the rapidly oscillating terms of the solution. The system to be solved now becomes:

$$\min\{(\tilde{A}w - \tilde{b})^T(\tilde{A}w - \tilde{b}) + \tau(Cw)^T Cw\}. \quad (4.3.7)$$

Matrix  $C$  describes the *a priori* condition imposed on the solution. The regularization parameter  $\tau$  determines the amount of regularization imposed, and essentially plays the role of a Lagrange multiplier. The assumption about the solution vector  $w$  is that it should not be wildly oscillating, but smooth, exhibiting small bin-to-bin variations. The curvature of the discrete distribution  $w$  is defined as:

$$\sum_i [(w_{i+1} - w_i) - (w_i - w_{i-1})]^2, \quad (4.3.8)$$

which is the sum of the squares of the second derivatives of  $w$ . Matrix  $C$  is then constructed as:

$$C = \begin{pmatrix} -1 & 1 & 0 & 0 & 0 & \dots & 0 & 0 & 0 & 0 & 0 \\ 1 & -2 & 1 & 0 & 0 & \dots & 0 & 0 & 0 & 0 & 0 \\ 0 & 1 & -2 & 1 & 0 & \dots & 0 & 0 & 0 & 0 & 0 \\ 0 & 0 & 1 & -2 & 1 & \dots & 0 & 0 & 0 & 0 & 0 \\ 0 & 0 & 0 & 1 & -2 & \dots & 0 & 0 & 0 & 0 & 0 \\ \vdots & \vdots & \vdots & \vdots & \vdots & \ddots & \vdots & \vdots & \vdots & \vdots & \vdots \\ 0 & 0 & 0 & 0 & 0 & \dots & -2 & 1 & 0 & 0 & 0 \\ 0 & 0 & 0 & 0 & 0 & \dots & 1 & -2 & 1 & 0 & 0 \\ 0 & 0 & 0 & 0 & 0 & \dots & 0 & 1 & -2 & 1 & 0 \\ 0 & 0 & 0 & 0 & 0 & \dots & 0 & 0 & 1 & -2 & 1 \\ 0 & 0 & 0 & 0 & 0 & \dots & 0 & 0 & 0 & 1 & -1 \end{pmatrix}, \quad (4.3.9)$$

in order to suppress solution vectors  $w$  which would exhibit large curvatures. Matrix  $C$  is the second derivative matrix operating on the solution vector  $w$ , and according to

equation (4.3.8),  $\|Cw\|_2^2$  is the curvature of  $w$ . For larger values of  $\tau$  the second term of equation (4.3.7) becomes more and more dominant. The minimization of the system (4.3.7) with a very large  $\tau$  is equivalent to searching for a solution vector  $w$  with small curvature, i.e. small fluctuations between neighboring bins. On the other hand if  $\tau = 0$  the system is equivalent to the original one without any constraint. Minimizing (4.3.7) leads to the following system of linear equations:

$$\begin{bmatrix} \tilde{A} \\ \sqrt{\tau}C \end{bmatrix} w = \begin{bmatrix} \tilde{b} \\ 0 \end{bmatrix}. \quad (4.3.10)$$

The solution of the above system for any  $\tau$  can be expressed in terms of the non-regularized solution ( $\tau = 0$ ). Rewriting (4.3.10) as:

$$\begin{bmatrix} \tilde{A}C^{-1} \\ \sqrt{\tau}I \end{bmatrix} Cw = \begin{bmatrix} \tilde{b} \\ 0 \end{bmatrix}, \quad (4.3.11)$$

brings the system in the standard form (remember (4.2.11)). Matrix  $C$  is degenerate so in order to make the inversion possible a small diagonal component  $C_{ik} \rightarrow C_{ik} + \xi\delta_{ik}$  is added, so that  $C$  now becomes:

$$C = \begin{pmatrix} -1+\xi & 1 & 0 & 0 & \dots & 0 & 0 & 0 & 0 \\ 1 & -2+\xi & 1 & 0 & \dots & 0 & 0 & 0 & 0 \\ 0 & 1 & -2+\xi & 1 & \dots & 0 & 0 & 0 & 0 \\ 0 & 0 & 1 & -2+\xi & \dots & 0 & 0 & 0 & 0 \\ \vdots & \vdots & \vdots & \vdots & \ddots & \vdots & \vdots & \vdots & \vdots \\ 0 & 0 & 0 & 0 & \dots & -2+\xi & 1 & 0 & 0 \\ 0 & 0 & 0 & 0 & \dots & 1 & -2+\xi & 1 & 0 \\ 0 & 0 & 0 & 0 & \dots & 0 & 1 & -2+\xi & 1 \\ 0 & 0 & 0 & 0 & \dots & 0 & 0 & 1 & -1+\xi \end{pmatrix}. \quad (4.3.12)$$

The diagonal component  $\xi$  should be small enough in order to retain the minimum curvature constraint of equation (4.3.7), but large enough to allow inversion. Performing SVD on  $\tilde{A}C^{-1} = USV^T$  and rotating  $\tilde{b}$  and  $Cw$  one gets:

$$s_i z_i = d_i, \quad i = 1, \dots, n_x \quad (4.3.13)$$

which provides the non-regularized solution ( $\tau = 0$ ), where:

$$d \equiv U^T \tilde{b}, \quad z \equiv V^T Cw. \quad (4.3.14)$$

The solution for the non-regularized system is written as:

$$z_i^{(0)} = \frac{d_i}{s_i}, \quad x^{(0)} = C^{-1}Vz^{(0)}, \quad (4.3.15)$$

which provides the true distribution  $x$  after multiplying by  $x^{ini}$ . It can be shown [Laws 95] that introducing non-zero  $\tau$  changes  $d_i$  to  $d_i^{(\tau)}$  as:

$$d_i^{(\tau)} = d_i \frac{s_i^2}{s_i^2 + \tau}, \quad (4.3.16)$$

and the solution becomes:

$$z_i^{(\tau)} = \frac{d_i s_i}{s_i^2 + \tau}, \quad w^{(\tau)} = C^{-1} V z^{(\tau)}. \quad (4.3.17)$$

Introducing a non-zero  $\tau$  is effectively imposing a Fourier low-pass filter cutoff in the solution, damping the high frequency components of the solution (see also (4.2.12), (4.2.13)). This means that this unfolding method will suppress the terms that are responsible for the large oscillations obtained in the result shown in figure 4.3, obtained with a direct inversion of the response matrix. The solution will be smooth, determined mainly by the significant terms, and it will be less affected by the statistical errors on the data vector as will be illustrated in the following section.

## 4.4 Performance and stability of the method

In order to test the stability of the unfolding method under different assumptions of the true underlying neutrino spectrum, four different fluxes were used to train the response matrix. The distribution of the number of neutrino events expected at the detector level are shown in figure 4.6. The flux denoted as *response flux 0* is the one that was also used to generate the pseudo data to test the method under the different assumptions for the true spectrum. In figure 4.7, the four different expected reconstructed spectra from Monte Carlo are shown in comparison with the test data. Poisson fluctuations were added to the expected distribution of the test data. In the upper left plot, corresponding to the case where the initial assumption is the same as the distribution that provided the test data, the difference is only due to these statistical fluctuations.

The distribution of the singular values  $s_i$  of the response matrices constructed using the three test fluxes, as well as the true flux (*response 0*) are shown in figure 4.8. It is evident that the matrices are highly singular with singular values decreasing rapidly for increasing  $i$ . The condition of the response matrices is much larger than one (equation (4.2.10)), indicating the ill-posedness of these kernels. Additionally, these response matrices are also rank-deficient, having rank equal to the matrix dimension minus one. This can of course be avoided by choosing different maximum energies or different binning in order to avoid empty bins that are responsible for the rank reduction. However this poses no problem to the application of the method.

Before proceeding with the unfolding, one has to chose the appropriate value of the regularization parameter. A small regularization parameter  $\tau$  favors the data. If  $\tau$  is close to zero, the system is virtually equivalent to the non-regularized system, and the solution obtained is very close to the one obtained by simply inverting the response matrix. On the other hand, large values of  $\tau$  impose stronger constraints on the solution with the possible danger of over-regularization, leading to a solution biased towards the assumed spectrum. The authors of the method presented here [Höck 96], suggest examining the distribution of the absolute values of the expansion coefficients  $|d_i| = |u_i^T \tilde{b}|$ . The values of  $|d_i|$  fall rapidly with increasing  $i$ , reaching a level where they are compatible with zero. The optimal regularization parameter is  $\tau = s_k^2$ , where

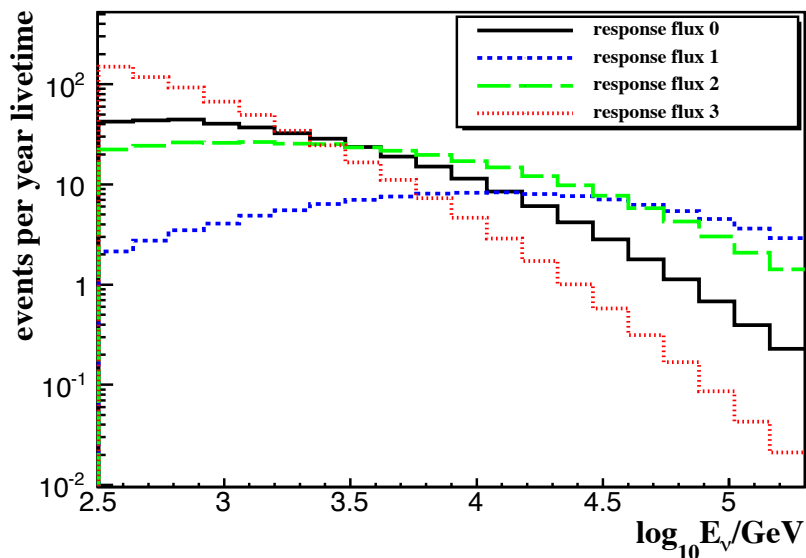


Figure 4.6: Distributions of atmospheric neutrino events at the detector level after quality cuts. The *response 0* test distribution corresponds to the [Hond 07],[Mart 03] atmospheric neutrino flux. The distributions denoted as *response 1*, *2* and *3* are constructed in order to test the stability of the unfolding method to different initial assumptions and do not correspond to physical spectra. The fluxes that produce them are  $\Phi_1 \sim E^{-2.5}$ ,  $\Phi_2 \sim E^{-3}$  and  $\Phi_3 \sim E^{-4}$ .

$k$  is the index of the coefficient after which  $|d_i|$ 's settle at the noise level. The first coefficients correspond to large singular values of the response matrix and represent significant equations on the system of linear equations that we have to solve. When  $|d_i|$ 's are compatible with zero, or equivalently the vectors  $u_i$  are highly oscillatory, their significance in the expansion of the final solution is small. In addition, the fact that they correspond to small singular values, makes them even more problematic since they are enhanced by the inverse of the corresponding singular value. This means that singular values smaller than one, that correspond to non-significant coefficients, will have a catastrophic effect on the solution giving an unreasonably high weight to equations that contribute little other than noise to the solution. This can be viewed in connection with the Picard condition (see eq. (4.1.7)), stating that the coefficients should decay faster than the singular values. The expansion coefficients for the four different fluxes are shown in figure 4.9. When the true flux is used to train the response matrix, there is only one significant coefficient since the test data were generated according to the same spectrum. In the cases where the kernel was constructed using a different initial assumption, the coefficients decay slower, reaching the level where they are compatible with zero at higher indices  $i$ . The spectrum has been unfolded using these four response matrices. The choice of the regularization parameter is  $\tau = s_2^2$  for the *response 0* case (obtained with the true spectrum),  $\tau = s_4^2$  for *response 1*, and finally  $\tau = s_3^2$  for *response 2* and *response 3*, obtained using the fluxes *2* and *3* respectively.

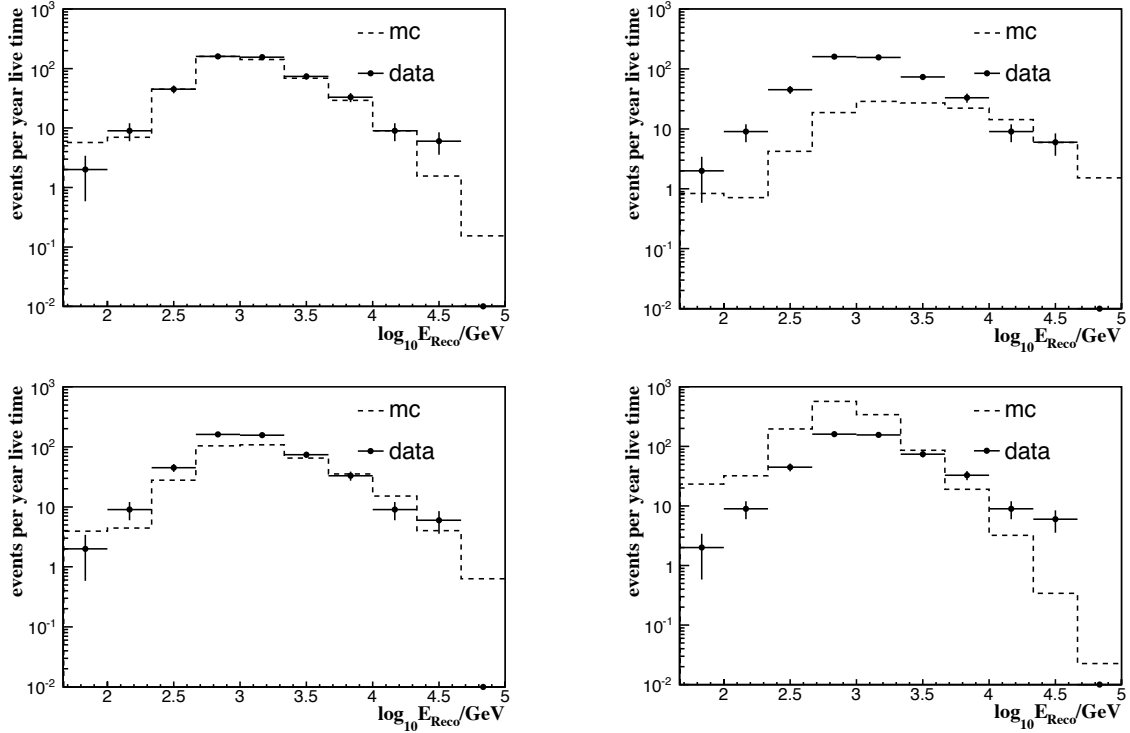


Figure 4.7: Distributions of the reconstructed muon energies for the four fluxes used to create the different response matrices together with the test data generated according to the [Hond 07],[Mart 03] flux. Poisson fluctuations are added to each bin of the test data histogram. The assumed spectra used to build the response matrices in reading order are *response flux 0*, *response flux 1,2* and *3* (see fig. 4.6).

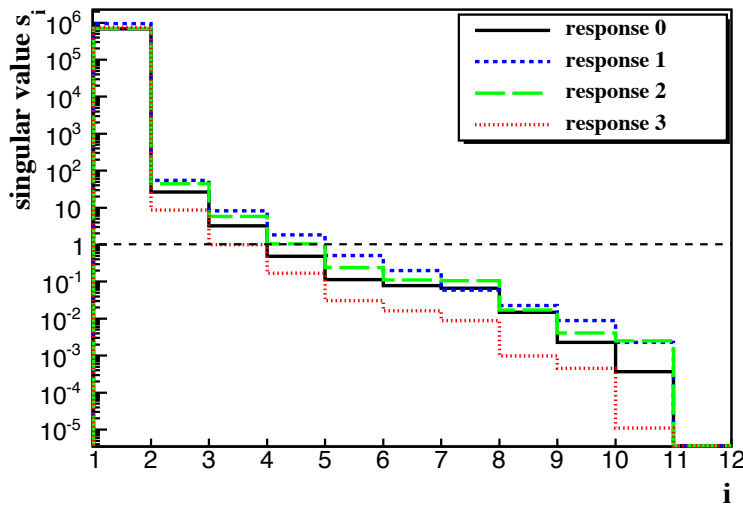


Figure 4.8: Distribution of singular values  $s_i$  for the four different response matrices. The singular values decrease rapidly with increasing  $i$ . The response matrices are ill-conditioned and the problem is underdetermined.

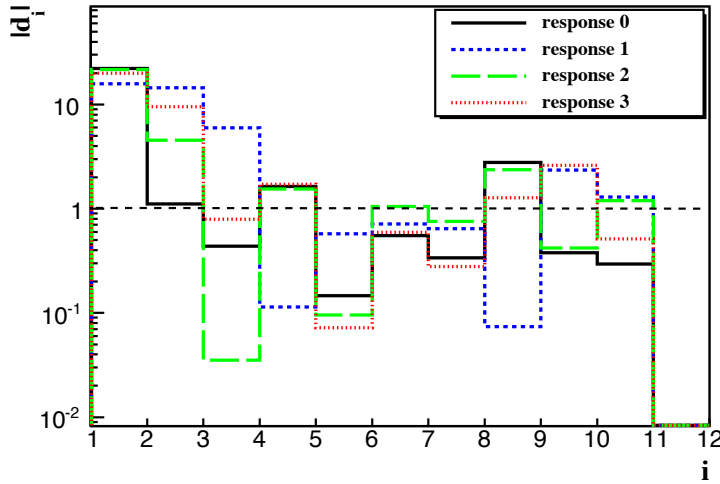


Figure 4.9: Distribution of expansion coefficients  $|d_i|$  for the four response matrices. The test data were generated with the same flux as the one used to create response matrix 0. This is why for this case there is only one significant coefficient while for the other three response matrices the  $|d_i|$ 's become stable after the third or fourth bin.

There is no unique way of determining the optimal regularization and several suggestions exist in the literature [Blob 10]. An alternative method to determine the best choice of the regularization parameter is to examine the so-called L-curve. It is a plot of the logarithm of the norm of the regularized solution against the logarithm of the norm of the corresponding residual. The quantity we want to minimize is  $\|Ax - y\|_2^2 + \tau \|Lx\|_2^2$ . For large values of  $\tau$ , i.e. too much regularization or over-smoothing, the solution will be biased and the norm of the residuals  $\|A\bar{x} - y\|_2$  will be large. On the other hand, for under-smoothing, i.e. too little regularization, the solution is dominated by statistical fluctuations and  $\|Lx\|_2$  will be large. The L-curve has often an L shape, hence its name, and the optimal amount of regularization lies at the corner of that curve, where there is a compromise between the magnitude of the norm of the residual and the magnitude of the norm of the regularized solution. The L-curves for the four different unfoldings are shown in figure 4.10. The square point indicates the critical value used in the regularization.

The results after the unfolding for the four different cases are shown in figure 4.11. In the left column, the unfolded distributions, together with the test distributions as well as the distributions that were used to construct the response matrices are shown. In all four cases, the method exhibits a stable behavior, succeeding in reconstructing the test spectrum. The easiest case is of course the first one, where the test spectrum is the same as the one used to provide the initial assumption. In this case, the algorithm has to deal only with statistical fluctuations. In the right column, the residuals between the test and the unfolded distributions are plotted. The colored bands represent the one and two sigma statistical errors on the true test distribution. The results are satisfactory,

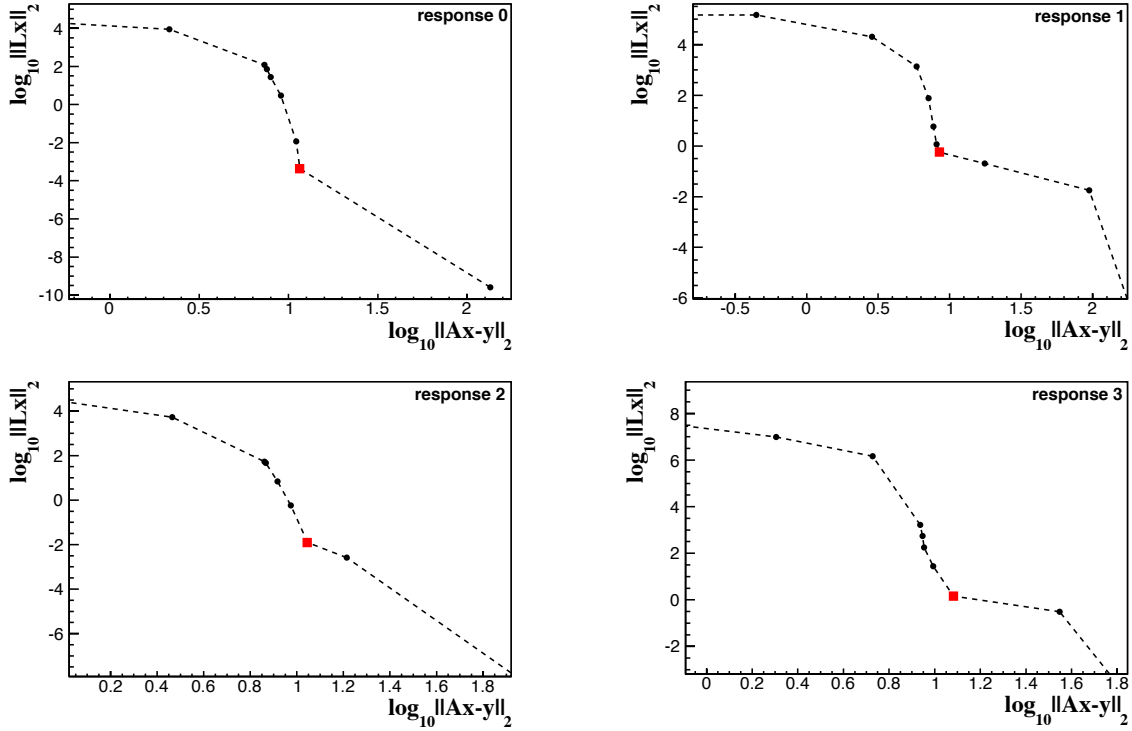


Figure 4.10: L-curves for the four different cases under study. Points on the lower right corners of the plots correspond to over-regularized systems while points on the uppermost left parts correspond to systems with too little regularization. Each point corresponds to a different choice of regularization parameter  $\tau = s_i^2$ . The curves correspond in reading order to *response 0*, *1*, *2* and *3*. See text for explanation.

especially taking into account that the distributions span three orders of magnitude, with differences between test and unfolded distributions remaining within the statistical uncertainties of the true test spectrum.

Let us now take the example of *response 2* to look more closely into what happens for different choices of regularization parameters. As a reminder, the distribution that is used to create the response matrix, i.e. our best initial guess, is *flux 2* in figure 4.6, while the distribution providing the test data is denoted as *response 0*. The distribution of  $|d_i|$ 's is illustrated in figure 4.12 in black. The distribution of coefficients decreases in the first few bins and then remains relatively flat for the remaining part. Choosing the third bin as the level at which the coefficients become compatible with zero, we set the regularization parameter at  $\tau = s_3^2$ . The red line shows the behavior of the regularized coefficients  $|d_i^{(3)}| = |d_i \frac{s_i^2}{s_i^2 + s_3^2}|$  (equation (4.3.16)). This plot illustrates how the choice of a regularization parameter acts as a low-pass filter for insignificant coefficients above the critical value. The unfolding procedure has been repeated for different values of the regularization parameter, namely from  $\tau = s_1^2$  up to  $\tau = s_6^2$ . The unfolded spectra for the different  $\tau$  are shown in figure 4.13 together with the test and the assumed true

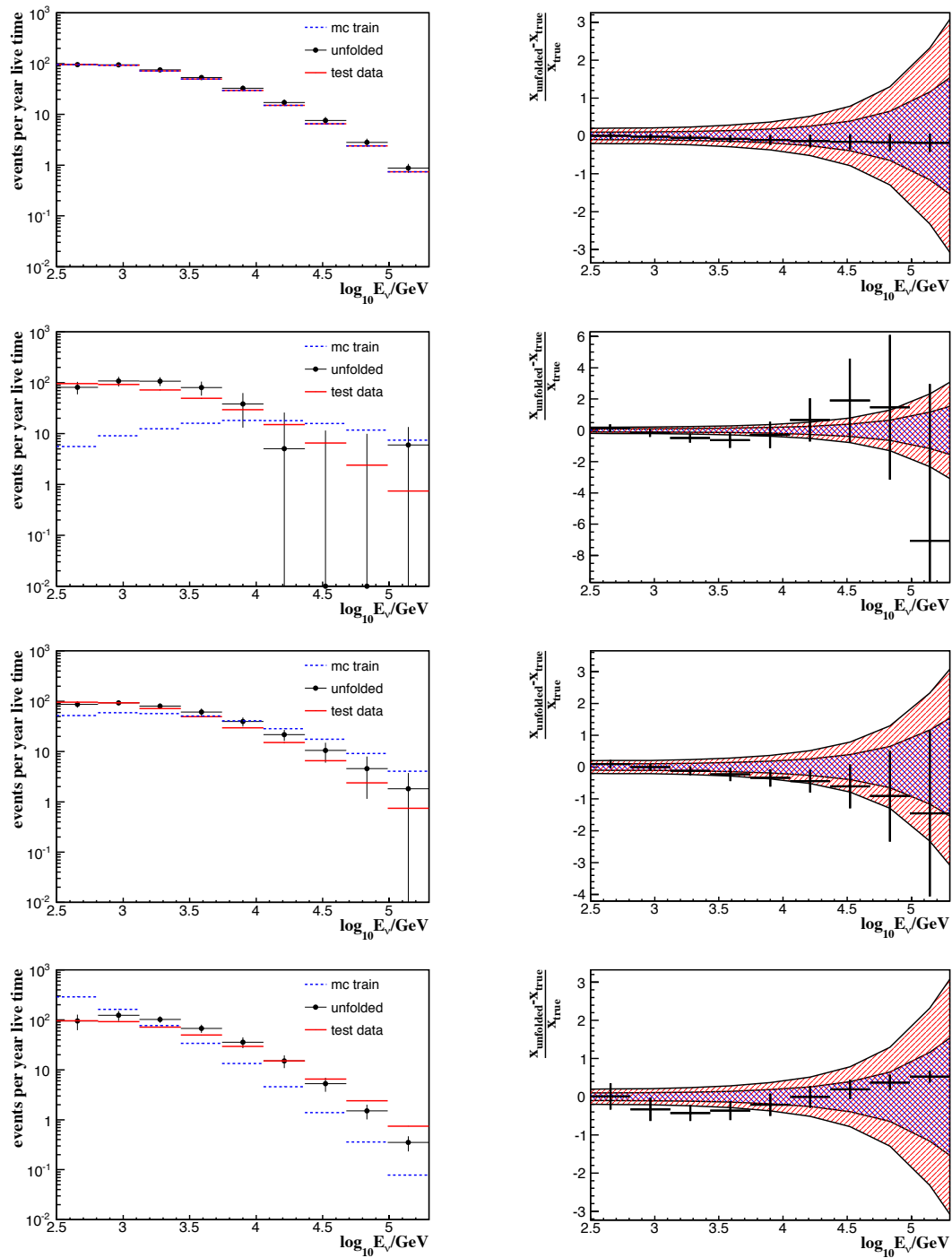


Figure 4.11: *Left column*: Unfolded test spectrum using the response matrices 0,1,2 and 3 (top to bottom). The spectra used for constructing the response matrices are shown for comparison. *Right column*: Difference between the test and unfolded distributions and the one and two sigma statistical errors on the true test flux.

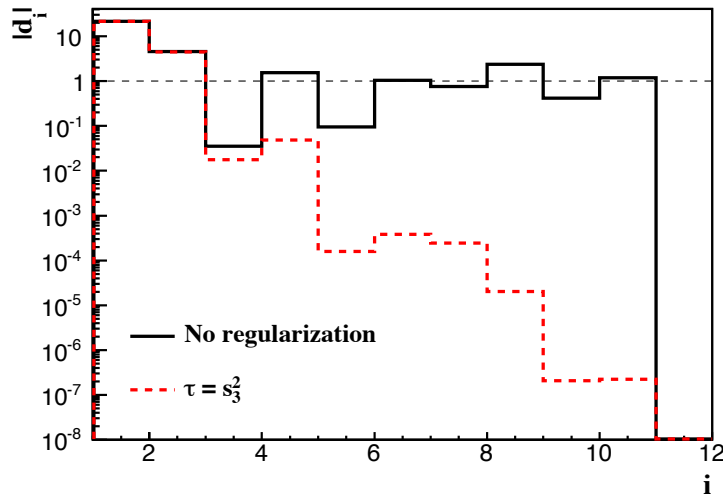


Figure 4.12: Distribution of expansion coefficients  $|d_i|$  for the 2nd flux. The coefficients drop in the first few bins and after the 3rd bin become stable and compatible with randomly distributed Gaussian variables with mean close to zero and variance equal to one. The choice of regularization parameter is  $\tau = s_3^2$ . The steadily decreasing line indicates the values of the coefficients in the solution expansion after the filtering that the regularization imposes.

$x^{ini}$  distributions. For  $\tau = s_1^2$  the filter cuts deeply into the first coefficient, effectively reducing even the most significant term in the solution expansion. This is the reason why the unfolded distribution is systematically much lower than the one used to train the kernel. It has the same shape as our initial assumption however, indicating a strong bias. The situation is more clear when  $\tau = s_2^2$ . Here, the most significant term in the solution expansion is kept while the rest of the terms are damped considerably, leading to a biased solution. As the regularization parameter  $\tau$  decreases (i.e. index  $i$  increases) more weight is placed on the measured data and more terms in the expansion are taken into account. This has the effect of revealing gradually the shape of the true underlying distribution. After a certain level ( $\tau = s_4^2$ ), more insignificant terms are taken into account in the solution expansion (4.2.12). They are enhanced by small singular values, resulting in the oscillatory patterns shown in all plots above this critical level. The difference between the test and unfolded distributions for all  $\tau$  is shown in figure 4.14. As we place more significance on less important coefficients in the solution by choosing a small  $\tau$ , we essentially numerically invert the response matrix. For  $\tau = 0$  the result will be the one shown in figure 4.3.

The unfolded spectrum's correlation and covariance matrices for the different regularization parameters are shown in figures 4.15 and 4.16 respectively. In these two figures the compromise between the size of the covariance matrix and the bias towards our expectation is clearly illustrated. For large values of the regularization parameter, the bin-to-bin correlations are very large. At the same time, the size of the covariance

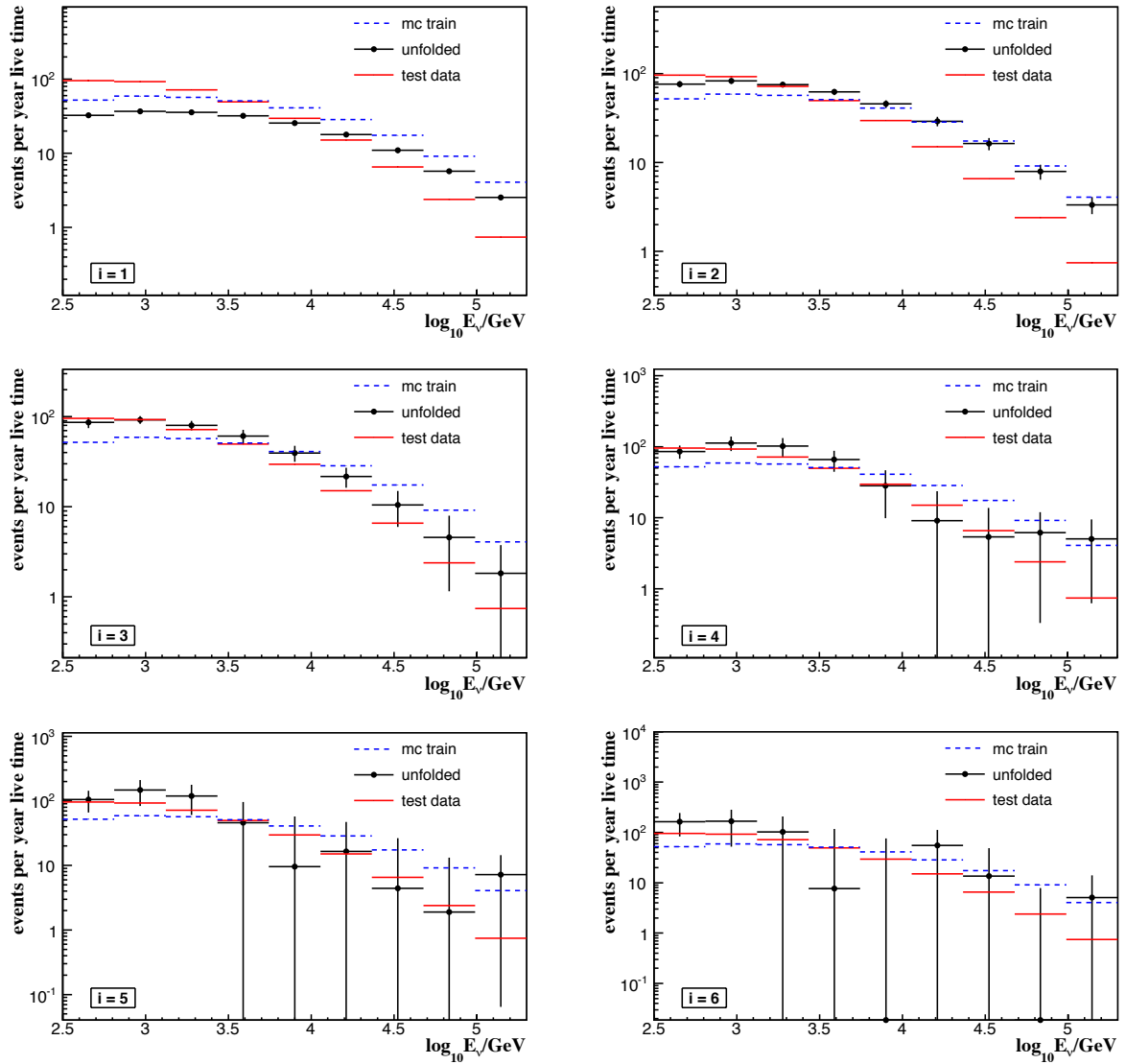


Figure 4.13: Unfolded spectrum for different choices of the regularization parameter. The value of  $\tau = s_i^2$  decreases in reading order. For the first few plots there is a strong bias towards the expected solution, while above the optimal value of  $\tau = s_3^2$  statistical fluctuations start dominating the result. The large errors that appear for lower values of  $\tau$  reflect the contamination from highly oscillatory terms in the solution expansion. This demonstrates the effect of propagating and enhancing statistical fluctuations from the data to the solution.

matrix is small and the errors on the unfolded solution reflect this fact. This is of course expected since the constraints that are imposed on the solution are rather strong. It is not allowed to vary outside certain limits. In our case this translates to a minimum curvature of the ratio between the solution and our assumption, i.e. the assumed spectrum

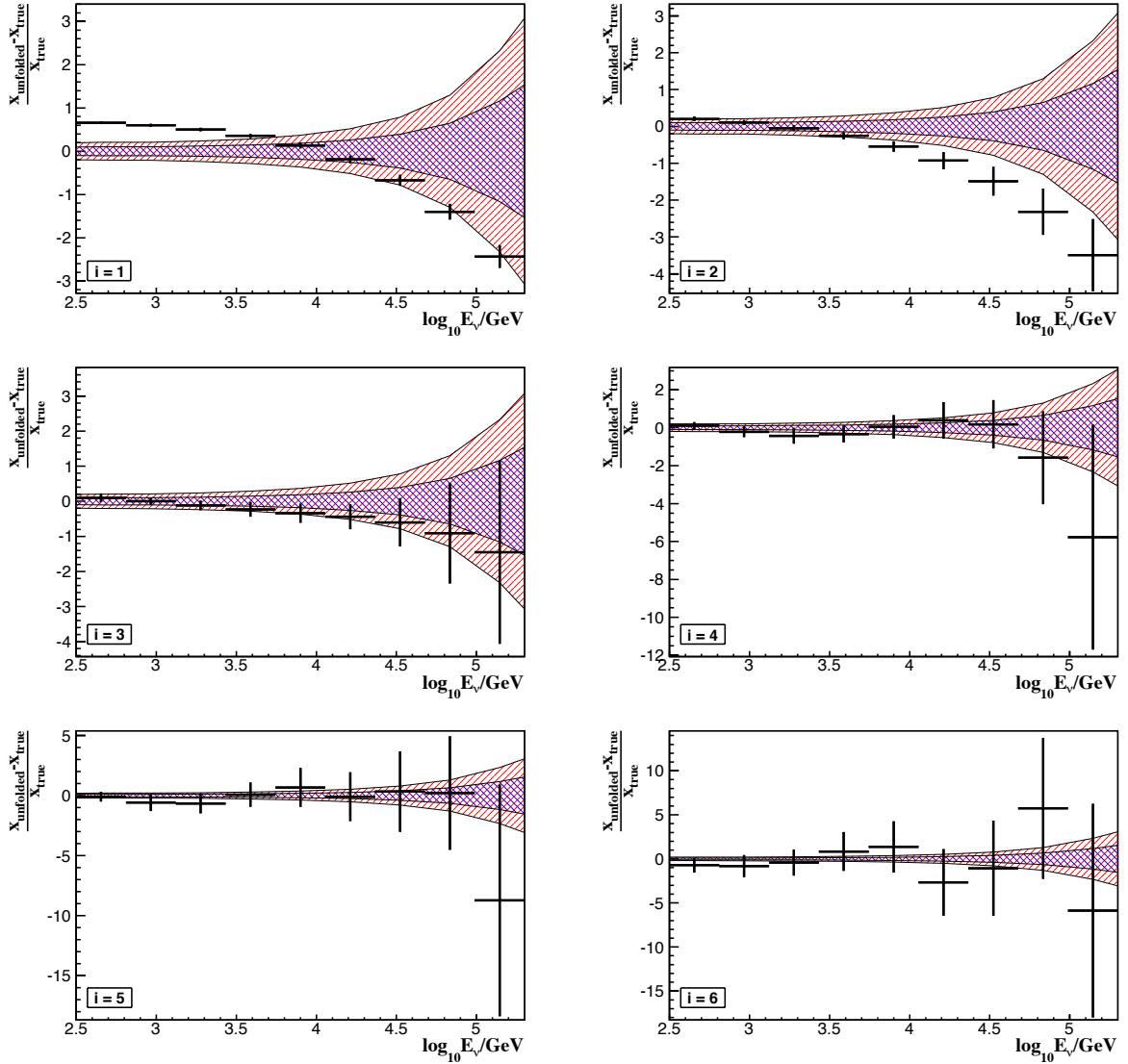


Figure 4.14: Differences between the unfolded and test distributions for different choices of the regularization parameter. The optimal value of the regularization parameter is found to be  $\tau = s_3^2$ . See text for explanation.

itself. On the other hand, smaller values of  $\tau$  tend to decrease the positive correlations but gradually introduce negative bin-to-bin correlations. These negative correlations, together with the fact that the size of the covariance increases rapidly lead to oscillatory solutions, dominated by statistical fluctuations from the data vector  $b$ . In conclusion, small values of  $\tau$  have a minor effect and there exist large negative correlations in the solution, while large values of  $\tau$  effectively reduce the number of degrees of freedom of the solution and are equivalent to having strong positive bin-to-bin correlations.

A final test is performed to examine whether the unfolded result depends on the

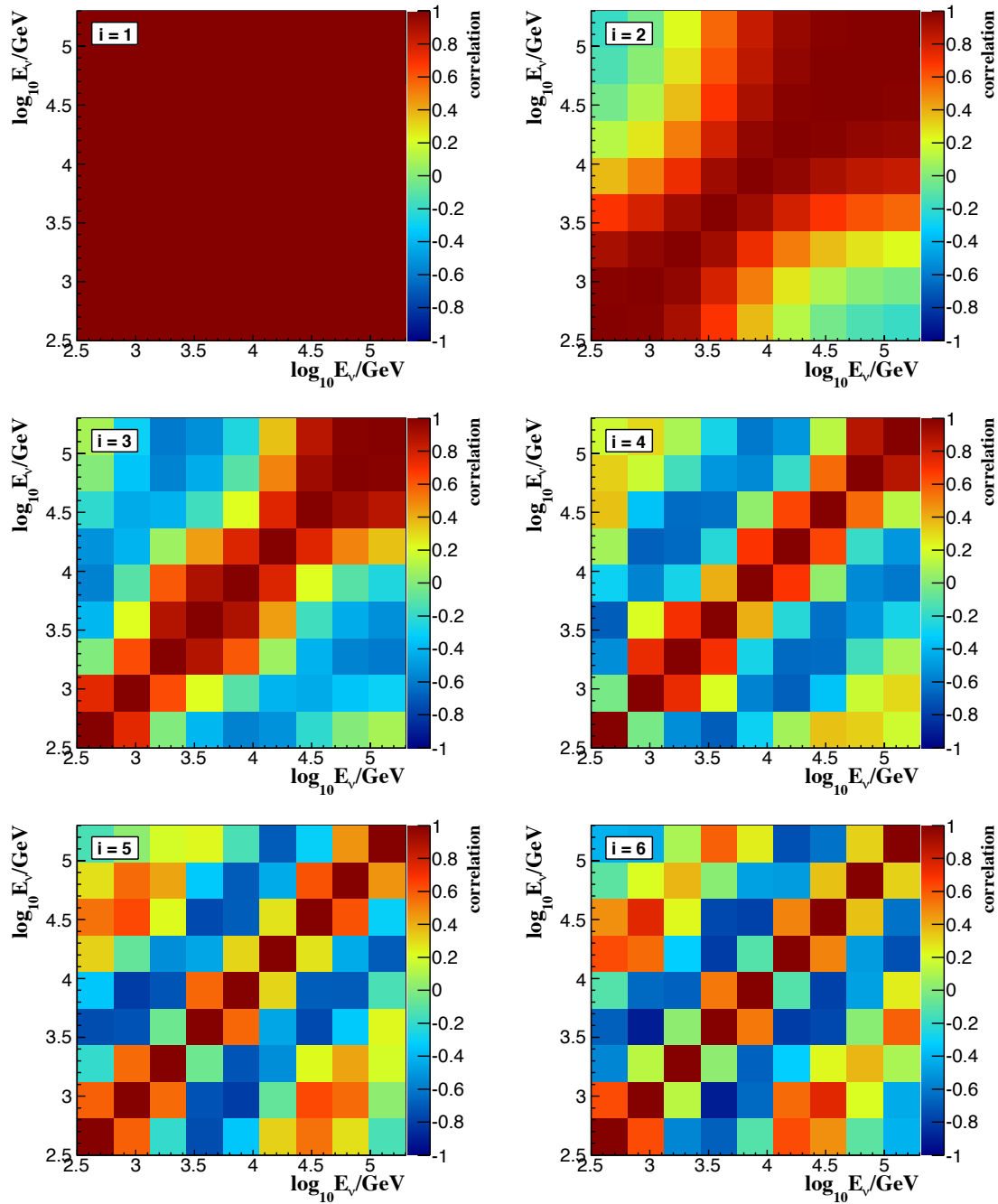


Figure 4.15: Correlation matrix of the unfolded neutrino spectrum for different choices of the regularization parameter. Large bin-to-bin correlations are present when  $\tau$  is large, reflecting the strong constraints that are imposed on the solution. The negative correlations that correspond to smaller values of  $\tau$  reflect the statistical fluctuations in the measured distribution. The optimal value of the regularization parameter is  $\tau = s_3^2$

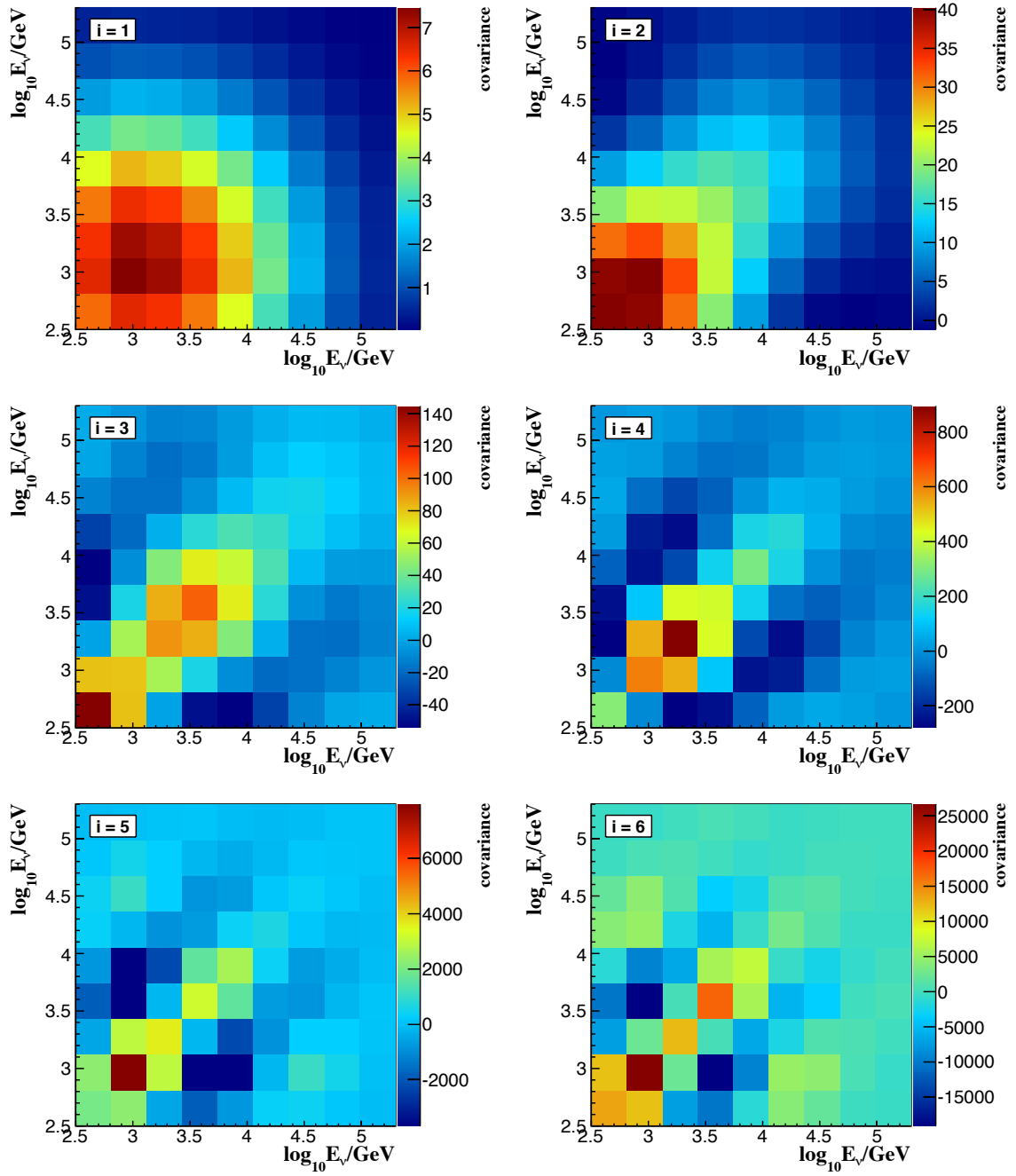


Figure 4.16: Covariance matrix for different choices of the regularization parameter. The size of the covariance matrix depends on the choice of regularization parameter. Small regularization results in large errors while strong regularization constrains the size of the matrix, introducing at the same time a bias to the solution. The optimal value of the regularization parameter is  $\tau = s_3^2$

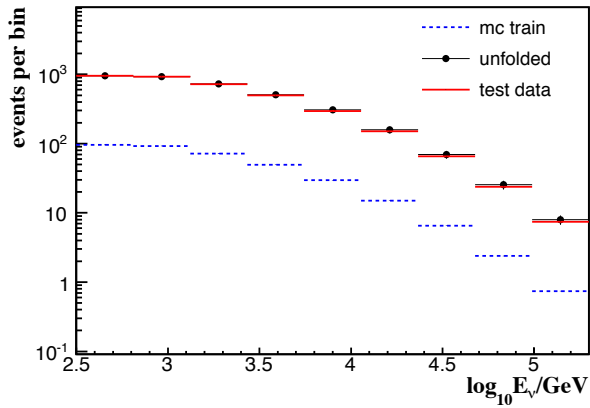


Figure 4.17: Unfolded neutrino spectrum at the detector level, where the hypothetical true flux is higher than the initial assumption by a factor of 10. The result coincides with the true spectrum and the unfolding method is not affected by differences in overall normalization.

absolute normalization between the spectrum used to construct the response matrix and the true spectrum. For this reason we unfold a hypothetical neutrino spectrum that is ten times higher than the expected one. *Flux 0* is used both for the construction of the response matrix and the generation of the test data. The result is shown in figure 4.17, where it is apparent that the overall normalization difference between the initial assumption and the true flux does not affect the final result.

## 4.5 Neutrino effective area

What we have hitherto tried to reconstruct is the neutrino energy spectrum in the vicinity of the detector. This distribution consists of neutrinos that have been triggered, reconstructed and passed the selection cuts. It is not however the atmospheric neutrino spectrum at the surface of the Earth, which is the goal of this measurement. The overall efficiency of the detector to the incoming neutrino flux has to be taken into account, as well as the fact that not all neutrinos will interact close enough to the detector, or even at all, in order to produce a detectable muon.

Calculating the neutrino effective area is the next step towards the determination of the atmospheric neutrino energy spectrum. The effective area is a measure of the experiment's overall efficiency. It is defined as the ratio of the rate of selected events over the total neutrino flux at the surface of the Earth,

$$A_{\text{eff},\nu}(E_\nu, \theta, \phi) \equiv \frac{R_{\text{det}}(E_\nu, \theta, \phi)}{\Phi_\nu(E_\nu, \theta, \phi)}. \quad (4.5.1)$$

The neutrino effective area depends on the event selection criteria. Assuming a flux of neutrinos  $\Phi$  before entering the Earth as shown in figure 4.18, the differential rate of detected events determined from Monte Carlo simulations is shown in figure 4.19.

This rate will naturally be different for different triggers as well as different quality selection criteria. The ratio of these two histograms gives the neutrino effective area, which is shown in figure 4.20. The neutrino effective area includes information about the neutrino survival probability while traversing the Earth, the neutrino-nucleon cross section, as well as the effect of the selection criteria to the detector performance. In

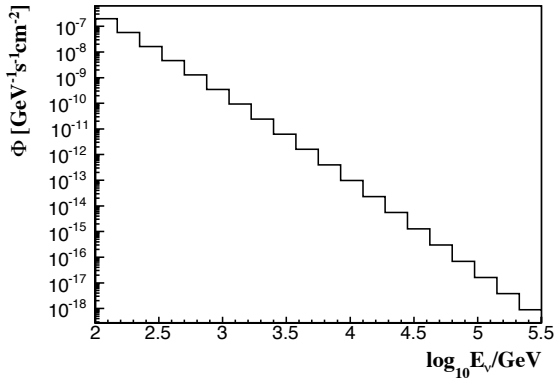


Figure 4.18: Atmospheric neutrino flux ([Hond 07; Mart 03]) at the surface of the Earth.

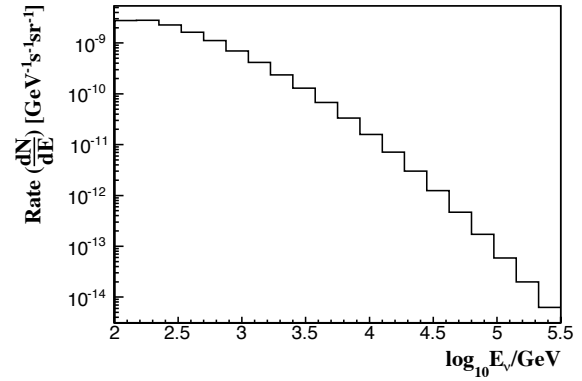


Figure 4.19: Rate of detected events after quality cuts assuming the flux of [Hond 07; Mart 03].

addition, it carries information about the detection efficiency of the detector, taking into account the size of the instrumented volume and the energy threshold. The number of events passing the final cuts is given by:

$$N_{events} = \int dt \int d\Omega \int dE \Phi_{\nu}(E_{\nu}, \theta, \phi) A_{eff,\nu}(E_{\nu}, \theta, \phi). \quad (4.5.2)$$

The neutrino effective area is essentially the geometrical area covered by a perfectly efficient detector, detecting the same number of events as the ANTARES detector.

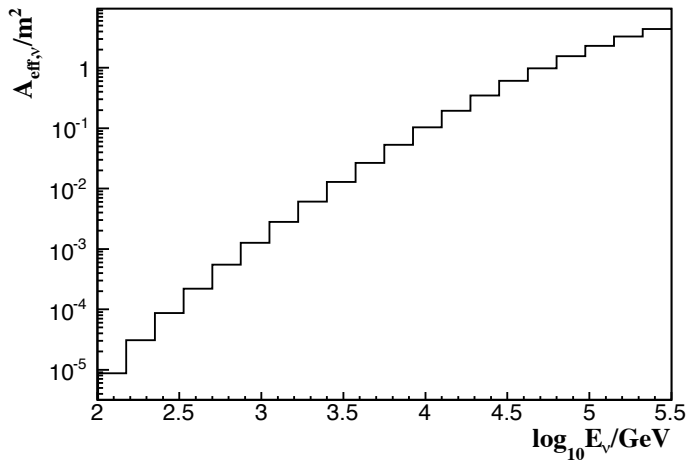


Figure 4.20: Effective area for neutrinos triggered with the 3N or T3 trigger, reconstructed as upward-going with  $\Lambda > -4.8$  and  $\hat{\beta} < 1^\circ$ .

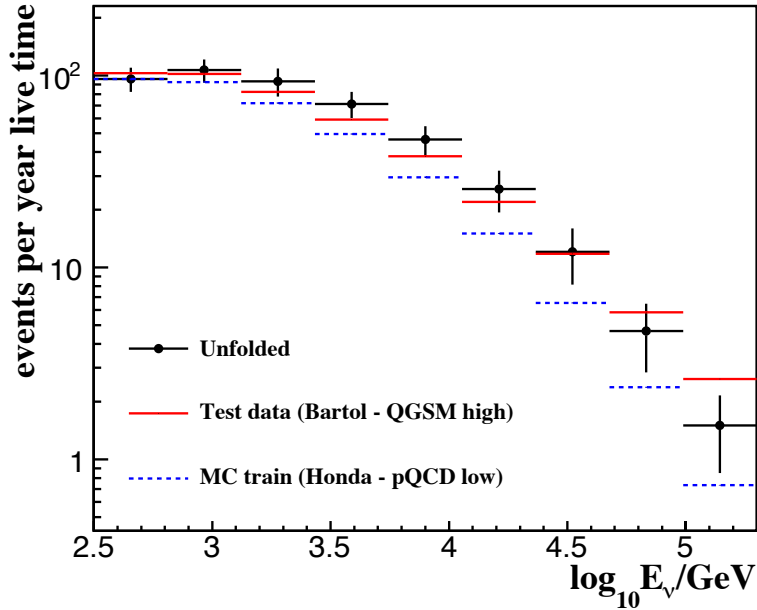


Figure 4.21: Unfolded neutrino spectrum at the detector level. The response matrix was constructed using the fluxes from Honda *et al.* [Hond 07] with a prompt contribution corresponding to the low pQCD flux from Costa [Cost 01], while the test flux that we attempt to reconstruct is taken from Barr *et al.* [Barr 04] with a high QGSM prompt contribution [Cost 01].

## 4.6 Atmospheric neutrino energy spectrum

In the example that follows we use the flux by Honda *et al.* [Hond 07] and with the lowest prompt contribution from Costa [Cost 01] to train the response matrix. We will attempt to reconstruct the atmospheric neutrino flux, generating the test data using the predictions by Barr *et al.* [Barr 04] and the high QGSM contribution calculated by Costa [Cost 01]. The neutrino flux at the detector level for both the initial assumption and the test data are shown in figure 4.21, together with the unfolded neutrino energy spectrum at the detector level. After calculating the effective area of the detector, which does not depend on the flux used to calculate it, the determination of the atmospheric neutrino energy spectrum at the surface of the Earth is a straightforward step. Dividing the unfolded neutrino energy spectrum by the neutrino effective area leads to the final atmospheric neutrino flux shown in figure 4.23. The underestimation at the last bin can be attributed to the limited statistics at the edge of the energy spectrum. In this case, the unfolding works as an extrapolation, something that can be seen from the correlation matrix in figure 4.22 too. There are strong correlations present between the last few bins and the fit is essentially pulled towards the initial assumption.

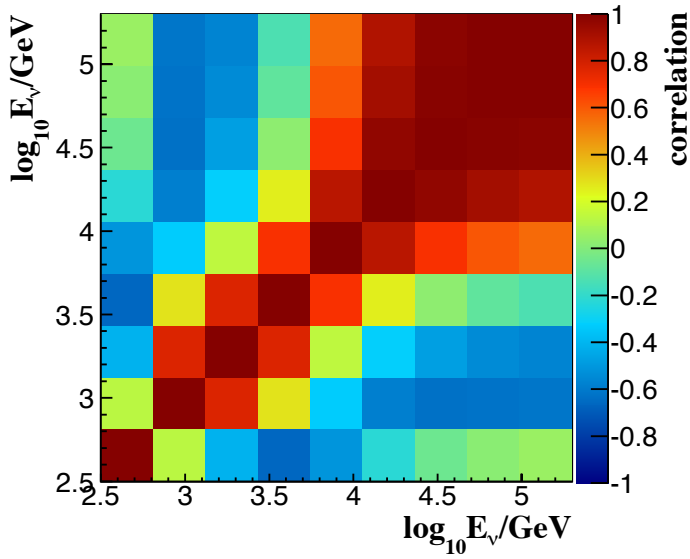


Figure 4.22: Correlation matrix of the unfolded neutrino spectrum at the detector level.

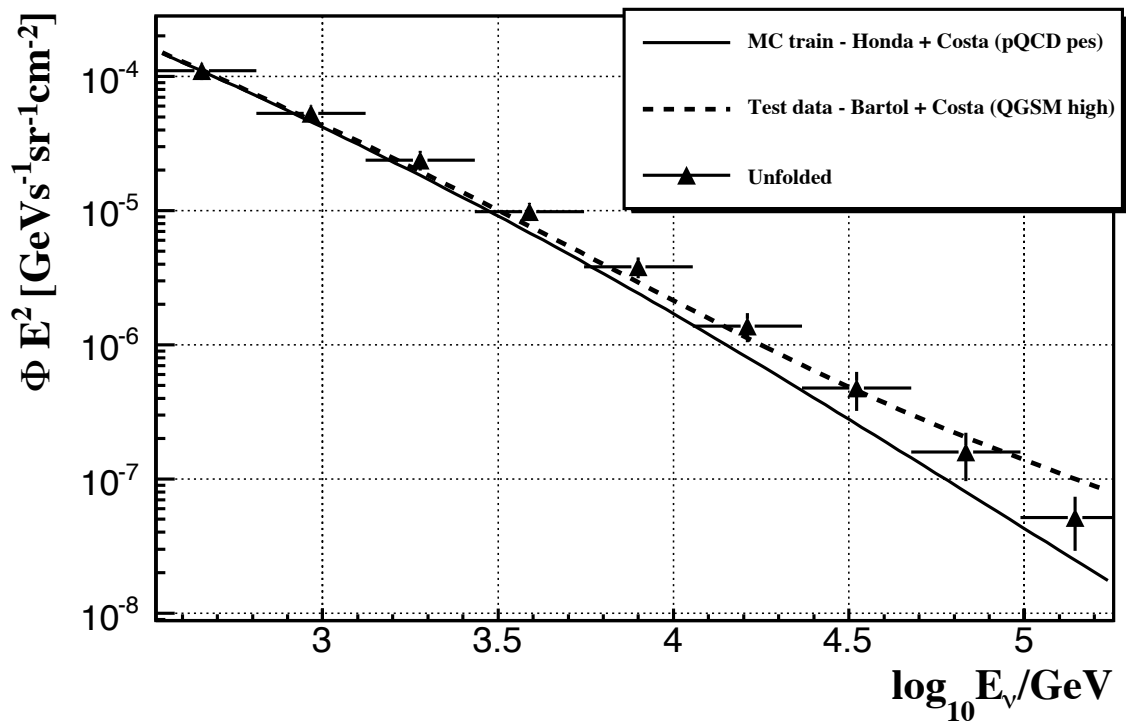


Figure 4.23: Unfolded atmospheric neutrino energy spectrum in units of  $\text{GeV s}^{-1} \text{sr}^{-1} \text{cm}^{-2}$ . The solid line is the initial assumption used to train the response matrix. The dotted line is the true Monte Carlo spectrum used to test the method.

## 4.7 Systematic Uncertainties

A study of systematic uncertainties in the detector, relevant for the present analysis, is presented in this section. The effects that we examine are related to the absorption length of the medium and the angular acceptance and efficiency of the optical modules. The quantification of the impact of these effects is necessary in order to take them into account as systematic errors in the final measurement of the neutrino spectrum.

For each effect under study we use two different Monte Carlo samples, exhibiting two extreme cases on the values or behavior of the related parameter. Let us call the two samples  $MC_1$  and  $MC_2$ . We use the first sample  $MC_1$  to train the response matrix and the second sample  $MC_2$  as the true distribution in order to simulate the test data. After reconstructing the energy, we perform the unfolding to obtain the distribution  $MC'_2$ , in general different from the true  $MC_2$ . This is of course due to faulty assumptions on the construction of the response matrix. We quote the deviation of the result  $MC'_2$  from the true spectrum  $MC_2$  as the systematic uncertainty,

$$\text{Uncertainty}[\%] = \frac{MC_2 - MC'_2}{MC'_2} \times 100. \quad (4.7.1)$$

The regularization parameter we chose is  $\tau = s_2^2$  and the underlying physical spectra are based on the calculations by Honda *et al.* and Martin *et al.*. No statistical fluctuations are applied in the pseudo data for this study.

The first effect we study is the combined effect of angular acceptance of the optical modules and the absorption length of light in water. The sample  $MC_1$  uses the angular acceptance labeled *dic08* [Angh 08] and a maximum absorption length of 55 m at 470 nm. The second sample  $MC_2$  which is used to generate the pseudo data uses a more recent and wider angular acceptance parametrization labeled *jun09* and an absorption length with a maximum of 63 m at 470 nm. The only difference between the two assumptions for the absorption length is a scale factor, scaling the curve of figure 2.10 down in order to have a maximum of 55 m. Figure 4.24 shows the difference between the reconstructed energy distributions for the two different Monte Carlo simulations. The distribution that corresponds to a shorter absorption length appears shifted towards lower energies. This can be understood as follows. A muon with a certain fixed energy

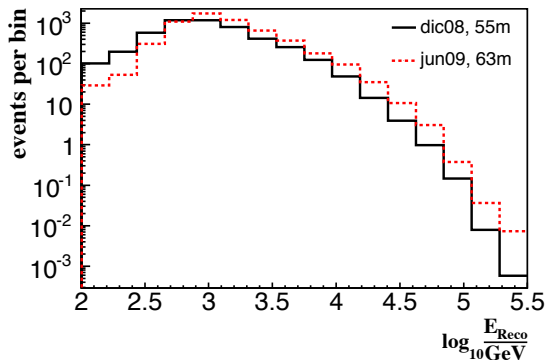


Figure 4.24: Distribution of the reconstructed energies before unfolding for two Monte Carlo samples with different angular acceptance parametrization for the OM's and different light absorption length in water.

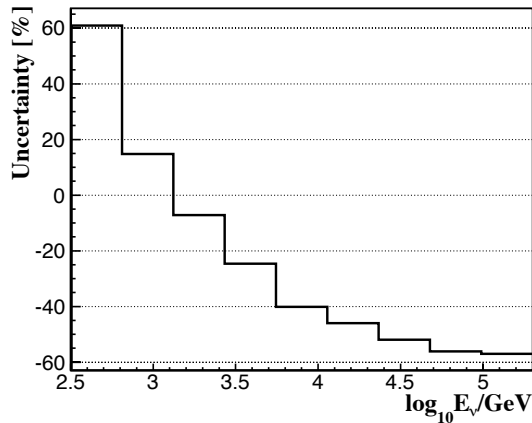


Figure 4.25: Uncertainty on the unfolded result due to uncertainties in the absorption length of light in water and the angular acceptance of the optical modules.

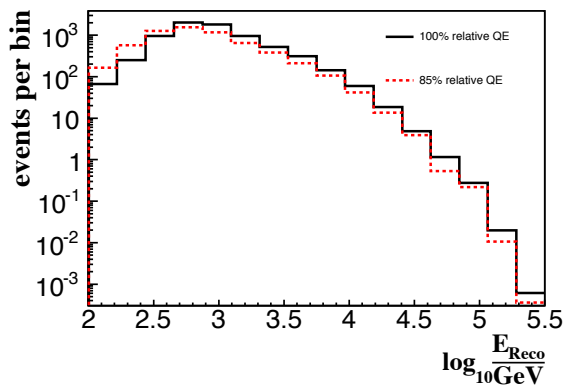


Figure 4.26: Reconstructed energy distributions for two Monte Carlo samples with different relative optical module efficiency.

will give less light in the OM's when the assumed absorption length is shorter. Therefore the reconstructed spectrum will be depleted of higher energy entries and exhibit an abundance at lower energies. After unfolding, we observe a tendency to underestimate at lower energies and overestimate gradually above 1 TeV as shown in figure 4.25, which shows the error in percentage that needs to be applied to the unfolded result.

Another source of uncertainty is the relative OM efficiency. A lower OM efficiency than what is obtained in calibration can have a large effect on the event rates and energy distribution. The actual efficiency is not expected to be lower than 85% of the expected one therefore we use this value as the lower limit [Boga 11]. As before, a Monte Carlo sample  $MC_2$  is used to train the response matrix and represents our original assumptions, i.e. 100% relative efficiency. A second Monte Carlo with a reduced OM efficiency by 15% is used to generate the pseudo data, representing the true spectrum we are measuring. The reduction in the efficiency is applied at the trigger level and it affects the number of triggered as well as reconstructed events. The distributions of the reconstructed energy before unfolding the two Monte Carlo samples is shown in figure 4.26. As expected, when one overestimates the efficiency of the modules and consequently the amount of light that is detected, the expected distribution is shifted towards higher energies, appearing more rich in high energies than what it is in reality. Figure 4.27 shows the uncertainty on the unfolded result due to a possible reduced OM efficiency up to 15%.

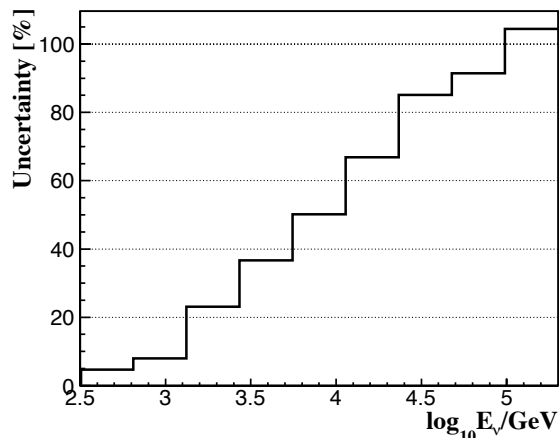


Figure 4.27: Uncertainty on the unfolded result as a function of neutrino energy for two different assumptions on the relative OM efficiency.

## 4.8 Conclusions and outlook

In the present chapter we have described the problems arising by linear inverse problems, characterized by an ill-conditioned kernel. Various methods have been developed in the literature for solving these classes of problems. The approach taken here is based on a regularized unfolding using a singular value decomposition of the response matrix. The method performs well and is reasonably stable under different assumptions on the shape of the underlying neutrino energy distribution. An important remark to make here, is the fact that this method is driven to a large extent by the available statistics. Fine details in the tail of the distribution, where statistics due to the very steeply falling spectrum of atmospheric neutrinos are limited, are difficult to reconstruct. A more diagonal response matrix, providing us with a better energy resolution or a better background discrimination leading to higher statistics of the final neutrino sample can improve the situation. However, when the expected rates on the detector between two different fluxes are close and especially within the statistical uncertainties of each other, unfolding cannot help and more statistics is the only solution. A larger detector with higher rates and thus higher effective area will lead to a better measurement.

# EVENT SELECTION

The present chapter contains information about data selection, the background rejection of atmospheric muons and the event selection criteria applied to define the final data sample. The vast majority of events detected in ANTARES are due to downward-going atmospheric muons that dominate over the incoming neutrino flux by many orders of magnitude. As we will see in the following sections, rejecting the events arriving above the horizon is not enough to purify the final sample and additional selection criteria need to be introduced. Section 5.1 contains the description of the selection of runs for this analysis, taking into account various characteristics of the data taking conditions. In section 5.2 we discuss the atmospheric muon background and define the cuts used in this analysis. Sections 5.3 and 5.4 contain a series of comparisons between data and Monte Carlo which allow for an evaluation of our understanding of the detector and the physical processes that take place.

## 5.1 Data selection

The data used for this analysis were collected during the period May 2008 to December 2010 with a 12-line detector configuration. The run numbers and the corresponding data taking periods are shown in table 5.1.

There are various quantities that characterize the quality of the data taking conditions, such as the percentage of active optical modules during a run or the hit rates. The baseline of a run is defined as the mean of a gaussian fit on the L0 rate of each PMT, averaged over all PMTs. The percentage of *TimeSlices* where the rate was higher than the baseline plus 20% is averaged over all PMTs to give the burst fraction. The mean rate is the average rate over all ARS's that measured more than 10 kHz. Quality Basic (QB) is a flag that characterizes the quality of the data taking conditions, based on optical background and detector state information. It is defined as follows:

- QB = 1 : Basic selection of runs available for physics analyses.
- QB = 2 : At least 80% of the OMs that are expected to work are active.

Run number	Data taking period
034419 - 035878	May - September 2008
035880 - 038230	October - December 2008
038233 - 039775	January - March 2009
040098 - 041626	April - June 2009
041628 - 043534	July - September 2009
043540 - 045536	October - December 2009
045540 - 047694	January - March 2010
047706 - 049766	April - June 2010
049770 - 052305	July - September 2010
052307 - 054250	October - December 2010

Table 5.1: Data taking periods in groups of three months and the corresponding run numbers. The physics runs are not consecutive since calibration and acoustic data taking runs are excluded.

- QB = 3 : Baseline  $\leq$  120 kHz and burst fraction  $\leq$  0.4.
- QB = 4 : Baseline  $\leq$  120 kHz and burst fraction  $\leq$  0.2.

These run sets are cumulative, i.e. runs that satisfy QB=3, satisfy QB=2 as well. All runs from the database with QB  $\geq$  1 are chosen for the final data sample. Additionally, calibration runs and runs that were used for tests or high voltage tunings, as well as runs where both T3 and 3N triggers were absent are excluded from the analysis. In rare occasions electrical breakdowns can occur in the PMT's causing them to spark, producing a signal similar to a hadronic or electromagnetic shower. Runs where such "sparking events" were identified are also excluded. Only runs that are longer than 5 minutes and contain more than one hundred events are kept. The final data sample consists of 5037 runs corresponding to 517.8 days of live time. After the application of all quality cuts, described in the following sections, 831 neutrino events were found. For the energy reconstruction of each event, only working optical modules were considered, while OM's with unusually high or low rates were excluded from the fit.

Distributions of the baseline, burst fraction, mean number of active OM's and mean rates for the final run selection are plotted against run number in figure 5.1. The trend observed on the mean number of active optical modules is due to the fact that some lines were not operational for certain periods of time as discussed in section 2.9. The hit rates remain stable and at a low level (less than 80-90 kHz for the baseline) for most of the used runs, with some short periods of increased optical background activity. Around 33% of the runs used have a burst fraction higher than 0.4, 81% of which have less than 80% of the expected active OMs actually operational.

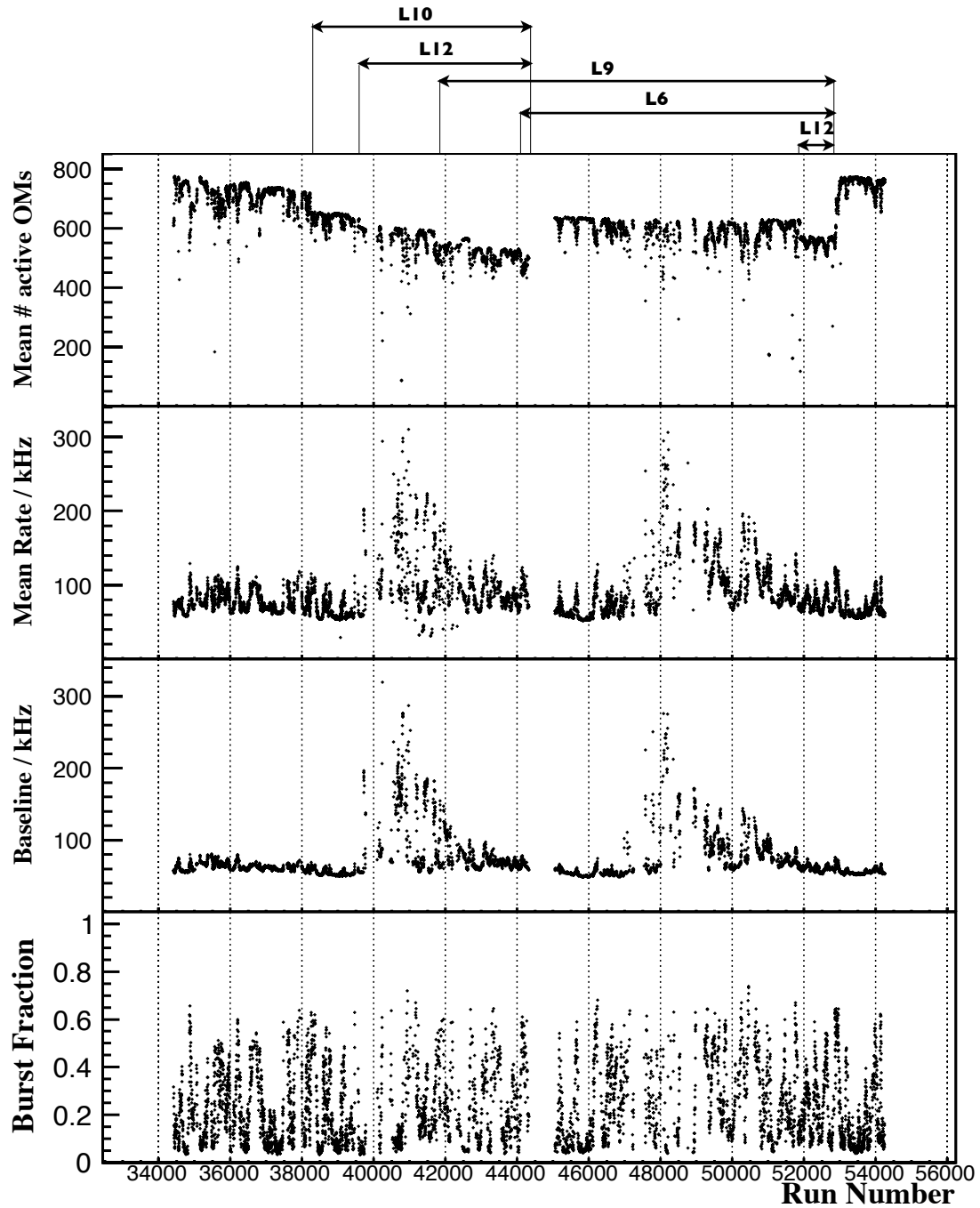


Figure 5.1: The mean number of active OMs, the mean rates and the baseline rate in kHz, and the burst fraction for all the runs of the period May 2008 to December 2010 that are used in this analysis. On top of the figure the periods where certain lines were not operational are indicated. These are responsible for the drops and rises on the number of active OMs.

## 5.2 Atmospheric muon background rejection

The goal of the event selection is to obtain a neutrino candidate sample with the following characteristics:

- well reconstructed tracks
- high purity sample of neutrino events i.e. low atmospheric muon contamination and
- as large an efficiency as possible in order to keep statistics high.

### 5.2.1 Atmospheric muon background

The atmospheric muon flux is the dominant background in the search for neutrino candidate events as shown in figure 5.2. The rates that correspond to atmospheric muons

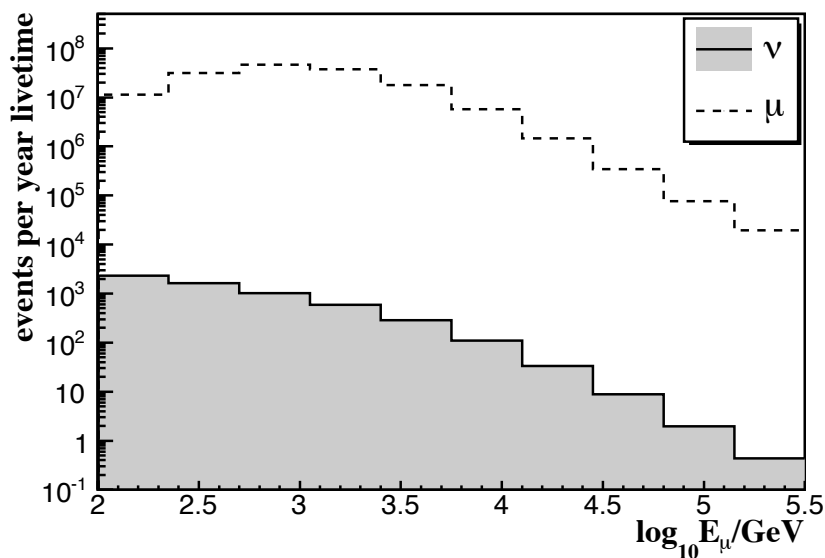


Figure 5.2: Simulated atmospheric muon ( $\mu^{\pm}$ ) and neutrino ( $\nu_{\mu} + \bar{\nu}_{\mu}$ ) induced muon events per year livetime at the detector level. No cuts are applied. The atmospheric muon background dominates the neutrino flux, being around four orders of magnitude higher. The energy range shown here is from  $10^2$  GeV to  $10^{5.5}$  GeV, divided in 10 bins.

lie  $\sim 4$  orders of magnitude above the neutrino rates. The first step towards the reduction of this background is to reject all events that are reconstructed as downward-going. Atmospheric muons that are created in the atmosphere above the horizon will reach the detector, leading to a downward-going event signature. On the other hand, atmospheric muons created below the horizon, that should give an upward-going event signature, will never be able to traverse the Earth and reach the detector. This directional selection decreases the rates of atmospheric muons by an order of magnitude, as shown in

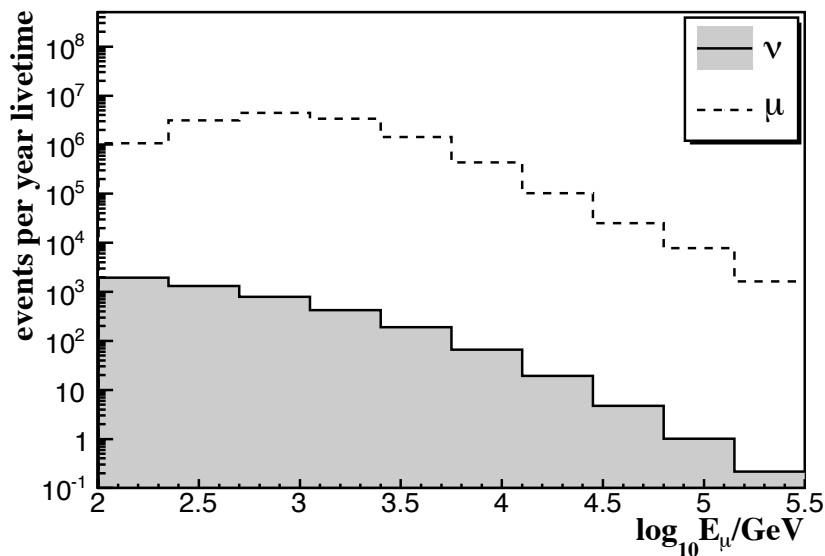


Figure 5.3: Simulated atmospheric muon ( $\mu^\pm$ ) and neutrino ( $\nu_\mu + \bar{\nu}_\mu$ ) induced muon events per year livetime at the detector level. Events reconstructed as downward-going are rejected. No additional quality cuts are performed. The muon background is still higher than the muon neutrino rates due to mis-reconstructed atmospheric muon contamination. The energy range shown here is from  $10^2$  GeV to  $10^{5.5}$  GeV, divided in 10 bins.

figure 5.3 where only upward-going events are shown. This step is clearly not sufficient for the complete suppression of the muon background, since the muon rates are still a few orders of magnitude above the neutrino flux. The reason for this is that many atmospheric muon events are mis-reconstructed as upward-going, thus faking neutrino events. In order to reject these muon events, we need to examine the quality of the track fit in more detail.

The left and right plots of figure 5.4 show the relation between the reconstructed zenith angle and the track reconstruction quality parameter  $\Lambda$  for atmospheric muons and neutrinos respectively. Most of the atmospheric muon events belong to the upper half of the left plot in figure 5.4, corresponding to downward-going events. The ones that have been reconstructed as upward-going (lower half) tend to have lower values of  $\Lambda$  as well. This is expected since we have seen that lower values of  $\Lambda$  correspond to less well-reconstructed tracks. Upward-going neutrinos on the other hand, can take higher  $\Lambda$  values, indicating well-reconstructed tracks. Figure 5.5 illustrates what this situation looks like for real data. Both muon and neutrino events populate this plot. A cut rejecting all downward-going events suppresses a large fraction of the atmospheric muon flux. An additional  $\Lambda$  cut rejects the rest of the atmospheric muon contamination, leaving the well-reconstructed upward-going neutrinos still in the sample. Finally, a cut on the estimated angular error from the track reconstruction algorithm is applied, in order to keep well-reconstructed events with small uncertainty in their direction. This

is relevant for the reconstruction of the energy, where well-reconstructed tracks provide the best results.

The cumulative distribution of the  $\Lambda$  value for simulated muon and neutrino events reconstructed as upward-going is shown in figure 5.6. Due to low statistics on the simulation of atmospheric muons, there are very few entries for high  $\Lambda$  values (see section 3.2). In order to circumvent this problem and determine the most appropriate cut at  $\Lambda$  successfully, we fit the tail of the  $\Lambda$  cumulative distribution for muons with an exponential function, indicated in the figure with a dashed line. A cut at  $\Lambda = -4.8$  suppresses the atmospheric muon background contamination to less than one percent.

## 5.2.2 Selection criteria

We summarize here the cuts used, in this analysis, to reject the atmospheric muon background and select the most well-reconstructed events. The selection criteria chosen are the following:

- The event must be reconstructed as upward-going, i.e.  $\cos \theta_{rec} < 0^\circ$ .
- The value of  $\Lambda$  must be larger than  $-4.8$ .
- The angular error estimate  $\hat{\beta}$  from the track fit must be smaller than one degree.

After applying these selection criteria to the data sample and comparing it to the Monte Carlo distribution we find an overall normalization difference of 22%. Figure 5.7 shows the distribution of the cosine of the reconstructed zenith angle for data and Monte Carlo for the whole period of 517.8 days. The neutrino simulation is lower by 22% as indicated by the linear fit on the ratio of data over Monte Carlo shown in figure 5.8. This is within the theoretical normalization uncertainties of the level of 30%. For

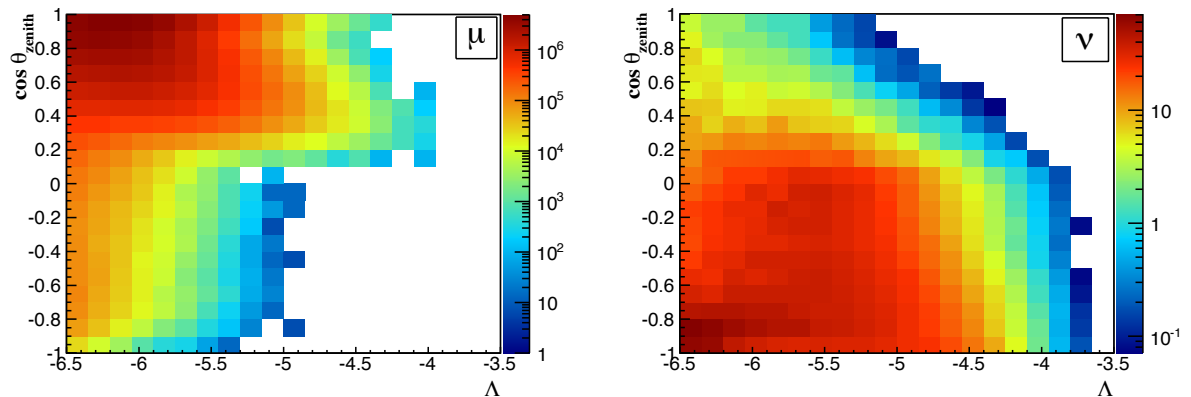


Figure 5.4: Zenith angle of the reconstructed track as a function of  $\Lambda$ . The z-axis stands for the number of events per bin. The left plot corresponds to the atmospheric muon background and the right one to the atmospheric neutrinos. The entries are normalized to one year livetime.

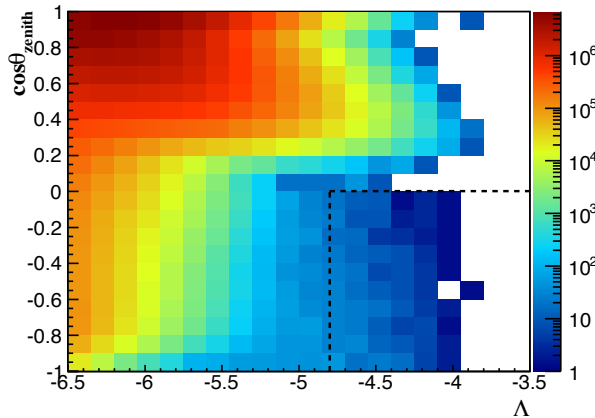


Figure 5.5: Zenith angle of the reconstructed track as a function of  $\Lambda$  for one year of data. The z-axis stands for the number of events per bin. This plot contains atmospheric muon as well as neutrino events. Events with  $\cos\theta_{\text{zenith}} < 0$  and  $\Lambda > -4.8$  are kept.

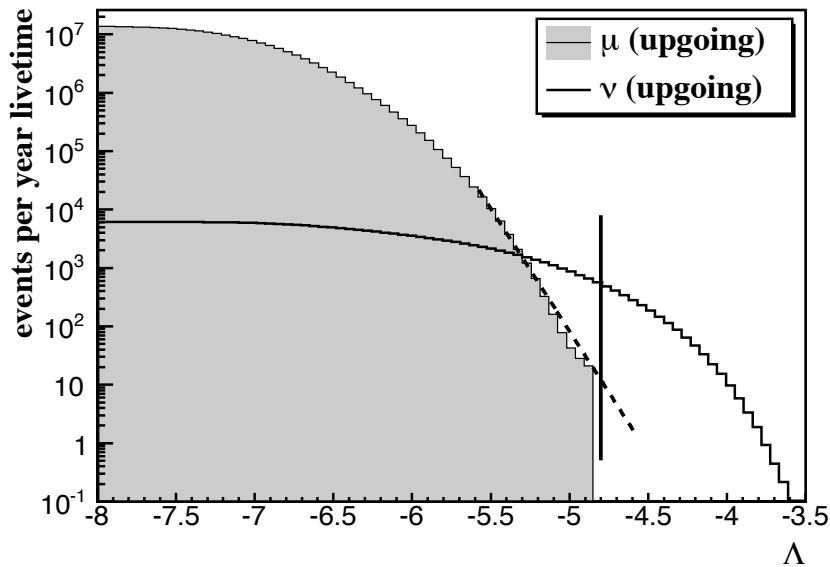


Figure 5.6: Cumulative distribution of the track fit quality parameter  $\Lambda$  for atmospheric muons ( $\mu^\pm$ ) and neutrinos ( $\nu_\mu + \bar{\nu}_\mu$ ). The dashed line indicates the exponential fit used to estimate the muon contribution at higher  $\Lambda$  values (see text) and the straight vertical line denotes the value of the cut.

the remainder of this work, the neutrino Monte Carlo is scaled up to match the data. Such an overall normalization will not affect the unfolded result, as discussed in section 4.4.

Let us now consider the efficiency of the aforementioned selection criteria and the purity of the selected sample. The efficiency of a selection process is defined as the fraction of the size of the selected sample corresponding to the signal after the cuts, over the size of the initial signal sample before any cuts:

$$\text{Efficiency} = \frac{N_{\text{cut}}^{\text{signal}}}{N_{\text{all}}^{\text{signal}}}. \quad (5.2.1)$$

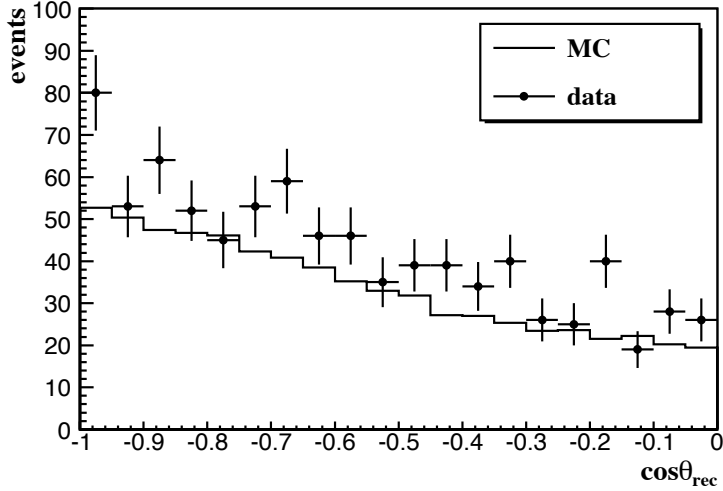


Figure 5.7: Distribution of the cosine of the reconstructed zenith angle after quality cuts for data and Monte Carlo corresponding to 517.8 days of livetime.

For the purposes of this analysis, all neutrinos are considered to be our signal while atmospheric muons constitute our background. The purity of a selected sample is defined as the ratio of the selected sample size corresponding to the signal over the size of the selected sample, counting both signal and background:

$$\text{Purity} = \frac{N_{\text{cut}}^{\text{signal}}}{N_{\text{cut}}^{\text{signal}} + N_{\text{cut}}^{\text{background}}}. \quad (5.2.2)$$

The atmospheric muon and neutrino simulation rates per year, as well as the corresponding rate calculated from data are shown in table 5.2. The last two columns give the efficiency and purity levels. Sample I refers to the initial sample of all reconstructed tracks. Sample II is the resulting sample after rejecting the downward-going tracks, suppressing the atmospheric muon background by around an order of magnitude. After the  $\Lambda$  and  $\beta$  cuts, we obtain sample III, where the atmospheric muon flux is almost completely suppressed, leading to a pure neutrino sample. The last sample contains only those events whose energy was reconstructed. This final selection has practically no effect at such an advanced stage of the selection process. This was anticipated already due to the high efficiency of the energy reconstruction algorithm (see figure 3.29).

### 5.3 Data - Monte Carlo comparisons

In order to verify that the detector and the physics that govern the experiment are well understood it is necessary to perform a series of comparisons between data and Monte Carlo. In what follows, the atmospheric neutrino flux by Honda and Martin *et. al* is used to provide the Monte Carlo distributions normalized for the data livetime of 517.8 days and multiplied by a scale factor of 1.22 as discussed in section 5.2.2.

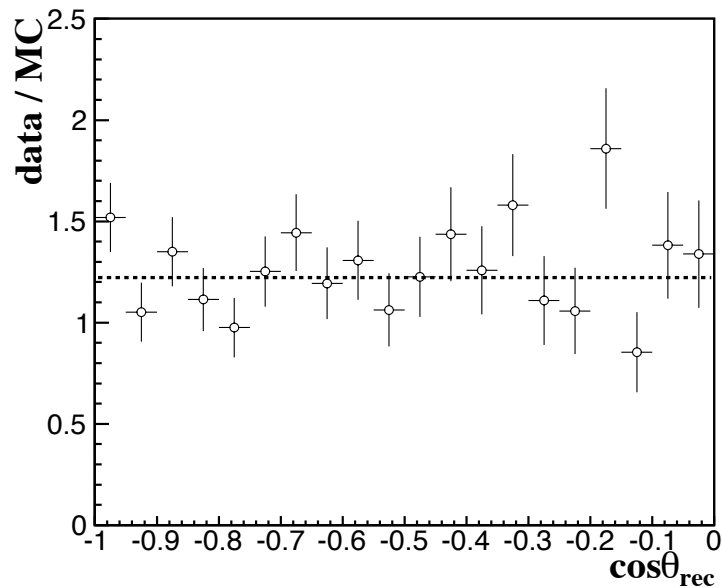


Figure 5.8: Distribution of the ratio of data over Monte Carlo for the cosine of the reconstructed zenith angle. A linear fit indicates an overall normalization difference of 22%.

We begin the examination of the data and Monte Carlo distributions by looking at the angular information provided by the track reconstruction. The zenith and azimuthal distributions before the selection process and after the application of all quality cuts are shown in figures 5.9 and 5.10 respectively.

The applied cuts completely suppress the atmospheric muon flux, visible in both figures on the right, where only atmospheric neutrino events remain. The flatness of the azimuthal distribution reflects the symmetry of the neutrino flux for this angle.

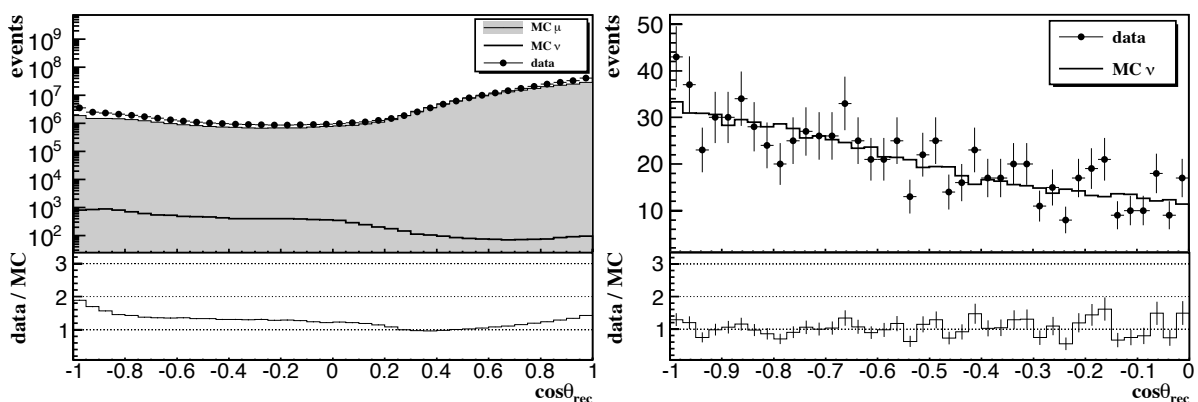


Figure 5.9: Zenith angle of the reconstructed track for data and Monte Carlo. A cosine of -1 corresponds to tracks traveling vertically upward. The left plot includes all events. Events after selection are shown on the right plot.

Sample	$\mu^\pm$ (yr $^{-1}$ )	$\nu_\mu + \bar{\nu}_\mu$ (yr $^{-1}$ )	data (yr $^{-1}$ )	efficiency	purity
I	$1.53 \times 10^8$	9413.69	$1.88 \times 10^8$	1	$6.17 \times 10^{-5}$
II	$1.41 \times 10^7$	7577.34	$2.03 \times 10^7$	0.8	$5.37 \times 10^{-4}$
III	0	580.434	598.473	0.06	$\sim 1$
IV	0	571.703	585.784	0.06	$\sim 1$

Table 5.2: Atmospheric muon and neutrino rates per year, for different samples. The efficiency and purity of the selection is also shown in the last columns. Samples correspond to all reconstructed tracks (sample I), tracks reconstructed as upward-going (sample II), events after the  $\Lambda$  and  $\hat{\beta}$  cuts (sample III) and events where the energy reconstruction algorithm succeeded in finding a most probable energy (sample IV).

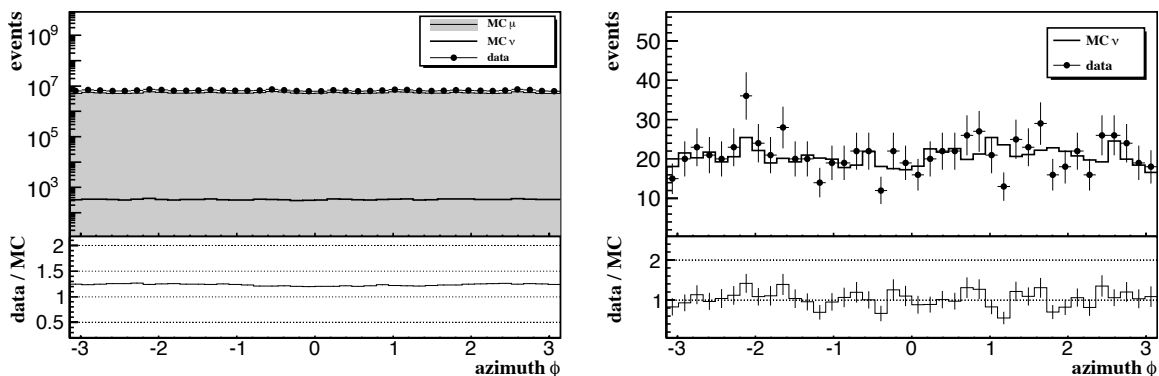


Figure 5.10: Reconstructed azimuthal distribution for atmospheric muons, neutrinos and data. The left plot shows all events while the right plot contains all the events that belong to the sample after quality cuts.

The situation is different for the zenith distribution which drops as we approach the horizontal direction. This is due to the different path length neutrinos have to travel as they traverse the Earth. Vertically upward neutrinos have a higher probability of interacting in rock and producing a detectable muon, whereas for horizontal neutrinos this probability is lower. The distribution of the track fit quality parameter  $\Lambda$  as well as its cumulative distribution for data and Monte Carlo are shown in figure 5.11. Only tracks reconstructed as upward-going are included in these plots. It is evident that an additional  $\Lambda$  cut at this stage is sufficient to eliminate the atmospheric muon contamination in the sample.

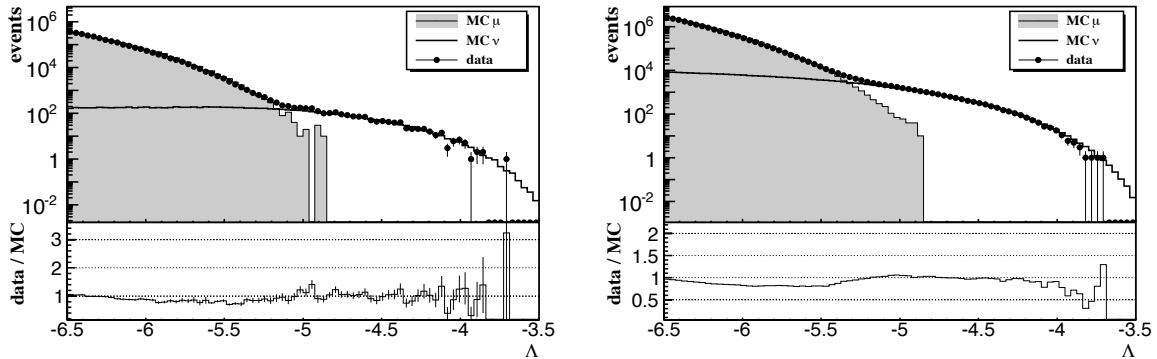


Figure 5.11: *Left plot:*  $\Lambda$  distribution for data and atmospheric muon and neutrino simulations. *Right plot:*  $\Lambda$  cumulative distribution for data and simulations. Only tracks reconstructed as upward-going are shown here. No additional quality cuts are applied.

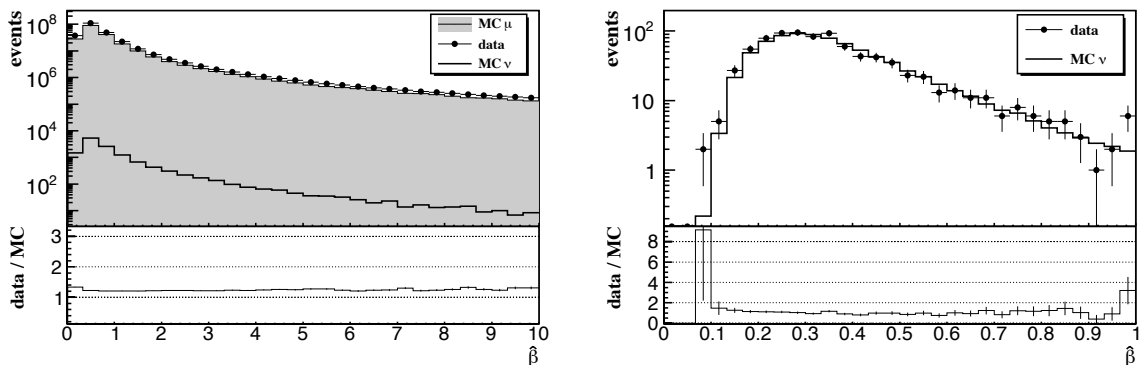


Figure 5.12: Distribution of the angular error estimate  $\hat{\beta}$  from the track fit for data and Monte Carlo. The left plot shows all events while the right plot shows all the events that passed the selection criteria.

Figure 5.12 shows the distribution of the angular error estimate  $\hat{\beta}$  from the track fit. The left plot shows the data and Monte Carlo distributions for all track reconstructed events while on the right only the final selection is shown. Finally, the distributions for the number of lines and the number of hits used in the final stage of the track fit, for both data and Monte Carlo, are shown in figures 5.13 and 5.14 respectively. In both figures, the right plot consists only of neutrino events, since atmospheric muons are completely suppressed after the directional and  $\Lambda$  cuts. There is an overall good agreement between data and Monte Carlo, with only a normalization difference of 22%.

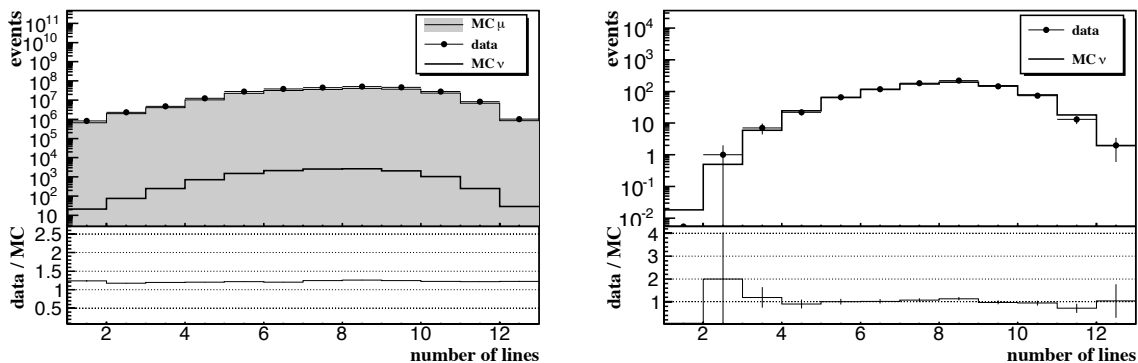


Figure 5.13: Distribution of the number of lines that were used in the final fit stage of the track reconstruction. On the left plot all events are shown. The right plot includes only events that passed the selection cuts.

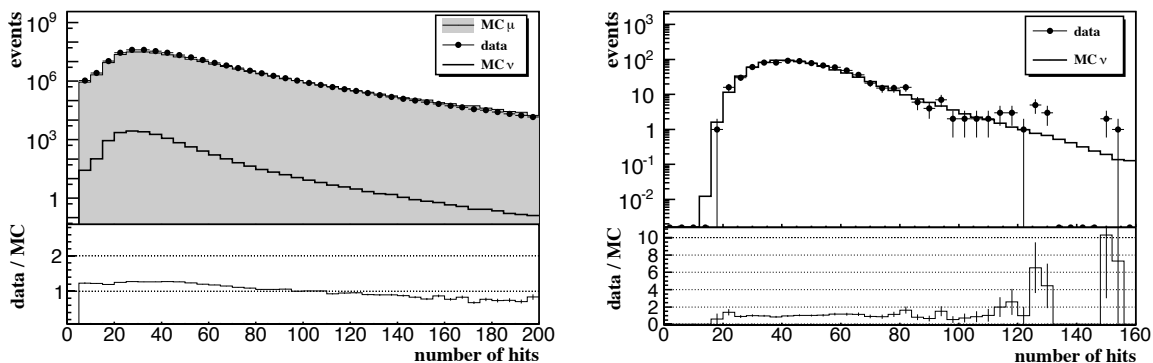


Figure 5.14: Distribution of the number of hits used in the final fit stage of the track reconstruction. The left plot includes all events. Events reconstructed as upward-going that passed the quality cuts are shown on the right.

## 5.4 Distribution of the energy observable

The most important quantity for the unfolding of the atmospheric neutrino spectrum is the reconstructed energy, i.e. our energy observable. This section contains the comparisons between data and simulations regarding the output of the energy reconstruction algorithm described in detail in chapter 3. Figure 5.15 shows the distribution of the energy reconstruction variable for upward-going events with an angular error estimate of less than one degree and different  $\Lambda$  cuts. The sample is dominated by atmospheric muons especially at higher energies when  $\Lambda > -5.6$ . The reconstructed energy distribution in data follows the simulations as more strict  $\Lambda$  cuts are applied and the atmospheric muon background is increasingly suppressed. For  $\Lambda > -5$  there is still a small atmospheric muon component present. The sensitivity of the unfolded result for different choices of  $\Lambda$  in the vicinity of  $\Lambda = -4.8$  will be examined in the next chapter, in section 6.2.

After applying the event selection cuts described in the previous sections, the at-

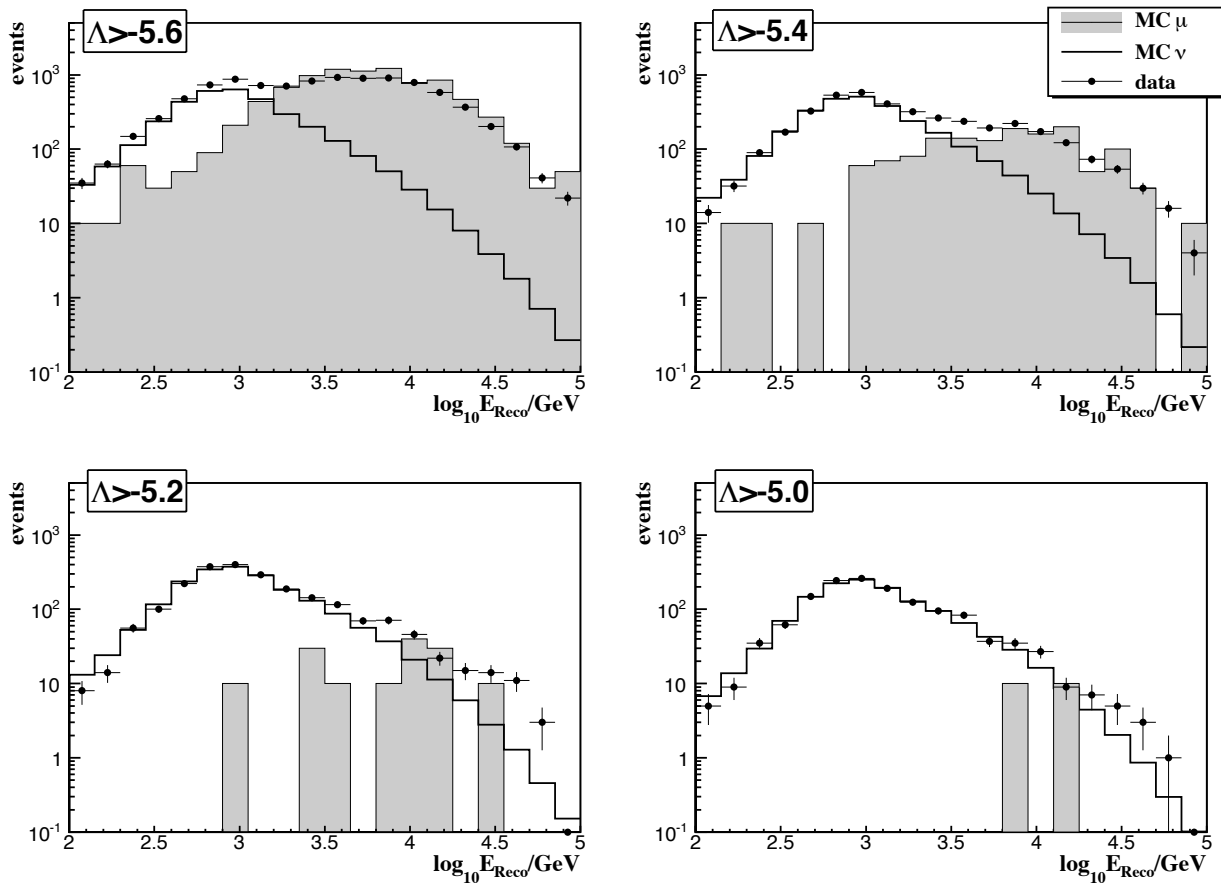


Figure 5.15: Distribution of the reconstructed energy variable for data and simulations. All events reconstructed as upward going and with  $\hat{\beta} < 1^\circ$  are shown for the different  $\Lambda$  indicated in each figure. The atmospheric muon Monte Carlo sample corresponds to 1/10th of the livetime and each event is weighted accordingly (see section 3.2).

atmospheric muon flux is completely suppressed. This is shown in figure 5.16. In this plot we see the distribution of the energy reconstruction variable in data, following the Monte Carlo prediction for the atmospheric neutrino energy distribution. The agreement between the reconstructed energy distributions for data and neutrino simulations is satisfactory. This energy spectrum is the distribution that is used as the measured input vector in the unfolding process described in chapter 4.

## 5.5 Summary

In order to unfold the spectrum of atmospheric neutrinos we need to have a pure neutrino sample. The aim of the event selection process introduced in this chapter was to eliminate as much as possible the presence of atmospheric muon contamination in the final sample. Additionally, well-reconstructed tracks have a higher probability of

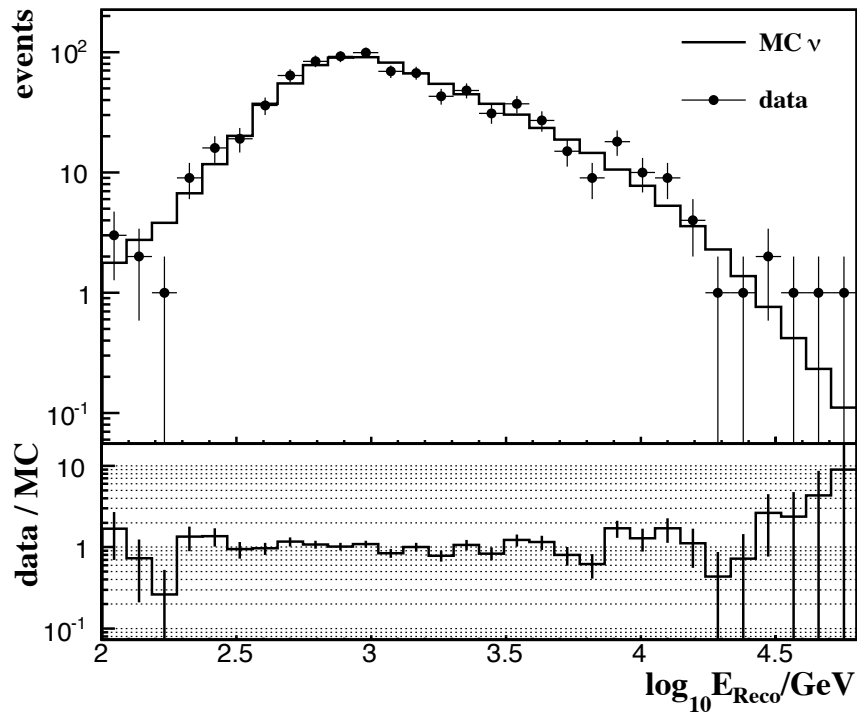


Figure 5.16: Distribution of the reconstructed energy for data and Monte Carlo after the application of the selection criteria described in section 5.2.2. No atmospheric muon events are present in the sample.

having their energy reconstructed accurately. The selection criteria that satisfy these conditions consist of selecting upward-going tracks, with  $\Lambda$  and  $\hat{\beta}$  values that indicate a high quality track fit. The purity of the final sample is almost 100% with an efficiency over the total number of upward-going events of  $\sim 8\%$ . Finally, the data - Monte Carlo comparisons show a satisfactory level of agreement, indicating a good understanding of the detector and the physical processes taking place.

# MEASUREMENT OF THE ATMOSPHERIC NEUTRINO SPECTRUM

The measurement of the atmospheric neutrino energy spectrum based on data taken between May 2008 and December 2010 is presented in this chapter. The deconvoluted energy spectrum of atmospheric neutrinos at the detector level is presented in section 6.1. Section 6.2 includes the estimated systematic uncertainties due to various factors such as the assumption of the underlying physical spectrum used for the construction of the response matrix and the effect of the applied cuts. The measurement of the atmospheric neutrino flux as a function of energy is presented in section 6.3. We conclude this work with a discussion of the results and future prospects.

## 6.1 Atmospheric neutrino energy deconvolution

The atmospheric neutrino energy spectrum, from  $10^{2.5}$  GeV to  $10^{5.3}$  GeV, at the detector level is unfolded using  $\tau = s_2^2$  as the regularization parameter, following the criteria described in chapter 4, and is shown in figure 6.1. The small error bars reflect the regularization imposed on the solution due to the choice of the regularization parameter as discussed in section 4.4. A possible over-regularization bias has been taken into account through examining the sensitivity of the solution to different assumptions on the energy spectrum used in the response matrix (see section 6.2). The number of atmospheric neutrino events per bin at the detector level are given in table 6.1. The spectrum used to train the response matrix corresponds to the conventional and prompt flux calculations by Honda and Martin *et al.* respectively. The Monte Carlo spectrum shown in the figure is scaled up by 22% as discussed in section 5.2.2. This does not affect the unfolded result, which is the same regardless of the overall normalization of the initial assumption (see section 4.4).

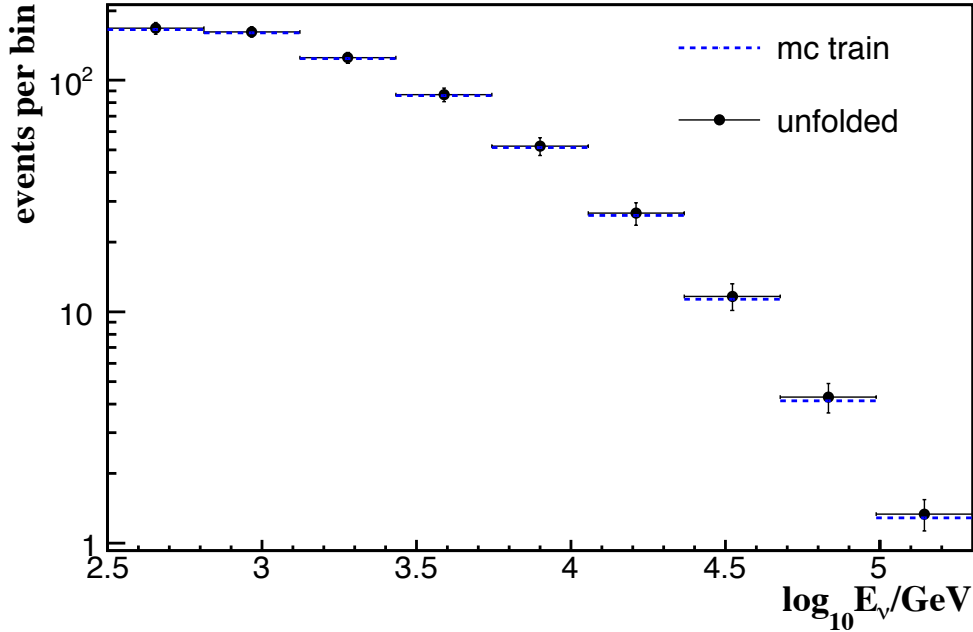


Figure 6.1: Unfolded neutrino energy distribution at the detector level, obtained from the reconstructed muon energy. The error bars do not include systematic uncertainties.

## 6.2 Systematic uncertainties

The effect of uncertainties on the optical module efficiency, angular acceptance and light absorption length in water has been estimated in section 4.7 based on Monte Carlo simulations. We have seen that the uncertainties on the OM efficiency induce an uncertainty of +4.6% to +104.5% from  $10^{2.5}$  to  $10^{5.3}$  GeV, while the effect of absorption length and angular acceptance introduces a +60.9% uncertainty in the lowest energy bin, pulling the spectrum higher by 57% in the last bin. Additional sources of uncertainty in the final measurement are described in this section and are based on the sensitivity of the unfolded data result on various choices, such as data sample background conditions or the applied quality cuts.

The first source of uncertainty we consider is the choice of the track quality cut  $\Lambda$ . A strict cut will reject effectively all the muon background while at the same time decrease the statistics of the final sample. On the other hand, a lower value of  $\Lambda$  cut will allow for increased atmospheric muon contamination in our sample. To examine the effect of the choice of the value of the cut, the neutrino spectrum is unfolded using different values for the cut on  $\Lambda$ . The deviation from the result with the standard cut of  $\Lambda = -4.8$  for this analysis is determined by varying the value of  $\Lambda$  in the range -4.6 to -5.0. For lower values of  $\Lambda$ , the muon contamination of the sample increases considerably as illustrated in section 5.4. The effect is negligible at lower energies while at energies above  $10^{4.5}$  GeV, the choice of the cut induces an uncertainty of approximately +15% and -10%.

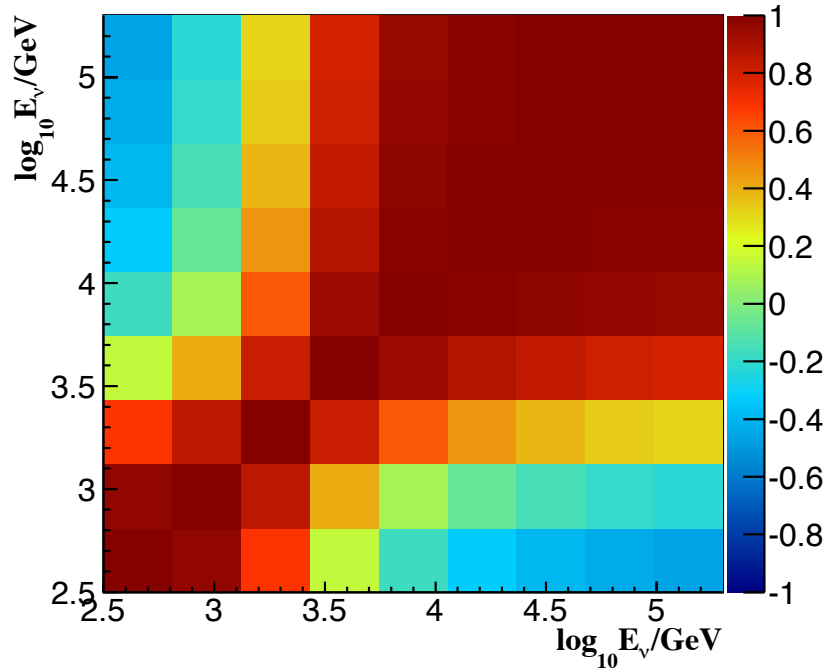


Figure 6.2: Correlation matrix for the unfolded result. Strong bin-to-bin correlations are present in the lowest and highest energy bins, reflecting the low statistics in the corresponding bins of the reconstructed energy distribution shown in figure 5.16.

$\log_{10} E_\nu / \text{GeV}$	Number of events
2.5 - 2.8	169.28
2.8 - 3.1	163.11
3.1 - 3.4	126.26
3.4 - 3.7	87.14
3.7 - 4.1	52.12
4.1 - 4.4	26.63
4.4 - 4.7	11.63
4.7 - 5.0	4.25
5.0 - 5.3	1.33

Table 6.1: Unfolded number of neutrino events in the different energy bins.

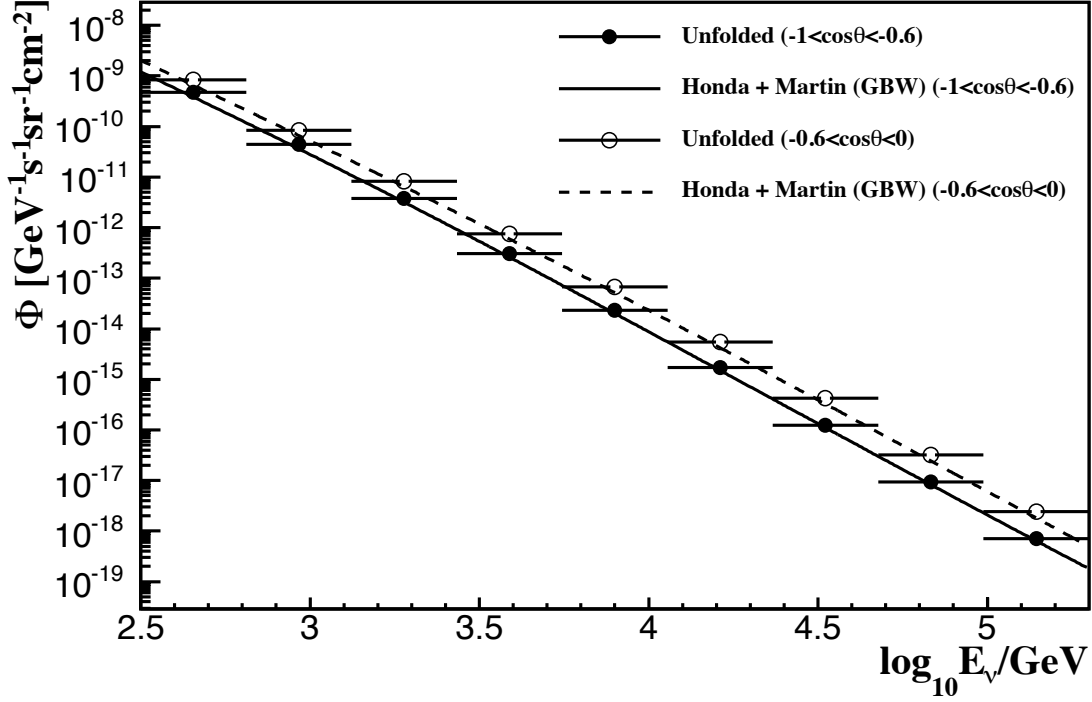


Figure 6.3: Unfolded atmospheric neutrino ( $\nu_\mu + \bar{\nu}_\mu$ ) spectra for the two angular ranges indicated on the legend. See text for explanation.

Another important consideration is the selection of the underlying physical spectrum assumption used for the construction of the unfolding matrix. For this reason the lowest and highest predictions for the conventional and prompt fluxes have been used for the construction of the response matrix. The effect we are trying to estimate here is the bias we came across in section 4.6 due to the different true and assumed spectra. The deviation from the spectrum unfolded with the matrix constructed using the fluxes of Honda *et al.* and Martin *et al.* is added to the uncertainty of the final flux. There is a significant bias, especially for the highest energies, which induces an uncertainty at the level of 68.7% and 168.8% for the last two bins. The reason for that is that the number of detected events in these bins is very low and therefore the unfolded spectrum is very sensitive to our assumptions on the true flux.

To determine the effect of possible zenith angle dependent inconsistencies between the unfolded results for different angular ranges we split our data sample in two groups. We unfold the energy spectrum averaged in two angular ranges, i.e.  $-1 < \cos \theta_{\text{rec}} < -0.6$  and  $-0.6 < \cos \theta_{\text{rec}} < 0$ . The first range corresponds to events closer to vertically upward going and the second one to events with a trajectory closer to the horizontal direction. The unfolded spectra for the two angular ranges are shown in figure 6.3. The theoretically predicted ratios of zenith averaged fluxes  $\frac{\Phi_{[0, -0.6]}}{\Phi_{[0, -1]}}$  and  $\frac{\Phi_{[-0.6, -1]}}{\Phi_{[0, -1]}}$  are compared with the corresponding measured ratios in figure 6.4. The continuous lines correspond to the ratio of the theoretical calculations while the binned histograms are the ratios of

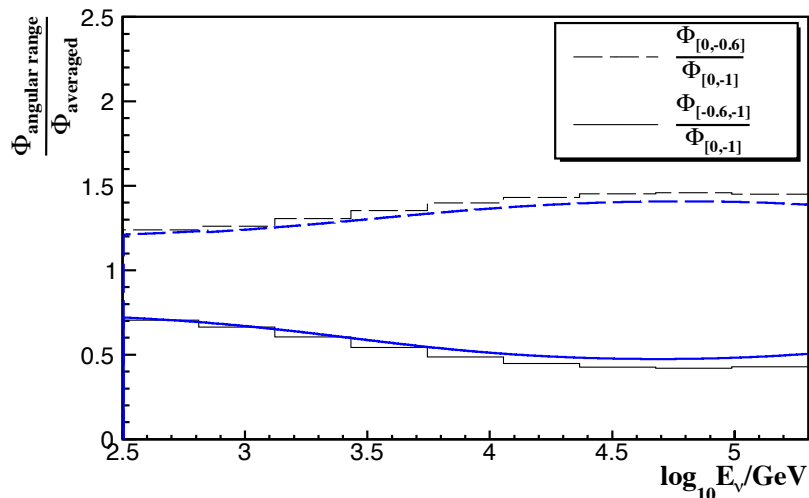


Figure 6.4: Unfolded spectra ratios for the two angular ranges. The data ratios are shown in the black histograms while the theoretical ratios in the blue continuous lines.

the unfolded results. We see that for energies above a few TeV, the unfolded results are not consistent with the calculated fluxes. The unfolded result for the more horizontal angular range is higher than the averaged result as expected (see section 1.3.5). However, according to the theoretical prediction this ratio must be lower. The opposite is true for the more vertical tracks. The relative deviations of the measured fractions from the predictions are quoted as the uncertainty due to zenith angle discrepancies. The uncertainties are well within +15% and -4% throughout the whole energy range. This could be possibly a real effect unaccounted for in the theoretical calculations. However, we chose to include it in our total systematic uncertainty estimation even though its contribution relative to other sources of uncertainty is minor.

The effect of including runs with a quality flag  $QB = 1$  has also been studied. These runs have less than ideal optical background conditions and in many cases a significant fraction of the detector inactive. Including them in the analysis could have a significant impact on the result. The deviation of the unfolded spectrum using runs with the flag  $QB = 2,3$  and 4 from the spectrum using all runs is estimated and the effect is minor and well within  $\pm 5\%$ . Therefore all runs with a quality flag  $QB \geq 1$ , as discussed in section 5.1, are included in the analysis in order to maximize the statistics of the data sample.

The uncertainties are added quadratically for positive and negative deviations separately. The total uncertainty on the measured flux as a function of energy is shown in figure 6.5. The statistical uncertainties calculated within *RooUnfold* are also shown and indicated as “Unfolding” in the figure. They are not above  $\pm 15\%$  for the highest energy bins.

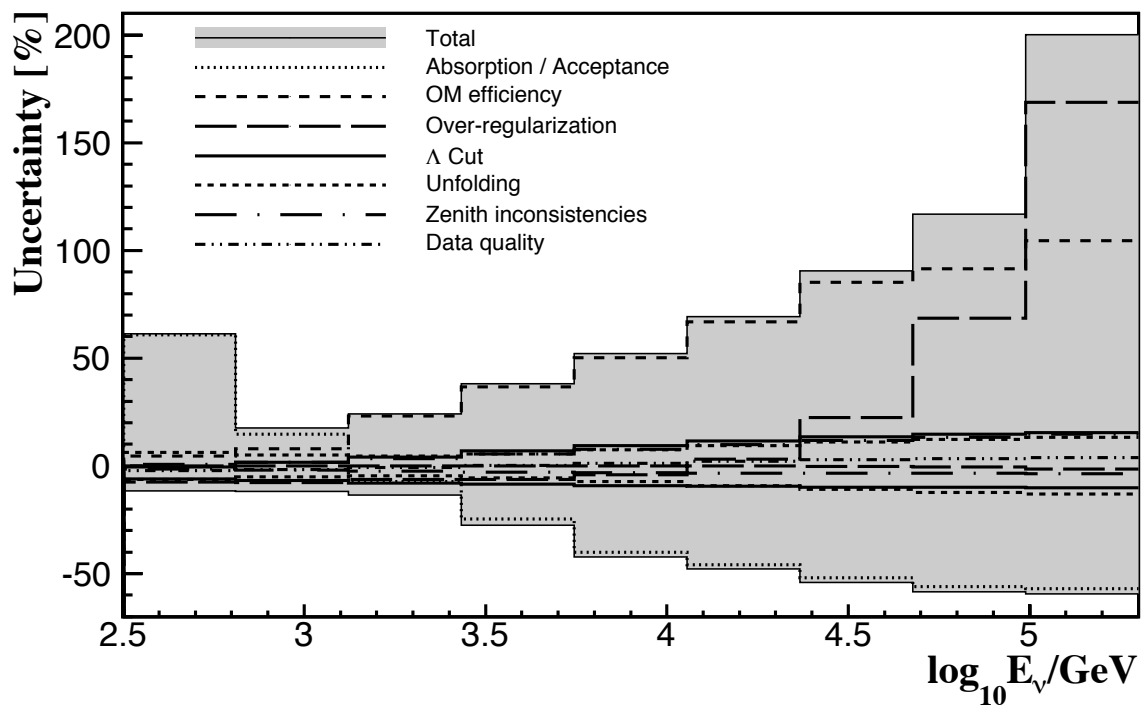


Figure 6.5: Uncertainties as a function of neutrino energy, given as a percentage of the measured atmospheric neutrino flux.

Energy range	2.5 - 2.8	2.8 - 3.1	3.1 - 3.4	3.4 - 3.7	3.7 - 4.1	4.1 - 4.4	4.4 - 4.7	4.7 - 5	5 - 5.3
OM efficiency	+4.6	+8.0	+23.1	+36.7	+50.1	+66.9	+85.1	+91.4	+104.5
Absorption/acceptance	+60.9	+14.8	-7.2	-24.6	-40.2	-45.9	-51.9	-56.1	-57.0
$\Lambda$ cut	-	+1.7	+4.2	+7.0	+9.5	+11.7	+13.5	+14.7	+15.4
Response Matrix flux	-6	-6.9	-7.9	-8.6	-9.1	-9.5	-9.8	-10.0	-10.1
Response Matrix flux	-	-	+0.1	+0.1	-	+3.0	+22.5	+68.7	+168.8
Response Matrix flux	-7.4	-7.8	-6.3	-6.3	-4.2	-	-0.2	-0.6	-1.5
Data selection	-2.2	-1.7	-0.7	+0.2	+1.2	+2.2	+2.9	+3.5	+3.9
Zenith	+0.6	+1.7	+3.5	+5.5	+7.7	+9.8	+11.9	+13.3	+14.8
Zenith	-1.4	-1.9	-2.5	-2.9	-3.2	-3.3	-3.4	-3.5	-3.6
Unfolding	$\pm 6.3$	$\pm 5.1$	$\pm 4.6$	$\pm 5.5$	$\pm 7.4$	$\pm 9.3$	$\pm 11.0$	$\pm 12.3$	$\pm 13.2$
<b>Total</b>	+61.4	+17.7	+24.2	+38.1	+52.1	+69.3	+90.6	+116.7	+200.1
<b>Total</b>	-11.7	-11.9	-13.5	-27.5	-42.2	-47.9	-54.0	-58.4	-59.5

Table 6.2: Table of all the systematic uncertainties considered in this work, for each energy bin of the unfolded neutrino energy spectrum. The numbers are the percentage of the measured flux that must be added to the value of each bin.

### 6.3 Results

In order to calculate the atmospheric neutrino energy spectrum, the detector effective area has to be used to account for the neutrino propagation in the Earth and the efficiency of the detector for the selection cuts applied in this analysis, as described in chapter 4. Figure 6.6 shows the neutrino energy spectrum for upward going events, averaged over the zenith angle and weighted with  $E_\nu^3$  in the same way as the conventional and prompt fluxes were presented in chapter 1. In the results presented from now on, a bin centering correction is applied to each energy bin to account for the steepness of the energy spectrum. This is performed by determining the median of the neutrino energy distribution for each energy bin in the neutrino energy distribution at the detector level, shown in figure 6.1, from Monte Carlo simulations. This value is used as the bin center as well as for re-weighting the spectra with energy for better illustration purposes, e.g. when plotting  $E_\nu^3\Phi$ . The differential flux of atmospheric neutrinos and antineutrinos averaged over the zenith angle without weighting with the neutrino energy is shown in figure 6.7. It is a very steep spectrum spanning nine to ten orders of magnitude in the energy range considered in this analysis.

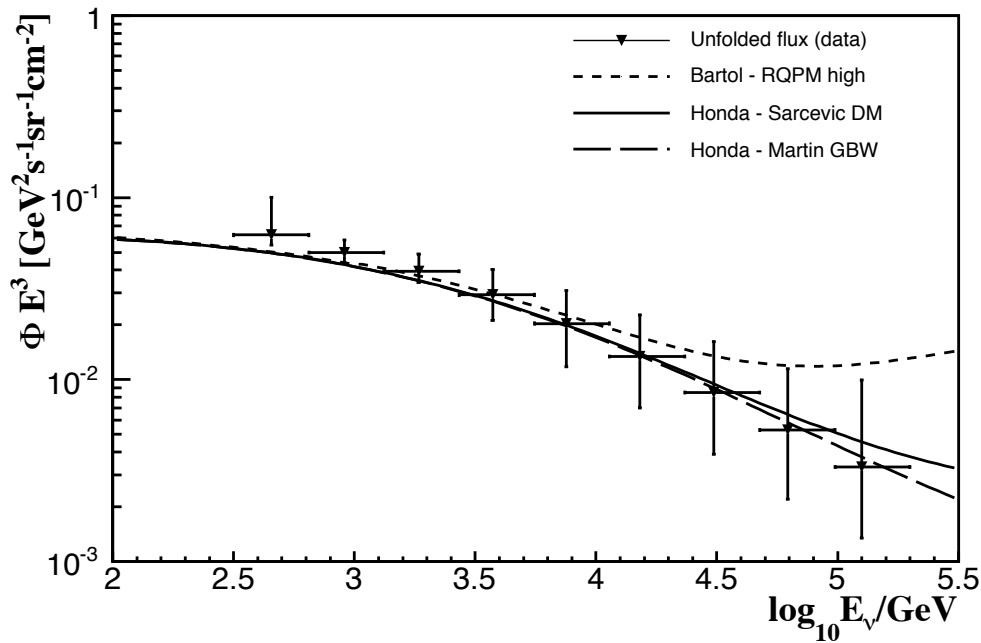


Figure 6.6: Atmospheric neutrino ( $\nu_\mu + \bar{\nu}_\mu$ ) energy spectrum weighted with  $E_\nu^3$  and averaged over the zenith angle. The total uncertainty, shown in figure 6.5, is represented here by the vertical error bars.

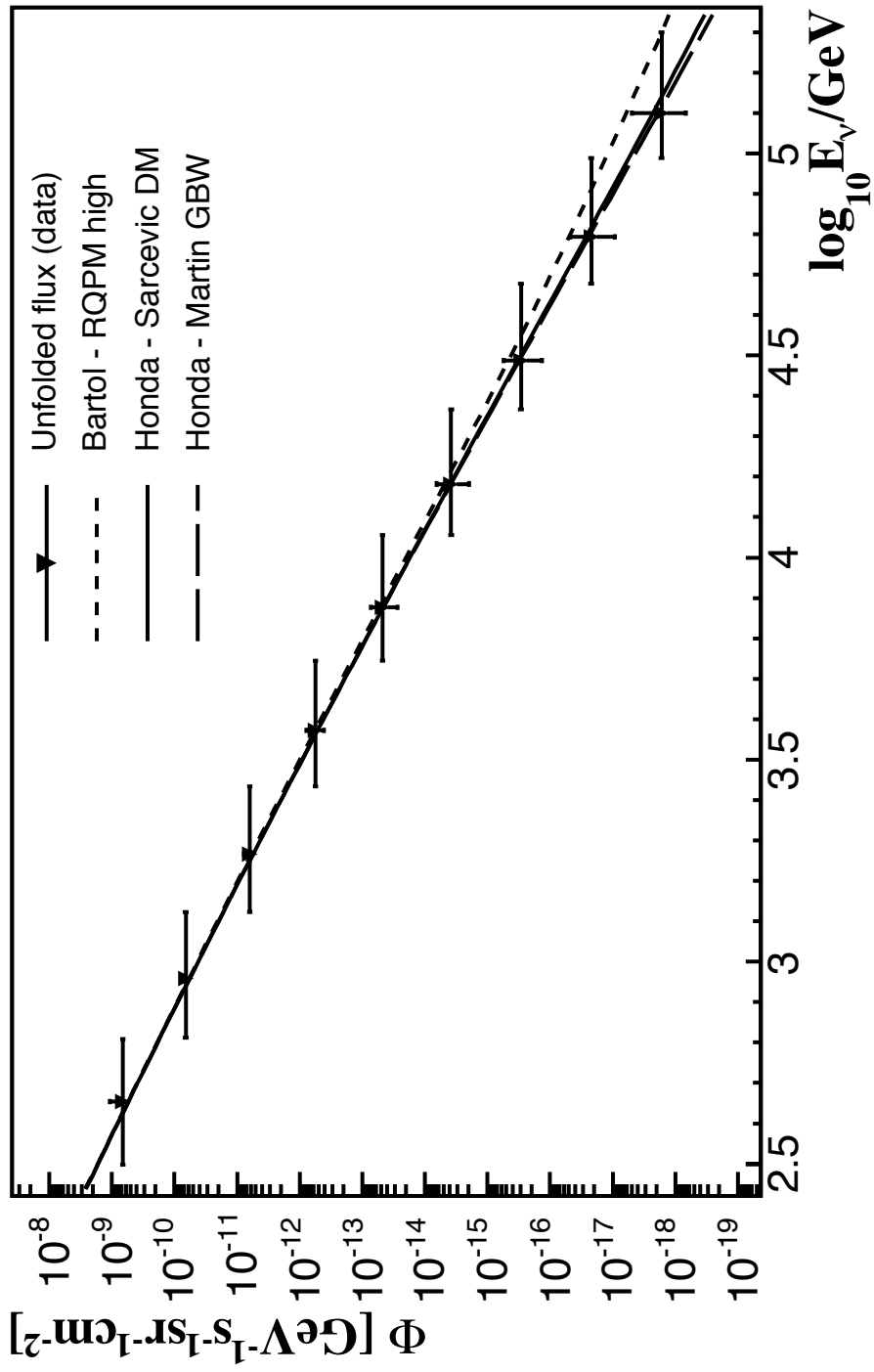


Figure 6.7: Atmospheric neutrino ( $\nu_{\mu} + \bar{\nu}_{\mu}$ ) energy spectrum averaged over the zenith angle. The total uncertainty, including systematic and statistical errors shown in figure 6.5, is represented here by the vertical error bars.

The result of the measurement is compatible with the theoretical predictions and within the minimum theoretical uncertainties of the order of 30%. A comparison with the results from analyses performed by the AMANDA and IceCube collaborations is shown in figure 6.8. Table 6.3 summarizes the values of the differential atmospheric neutrino energy spectrum for each energy bin, together with the total estimated uncertainties as a percent of the measured flux value for this work.

The IceCube measurement is performed with a 40 strings configuration in the energy range between 100 GeV to 400 TeV. 18000 upward going candidates were collected during April 2008 to May 2009 in the angular range  $97^\circ - 180^\circ$ . The muon energy determination is performed through an average energy loss per unit propagation length estimation, based on the number of detected photons, incorporating detailed information on the ice properties and photon propagation. The atmospheric muon background rejection is done using boosted decision trees and the unfolding is performed using the singular value decomposition method that was also applied in this work. The main systematic uncertainties in this measurement are due to optical module efficiency and ice properties uncertainties in the high end of the spectrum, while for middle and lower energies zenith dependent inconsistencies dominate the errors. The AMANDA measurement from 2 TeV to 200 TeV is performed in the angular range  $100^\circ - 180^\circ$  and is based on a sample of 2972 neutrino candidates collected during the years 2000-2003. The muon energy is reconstructed using a neural network approach based on several energy dependent variables. The neutrino candidate events are selected through examination of track quality parameters and topological parameters describing the hits distributions [Acht 07]. The unfolding is performed using the RUN algorithm [Blob 96].

The result we obtain is consistent with the theoretical predictions on the conventional and prompt neutrino fluxes as well as with the measurements performed by the AMANDA and IceCube collaborations. The unfolded energy spectrum is less than 20% higher than the calculation by Honda for the whole energy range, which is within the theoretical uncertainties of around 30%. The measurement in this work is above the IC40 measurement throughout the whole energy range. For energies below 1 TeV the measurement obtained with the IC40 analysis is approximately 30% lower than this work. The difference decreases for higher energies reaching a level of 10% above a few tens of TeV. Compared to the AMANDA measurement, there is a good agreement at low energies, at the level of 5% around a few TeV. As the energy increases, the AMANDA spectrum lies 30-40% higher than this work at energies above a few tens of TeV. The AMANDA measurement is also consistently higher than the IC40 result by 30-50% for all energies. These differences however lie within the estimated uncertainties for the three experiments. The systematic uncertainties estimated in this analysis are comparable with the ones published in the IC40 measurement. The older AMANDA measurement has smaller systematic uncertainties than the IC40 measurement and this work throughout the whole energy range.

A possible prompt contribution at the highest energies cannot be resolved at present with this measurement. The systematic uncertainties need to be reduced and work is ongoing within the ANTARES collaboration for a better understanding of light propagation in sea water at the ANTARES site.

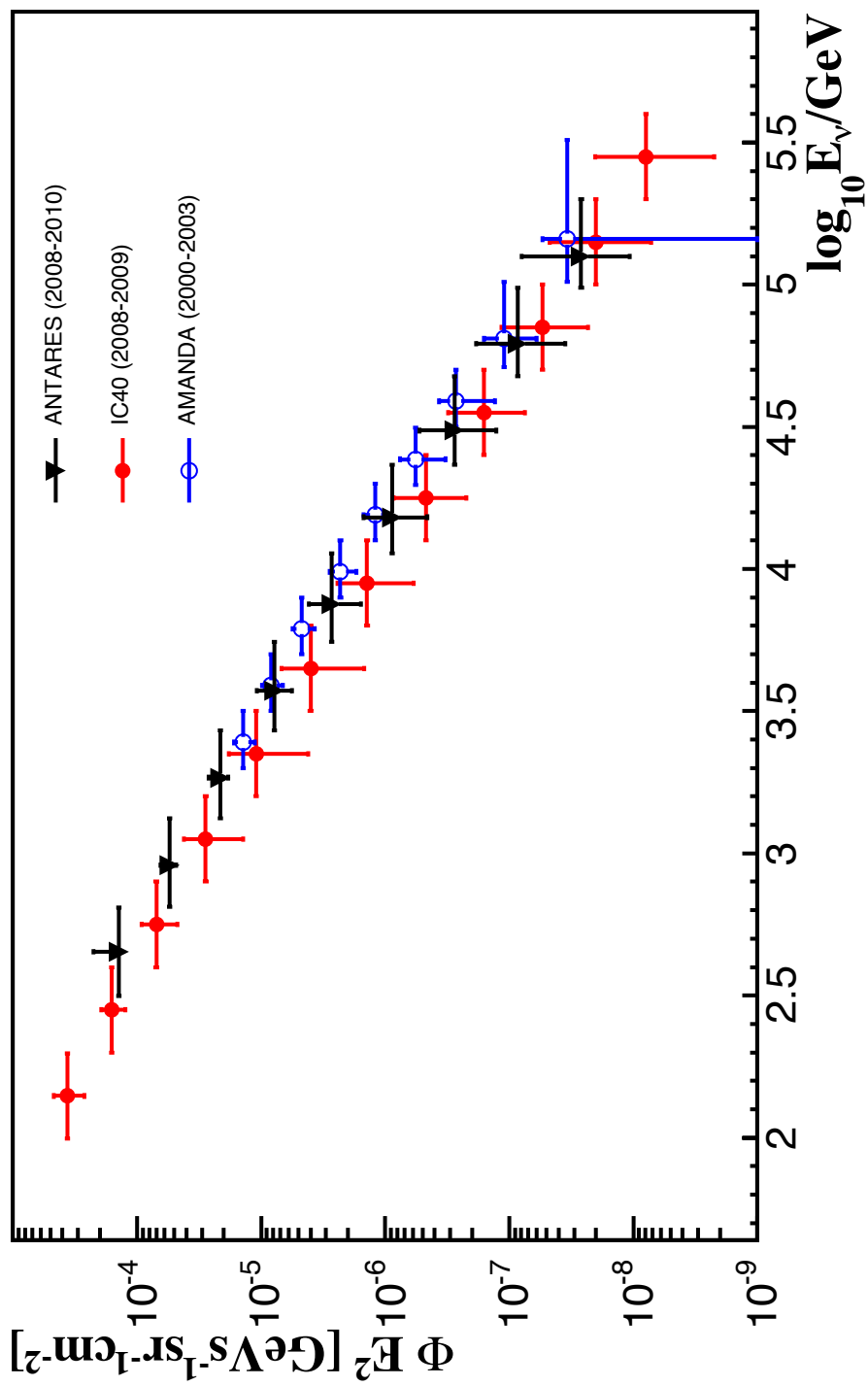


Figure 6.8: Comparison of the atmospheric neutrino energy spectrum measurements from IceCube [Abba 11] (averaged over the zenith range  $97^\circ - 180^\circ$ ) and AMANDA [Abba 10] (averaged over the zenith range  $100^\circ - 180^\circ$ ) with this work (averaged over the zenith range  $90^\circ - 180^\circ$ ). The error bars represent the total uncertainties of the measurements.

$\log_{10} E_\nu / \text{GeV}$	$dN/dE_\nu \times E_\nu^2$ [GeV s <sup>-1</sup> sr <sup>-1</sup> cm <sup>-2</sup> ]	$dN/dE_\nu$ [GeV <sup>-1</sup> s <sup>-1</sup> sr <sup>-1</sup> cm <sup>-2</sup> ]	% Uncertainty	
2.5 - 2.8	$1.37 \cdot 10^{-4}$	$6.65 \cdot 10^{-10}$	+61.4	-11.7
2.8 - 3.1	$5.48 \cdot 10^{-5}$	$6.62 \cdot 10^{-11}$	+17.7	-11.9
3.1 - 3.4	$2.14 \cdot 10^{-5}$	$6.28 \cdot 10^{-12}$	+24.2	-13.5
3.4 - 3.7	$7.83 \cdot 10^{-6}$	$5.62 \cdot 10^{-13}$	+38.1	-27.5
3.7 - 4.1	$2.70 \cdot 10^{-6}$	$4.76 \cdot 10^{-14}$	+52.1	-42.2
4.1 - 4.4	$8.81 \cdot 10^{-7}$	$3.81 \cdot 10^{-15}$	+69.3	-47.9
4.4 - 4.7	$2.76 \cdot 10^{-7}$	$2.93 \cdot 10^{-16}$	+90.6	-54.0
4.7 - 5.0	$8.51 \cdot 10^{-8}$	$2.21 \cdot 10^{-17}$	+116.7	-58.4
5.0 - 5.3	$2.63 \cdot 10^{-8}$	$1.66 \cdot 10^{-18}$	+200.1	-59.5

Table 6.3: Atmospheric neutrino energy spectrum averaged over the zenith angle.

## 6.4 Summary and outlook

The goal of this work has been the measurement of the atmospheric neutrino and antineutrino energy spectrum. A muon energy reconstruction algorithm based on a maximum likelihood method was developed to estimate the energy of muons passing through the ANTARES detector. Due to the challenging nature of energy determination in neutrino telescopes, the limitations in the energy resolution are significant. The bin-to-bin migrations in the distribution of the reconstructed energy, as well as the fact that the muon energy is always less than that of the neutrino that produced it, call for a different approach than simply determining the energy of the passing muon. A well known unfolding method, based on the singular value decomposition of the matrix describing the bin migrations, has been used to overcome these problems and provide a reliable measurement of the atmospheric neutrino flux.

Significant improvements to the measurement presented in this work can be achieved by a better energy resolution, muon background discrimination and higher statistics. An improved energy reconstruction may contribute to a more diagonal response matrix, while a better energy resolution will allow for finer binning. More significant coefficients will be available in the expansion and it will therefore become easier to isolate and damp terms that predominantly contribute statistical noise. Additionally, the bin-to-bin correlations on the unfolded result and its sensitivity to the assumed true spectrum will decrease. A muon background discrimination that provides a higher sample purity without decreasing the detection efficiency can contribute to a more precise measurement as well. The same is true for the overall statistics of the data sample that is used. This is especially true for the highest energies where the very low number of events does not provide enough information and the unfolded spectrum tends to be very sensitive to the choice of the spectrum in the construction of the response matrix. Finally, the largest systematic uncertainties are related to the quantum efficiency and acceptance

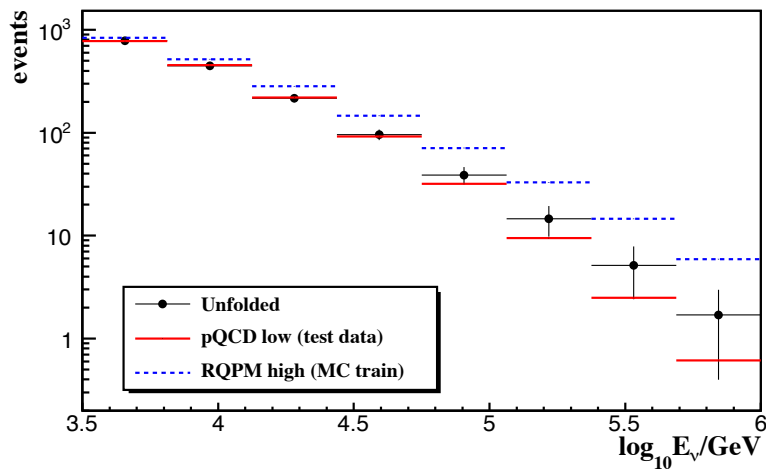


Figure 6.9: Example of the deconvolution of the low pQCD flux using the high RQPM flux for the response matrix in the case of ten times more data.

of the phototubes as well as the light absorption in water. Future studies may provide stronger constraints on these quantities, reducing the overall measurement uncertainties. Laser beacon studies could constrain the uncertainties on the absorption length by providing valuable information on water properties and light propagation. The determination of the overall efficiency of the optical modules can be a more challenging task, but a combination of *in situ* and test bench measurements could lead to a reduced uncertainty on the optical modules' detection efficiency.

Many of these problems will be addressed and solved with future ANTARES analyses with more data, reduced uncertainties and possible improvements in the energy determination. The next generation of neutrino telescopes in the Mediterranean sea will reach detection volumes of a few cubic kilometers, gathering much more data and therefore being more sensitive to the shape of the neutrino flux at the highest energies. This will make it easier to confirm or reject some of the prompt neutrino flux models. For example, using the same method described in this work for the muon energy reconstruction and the unfolding of the neutrino spectrum we examine an example where the gathered statistics are ten times higher than in the current work. We use the high RQPM contribution to construct the response matrix and generate pseudo data based on the low pQCD calculation. The result of this test is shown in figure 6.9. In such a scenario it would be possible to exclude the higher flux. As the difference between prompt flux predictions decreases, so does the difference between the expected number of events in a certain energy range. This makes it very challenging to distinguish between different models with similar yields and an excellent energy resolution and even higher statistics are required. The larger detection volumes of the next generation of neutrino telescopes as well as the use of multi PMT's will allow for a better muon background discrimination and optical background rejection. In addition, the energy estimation will improve since a larger fraction of high energy tracks will be visible inside the detector.

Finally, going to higher energies, where the prompt flux is expected to dominate above the conventional component and the differences between various prompt models are more pronounced, will make the discrimination easier. These improvements will prove crucial to the determination of the value of the flux from the prompt contribution and its crossover energy over the conventional component.

# BIBLIOGRAPHY

- [Abba 08] R. U. Abbasi *et al.* “First Observation of the Greisen-Zatsepin-Kuzmin Suppression”. *Phys. Rev. Lett.*, Vol. 100, p. 101101, Mar 2008.
- [Abba 10] R. Abbasi *et al.* “The energy spectrum of atmospheric neutrinos between 2 and 200TeV with the AMANDA-II detector”. *Astroparticle Physics*, Vol. 34, No. 1, pp. 48 – 58, 2010.
- [Abba 11] R. Abbasi *et al.* “Measurement of the atmospheric neutrino energy spectrum from 100 GeV to 400 TeV with IceCube”. *Phys. Rev. D*, Vol. 83, p. 012001, Jan 2011.
- [Abba 12] R. Abbasi *et al.* “An absence of neutrinos associated with cosmic-ray acceleration in  $\gamma$ -ray bursts”. *Nature*, Vol. 484, pp. 351–354, 2012.
- [Abra 08] J. Abraham *et al.* “Observation of the Suppression of the Flux of Cosmic Rays above  $4 \times 10^{19}$  eV”. *Phys. Rev. Lett.*, Vol. 101, p. 061101, Aug 2008.
- [Abra 10] J. Abraham *et al.* “Measurement of the energy spectrum of cosmic rays above  $10^{18}$  eV using the Pierre Auger Observatory”. *Phys. Lett.*, Vol. B685, pp. 239–246, 2010.
- [Acht 07] A. Achterberg *et al.* “Five years of searches for point sources of astrophysical neutrinos with the AMANDA-II neutrino telescope”. *Phys. Rev. D*, Vol. 75, p. 102001, May 2007.
- [Adye] T. Adye. “RooUnfold: ROOT Unfolding Framework”. <http://hepunx.rl.ac.uk/~adye/software/unfold/RooUnfold.html>.
- [Agos 03] S. Agostinelli *et al.* “Geant4 - a simulation toolkit”. *Nuclear Instruments and Methods in Physics Research Section A: Accelerators, Spectrometers, Detectors and Associated Equipment*, Vol. 506, No. 3, pp. 250 – 303, 2003.
- [Agra 96] V. Agrawal, T. K. Gaisser, P. Lipari, and T. Stanev. “Atmospheric neutrino flux above 1 GeV”. *Phys. Rev. D*, Vol. 53, pp. 1314–1323, Feb 1996.

- [Agui 07] J. Aguilar *et al.* “The data acquisition system for the ANTARES neutrino telescope”. *Nuclear Instruments and Methods in Physics Research Section A: Accelerators, Spectrometers, Detectors and Associated Equipment*, Vol. 570, No. 1, pp. 107 – 116, 2007.
- [Agui 10] J. A. Aguilar *et al.* “Performance of the front-end electronics of the ANTARES neutrino telescope”. *Nuclear Instruments and Methods in Physics Research Section A: Accelerators, Spectrometers, Detectors and Associated Equipment*, Vol. 622, No. 1, pp. 59 – 73, 2010.
- [Agui 11] J. A. Aguilar *et al.* “Time calibration of the ANTARES neutrino telescope”. *Astroparticle Physics*, Vol. 34, No. 7, pp. 539 – 549, 2011.
- [Ahma 02] Q. R. Ahmad *et al.* “Direct Evidence for Neutrino Flavor Transformation from Neutral-Current Interactions in the Sudbury Neutrino Observatory”. *Phys. Rev. Lett.*, Vol. 89, p. 011301, Jun 2002.
- [Alca 00a] J. Alcaraz *et al.* “Cosmic protons”. *Physics Letters B*, Vol. 490, No. 1-2, pp. 27 – 35, 2000.
- [Alca 00b] J. Alcaraz *et al.* “Helium in near Earth orbit”. *Physics Letters B*, Vol. 494, pp. 193 – 202, 2000.
- [Alek 88] E. N. Alekseev, L. N. Alekseeva, I. V. Krivosheina, and V. I. Volchenko. “Detection of the neutrino signal from SN 1987A in the LMC using the INR Baksan underground scintillation telescope”. *Phys. Lett.*, Vol. B205, pp. 209–214, 1988.
- [Alle 99] C. W. Allen. *Allen’s Astrophysical Quantities*. Springer, 4th Ed., Jan. 1999.
- [Amak 06] K. Amako *et al.* “Geant4 developments and applications”. *IEEE Transactions on Nuclear Science*, Vol. 53, No. 1, pp. 270 – 378, 2006.
- [Amor 07] I. Amore *et al.* “NEMO: A Project for a km<sup>3</sup> Underwater Detector for Astrophysical Neutrinos in the Mediterranean Sea”. *Int. J. Mod. Phys.*, Vol. A22, pp. 3509–3520, 2007.
- [Amra 00] P. Amram *et al.* “Background light in potential sites for the ANTARES undersea neutrino telescope”. *Astroparticle Physics*, Vol. 13, No. 2-3, pp. 127 – 136, 2000.
- [An 12] F. P. An *et al.* “Observation of electron-antineutrino disappearance at Daya Bay”. *ArXiv e-prints*, March 2012.
- [Ande 83] B. Andersson, G. Gustafson, G. Ingelman, and T. Sjostrand. “Parton Fragmentation and String Dynamics”. *Phys. Rept.*, Vol. 97, pp. 31–145, 1983.

- [Andr 99] E. C. Andrés *et al.* “The AMANDA neutrino telescope”. *Nuclear Physics B - Proceedings Supplements*, Vol. 77, No. 1-3, pp. 474 – 485, 1999.
- [Angh 08] M. Anghinolfi, H. Costantini, K. Fratini, D. Piombo, and M. Taiuti. “New measurement of the angular acceptance of the Antares Optical Module”. *ANTARES Internal Note*, 2008.
- [ANTA 02] ANTARES Collaboration, P. Amram *et al.* “The ANTARES optical module”. *Nuclear Instruments and Methods in Physics Research Section A: Accelerators, Spectrometers, Detectors and Associated Equipment*, Vol. 484, No. 1-3, pp. 369 – 383, 2002.
- [ANTA 03] ANTARES Collaboration, P. Amram *et al.* “Sedimentation and fouling of optical surfaces at the ANTARES site”. *Astroparticle Physics*, Vol. 19, No. 2, pp. 253 – 267, 2003.
- [ANTA 04] ANTARES Collaboration: Aguilar, J. A. *et al.* “Transmission of light in deep sea water at the site of the Antares neutrino telescope”. *Astropart. Phys.*, Vol. 23, No. 1, pp. 131–155. 40 p, Dec 2004.
- [ANTA 07] ANTARES Collaboration: Ageron, M. *et al.* “The ANTARES optical beacon system”. *Nuclear Instruments and Methods in Physics Research Section A: Accelerators, Spectrometers, Detectors and Associated Equipment*, Vol. 578, No. 3, pp. 498 – 509, 2007.
- [ANTA 09] ANTARES Collaboration: M. Ageron *et al.* “Performance of the first ANTARES detector line”. *Astroparticle Physics*, Vol. 31, pp. 277–283, May 2009.
- [Anto 97] P. Antonioli, C. Ghetti, E. Korolkova, V. Kudryavtsev, and G. Sartorelli. “A three-dimensional code for muon propagation through the rock: MUSIC”. *Astroparticle Physics*, Vol. 7, No. 4, pp. 357 – 368, 1997.
- [Aoki 98] T. Aoki *et al.* “A highly sensitive optical detector for use in deep underwater.”. *Nuclear Instruments and Methods in Physics Research A*, Vol. 408, pp. 425–437, May 1998.
- [Arak 05] T. Araki *et al.* “Measurement of Neutrino Oscillation with KamLAND: Evidence of Spectral Distortion”. *Phys. Rev. Lett.*, Vol. 94, p. 081801, Mar 2005.
- [Ardi 09] M. Ardid. “Positioning system of the ANTARES neutrino telescope”. *Nuclear Instruments and Methods in Physics Research Section A: Accelerators, Spectrometers, Detectors and Associated Equipment*, Vol. 602, No. 1, pp. 174 – 176, 2009. Proceedings of the 3rd International Workshop on a Very Large Volume Neutrino Telescope for the Mediterranean Sea.

- [Bail 00] D. J. L. Bailey. “The effect of scattering on the ANTARES detector performance”. *Antares Internal Note*, 2000.
- [Bail 02a] D. J. L. Bailey. “Genhen v5r1: software documentation”. *ANTARES Internal Note*, 2002.
- [Bail 02b] D. J. L. Bailey. “KM3 v2r1: User Guide”. *ANTARES Internal Note*, 2002.
- [Balk 01] V. A. Balkanov *et al.* “The BAIKAL neutrino project: status report”. *Nuclear Physics B - Proceedings Supplements*, Vol. 91, No. 1-3, pp. 438 – 444, 2001. Neutrino 2000.
- [Bare 09] Baret B. for the ANTARES collaboration. “Charge Calibration of the ANTARES high energy neutrino telescope”. *ArXiv e-prints*, Aug. 2009.
- [Barr 04] G. D. Barr, T. K. Gaisser, P. Lipari, S. Robbins, and T. Stanev. “A 3-dimensional calculation of atmospheric neutrinos”. *Phys. Rev. D*, Vol. 70, p. 023006, 2004.
- [Batt 00] G. Battistoni *et al.* *Astropart. Phys.*, Vol. 12, p. 315, 2000.
- [Bere 06] V. Berezhinsky, A. Gazizov, and S. Grigorieva. “On astrophysical solution to ultrahigh energy cosmic rays”. *Phys. Rev. D*, Vol. 74, p. 043005, Aug 2006.
- [Bere 96] E. G. Berezhko. “Maximum energy of cosmic rays accelerated by supernova shocks”. *Astroparticle Physics*, Vol. 5, pp. 367–378, Oct. 1996.
- [Blob 10] V. Blobel. “Unfolding: Linear Inverse Problems”. Notes for the Terrascale workshop at DESY, 2010.
- [Blob 96] V. Blobel. “The RUN Manual-Regularized Unfolding for High-Energy Physics Experiments”. *Technical Note TN361, OPAL*, 1996.
- [Blue 09] J. Bluemer, R. Engel, and J. R. Hoerandel. “Cosmic Rays from the Knee to the Highest Energies”. *Prog. Part. Nucl. Phys.*, Vol. 63, pp. 293–338, 2009.
- [Boga 11] C. Bogazzi and A. Heijboer. “Point source search with 2007 - 2010 data”. *Antares Internal Note*, 2011.
- [Brow 09] Brown A. M. for the ANTARES collaboration. “Positioning system of the ANTARES Neutrino Telescope”. 2009. Proceedings of 31st ICRC conference.
- [Brun] J. Brunner. “ANTARES detector simulation based on GEANT 3.21”. <http://antares.in2p3.fr/internal/software/geasim.html>.

- [Buga 89] E. Bugaev, V. Naumov, S. Sinegovsky, and E. Zaslavskaya. “Prompt leptons in cosmic rays”. *Il Nuovo Cimento C*, Vol. 12, pp. 41–73, 1989.
- [Buga 98] E. V. Bugaev, A. Misaki, V. A. Naumov, T. S. Sinegovskaya, S. I. Sinegovsky, and N. Takahashi. “Atmospheric muon flux at sea level, underground, and underwater”. *Phys. Rev. D*, Vol. 58, p. 054001, Jul 1998.
- [Carm 09] G. Carminati, A. Margiotta, and M. Spurio. “MUons from PArametric formulas: A fast GEnerator of atmospheric  $\nu$ -bundles for neutrino telescopes (MUPAGE)”. *Nuclear Instruments and Methods in Physics Research Section A: Accelerators, Spectrometers, Detectors and Associated Equipment*, Vol. 602, No. 1, pp. 95 – 97, 2009. Proceedings of the 3rd International Workshop on a Very Large Volume Neutrino Telescope for the Mediterranean Sea.
- [Carr 07] J. Carr, S. Escoffier, and D. Zaborov. “Proposition for an alternative trigger based on the T3 cluster trigger”. *Antares Internal Note*, 2007.
- [Cere 37] P. A. Čerenkov. “Visible Radiation Produced by Electrons Moving in a Medium with Velocities Exceeding that of Light”. *Phys. Rev.*, Vol. 52, No. 4, pp. 378–379, Aug 1937.
- [Chia 10] T. Chiarusi and M. Spurio. “High-energy astrophysics with neutrino telescopes”. *The European Physical Journal C - Particles and Fields*, Vol. 65, pp. 649–701, 2010.
- [Clev 98] B. T. Cleveland, T. Daily, R. Davis, Jr., J. R. Distel, K. Lande, C. K. Lee, P. S. Wildenhain, and J. Ullman. “Measurement of the Solar Electron Neutrino Flux with the Homestake Chlorine Detector”. *Astrophys. J.*, Vol. 496, p. 505, 1998.
- [Comb 79] B. L. Combridge. “Associated production of heavy flavour states in  $pp$  and  $\bar{p}p$  interactions: Some QCD estimates”. *Nuclear Physics B*, Vol. 151, No. 0, pp. 429 – 456, 1979.
- [Comp 35] A. H. Compton and I. A. Getting. “An Apparent Effect of Galactic Rotation on the Intensity of Cosmic Rays”. *Phys. Rev.*, Vol. 47, pp. 817–821, Jun 1935.
- [Coop 08] A. Cooper-Sarkar and S. Sarkar. “Predictions for high energy neutrino cross-sections from the ZEUS global PDF fits”. *Journal of High Energy Physics*, Vol. 2008, No. 01, p. 075, 2008.
- [Cost 01] C. G. S. Costa. “The prompt lepton cookbook”. *Astropart. Phys.*, pp. 193–204, 2001.

- [Cost 95] C. G. S. Costa, F. Halzen, and C. Salles. “Particle production in very-high-energy cosmic-ray emulsion chamber events: Usual and unusual events”. *Phys. Rev. D*, Vol. 52, pp. 3890–3893, Oct 1995.
- [Eguc 03] K. Eguchi *et al.* “First Results from KamLAND: Evidence for Reactor Antineutrino Disappearance”. *Phys. Rev. Lett.*, Vol. 90, p. 021802, Jan 2003.
- [Enbe 08] R. Enberg, M. H. Reno, and I. Sarcevic. “Prompt neutrino fluxes from atmospheric charm”. *Phys. Rev. D*, Vol. 78, p. 043005, Aug 2008.
- [Enge 01] R. Engel, T. Gaisser, P. Lipari, and T. Stanev. *Proc. 27th Int. Cosmic Ray Conf.*, p. 1381, 2001.
- [Enge 97] R. Engel, J. Ranft, and S. Roesler. “Photoproduction off nuclei and point-like photon interactions. I. Cross sections and nuclear shadowing”. *Phys. Rev. D*, Vol. 55, pp. 6957–6967, Jun 1997.
- [Fehr 10] F. Fehr. *Systematic studies, calibration, and software development for event reconstruction and data analysis using the ANTARES deep-sea neutrino telescope*. PhD thesis, University of Erlangen, 2010.
- [Fein 03] F. Feinstein. “The analogue ring sampler: A front-end chip for ANTARES”. *Nuclear Instruments and Methods in Physics Research Section A: Accelerators, Spectrometers, Detectors and Associated Equipment*, Vol. 504, No. 1-3, pp. 258 – 261, 2003. Proceedings of the 3rd International Conference on New Developments in Photodetection.
- [Ferm 40] E. Fermi. “The Ionization Loss of Energy in Gases and in Condensed Materials”. *Phys. Rev.*, Vol. 57, p. 485, 1940.
- [Fogl 11] G. L. Fogli, E. Lisi, A. Marrone, A. Palazzo, and A. M. Rotunno. “Evidence of  $\theta_{13} > 0$  from global neutrino data analysis”. *Phys. Rev. D*, Vol. 84, p. 053007, Sep 2011.
- [Fuku 98] Y. Fukuda *et al.* “Evidence for Oscillation of Atmospheric Neutrinos”. *Phys. Rev. Lett.*, Vol. 81, pp. 1562–1567, Aug 1998.
- [Futa 99] T. Futagami *et al.* “Observation of the East-West Anisotropy of the Atmospheric Neutrino Flux”. *Phys. Rev. Lett.*, Vol. 82, pp. 5194–5197, Jun 1999.
- [Gais 00] T. Gaisser. “Atmospheric neutrino flux: a review of calculations”. *Nuclear Physics B - Proceedings Supplements*, Vol. 87, No. 1-3, pp. 145 – 151, 2000. Proceedings of the Sixth International Workshop on Topics in Astroparticle and Underground Physics.

- [Gais 01] T. Gaisser, M. Honda, P. Lipari, and T. Stanev. “Primary spectrum to 1TeV and beyond”. *Proc. 27th Int. Cosmic Ray Conf.*, p. 1643, 2001.
- [Gais 02] T. K. Gaisser and M. Honda. “FLUX OF ATMOSPHERIC NEUTRINOS”. *Annual Review of Nuclear and Particle Science*, Vol. 52, No. 1, pp. 153–199, 2002.
- [Gais 03] T. K. Gaisser. “Atmospheric Neutrino Fluxes”. *Nucl. Phys. Proc.*, Vol. 118, p. 109, 2003.
- [Gand 98] R. Gandhi, C. Quigg, M. H. Reno, and I. Sarcevic. “Neutrino interactions at ultrahigh-energies”. *Phys. Rev. D*, Vol. 58, p. 093009, 1998.
- [Gelm 00a] G. Gelmini, P. Gondolo, and G. Varieschi. “Prompt atmospheric neutrinos and muons: NLO versus LO QCD predictions”. *Phys. Rev. D*, Vol. 61, p. 036005, Jan 2000.
- [Gelm 00b] G. Gelmini, P. Gondolo, and G. Varieschi. “Prompt atmospheric neutrinos and muons: dependence on the gluon distribution function”. *Phys. Rev. D*, Vol. 61, p. 056011, 2000.
- [Ginn 86] A. V. Ginneken. “Energy loss and angular characteristics of high energy electromagnetic processes”. *Nuclear Instruments and Methods in Physics Research Section A: Accelerators, Spectrometers, Detectors and Associated Equipment*, Vol. 251, No. 1, pp. 21 – 39, 1986.
- [Glas 60] S. L. Glashow. “Resonant Scattering of Antineutrinos”. *Phys. Rev.*, Vol. 118, No. 1, pp. 316–317, Apr 1960.
- [Gold 02] A. Goldschmidt. “Scientific Goals of the IceCube Neutrino Detector at the South Pole”. *Nuclear Physics B - Proceedings Supplements*, Vol. 110, No. , pp. 516 – 518, 2002.
- [Gole 98] K. Golec-Biernat and M. Wüsthoff. “Saturation effects in deep inelastic scattering at low  $Q^2$  and its implications on diffraction”. *Phys. Rev. D*, Vol. 59, p. 014017, Nov 1998.
- [Graf 08] K. Graf. *Experimental Studies within ANTARES towards Acoustic Detection of Ultra-High Energy Neutrinos in the Deep-Sea*. PhD thesis, University Erlangen-Nuremberg, 2008.
- [Grei 66] K. Greisen. “End to the Cosmic-Ray Spectrum?”. *Phys. Rev. Lett.*, Vol. 16, pp. 748–750, Apr 1966.
- [Grup 05] C. Grupen. *Astroparticle Physics*. Springer, 2005.
- [Guil 11] G. Guillard and J. Brunner. “On neutrino oscillations searches with ANTARES”. *Proc. 32nd Int. Cosmic Ray Conf.*, 2011.

- [Guri 95] Gurin, R. and Maslennikov, A. *ControlHost: Distributed Data Handling Package*. 1995.
- [Hain 04] S. Haino *et al.* “Measurements of primary and atmospheric cosmic-ray spectra with the BESS-TeV spectrometer”. *Physics Letters B*, Vol. 594, p. 35, 2004.
- [Hain 88] T. Haines, C. Bratton, D. Casper, A. Ciocio, R. Claus, M. Crouch, S. Dye, S. Errede, W. Gajewski, M. Goldhaber, T. Haines, T. Jones, D. Kielczewska, W. Kropp, J. Learned, J. Losecco, J. Matthews, R. Miller, M. Mudan, L. Price, F. Reines, J. Schultz, S. Seidel, E. Shumard, D. Sinclair, H. Sobel, L. Sulak, R. Svoboda, G. Thornton, and J. V. D. Velde. “Neutrinos from SN1987a in the IMB detector”. *Nuclear Instruments and Methods in Physics Research Section A: Accelerators, Spectrometers, Detectors and Associated Equipment*, Vol. 264, No. 1, pp. 28 – 31, 1988.
- [Hama] “Hamamatsu Photonics K.K.”. <http://www.hamamatsu.com>.
- [Hans 98] P. C. Hansen. *Rank-deficient and discrete ill-posed problems: numerical aspects of linear inversion*. Society for Industrial and Applied Mathematics, Philadelphia, PA, USA, 1998.
- [Heij 02] A. Heijboer. “An algorithm for track reconstruction in ANTARES”. *Antares Internal Note*, 2002.
- [Heij 04] A. Heijboer. *Track Reconstruction and Point Source Searches with ANTARES*. PhD thesis, University of Amsterdam, 2004.
- [Hira 87] K. Hirata *et al.* “Observation of a neutrino burst from the supernova SN1987A”. *Phys. Rev. Lett.*, Vol. 58, pp. 1490–1493, Apr 1987.
- [Hoer 04] J. R. Hoerandel. “Models of the Knee in the Energy Spectrum of Cosmic Rays”. *Astropart. Phys.*, Vol. 21, p. 241, 2004.
- [Hond 01] M. Honda, T. Kajita, K. Kasahara, and S. Midorikawa. “Comparison of 3-dimensional and 1-dimensional schemes in the calculation of atmospheric neutrinos”. *Phys. Rev. D*, Vol. 64, p. 053011, Aug 2001.
- [Hond 04] M. Honda, T. Kajita, K. Kasahara, and S. Midorikawa. “New calculation of the atmospheric neutrino flux in a three-dimensional scheme”. *Phys. Rev. D*, Vol. 70, p. 043008, Aug 2004.
- [Hond 07] M. Honda, T. Kajita, K. Kasahara, S. Midorikawa, and T. Sanuki. “Calculation of atmospheric neutrino flux using the interaction model calibrated with atmospheric muon data”. *Phys. Rev. D*, Vol. 75, p. 043006, Feb 2007.

- [Huba 99] F. Hubaut. *Optimisation et caractérisation des performances d'un télescope sous-marin a neutrinos pour le projet ANTARES*. PhD thesis, Université de la Méditerranée, 1999.
- [Höck 96] A. Höcker and V. Kartvelishvili. "SVD approach to data unfolding". *Nuclear Instruments and Methods in Physics Research Section A: Accelerators, Spectrometers, Detectors and Associated Equipment*, Vol. 372, No. 3, pp. 469 – 481, 1996.
- [Ianc 04] E. Iancu, K. Itakura, and S. Munier. "Saturation and BFKL dynamics in the HERA data at small x". *Phys. Lett. B*, Vol. 590, p. 199, 2004.
- [Inge 97] G. Ingelman, A. Edin, and J. Rathsmann. "LEPTO 6.5 - A Monte Carlo generator for deep inelastic lepton-nucleon scattering". *Computer Physics Communications*, Vol. 101, No. 1-2, pp. 108 – 134, 1997.
- [Jack 99] J. D. Jackson. *Classical electrodynamics*. Wiley, New York, NY, 3rd Ed., 1999.
- [Jong 05a] M. de Jong. "The ANTARES Trigger Software". *Antares Internal Note*, 2005.
- [Jong 05b] M. de Jong. "The ARS AVC calibration". *Antares Internal Note*, 2005.
- [Jong 09] M. de Jong. "The TriggerEfficiency program". *Antares Internal Note*, 2009.
- [Jong 10] M. de Jong. "The probability density function of the arrival time of light". *Antares Internal Note*, 2010.
- [Kaid 86] A. B. Kaidalov and O. I. Piskunova. "Inclusive spectra of baryons in the quark-gluon strings model". *Zeitschrift für Physik C Particles and Fields*, Vol. 30, pp. 145–150, 1986.
- [Katz 06a] U. Katz. "KM3NeT: Towards a km<sup>3</sup> Mediterranean neutrino telescope". *Nuclear Instruments and Methods in Physics Research Section A: Accelerators, Spectrometers, Detectors and Associated Equipment*, Vol. 567, No. 2, pp. 457 – 461, 2006. VLVnT2 - Proceedings of the 2nd International Workshop on Very Large Volume Neutrino Telescopes, 2nd International Workshop on Very Large Volume Neutrino Telescopes.
- [Katz 06b] U. F. Katz. "Neutrino telescoping in the Mediterranean sea". *Prog. Part. Nucl. Phys.*, Vol. 57, pp. 273–282, 2006.
- [Keln 67] S. R. Kel'ner. *Sov. J. Nucl. Phys.*, Vol. 5, p. 778, 1967.
- [Klim 01] S. I. Klimushin, E. V. Bugaev, and I. A. Sokalski. "Precise parametrizations of muon energy losses in water". 2001. Contribution to the 27th ICRC, Hamburg.

- [Knie 06] B. A. Kniehl and G. Kramer. “Charmed-hadron fragmentation functions from CERN LEP1 revisited”. *Phys. Rev. D*, Vol. 74, p. 037502, Aug 2006.
- [Kopp 09] C. Kopper. “A software framework for KM3NeT”. *Nuclear Instruments and Methods in Physics Research Section A: Accelerators, Spectrometers, Detectors and Associated Equipment*, Vol. 602, No. 1, pp. 107 – 110, 2009. Proceedings of the 3rd International Workshop on a Very Large Volume Neutrino Telescope for the Mediterranean Sea.
- [Kwie 97] J. Kwiecinski, A. D. Martin, and A. M. Stasto. “Unified BFKL and Gribov-Lipatov-Altarelli-Parisi description of  $F_2$  data”. *Phys. Rev. D*, Vol. 56, pp. 3991–4006, Oct 1997.
- [Laws 95] C. Lawson and R. Hanson. *Solving least squares problems. Classics in applied mathematics*, SIAM, 1995.
- [Lear 95] J. G. Learned and S. Pakvasa. “Detecting  $\nu_\tau$  oscillations at PeV energies”. *Astroparticle Physics*, Vol. 3, No. 3, pp. 267 – 274, 1995.
- [Leo 94] W. Leo. *Techniques for nuclear and particle physics experiments: a how-to approach*. Springer, 1994.
- [Lipa 00] P. Lipari. “The geometry of atmospheric neutrino production”. *Astroparticle Physics*, Vol. 14, No. 3, pp. 153 – 170, 2000.
- [Lipa 93] P. Lipari. “Lepton spectra in the earth’s atmosphere”. *Astroparticle Physics*, Vol. 1, No. 2, pp. 195 – 227, 1993.
- [Luce 00] S. G. Lucek and A. R. Bell. “Non-linear amplification of a magnetic field driven by cosmic ray streaming.”. *Monthly Notices of the Royal Astronomical Society*, Vol. 314, pp. 65–74, 2000.
- [Maki 62] Z. Maki, M. Nakagawa, and S. Sakata. “Remarks on the Unified Model of Elementary Particles”. *Progress of Theoretical Physics*, Vol. 28, No. 5, pp. 870–880, 1962.
- [Mark 61] Markov and Zheleznykh. “On high energy neutrino physics in cosmic rays”. *Nuclear Physics*, Vol. 27, No. 3, pp. 385–394, 1961.
- [Mart 02a] A. D. Martin, R. G. Roberts, W. J. Stirling, and R. S. Thorne. “NNLO global parton analysis”. *Phys. Lett. B*, Vol. 531, p. 216, 2002.
- [Mart 02b] A. Martin, R. Roberts, W. Stirling, and R. Thorne. *The European Physical Journal C - Particles and Fields*, Vol. 23, pp. 73–87, 2002.
- [Mart 03] A. Martin, M. Ryskin, and A. Stasto. “Prompt neutrinos from atmospheric  $c\bar{c}$  and  $b\bar{b}$  production and the gluon at very small x”. *Acta Phys. Pol. B*, p. 3273, 2003.

- [Mie 08] G. Mie. “Beiträge zur optik trüber medien, speziell kolloidaler metallösungen”. *Ann. der Physik*, Vol. 25, pp. 377–445, 1908.
- [Miov 01] P. Miočinović. *Muon energy reconstruction in the Antarctic Muon And Neutrino Detector Array (AMANDA)*. PhD thesis, University of California, Berkeley, 2001.
- [Mira 02] R. Mirani. “Parametrisation of EM-showers in the ANTARES detector volume”. 2002. Doctoral Thesis.
- [Mo 69] L. W. Mo and Y. S. Tsai. “Radiative Corrections to Elastic and Inelastic ep and up Scattering”. *Rev. Mod. Phys.*, Vol. 41, pp. 205–235, Jan 1969.
- [Mont] T. Montaruli and J. C. Diaz-Velez. “NeutrinoFlux”. [http://www.icecube.wisc.edu/~tmontaruli/neutrinoflux/NeutrinoFlux\\_Teresa.html](http://www.icecube.wisc.edu/~tmontaruli/neutrinoflux/NeutrinoFlux_Teresa.html).
- [Naga 84] M. Nagano, T. Hara, Y. Hatano, N. Hayashida, S. Kawaguchi, K. Kamata, T. Kifune, and Y. Mizumoto. “Energy spectrum of primary cosmic rays between  $10^{14.5}$  and  $10^{18}$  eV”. *Journal of Physics G: Nuclear Physics*, Vol. 10, No. 9, p. 1295, 1984.
- [NASAa] NASA. <http://nssdc.gsfc.nasa.gov/space/model/models/igrf.html>.
- [NASAb] NASA. <http://www.ngdc.noaa.gov/IAGA/vmod/igrf.html>.
- [Niko 96] N. Nikolaev, G. Piller, and B. Zakharov. “Inclusive heavy-flavor production from nuclei”. *Zeitschrift für Physik A Hadrons and Nuclei*, Vol. 354, pp. 99–105, 1996.
- [Pete 83] C. Peterson, D. Schlatter, I. Schmitt, and P. M. Zerwas. “Scaling violations in inclusive  $e^+e^-$  annihilation spectra”. *Phys. Rev. D*, Vol. 27, pp. 105–111, Jan 1983.
- [Povh 02] N. Povh, K. Rith, C. Scholz, and F. Zetsche. *Particles and Nuclei: An Introduction to the Physical Concepts*. Springer, 3rd Ed., 2002.
- [Pump 02a] J. Pumplin *et al.* “New generation of parton distributions with uncertainties from global QCD analysis”. *JHEP*, Vol. 07, p. 012, 2002.
- [Pump 02b] J. Pumplin, D. R. Stump, J. Huston, H. L. Lai, P. Nadolsky, and W. K. Tung. “New Generation of Parton Distributions with Uncertainties from Global QCD Analysis”. *JHEP*, Vol. 0207, p. 012, 2002.
- [Rapi 09] P. A. Rapidis. “The NESTOR underwater neutrino telescope project”. *Nucl. Instrum. Meth.*, Vol. A602, pp. 54–57, 2009.
- [Rayl 71] L. Rayleigh. *Phil. Mag.*, Vol. 41, pp. 107–120, 274–279, 1871.

- [Revi 06] “Review of Particle Physics”. *Journal of Physics G*, Vol. 33, p. 1+, 2006.
- [Revi 11] “Review of Particle Physics”. *Journal of Physics G*, Vol. 37, p. 1+, 2011.
- [Rivi 12] C. Rivière. “Run-by-run Monte Carlo simulation for ANTARES: v2”. *Antares Internal Note*, 2012.
- [Roes 98] S. Roesler, R. Engel, and J. Ranft. “Photoproduction off nuclei: Particle and jet production”. *Phys. Rev. D*, Vol. 57, pp. 2889–2902, Mar 1998.
- [ROOT] “ROOT. A Data Analysis Framework”. <http://root.cern.ch/drupal/>.
- [Sanu 00] T. Sanuki *et al.* “Precise Measurement of Cosmic-Ray Proton and Helium Spectra with the BESS Spectrometer”. *The Astrophysical Journal*, Vol. 545, No. 2, p. 1135, 2000.
- [Sanu 07] T. Sanuki, M. Honda, T. Kajita, K. Kasahara, and S. Midorikawa. “Study of cosmic ray interaction model based on atmospheric muons for the neutrino flux calculation”. *Phys. Rev. D*, Vol. 75, p. 043005, Feb 2007.
- [Seni 92] J. Senior. *Optical Fiber Communications: Principles and Practice*. Prentice-Hall, Englewood Cliffs, NJ, 1992.
- [Smit 37] F. Smithies. “The eigenvalues and singular values of integral equations”. *Proc. London Math. Soc.*, Vol. 43, pp. 255–279, 1937.
- [Soye 07] G. Soyez. “Saturation QCD predictions with heavy quarks at HERA”. *Phys. Lett. B*, Vol. 655, p. 32, 2007.
- [Take 98] M. Takeda, N. Hayashida, K. Honda, N. Inoue, K. Kadota, F. Kaki-moto, K. Kamata, S. Kawaguchi, Y. Kawasaki, N. Kawasumi, H. Kitamura, E. Kusano, Y. Matsubara, K. Murakami, M. Nagano, D. Nishikawa, H. Ohoka, N. Sakaki, M. Sasaki, K. Shinozaki, N. Souma, M. Teshima, R. Torii, I. Tsushima, Y. Uchihori, T. Yamamoto, S. Yoshida, and H. Yoshii. “Extension of the Cosmic-Ray Energy Spectrum beyond the Predicted Greisen-Zatsepin-Kuzmin Cutoff”. *Phys. Rev. Lett.*, Vol. 81, pp. 1163–1166, Aug 1998.
- [Thun 96] M. Thunman, G. Ingelman, and P. Gondolo. “Charm production and high energy atmospheric muon and neutrino fluxes”. *Astroparticle Physics*, Vol. 5, pp. 309 – 332, 1996.
- [Tsun 11] Y. Tsunesada *et al.* *Proc. 32th Int. Cosmic Ray Conf.*, 2011.
- [Volk 85] L. Volkova. “Neutrino detection at large distances from accelerators”. *Il Nuovo Cimento C*, Vol. 8, pp. 552–578, 1985.

- [Volk 87] L. Volkova, W. Fulgione, P. Galeotti, and O. Saavedra. “Prompt-muon production in cosmic rays”. *Il Nuovo Cimento C*, Vol. 10, pp. 465–476, 1987.
- [Wins 08] A. L. Winslow. *First Solar Neutrinos from KamLAND: A Measurement of the  $^8B$  Solar Neutrino Flux*. PhD thesis, University of California, Berkeley, 2008.
- [Zats 66] G. T. Zatsepin and V. A. Kuz'min. “Upper limit of the spectrum of cosmic rays”. *JETP Lett.*, Vol. 4, pp. 78–80, 1966.
- [Zhan 97] Z. Zhang. “Parameter estimation techniques: A tutorial with application to conic fitting”. *Image and Vision Computing Journal*, Vol. 15, p. 59, 1997.
- [Zorn 05] J. Zornoza. *Sensitivity to diffuse fluxes and energy spectrum reconstruction in the Antares neutrino telescope*. PhD thesis, Universitat de València, Spain, 2005.



# SUMMARY

Cosmic rays are highly energetic particles, mostly protons, that arrive at our Earth from various astrophysical sources. The identification of these sources as well as the mechanisms that accelerate particles to such high energies are topics of great interest in modern day research. The topic of this work is the measurement of the atmospheric neutrino energy spectrum. Atmospheric neutrinos are produced in the interactions of cosmic ray particles with nuclei in the Earth's atmosphere. Secondary hadrons, produced in these high energy collisions, decay and among the products of these decays are neutrinos. The study of the atmospheric neutrino energy distribution can provide insight and valuable information on the high energy collision processes that take place in the atmosphere and are outside the energy reach of present day accelerators, as well as on the intensity of the cosmic ray spectrum. Additionally, atmospheric neutrinos constitute the irreducible background for searches of cosmic neutrinos, which are produced in the vicinity of the cosmic rays' sources. A precise knowledge of the background can significantly enhance the sensitivity for cosmic neutrino source searches.

The ANTARES detector is a neutrino telescope, located at a depth of 2475 m on the bottom of the Mediterranean sea. It consists of 12 vertically positioned flexible strings, equipped with a total of 885 photomultiplier tubes that detect light produced by muons traversing the instrumented volume. These muons can be products of collisions of cosmic rays in the atmosphere, but more importantly, they can be the products of charged current neutrino interactions in the vicinity of the detector. The time, position and pulse height of the hits recorded on the photomultipliers provide the necessary information to reconstruct the direction of the muons with high precision. The muon direction is very close to the neutrino direction, therefore the ANTARES detector is primarily used as a telescope.

Another important quantity characterizing each track, other than its direction, is its energy. This is especially relevant for the measurement described in this work. As muons travel through the ANTARES detector, they lose energy through a variety of processes. The amount of light emitted through these energy-loss processes is almost proportional to the energy of the muon. A maximum likelihood based method was developed for the reconstruction of the muon energy. It uses the time, position and pulse height of each hit and attempts to find the muon energy that maximizes the agreement between the observed hit signature at the detector and the expected amount of light for a given muon

energy. The expected amount of light for a given photomultiplier tube and time window is calculated as a function of the muon energy, taking into account the absorption and scattering of light in water, as well as the electronics response of the phototubes. A resolution better than 0.4 - 0.3 in the logarithm of the energy is achieved throughout the whole energy range we consider, namely from 100 GeV to a few hundreds of TeV.

The vast majority of detected events in ANTARES are due to atmospheric muons. For the work presented here, this is a background that needs to be suppressed. Since muons, in contrast to neutrinos, cannot traverse the Earth, a directional cut where only upward going events are selected reduces this background significantly. There are still, however, atmospheric muons present after this cut due to downward going events mis-reconstructed as upward going. A cut on the quality of the track-reconstruction suppresses the muon background to levels below 1%. The selection criteria ensure a pure sample of very well-reconstructed events, and consequently an increased performance of the energy reconstruction.

The shape of the reconstructed muon energy distribution is different from the shape of the atmospheric neutrino energy spectrum at the surface of the Earth, which is the goal of this measurement. The reason for that is the limited energy resolution as well as the overall acceptance of the ANTARES detector. The transformation between the reconstructed muon energy distribution and the atmospheric neutrino energy distribution is described by a response matrix, determined from Monte Carlo simulations. The problem at hand belongs to a class of problems called ill-posed problems. A direct inversion of the transformation matrix is not sufficient and a different approach is implemented. A singular value decomposition is performed on the matrix and the solution is written as a series expansion. In addition, to suppress components in this expansion that predominantly contribute statistical noise, a constraint is imposed that controls the smoothness of the solution, effectively filtering out insignificant terms.

A measurement of the atmospheric neutrino energy spectrum in the range of  $10^{2.5}$  GeV to  $10^{5.3}$  GeV has been performed. The result obtained is compatible with the theoretical predictions and the measurements performed by the AMANDA and IceCube collaborations. The systematic uncertainties of the measurement have been estimated and the largest contributions arise from uncertainties in light propagation in water and the efficiency of the photomultiplier tubes. The limited statistics at the highest energies also affect the final result uncertainties. The next generation of neutrino telescopes will provide tighter constraints in these uncertainties and a more precise determination of the atmospheric neutrino energy spectrum reaching much higher energies.

# SAMENVATTING

Kosmische stralen zijn hoog-energetische deeltjes, voornamelijk protonen, die richting Aarde geschoten worden door verschillende astrofysische bronnen. Zowel het bepalen van de bronnen als de mechanismes die de deeltje versnellen tot zulke hoge energieën zijn onderwerpen die van groot belang zijn in het hedendaagse onderzoek. Het onderwerp van dit werk is de meting van het energiespectrum van atmosferische neutrino's. Atmosferische neutrino's worden geproduceerd in interacties van kosmische deeltjes met kernen in de atmosfeer. Secundaire hadronen, geproduceerd in deze hoge energetische botsingen, vervallen en onder de producten van deze vervallen zijn neutrino's te vinden. De studie van de energieverdeling van atmosferischeneutrino's kan inzicht en waardevolle informatie geven over de hoog energetische botsingsprocessen die plaatsvinden in de atmosfeer en buiten het bereik zijn van het energiebereik van huidige versnellers. Ook bepalen atmosferische neutrino's de irreducibele achtergrond voor zoektochten naar kosmische neutrino's welke geproduceerd worden in de nabijheid van bronnen van kosmische straling.

De ANTARES detector is een neutrinotelescoop, geplaatst op een diepte van 2475 m op de bodem van de Middelandse Zee. Het bestaat uit 12 verticaal gepositioneerde flexibele kabels, uitgerust met in totaal 885 fotoversterkerbuizen, die licht detecteren, geproduceerd door muonen die door de detector heenreizen. Deze muonen kunnen het product zijn van botsingen van kosmische stralen in de atmosfeer, maar, zij kunnen ook het product zijn van geladen-stroom neutrino-interacties in de nabijheid van de detector. De tijd, positie en lading van het signaal afgegeven in de fotoversterkerbuis bevat genoeg informatie om de oorspronkelijke richting van de muonen met hoge precisie te achterhalen. De muonrichting is bijna gelijk aan de neutrinorichting, daarom kan de ANTARES detector gebruikt worden als telescoop.

Een ander belangrijk kenmerk waarmee ieder spoor gekarakteriseerd wordt is behalve zijn richting zijn energie. Dit is vooral belangrijk voor de meting beschreven in dit werk. Wanneer muonen door de ANTARES detector heenreizen verliezen ze energie aan diverse processen. De mate waarin een muon energie verliest is proportioneel met de hoeveelheid licht die wordt uitgezonden door deze energie verlies interacties. Een maximale waarschijnlijkheidsanalyse is ontwikkeld voor de reconstructie van de muon energie. Het gebruikt tijd, positie en lading van iedere signaal en probeert de muon energie te vinden waarvoor de overeenkomst tussen signaal vorm in de detector en

verwachte hoeveelheid licht voor een bepaalde muonenergie maximaal is. De verwachte hoeveelheid licht voor een gegeven fotoversterkerbuis en tijdstip wordt berekend als een functie van de muonenergie, daarbij worden de absorptie en verstrooiing van licht in water meegenomen, en ook de elektronische reactie van de fotobuizen. Een resolutie van meer dan 0.4 - 0.3 in het logaritme van de energie wordt bereikt voor het hele energie gebied van 100 GeV tot een paar honderd TeV die we hier bekijken. De overgrote meerderheid van gemeten gebeurtenissen in ANTARES worden veroorzaakt door atmosferische muonen. In het werk gepresenteerd in dit proefschrift worden deze als een achtergrond beschouwd die onderdrukt moet worden. Omdat muonen, in tegenstelling tot neutrino's niet door de Aarde heen kunnen reizen volstaat het om selectiecriteria op te leggen, waarbij alleen opwaartsgaande gebeurtenissen worden geselecteerd. Dit reduceert de achtergrond al enorm. Hoewel er nog steeds atmosferische muonen aanwezig zijn na deze selectie vanwege neerwaartse sporen die fout gereconstrueerd worden als opwaartse. De muon achtergrond tot een niveau onder 1% onderdrukt door een snede op de kwaliteit van de spoor reconstructie. De selectie waarborgt een puur monster van goed gereconstrueerde gebeurtenissen en dus ook een verhoogde prestatie van de energiereconstructie.

De vorm van de energieverdeling van gereconstrueerde muonen is verschillend van die van atmosferische neutrino's op het oppervlak van de Aarde, wat het doel is van de meting. De reden hiervoor is dat de beperkte energiebepaling als ook de algehele acceptantie van de ANTARES detector. De overgang van de energieverdeling van de gereconstrueerde muonen naar die van de atmosferische neutrino's wordt beschreven door een responsmatrix, bepaald door Monte Carlo simulaties. Het huidige probleem behoort toe aan een klasse van problemen die de zwak-geformuleerde of ill-posed problemen worden genoemd. Een directe inversie van de overgangsmatrix is niet voldoende en er is dus een andere aanpak geïmplementeerd. Een singuliere waardeontbinding wordt uitgevoerd op de matrix en de oplossing wordt geschreven als een machtreeksonwikkeling. Om componenten te onderdrukken in deze machtreeks die vooral bijdragen aan statistische ruis, wordt een beperking opgelegd die de gladheid van de oplossing controleert, waarbij effectief de onbelangrijke termen eruit worden gefilterd.

Een meting van het energiespectrum in het bereik van  $10^{2.5}$  GeV to  $10^{5.3}$  GeV van atmosferische neutrino's is uitgevoerd. Het verkregen resultaat komt overeen met theoretische voorspellingen en de metingen uitgevoerd bij de AMANDA en IceCube laboraties. De systematische onzekerheden van de meting zijn bepaald en de belangrijkste bijdragen worden veroorzaakt door de onzekerheden in de voorplanting van licht in water en de efficiëntie van fotoversterkerbuizen. De beperkte statistiek bij de hoogste energieën beïnvloedt de uiteindelijke onzekerheden. De volgende generatie van neutrino telescopen zullen strengere beperkingen op deze onzekerheden leggen en een preciezere bepaling van het het energiespectrum vooral bij hogere energieën mogelijk maken.

# ACKNOWLEDGEMENTS

It has been undoubtedly a rewarding journey. And the fact that it is complete is not one man's work alone. Many people have contributed in various ways to the completion of this thesis and I want to thank them here. I sincerely apologize to those that I forget due to my own fault, for I certainly do.

Paul Kooijman has been an excellent supervisor, with a deep knowledge and understanding of physics. Working next to him all these years gave me the opportunity to absorb some of this knowledge and have many fascinating discussions on physics; every now and again shifting our conversations to politics. I want to express my sincere thanks to Patrick Decowski who has taught me a lot, from the more technical aspects of this work, to the set of skills necessary to become a better physicist. Both of my advisors have been very supportive and I thank them for believing in me and providing me with confidence and courage, especially when my *reservoir* seemed to be running dry.

Maarten de Jong's work on the probability density functions has proved invaluable for the determination of the muon energy. I am grateful for the support he provided in many ways during my stay at Nikhef. I am thankful to Gerard van der Steenhoven and Els de Wolf for introducing me to the ANTARES crew, marking the start of this unique chapter in my life. I am very glad I had the chance to be part of the same group as Aart Heijboer and Claudio Kopper. I thank them for making their knowledge available to me when I needed it. I also want to thank all my collaborators in ANTARES and especially Maurizio Spurio, Cristina Carloganu, Juan de Dios Zornoza, Fabian Schüssler and Jutta Schnabel for their useful comments and discussions. I want to thank Tim Adye, the author of *RooUnfold*, for promptly replying and clarifying my questions. I also want to thank all the great physics and math mentors I met and worked together throughout the years I study physics; Piet Mulders, Stan Bentvelsen, Giorgos Lalazisis, Christos Eleftheriadis, Anastasios Liolios, Efthimios Palioselitis.

Eleonora Presani, I am so happy I had the chance to share an office with you at Nikhef. And that was only the beginning. Delicious dinners, doing Karate together, even your disapproval of my choice of a MacBook over a PS3. I would never exchange this experience for anything. Corey Reed, we attended the most awesome music festival ever in Madrid. 'Nough said! Lisa Hartgring, thank you for the unforgettable semi-spontaneous dinners and the *musica* intermezzos. I also want to thank Claudio Bogazzi,

for all the good times at Nikhef, watching each other's back when defending IMP from intruders and his motivating demotivational posters. The experience of working at Nikhef was infinitely enhanced by the presence of Tri Astraatmadja, Gordon Lim, Ching Cheng Hsu, Giada Carminati and Guus Wijnker. I want to thank all the great people I met during the last few years at Nikhef; Dorothea Samtleben, Mieke Bouwhuis, Joerg Mechnich, Jeroen Snijdwint, Jelena Petrovic, Tino Michel, Erwin Visser, Stephan Schulte, Siphon van der Putten, Hegoi Garitaonandia. I also wish to thank Teus van Egdome and Ed van Willigen for making all aspects of my stay at Nikhef, with the exception of research itself, so much easier.

Whatever I say about Menelaos Tsiakiris will not be enough. Thank you for the amazing MSc-PhD-trip we had together in the Netherlands, from the containers in the West to the neighborhood of Science Park. And the physics, the music, the food . . . . Miłosz Panfil has been a good friend. Thank you for the great times we had and our endless discussions on physics. Or on our twisted perception of what psychology and sociology is all about. I am more than grateful to Maria Tselengidou for the delicious muffins that gave me enough strength to work until past dinner time, her patience with a PhD candidate/patient in his last steps and so much more. Alexis Gillett, Susanne Waaijers, Chris White and Christian Mildner, thank you for the wonderful time we had playing music together, whether it was rock nights or jazz afternoons, among other reasons. Nefeli Georgoulia, thank you for the amazing time we spent together in Newtonstraat and a couple of other places around the globe. Cheers to Akis Gkaitatzis and Nikos Tsirintanis for all the fun times in Amsterdam and at Nikhef. My thanks, of course, to Vili Zampeli for the excellent dishes she prepared and for contributing significantly to the liveliness of our house every time she visited us. Andreas Stergiou and Dimitrios Korres, thank you for the beautiful memories I have from our living together as flatmates.

Many thanks to all my friends from Greece for being just that, friends who sent their words of support, and for all the experiences we shared so far and more that are still coming. That is a promise. My thanks to Elena Palioseliti, Giannis *Messlund Lump*tn Messaris, Sotiris Balatzis, George Balatzis, Eleni Siasiou, Theodore Pasahidis, Vassilis Kostopoulos, Asterios Kyriakou, Irimi Papachristou, Kostas Savvidis and of course to my beloved godparents, Kiki and Paschalis Kouimtzidis.

And finally, my family. My mother, my father, my grandmother and my grandfather, for always being there, supporting my choices. You know that none of this would have been possible without your help.

Dimitrios Palioselitis  
Amsterdam 2012